Cross-shell interactions at the $\mathrm{N} = 28$ shell closure via ^{47}K(d,p)^{48}K and ^{47}K(d,t)^{46}K

Charlie J. Paxman

Submitted for the degree of Doctor of Philosophy

Principal Supervisor: Prof. Wilton N. Catford
Secondary Supervisor: Dr. Daniel T. Doherty
Collaborative Supervisor: Dr. Adrien Matta

March 2024

Declaration of Originality

This thesis and the work to which it refers are the results of my own efforts. Any ideas, data, images or text resulting from the work of others (whether published or unpublished, and including any content generated by a deep learning/artificial intelligence tool) are fully identified as such within the work and attributed to their originator in the text, bibliography or in footnotes. This thesis has not been submitted in whole or in part for any other academic degree or professional qualification. I agree that the University has the right to submit my work to the plagiarism detection service TurnitinUK for originality checks. Whether or not drafts have been so-assessed, the University reserves the right to require an electronic version of the final document (as submitted) for assessment as above. The results of this thesis, outlined in Chapters 5 and 6, are being prepared for publication in forthcoming peer-reviewed journals.

Charlie J. Paxman
March 2024
Guildford, UK

Abstract

The evolution of shell closures in the region of $Z \leq 20$ and $N \geq 28$ is a topic of particular interest in the field of nuclear structure. It has been observed that the standard magic number $N = 28$ weakens in this region, and shell gaps begin to emerge at $N = 32, 34$. As such, there is considerable impetus for experimental studies of the cross-shell πsd $\otimes$ νfp interactions, which are expected to influence this shell evolution in proton-deficient $N = 28$ isotones. The isotope ^{48}K is uniquely situated for this purpose, as it is both one proton below $Z = 20$, and one neutron above $N = 28$. Additionally, the neighbouring ^{47}K isotope is known to be primarily $\pi s_{1/2}^{1} d_{3/2}^{4}$ structure in its ground state – as opposed to the naïvely expected $\pi s_{1/2}^{2} d_{3/2}^{3}$ structure, which is dominant in potassium isotopes – allowing the exotic $\pi s_{1/2}$ $\otimes$ νfp interaction to be probed by the selective neutron transfer reaction, ^{47}K(d,p)^{48}K.

The first experimental study of states arising from the interaction between $\pi s_{1/2}$ and the orbitals $\nu p_{3/2}$, $\nu p_{1/2}$ and $\nu f_{5/2}$ has been conducted, by way of the ^{47}K(d,p) reaction in inverse kinematics. The radioactive beam of ^{47}K from the GANIL-SPIRAL1+ facility had a beam energy of 7.7 MeV/nucleon and was of exceptional quality, as it had a typical intensity of 5×10^5 particles per second and was estimated to be $>$ 99.99% pure. The beam impinged upon a 0.32(3) mg/cm^2 CD_2 target. The coupling of the MUGAST-AGATA-VAMOS++ detection systems allowed for triple coincidence gating, providing a great amount of selectivity in the detection of light ejectiles, heavy recoils and prompt γ-ray emissions in transfer and scattering reactions. An analysis based both on excitation and γ-ray energy measurements has revealed many previously unobserved states in ^{48}K, up to and above the neutron separation threshold. Spin-parities and direct transfer spectroscopic factors of these states have been determined.

The experimentally measured excited structure of ^{48}K is compared to calculations performed using two modern shell model calculations, revealing several key failures of these interactions, and indicating areas for improvement. The insights gained from this work have implications extending down the rapidly evolving proton-deficient $N = 28$ isotonic chain, where the singly-occupied $\pi s_{1/2}$ orbital is expected to couple with neutrons in the orbitals immediately above $N = 28$ in the short-lived ^{44}P nucleus.

Acknowledgements

Firstly, I would like to thank my supervisor, Prof. Wilton Catford, for his guidance and kind encouragement over the last three and a half years. I'm very proud to be your student, and extremely grateful to have benefited from your seemingly endless knowledge; if I can gain even a fraction of your understanding of this field, I will count myself lucky. To my supervisor *de l'autre côté de la Manche*, Dr. Adrien Matta – thank you for always being available when things were going wrong, and for encouraging me to get involved in projects outside of my thesis. I look forward to working with you again soon! To Dr. Daniel Doherty, thank you for tackling every administrative challenge single-handedly, while the rest of us were getting distracted with the fun stuff – I really appreciate it. Additionally, I would like to thank Prof. Gavin Lotay, who has been a grounding presence throughout the last year, frequently pulling us out of the rabbit hole.

To my parents, thank you for all your support in getting me to this point. Dad, thank you for encouraging my interest in science; you opened the doors, and I'm pretty happy with the ones that I've walked through. Mum, thank you for believing in me, and teaching me to aim for things beyond the edges of our little town. To my in-laws, thank you for taking me into your home for months at a time, and caring for me when I was recovering from surgery. I'm honoured to be part of your family.

To the people who have made the last few years at Surrey so great – Gee and Joey, Tom and Ben, Reuben and Greg, Chris and Connor, Jacob and Laetitia – thank you. The indelible memories of my PhD won't be crashing codes and melting laptop fans, they will be lunchtime football, Thursday pub quizzes, swimming at the Lido, costume-obligatory Halloween parties and found-family Sunday roasts. I'm so grateful for you all.

And of course, how can I even begin to thank you, Ellie. You are my bedrock, and I absolutely would not have gotten this far without you, and your unending love and support – not least because you have kept me fed, watered, and rested! You are an unstoppable force of positive energy, and eloping with you will always be the best decision of my life. On to the next chapter!

Table of Contents

3 Experiment 29

List of Figures

List of Tables

Chapter 1

Introduction

The atomic nucleus is a uniquely complex and interesting physical system. As a many-body quantum system of non-identical particles, held together by the strong nuclear force, the structure of the nucleus has evaded simple explanations for more than a century. This is not aided by the incredible diversity of nuclei that have been observed; while some theoretical models can describe stable isotopes well, they are frequently stretched to breaking point when attempting to reproduce properties of the most exotic nuclei. As such, experimental examinations of nuclear structure are critical in determining where these theoretical models fail, and in moving towards a universal description of nuclear structure.

In this thesis, experimental measurements of unstable, neutron-rich potassium isotopes are performed, and the results are compared to modern single-particle shell model calculations. This work probes specific interactions that will dominate the structure of nuclei at the edges of what we can observe, and achieves this by exploiting localised phenomena in less extreme nuclear matter. As such, this work is a crucial first step towards future measurements, which may become possible in the coming generations of experimental facilities.

1.1 History and terminology

1.1.1 Major historical discoveries

The field of nuclear physics emerged from a series of critical discoveries in the late 19th and early 20th centuries, where each new development was a significant leap towards our detailed and complex modern understanding of the nucleus.

The discovery of radioactivity in uranium by Henri Becquerel in March of 1896 [1–5] sparked a flurry of scientific advancement, leading rapidly to the discovery of several other radioactive elements by Marie Skłodowska-Curie and Pierre Curie [6, 7], for which the

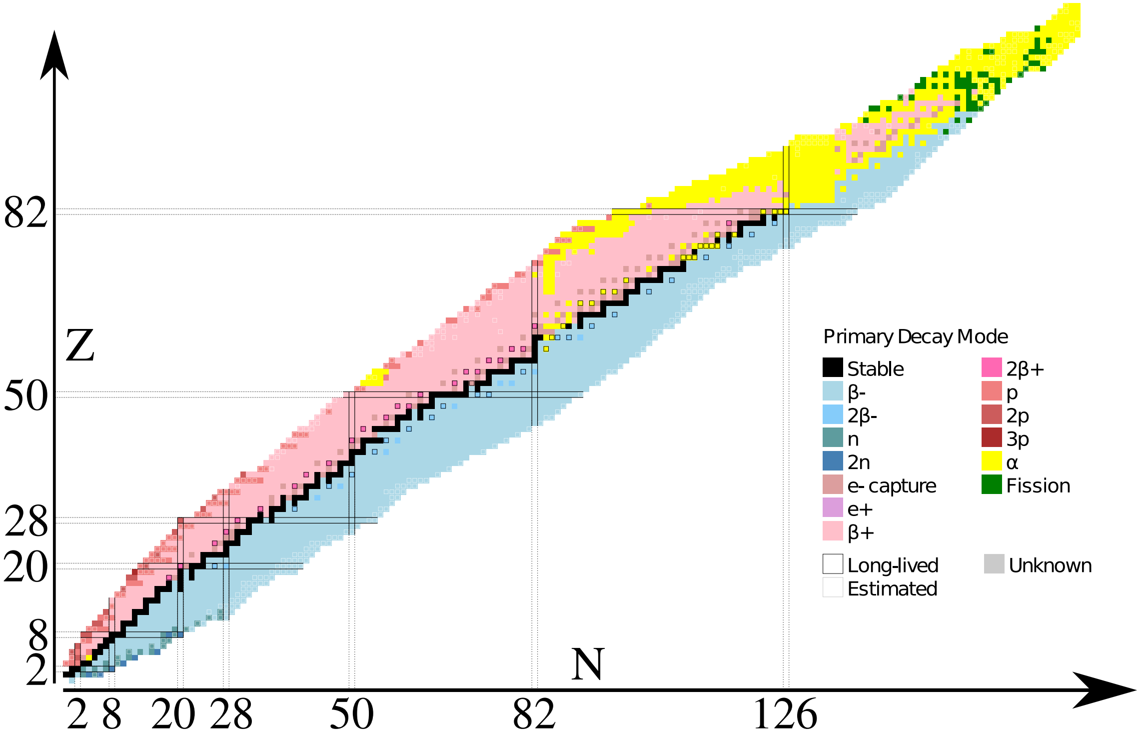

Figure 1.1: The chart of nuclides, where colours indicate the primary method of decay. The most common decay paths are β^- (blue), β^+ (pink), α (yellow) and fission (green). Standard magic numbers are indicated with black lines. Figure adapted from Ref. [13].

three shared the 1903 Nobel prize[1]. Ernest Rutherford then went on to build upon these insights, distinguishing α and β radioactivity in 1899 [8] (γ-rays being observed separately in 1900 by Paul Villard [9]), and then the atomic nucleus in 1911 [10]. This latter discovery laid the groundwork for Niels Bohr's planetary model of the atom [11] – which united quantum theory and nuclear theory – in 1913. The next significant advancement came about some years later with the discovery of the neutron by James Chadwick in 1932 [12]. With this final piece, the well-accepted model of the atom – negative electrons in stationary orbits around a nucleus composed of positively charged protons and uncharged neutrons – fell into place.

1.1.2 Nomenclature

When discussing nuclei, the clearest method of categorisation is by the number of protons and neutrons that form the nucleus. These values are assigned to the letters Z and N, respectively. The sum of these two values is the mass number, A, which is – to a first approximation – about the actual mass of the nucleus in atomic mass units (amu), where 1 amu $= 1.66 \times 10^{-27}$ kg. The nucleus of some element X, with A nucleons, N neutrons and Z protons would be written as ${}^{A}_{Z}\mathrm{X}_{N}$. It is often practical to discuss chains of nuclei that have one of these nuclear numbers in common – perhaps as some feature of structure

---

[1] The same year that Skłodowska-Curie was awarded her doctorate, the first woman in France to do so.

recurs, or breaks, in interesting ways along the chain. These are referred to as *isotopes* when Z is constant, *isotone*s when N is constant, and *isobars* when A is constant.

Much like the periodic table of elements, there is a clear way to organise the nuclear isotopes in a way that is revealing about their nature – by arranging them by Z against N. This chart of nuclides, or Segrè chart, is shown in **Figure 1.1**.

1.2 Magic numbers & the nuclear shell model

In much the same way that atomic structure can be investigated via patterns in ionisation energy in different elements, one revealing glimpse into the structure of nuclei comes from the two-proton (S_{2p}) and two-neutron (S_{2n}) separation energies of different isotopes.

When looking at the change in S_{2n} for the isotopes of a single element, it may be hard to see a pattern, however, when compiling data on a range of elements, distinct regions of rapid change become clear. In **Figure 1.2**, the measured S_{2n} values for the isotopic chains of $_{1}$H to $_{65}$Th are shown. It becomes quickly apparent that there are several distinct values of N after which S_{2n} decreases rapidly; N = 28, 50 and 82 are the clearest examples of this. This behaviour is analogous to the aforementioned ionisation energy of atoms. In the case of atomic elements, the phenomenon was explained by the modelling of electrons filling shells – the significant reduction in ionisation energy was due to the next electron occupying a new shell, which is much more weakly bound than the filled shell beneath.

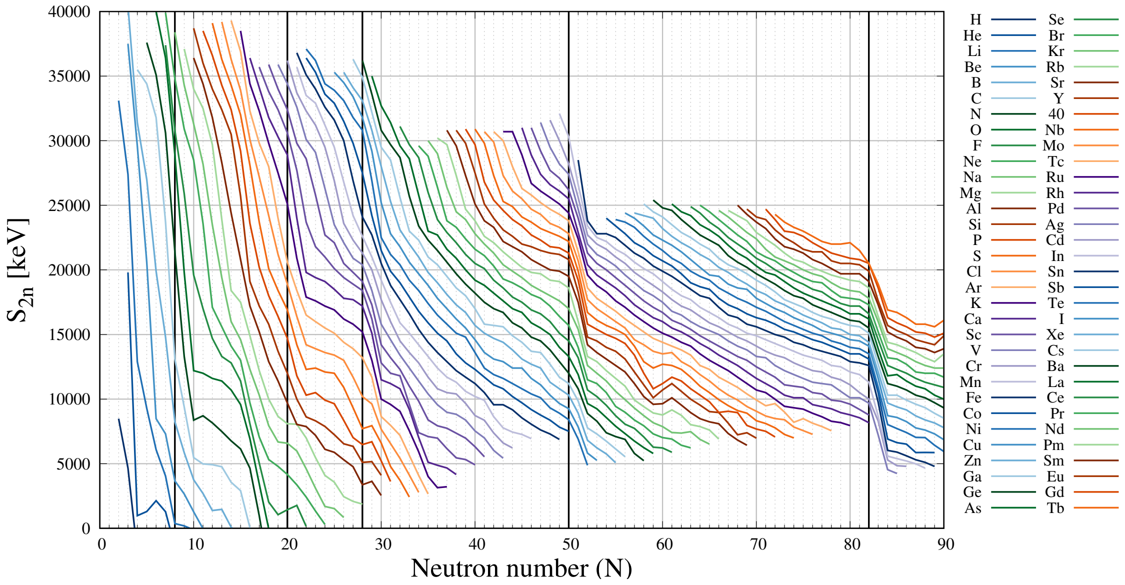

Figure 1.2: Variation in two-neutron separation energies (S_{2n}) of isotopes up to Z = 65 as N increases. Significant decreases in S_{2n} can be seen just after the magic numbers (marked with black lines). These are especially clear at N = 28, 50 and 82.

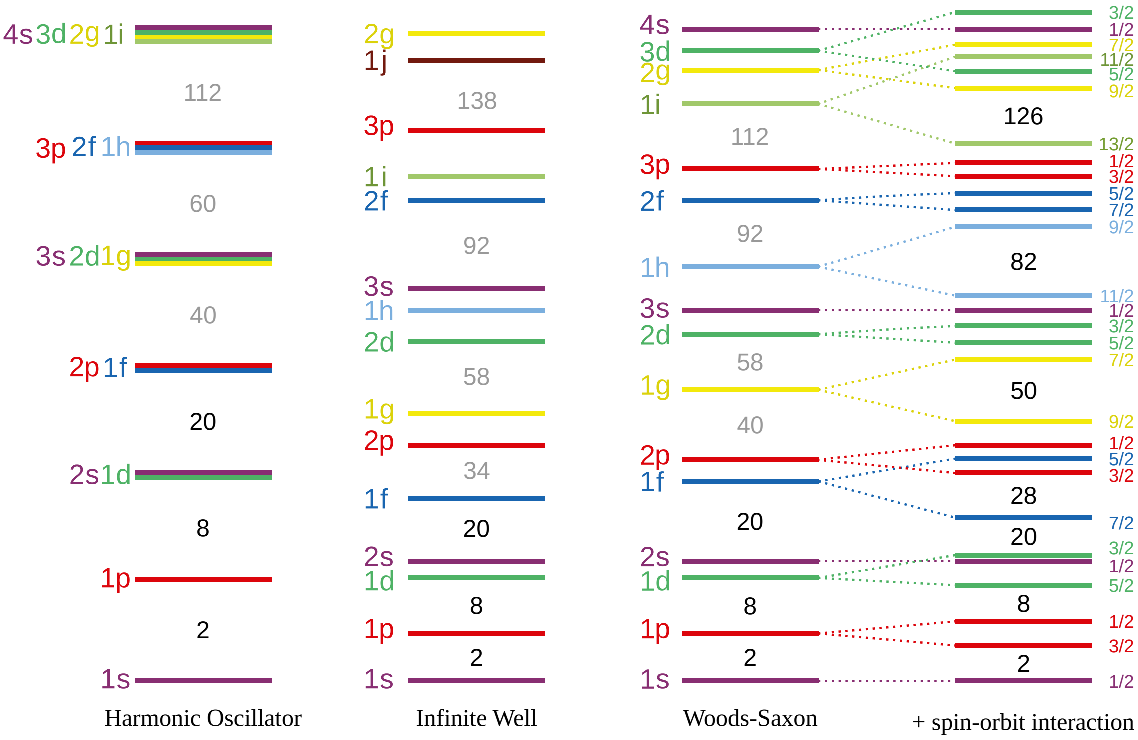

Figure 1.3: Diagram of the nuclear orbitals and magic numbers predicted by the harmonic oscillator and infinite well models, the Woods-Saxon form, and Woods-Saxon with the inclusion of the spin-orbit interaction. Predicted magic numbers are labelled in grey, with those that agree with experimental observations in black. Figure adapted from Ref. [15]

By adopting a similar method, Maria Goeppert Mayer proposed the *nuclear shell model* in 1949 [14], with protons and neutrons filling shells in Z and N; the nucleon numbers where shell closures were observed were named *magic numbers* [15].

The first challenge to developing a nuclear shell model is the establishment of a nuclear potential – what is constraining the nucleons, and how does this affect their quantised energy structure? In the case of a large enough nuclear system, this is best described by the nuclear mean field potential; that is, single nucleons moving in a potential created by the interaction of every other nucleon in the nucleus. After some standard potential models (the infinite well and the harmonic oscillator) failed to accurately recreate the observed magic numbers, a new potential was proposed to more realistically model the expected potential of a nucleus, which was a non-infinite potential well with a smooth rise, rather than a sharp step. This potential, $V(r)$, proposed by R. Woods and D. Saxon [16], has the form,

$$V(r) = \frac{-V_0}{1 + \exp\left[\frac{r-R}{a}\right]}, \tag{1.1}$$

where R is the mean radius of the nucleus, a defines the region over which the smooth rise occurs, and V_0 is the potential well depth. The energy levels resulting from this potential can be seen in **Figure 1.3**. The Woods-Saxon potential predicts magic numbers at 2, 8, 20, 40, 58, 92 and 112 – the first three of these align with experimentally observed values, but then the predictions quickly diverge. This model can be improved further through the introduction of *spin-orbit interactions* [17]. Nuclear energy levels are labelled according to their intrinsic orbital angular momentum ℓ, and the index number n. Levels with $\ell = 0, 1, 2, 3, 4, 5...$ are referred to with the letters s, p, d, f, g, h..., and n is a counter of the levels with that value of ℓ; e.g. the second level with $\ell = 1$ is 2p. This orbital angular momentum ℓ can be coupled to the intrinsic spin of the nucleons, $s = 1/2$, to give the total angular momentum, $j = \ell \pm s$. The spin-orbit potential V_{so} is taken to be

$$V_{so}(r) = V_{\ell s}(r)\boldsymbol{\ell} \cdot \mathbf{s}, \tag{1.2}$$

where $V_{\ell s}(r)$ is largely determined by the gradient of the nuclear density profile for radii near the nuclear surface [18].

The introduction of this nuclear spin-orbit interaction splits each $n\ell$ orbital state (except $\ell = 0$ states) in two, now additionally labelled with the total angular momentum as $n\ell_j$; for example, the state 1d now becomes two states, $1d_{3/2}$ and $1d_{5/2}$. The higher-j state will move down in energy, and vice versa, as can be seen in **Figure 1.3**. With this total angular momentum quantum number established, it is trivial to find the degeneracy of the orbital to be $2j + 1$, in order to satisfy the Pauli exclusion principle [15].

With this level splitting established, there are new major shell closures, now correctly occuring at the experimentally established magic numbers $2, 8, 20, 28, 50, 82$ and 126. Additionally, the mechanism behind the increasing deviation in the earlier Woods-Saxon potential model becomes clear – states with larger ℓ values have a larger spin-orbit energy splitting, characterised in some cases by the equation [18, Eq. 4.7]

$$\mathrm{E}_{\ell+\frac{1}{2}} - \mathrm{E}_{\ell-\frac{1}{2}} = -10(2\ell + 1)\mathrm{A}^{-\frac{2}{3}} \text{ [MeV]} \tag{1.3}$$

which leads to the larger splitting for the 1f, 1g and 1h states that are so crucial in creating the energy gaps at the magic numbers $28, 50$ and 82 [18].

1.3 Motivation for ^{47}K(d,p)^{48}K

The region around ^{48}Ca, at the intersection of N = 28 and Z = 20 shown in **Figure 1.4**, is of great interest for nuclear structure physics. The N = 28 isotopic chain, in particular, has drawn a lot of scientific attention, in part because of a "rich variety of behaviours and shapes" [20] in isotopes moving down from spherical ^{48}Ca to prolate ^{40}Mg [21, 22]. This is one of several indications that the N = 28 magic number fails below Z = 20 as the shell closure weakens, and other shells appear in its place [23]. Another unique feature

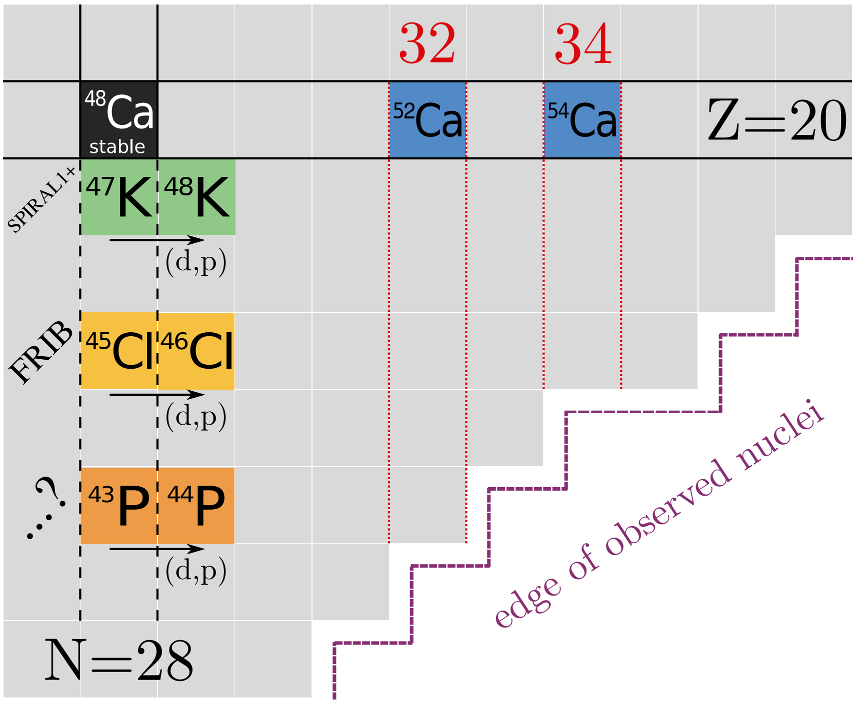

Figure 1.4: Section of the nuclear chart, highlighting the isotopes that are key to the scientific motivation behind ^{47}K(d,p)^{48}K. Magic numbers $N = 28$ and $Z = 20$ are marked, as well as the emergent $N = 32, 34$ shell closures [19]. Experimentally observed nuclei are shown in grey. Isotopes are marked with the experimental facility that could produce that beam.

of the $N = 28$ isotopic chain is the unusual proton configuration of some ground state nuclei, with the degeneracy of two proton orbitals, $2s_{1/2}$ and $1d_{3/2}$, producing two 'sets' of nuclear states of similar energies but with vastly different structures. This can allow for investigations into exotic cross-shell interactions with current radioactive beams, which would otherwise only be accessible through as-yet unavailable beams.

1.3.1 Shell evolution in neutron-rich $Z < 20$ isotopes

While the $N = 28$ shell closure weakens for proton-deficient isotopes, there is evidence that new shell closures may emerge in its place. In 2013, Steppenbeck *et al.* found that the first excited 2^+ state in ^{54}Ca had an energy of 2.04(2) MeV, which is far above the 'baseline' energy of $\approx$ 1 MeV for non-magic isotopes in that chain. These types of discontinuous jumps in the excitation energy of 2^+_1 states "typically [...] indicate the presence of large nuclear shell gaps" [19]. This, unusually, indicates that $^{54}_{20}$Ca$_{34}$ is a doubly-magic nucleus.

This shell gap was predicted by Otsuka *et al.* in 2001 [24]. As can be seen in **Figure 1.5**, for isotopes near stability such as ^{60}Fe, there is a triplet of close ν(fp) orbitals above the $\nu f_{7/2}$ orbital. As protons are removed from this system, the attractive² cross-shell monopole interaction between $\pi f_{7/2}$ and $\nu f_{5/2}$ weakens [25], and the central orbital of the

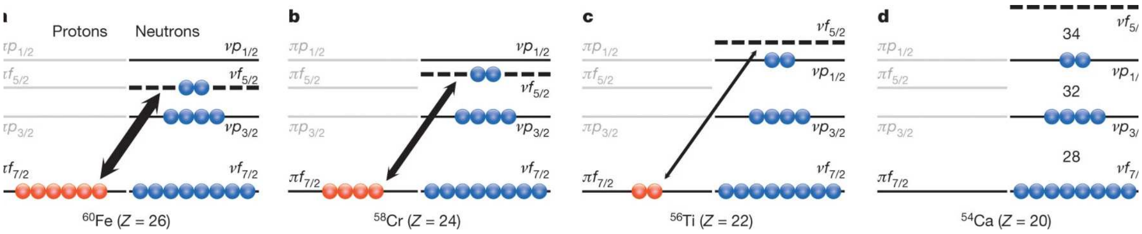

Figure 1.5: Emerging shell gaps at $N = 32, 34$ are expected to arise from the weakening interaction between $\pi f_{7/2}$ and $\nu f_{5/2}$, as $\pi f_{7/2}$ occupancy decreases. Figure from Ref. [19]

shell begins to move higher in energy, leading to a reordering of the neutron orbitals in this region. By ^{54}Ca, the $\nu f_{5/2}$ state has fully escaped the p-shell, and new shell gaps have arisen at $N = 32, 34$ [26].

Given this emergent $N = 34$ magicity at $Z = 20$, there is a significant impetus to investigate how the shells continue to evolve for more exotic proton-deficient isotopes. To examine this, the evolution of these neutron orbitals for $Z < 20$ must be determined.

A good test of this would be to start with the next lightest isotope with a single valence proton and perform a highly selective *direct transfer reaction*[3], placing a neutron into these interesting νfp orbital states. The structure in such a nucleus would be dominated by the proton-neutron interaction (annotated throughout this thesis as $\pi \otimes \nu$) between the two unpaired nucleons, with minor effects from other nucleon-nucleon interactions. An interesting candidate for this would be the $^{43}_{15}P_{28}$ isotope undergoing a (d,p) transfer reaction, as ^{43}P has one proton in $\pi s_{1/2}$ and a filled $\nu f_{7/2}$. This single neutron transfer experiment would allow for cross-shell interactions between this valence proton and a neutron in $\nu p_{1/2}$, $\nu p_{3/2}$ or $\nu f_{5/2}$ to be investigated.

Unfortunately, there is no radioactive beam facility in existence that can yet produce a beam of ^{43}P with enough intensity to perform such an experiment. Many factors contribute to the extreme difficulty of producing this beam. Firstly, ^{43}P is five protons removed from the nearest viable stable target isotope, ^{48}Ca, which makes it unlikely to be produced in a fragmentation reaction. Additionally, the refractory chemical properties of phosphorus "have prevented its escape from commonly employed [beam] production targets" [27], further worsening the achievable beam intensity. These issues are compounded by the short half-life of ^{43}P, 36.5 ± 1.5 ms [28], making experiments with this isotope inaccessible in the current generation of radioactive isotope beam facilities[4]. Despite this, the unusual structure of ^{47}K allows for an alternate route to investigate this key interaction.

---

[2] Not all proton-neutron interactions are attractive – this is determined by the total angular momnetum, j, of both orbitals. In the case of two $j = \ell + \frac{1}{2}$ or two $j = \ell - \frac{1}{2}$ orbitals, the interaction is repulsive. Alternatively, the interaction between a $j = \ell + \frac{1}{2}$ orbital and a $j = \ell - \frac{1}{2}$ orbital is attractive [24].

[3] Direct transfer reactions are detailed in Section 2.1

[4] It is estimated that the world-leading Facility for Rare Isotope Beams would only be able to produce reaccelerated ^{43}P on the order of one particle a second in its eventual final form [29]

1.3.2 ^{47}K as a facsimile of ^{43}P

In 2014, Papuga *et al.* [30] investigated the proton occupation of the $^{38-51}$K isotopic chain using collinear laser spectroscopy at COLLAPS, CERN. The isotopes were excited using a Ti:Sa laser, and the hyperfine structure was observed using photomultiplier tubes to detect resonance photons and hence determine the nuclear spins and magnetic moments. Their experimental results were compared with shell model calculations using two effective interactions (SDPF-NR [31] and SDPF-U [32]) using a core of ^{16}O and only allowing valence nucleons to excite within πsd, νsd and νpf. Through this combination of experimental and theoretical investigation, Papuga *et al.* were able to establish the occupations of the πsd orbitals, specifically $\pi s_{1/2}$ and $\pi d_{3/2}$, as shown in **Figure 1.6a**.

Interestingly, they determined that while most of the isotopes had the expected structure of a filled $\pi s_{1/2}$ and a hole in $\pi d_{3/2}$ (in compact notation, $\pi s_{1/2}^{2} d_{3/2}^{3}$, or $\pi d_{3/2}^{-1}$) this was not true of ^{47}K and ^{49}K. These two unusual isotopes have $\pi s_{1/2}^{1} d_{3/2}^{4}$ structure (alternately, $\pi s_{1/2}^{-1}$), with the odd proton in $\pi s_{1/2}$. This exotic proton configuration is of particular interest for this study, because the odd proton occupies the same $\pi s_{1/2}$ orbital as in the ideal candidate, ^{43}P.

As transfer reactions are so selective in the states that they occupy – detailed further in Section 2.1 – the ^{47}K(d,p) reaction populates states in ^{48}K that have a large wavefunction

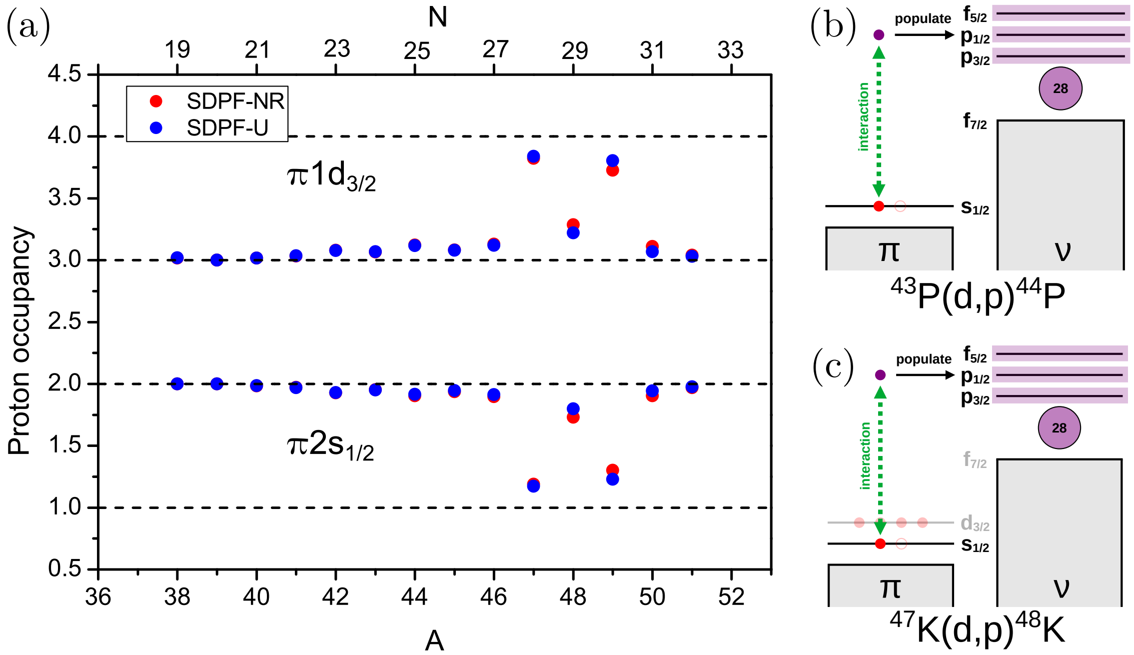

Figure 1.6: Evidence and arguments for ^{47}K(d,p)^{48}K as an effective model of ^{43}P(d,p)^{44}P. (a) Ground state proton configuration in potassium isotopes, from Ref. [30]. Note that the ^{47}K ground state has the configuration $\pi s_{1/2}^{1} d_{3/2}^{4}$. (b) and (c) Diagrams of the $\pi\nu$ structures populated by transferring a single neutron onto the ground state configurations of ^{43}P and ^{47}K, respectively.

overlap with ^{47}K+n; that is, states with this exotic proton configuration, plus a neutron in the interesting νfp orbitals. As such, the ^{47}K(d,p) reaction is an effective simulacrum of the ideal ^{43}P(d,p) reaction, populating states arising from the same cross-shell interaction, with only the addition of a filled $\pi d_{3/2}$ orbital (see **Figures 1.6b** and **c**). Experimental observation of the structure of ^{48}K, and the strength with which each state is populated by ^{47}K(d,p), would allow future shell model calculations to be adjusted to reproduce this result and, in turn, improve our understanding of the $\pi s_{1/2} \otimes \nu$fp interactions. Better modelling of these exotic cross-shell interactions will improve the predictive power of the shell model as we approach the extremes of nuclear existence.

The ^{47}K(d,p) transfer reaction represents the first step in what could be an eventual campaign, moving down in Z and observing these $\pi s_{1/2} \otimes \nu$fp states in ^{45}Cl(d,p) and ^{43}P(d,p) as the radioactive beams become available.

1.3.3 Complementary ^{47}K(d,t)^{46}K transfer

Whereas the ^{47}K(d,p)^{48}K transfer reaction provides information about unoccupied neutron orbitals critical for $N = 32, 34$ magicity, the transfer reaction ^{47}K(d,t)^{46}K provides information about the structure and neutron orbital occupation of the beam isotope, ^{47}K. This, critically, gives insight into the magicity of $N = 28$, which is a ‘soft’ shell closure in this region. Some population of $\nu p_{3/2}$ is expected in the ground state of ^{47}K, but if the shell closure were to be weaker than anticipated, the $\nu p_{3/2}$ population could significantly impact the results of the ^{47}K(d,p) reaction – that is, if the neutron orbital is already partially occupied, then the probability of transferring a nucleon into that state is reduced.

As such, the complementary ^{47}K(d,t) transfer reaction is also analysed in this work. This does not impede the physical measurement or analysis of the ^{47}K(d,p) reaction, but in fact provides completeness and confidence in the primary results of this work.

1.4 Previous works

1.4.1 Literature regarding ^{48}K

Very little is known about the excited structure of ^{48}K, particularly when considering that it is a neighbouring isobar of the doubly-magic nucleus ^{48}Ca. Prior to 2011, only three transitions had been observed; a $5^+ \rightarrow 3^- \rightarrow 2^- \rightarrow 1^-$ cascade of 1449 keV, 449 keV and 279 keV γ-rays [33]. The work of Królas *et al.* (2011) [34] expanded this level scheme greatly, through the combination of three deep-inelastic collision experiments.

High-resolution γ-ray spectroscopy A ^{48}Ca beam on ^{238}U was investigated first at the Argonne National Laboratory (ANL) with Gammasphere. This experiment gave good γ-ray coincidence information, but due to the lack of existing level scheme information for ^{48}K, they were unable to determine which γ-rays were associated with this isotope amongst the many reaction products.

Isotope identification The same reaction was studied again at the *Laboratori Nazionali di Legnaro* (LNL) with the PRISMA spectrometer and the CLARA γ-ray array. The inclusion of a spectrometer in this experiment allowed for unambiguous A and Z isotope identification, providing clarity on measurements made in the ANL experiment.

Lifetime measurement Finally, a ^{48}Ca beam on ^{208}Pb was studied at LNL, using the plunger technique [35] to establish the lifetime of the 5^+ isomeric state. This positive-parity state is not expected to be populated in the current work.

The level scheme established through this extensive analysis can be seen in **Figure 1.7a**.

1.4.2 Literature regarding ^{46}K

The existing literature regarding ^{46}K is far more complete, having been studied not only through the β^- decay of ^{46}Ar, but also through multiple-nucleon transfer reactions.

The early work of Paul *et al.* (1971) [36] populated excited states via ^{48}Ca(d,α)^{46}K, and while they successfully observed many states, the spin-parity assignments they made for the low-energy 0.59 MeV, 0.69 MeV and 0.89 MeV states were later contested and corrected by Daehnick *et al.* (1971)[5] with ^{48}Ca(d,α)^{46}K and Dupont *et al.* (1973) [37] with ^{48}Ca(p,^{3}He)^{46}K to 3^-, 4^- and 5^-, respectively. In order to explain this low-level structure, they explicitly include the $\pi s_{1/2}{}^1 d_{3/2}{}^4$ proton structure that is of such interest to this work [37, 38].

For a time, the spin-parity assignment of the 1.944 MeV state was a point of contention, being alternately assigned as 3^- [6], 4^- [37, 38] or left ambiguous [36]. The unusually weak population strength of the ^{46}Ca analogue state is used to suggest that an ‘unnatural’ positive parity could be more likely for this state [37]. It was Daehnick *et al.* (1973) [39] that first assigned the state as 1^+, noting that the differential cross section of the ^{48}Ca(p,^{3}He)^{46}K state is only satisfactorily reproduced by mixed $\ell = 0 + 2$ nature. This was later confirmed by the work of Petry *et al.* (1978) [40], observing that the β^- decay of the ^{46}Ar ground

---

[5] While the literature makes several references to *Daehnick et al. Bull. Am. Phys. Soc.* ***16****, 555 (1971)*, it is unfortunately not available online, as the Bulletin of the American Physical Society is only digitised from 1993. As such, details of this work are gleaned from references in Dupont *et al.* (1973) [37].

[6] Daehnick *et al.* Bull. Am. Phys. Soc. **16**, 555 (1971). See footnote 5

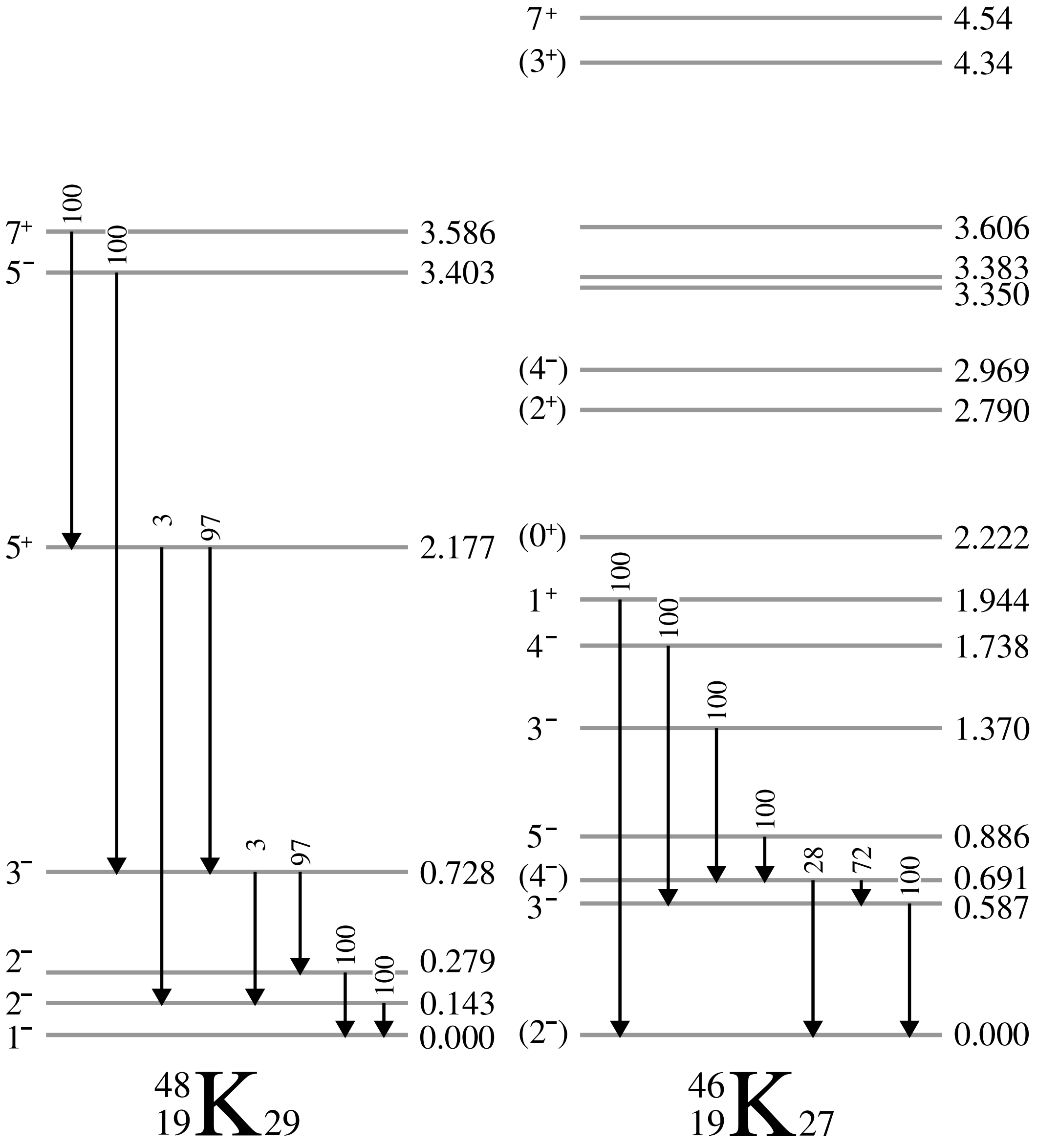

(a)

(b)

Figure 1.7: Level schemes of (a) ^{48}K and (b) ^{46}K established in previous works, as described in text.

state (0^+) decays to the 1.944 MeV state, with no other observed branching. They argue that, as the allowed β^- transitions limit the possible spin-parities of the final state to 0^+ or 1^+, and $0^+ \rightarrow 0^+$ decay is forbidden, the 1.944 MeV is firmly assigned as 1^+ in nature.

An additional point of note is that there is some suggestion of a doublet of states, at 3.350 MeV and 3.383 MeV. The work of Daehnick *et al.* (1973) [39] observed the higher energy of these two states, marking it as an unresolved doublet, but without in-text discussion. Following this, the work of Frascaria *et al.* (1974) [41] observed a well-populated state at 3.35 MeV via ^{48}Ca(d,α)^{46}K. The compiled and evaluated data sheet for this nucleus only includes the higher energy state, but notes the possibility of a doublet [42]. The current work is well-positioned to make a determination regarding a possible doublet in this region, through the inclusion of γ-ray spectroscopy.

Through these works, the present structure and decay of ^{46}K was established, as shown in **Figure 1.7b**.

1.5 Thesis structure

This thesis begins with an overview of the theoretical models critical to interpreting this work, and the calculations performed during this analysis, in Chapter 2. Then, the experimental method – i.e. the generation of a radioactive isotope beam, the types of detectors used, and the details of each particular detection system – are given in Chapter 3. The processing of the raw data from each detector, such as calibration and background removal, is detailed in Chapter 4. Then, with the intended observable variables extracted, the results of this experiment are presented in Chapter 5. These results are then interpreted in the broader context of the field in Chapter 6. Finally, brief concluding remarks are presented in Chapter 7.

Chapter 2

Theory

In order to understand and interpret the experimental measurements made during a direct transfer reaction measurement, several theoretical models and calculations are necessary. In this chapter, these models are introduced, and some key calculations are examined. First, a general overview of direct transfer reactions is given in Section 2.1. This is followed by a discussion of relevant assumptions and derivations in scattering reaction theory in Section 2.2, including some specific features of the calculations performed for this work. Following this, Section 2.3 introduces the shell model Hamiltonians used in this work, and highlights the similarities and critical differences between each model. The key results of these shell model calculations are discussed in Section 2.4.

2.1 Direct transfer reactions

One of the most powerful tools to investigate specific proton-neutron interactions is through the use of transfer reactions. These reactions characteristically add or remove a small number of nucleons from the original nucleus, which makes theoretical interpretation of the results far simpler because the reaction will very selectively populate certain states [43]. Transfer reactions can be either *cluster* transfer (more than one nucleon transferred) or *single-nucleon* transfer; this work will focus on single-nucleon transfer reactions.

For a neutron stripping[1] reaction ${}^{A}_{Z}\mathrm{X}_{\mathrm{N}}(\mathrm{d,p})^{A+1}_{\;\;\;Z}\mathrm{X}_{\mathrm{N+1}}$, the states populated in the final nucleus ${}^{A+1}\mathrm{X}$ are those with a wavefunction that is similar to the system of ${}^{A}\mathrm{X}$+n; that is, the initial nucleus ${}^{A}\mathrm{X}$ as a core with the transferred neutron orbiting it. Conversely, states which arise from a complex mixture of configurations are suppressed [44]. The same can be said of the neutron pick-up reaction, ${}^{A}_{Z}\mathrm{X}_{\mathrm{N}}(\mathrm{d,t})^{A-1}_{\;\;\;Z}\mathrm{X}_{\mathrm{N-1}}$, where the wavefunction overlap between the initial and final states is a probe of the neutron orbital occupation of the initial nucleus.

---

[1] This naming convention is inherited from reactions in normal kinematics; that is, a reaction *A(a,b)B* would be performed by bombarding a target of nucleus *A* with a beam of particle *a*. In such cases, a reaction that transferred a nucleon to the target nucleus would be 'stripping' the beam, and vice-versa for when the beam would 'pick up' a nucleon from the target nucleus. Given this convention, (d,p) is a stripping reaction, and (d,t) is a pickup reaction [15][18].

This simple theoretical picture is complicated by the mixed nature of nuclear state wavefunctions, as there are often many configurations of nucleons that can form the same spin and parity. This means that, even though transfer reactions populate the single-particle part of the state wavefunction, this will be mixed with more complex nuclear structures. The strength of the single-particle component of these states is characterised by a comparison of the actual population of the state with the expected population if the state was unmixed; that is, by comparing the cross sections σ_{meas} and σ_{calc}. In principle, these cross sections differ only by a scaling factor, known as the spectroscopic factor, S [15]:

$$\sigma_{\mathrm{meas}} = \mathrm{S}\sigma_{\mathrm{calc}} \quad \text{where} \quad \mathrm{S} \leq 1. \tag{2.1}$$

There is, however, a distinct advantage to comparing the cross sections as a function of scattering angle, instead defining the spectroscopic factor as

$$\left(\frac{d\sigma}{d\Omega}\right)_{\mathrm{meas}} = \mathrm{S}\left(\frac{d\sigma}{d\Omega}\right)_{\mathrm{calc}} \quad \text{where} \quad \mathrm{S} \leq 1. \tag{2.2}$$

Here, the shape of the differential cross section provides crucial information. The probability of scattering the light emitted particle at a given angle is related to the ℓ quantum number of the orbital occupied by the transferred particle. The expected shape for a given ℓ-transfer of a given energy can be calculated using scattering reaction models, such as those detailed in Section 2.2. Hence, a comparison between observed and calculated differential cross sections for various populated states can be used to distinguish between nuclear configurations.

By using Equation 2.2 to measure the spectroscopic factors of states populated in a single-nucleon transfer reaction, observations can be made regarding the average single-particle energies (SPEs) of the orbital. Averaging the energies of all states containing strength from a particular orbital, weighted by the spectroscopic factors of those components, would provide some measure of the SPE of that single-particle orbit [44]. This methodology is limited, particularly in the case of radioactive isotope beam experiments, by the implausibility of observing every state that is populated with some small fractional strength. In such cases, a more credible approach is to compare observations of the most strongly populated states to shell model calculations, such as those detailed in Section 2.3, adjusting the interactions to reproduce experimental observation. In this work, comparisons are made that highlight the predictive ability of the given shell model calculations, and aspects where the models require improvement.

2.2 Scattering reaction theory

In order to obtain the theoretical differential cross section $\left(\frac{d\sigma}{d\Omega}\right)_{\text{calc}}$ in Equation 2.2, calculations must be performed that can relate fundamental structural properties of the nucleus – such as the quantum numbers of a populated orbital – to the angle of the emitted light ejectile. These calculations are performed using Born approximation methodologies, introduced and summarised in this section. Here, the distorted-wave Born approximation (DWBA) and the adiabatic distorted-wave approximation (ADWA) are described. More detailed derivations can be found in Refs [45–47].

2.2.1 From wavefunction to transition matrix

For the three relevant types of direct reaction – elastic scattering, inelastic scattering, and transfer – the system in the state before and after the reaction can be described by different mass partitions. The initial mass partition, before the reaction, is denoted as α. For elastic scattering, the mass partition before and after the reaction are equal; that is, $\alpha \to \alpha$. For inelastic scattering, the exchange of energy in the system places it into the state α'. After a transfer reaction, the distribution of mass between the two bodies has changed, and as such this mass partition is denoted by β. Additionally, the $\alpha'\alpha$ and $\beta\alpha$ mass partitions are further separated into reaction channels, representing the different possible excitations of the light and heavy nucleus.

As a starting point, the incoming beam can represented by a plane wave of the form $e^{i\vec{k}\cdot\vec{R}}$. Possible reaction channels are represented by a set of outgoing spherical waves[2] of the form $\frac{e^{ikr}}{r}$. The wavefunction to solve the Schrödinger equation in this case, Ψ_{model}, is given by

$$\begin{aligned}\Psi_{\text{model}} \to\ & \Phi_\alpha\ e^{i\vec{k}_\alpha\cdot\vec{r}_\alpha} \\ & + \Phi_\alpha\ f_{\alpha\alpha}(\theta)\ \frac{e^{ik_\alpha r_\alpha}}{r_\alpha} \\ & + \sum_{\alpha'\neq\alpha}\Phi_{\alpha'}\ f_{\alpha'\alpha}(\theta)\ \frac{e^{ik_{\alpha'}r_\alpha}}{r_\alpha} \\ & + \sum_{\beta}\Phi_\beta\ f_{\beta\alpha}(\theta)\ \frac{e^{ik_\beta r_\beta}}{r_\beta},\end{aligned} \tag{2.3}$$

---

[2] These forms are chosen based on the assumption that, although the wavefunction will be highly deformed at small distances, any real measurements are taken at sufficiently large distances that the asymptotic form can be taken.

where the first term is the incoming plane wave, the second term is the spherical elastic scattering, the third term contains all outgoing inelastic scattering spherical waves and the final term contains all outgoing transfer spherical waves [45].

The functions $f_{\alpha\alpha}(\theta)$, $f_{\alpha'\alpha}(\theta)$ and $f_{\beta\alpha}(\theta)$ are the scattering amplitudes for those channels. Taking the transfer case as an example, the scattering amplitude is directly related to the differential cross section through the equation [45, 46]

$$\left(\frac{d\sigma}{d\Omega}\right)_{\alpha\to\beta} = \frac{v_\beta}{v_\alpha}\left|f_{\beta\alpha}(\theta)\right|^2, \tag{2.4}$$

where v_α and v_β are the velocities of the incoming and outgoing light particles relative to the target. From here, a matrix containing all likelihoods of transitions between states – the transition matrix T – can be found from these scattering amplitudes by the relationship [47]

$$T_{\beta\alpha} = -\frac{2\pi\hbar^2}{\mu_\beta} f_{\beta\alpha}(\theta), \tag{2.5}$$

but this requires a full knowledge of the wavefunction Ψ_{model}. Alternatively, the transition matrix can also be written as [47]

$$T_{\beta\alpha} =< \phi_\alpha\phi_\alpha|V|\sum_\beta \phi_\beta\psi_\beta >, \tag{2.6}$$

which still contains the full physics of the reaction, but several approximations and assumptions can be made from this point that allow the transition matrix $T_{\beta\alpha}$ to be accurately calculated.

2.2.2 Assumptions and approximations

First, the summation over the whole range of exit channels can be continually expanded into higher order powers of V, known as the Born series [46]. Here, the assumption is made that multi-step effects are negligible, and so only the first element of the Born series is taken. This first element corresponds to direct one-step reactions, i.e. elastic scattering. This is the Born approximation, which allows for the right-hand component of Equation 2.6 to be simplified to $\left|\phi_\beta\psi_\beta\right\rangle$.

Next, the distortion of the particle waves by the target nucleus is accounted for by applying a distorting potential W such that the central term becomes $V - W$. The unperturbed waves ϕ are then replaced with distorted waves χ, such that $[T + W - E]\,\chi = 0$.

Finally, the DWBA transition matrix for the direct transfer reaction can be written as

$$T_{\beta\alpha} = \langle\phi_\alpha\chi_\alpha|\,V - W\left|\phi_\beta\chi_\beta\right\rangle. \tag{2.7}$$

As it has been approximated that the entrance and exit channel distorting potentials, W, can be described by their associated elastic scattering optical potential, the accuracy of DWBA calculations depends on the appropriate choice of the potential V. The standard method used is to select some appropriate global optical potential. Several phenomenological global optical models have been developed for proton, deuteron and triton elastic scattering by harvesting a breadth of elastic scattering data and using these to constrain parameters of the potential, so as to produce broadly accurate predictions for scattering on a wide range of nuclei. This phenomenological approach also has the advantage of implicitly accounting for complex reaction processes outside of the model space that siphon flux away from the elastic channel.

DWBA is significantly limited in its approximation of the deuteron to a single particle with no internal structure – this excludes deuteron breakup channels and other three-body effects. This proves critical for this work, as the transfer reactions of interest involve a ^{47}K + d incoming channel. The adiabatic distorted-wave approximation (ADWA) is an alternative to DWBA, wherein these breakup channels are taken into account in an approximate way, rather than assuming that they are negligible. The adiabatic distorted wave ψ_{ADWA} is a sum of the deuteron elastic scattering and breakup components, where the breakup components are strongly coupled to the elastic channel. For these reactions, ADWA assumes that the energy exciting the deuteron is a small fraction of the total energy [46], and as such, the proton and neutron of the deuteron can be considered to be fixed relative to each other. This reduces a three-body n+p+^{47}K problem back down to a solvable two-body problem.

The importance of this breakup component can be seen in **Figure 2.1**, where the difference between DWBA and ADWA is shown for two cases; the removal of a strongly bound neutron, and the addition of a neutron to a doubly-magic nucleus [46]. While the improvement between DWBA and ADWA is more significant for the neutron removal case, where the

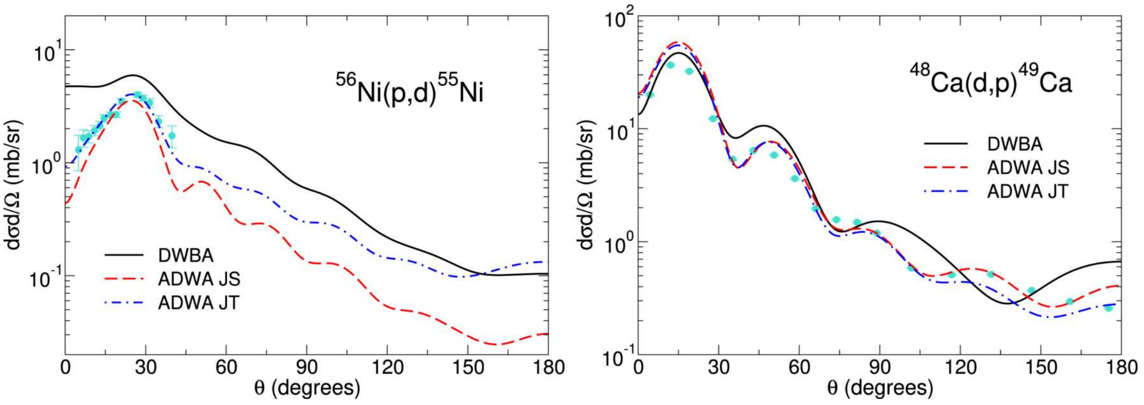

Figure 2.1: Comparison of DWBA, ADWA Johnson-Soper and ADWA Johnson-Tandy results for the removal of a deeply bound neutron (left) and the addition of a less bound neutron (right). Experimental data points are shown in cyan circles. Figure from Ref. [46].

Q-value of the reaction is larger, it is clear that the ADWA model is far better at accurately reproducing the shape of experimentally observed data in both cases. As such, the work presented in this thesis uses ADWA preferentially over DWBA.

2.2.3 Application to experimental measurements

It is clear from Equation 2.7 that the transition matrix is dependant on the internal wavefunctions ϕ_α and ϕ_β. These wavefunctions are of course dependant on the quantum numbers of the two systems. As such, the transition matrix $T_{\beta\alpha}$ is not only a measure of the overlap $\langle\phi_\alpha|\phi_\beta\rangle$, but an indication of the underlying nuclear structure. The shape of the differential cross section is strongly indicative of these quantum numbers, so in the case of a transfer reaction in inverse kinematics, the energy of the light ejectile can differentiate between different excited states of the heavy nucleus, and the angular distribution of the ejectile for a given state can reveal the $n\ell_j$ of the orbital that was populated or stripped during the reaction.

In the specific cases of the ^{47}K(d,p) and ^{47}K(d,t) transfer reactions investigated in this work, the differential cross sections $\left(\frac{d\sigma}{d\Omega}\right)_{\text{calc}}$ populating example states of E = 0 MeV, 2 MeV and 4 MeV can be found in **Figures 2.2** and **2.3**, respectively.

In the case of ^{47}K(d,p), shown in **Figure 2.2**:

Orbital ℓ The p-wave and f-wave differential cross sections are very distinct from each other, which is critical for the clear discrimination of $\ell = 1$ and $\ell = 3$ states in the experimental data.

Orbital j As $p_{1/2}$ and $p_{3/2}$ shapes are not distinct, they will instead be determined by arguments based on spin-parity and/or shell model calculations.

State E_x As excitation energy increases, the f-wave cross sections change magnitude but remain approximately the same shape – the opposite is the case for p-wave cross sections. Additionally, the first maximum moves to larger θ_{lab} angles for f-wave states.

Alternatively, in the case of ^{47}K(d,t), shown in **Figure 2.3**:

Orbital ℓ This determination is complicated by larger number of possible ℓ-transfers predicted by the shell model – discussed in Section 2.4. While the four projections are largely distinguishable, assignments are additionally assisted by comparison to the aforementioned shell model calculations.

Orbital j Only one j projection of each ℓ is available in this shell model region. Hence, j is given once ℓ is determined, which serves to ease interpretation.

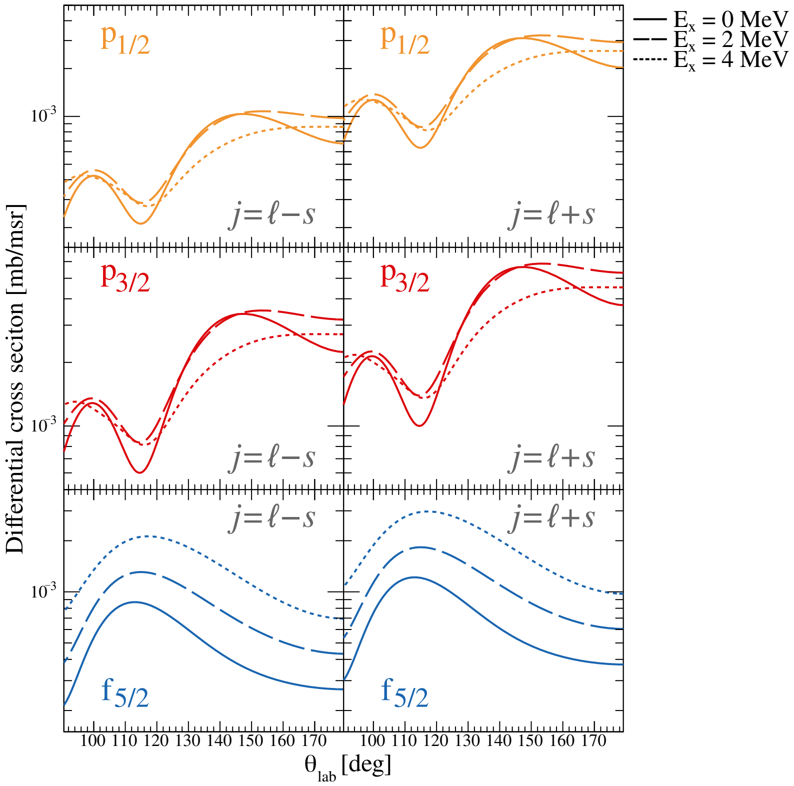

Figure 2.2: Example differential cross sections for the ^{47}K(d,p) reaction for a 7.7 MeV/u beam, performed with TWOFNR [48] using Koning-Delaroche [49] and Johnson-Tandy (Reid soft-core) [50] optical models. The different possible spins produced by each orbital are compared, for a range of energies.

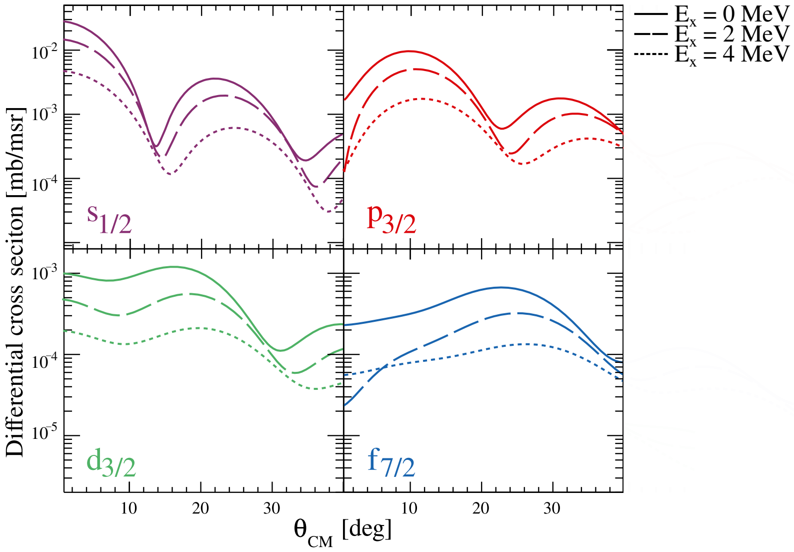

Figure 2.3: As **Figure 2.2**, for ^{47}K(d,t) reactions using Lohr-Haeberli [51] and Li-Chen [52] optical models. For convenience, only the higher spin state is shown in this figure.

State E_x In this reaction, increasing excitation decreases the cross section magnitude and moves the first minimum to larger θ_{CM} in all cases.

The interpretation of the experimental results to be presented in this thesis relies heavily on the accuracy and reliability of ^{47}K(d,d) and ^{47}K(p,p) elastic scattering optical modelling. This is especially critical for ^{47}K(d,d) elastic scattering, as this differential cross section is used to determine the number of deuterons in the target for the normalisation of ^{47}K(d,p) and ^{47}K(d,t) spectroscopic factors. As such, a detailed analysis of the elastic scattering calculations was performed, which can be found in Appendix A.1. Ultimately, multiple calculation codes and optical potentials produced consistent results, ensuring confidence in the normalisation factor used.

2.3 The Shell Model

Recalling the basis of the shell model, as introduced in Section 1.2, macroscopic behaviours of nuclei can be accurately described by considering the nucleus to be constructed of independent particles, each moving in a mean-field potential generated by the average interaction of every other nucleon. As these particles are confined by the nuclear mean field, they must occupy quantised levels, with eigenvectors ψ (i.e. the particle wavefunctions) and eigenvalues E (i.e. the single-particle energies) solving the time-independent Schrödinger equation in three dimensions. These discrete particle states – defined by their quantum numbers n,ℓ,j[3] and m_j – are assembled into orbitals of common $n\ell_j$. These orbitals are loosely organised into shells, whereby a large difference in energy between orbitals produces particularly stable configurations.

This concept allows calculations of ground state and excited state properties of an isotope to be performed. The single-particle eigenstates form the basis of state for the N-body problem in the form of a Slater determinant. There are, of course, many complex interactions occurring within the real N-body nucleus – these various processes are represented as off-diagonal two-body matrix elements in the Hamiltonian. These off-diagonal elements encompass the effects of the central potential, spin-orbit coupling, tensor forces, Coulomb interaction, meson exchange, isospin mixing, and many other higher-order effects.

While this Hamiltonian can be determined purely from first principles (the *ab initio* approach), this is computationally intensive – a problem which worsens for heavier isotopes – and often limited to ground state properties. More commonly, the off-diagonal two-body matrix elements are initially determined by the truncation of two- and three-nucleon interactions [53], and then adjusted to improve agreement with experimental data [54],

---

[3] Here, resulting from the coupling of ℓ to the intrinsic nucleon spin $s = 1/2$.

such as excitation energies, spin-parities and spectroscopic factors.

Many Hamiltonians have been produced and iterated upon with improving experimental data and theoretical considerations, branching out to specialise in different regions. The three shell model Hamiltonians used during this work – SDPF-U [32], SDPF-MU [55] and ZBM2* [56] – are described in the following sections. For each model, the most critical features are:

Model space Which of the orbitals are treated as filled and inexcitable (*inert core*) and which orbitals are within the scope of the calculation? Are there any restrictions regarding cross-shell excitation?

Interactions Which interactions are used? Are they G-matrix or empirical interactions? If empirical, what modifications have been made?

2.3.1 SDPF-U Hamiltonian

Developed in 2009 by F. Nowacki and A. Poves [32], the SDPF-U Hamiltonian is specialised for calculations in the sd- and fp-shells. This model has an inert core of ^{16}O, and a valence space of πsd and νsd, νfp as indicated in **Figure 2.4**. While calculations are unrestricted in πsd and νfp, excitations between sd- and fp-shells are disallowed, restricting the possible excitations of sd-shell neutrons.

Three interactions are used for three different blocks; the empirical universal sd-shell (USD) interaction [57] for the sd-shell, the empirical Kuo-Brown (KB') interaction [58] for the fp-shell, and the Kahana, Lee and Scott G-matrix (KLS) interaction [59] for the cross-shell sd $\otimes$ fp interaction.

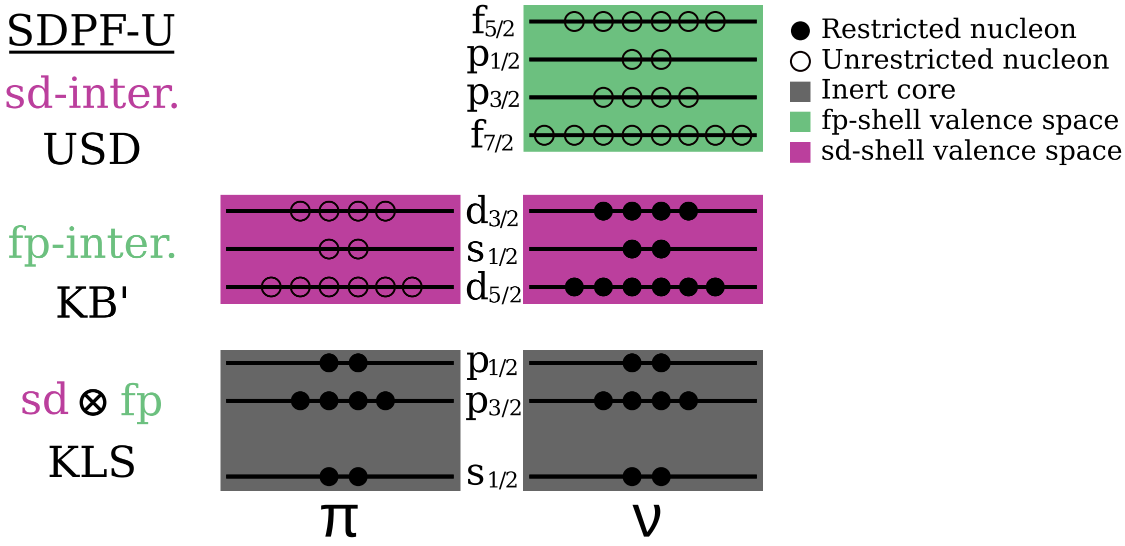

Figure 2.4: Simple diagram of the key features of the SDPF-U shell model Hamiltonian. Interactions included in the Hamiltonian are indicated on the left.

These three interactions are then adapted in order to more accurately reflect three experimental measurements: (1) the $p_{3/2}s_{1/2}$ and $p_{3/2}d_{3/2}$ monopoles were adjusted to reflect β-decay spectroscopy of ^{35}Al to ^{35}Si [60], (2) p-orbital spin-orbit splitting was reduced to match charged particle spectroscopy of ^{46}Ar(d,p)^{47}Ar [61], and (3) strict agreement with fp-shell centroids observed in magnetic spectroscopy of ^{40}Ca(d,p)^{41}Ca in direct kinematics [62] was required.

2.3.2 SDPF-MU Hamiltonian

Developed in the early 2010's [55], based on the V_{MU} [63] construction of a monopole interaction, the SDPF-MU Hamiltonian is very distinct from SDPF-U. While the inert core, model space and valence shells are the same (see **Figure 2.5**), the SDPF-MU model has undergone less empirical adjustment than SDPF-U, relying instead on properties of the monopole effective nucleon-nucleon interaction.

Here, the sd-interaction is USD [57], and the fp-interaction is the empirical GXPF1B [64] interaction. Some matrix elements relating to $f_{7/2}$ are replaced by those of KB [58]. The key difference in this model is that V_{MU} – the sd ⊗ fp cross-shell component of SDPF-MU, and the interaction most critical to this work – is not empirically derived, being composed of strongly renormalised Gaussian central forces and tensor forces. The Gaussian central force contains many of the more complex interactions in the nucleus and has long-range *global* effects. Conversely, the tensor force is a result of meson exchanges, and has specific *local* effects. For details of this derivation, the reader is directed to Ref. [63].

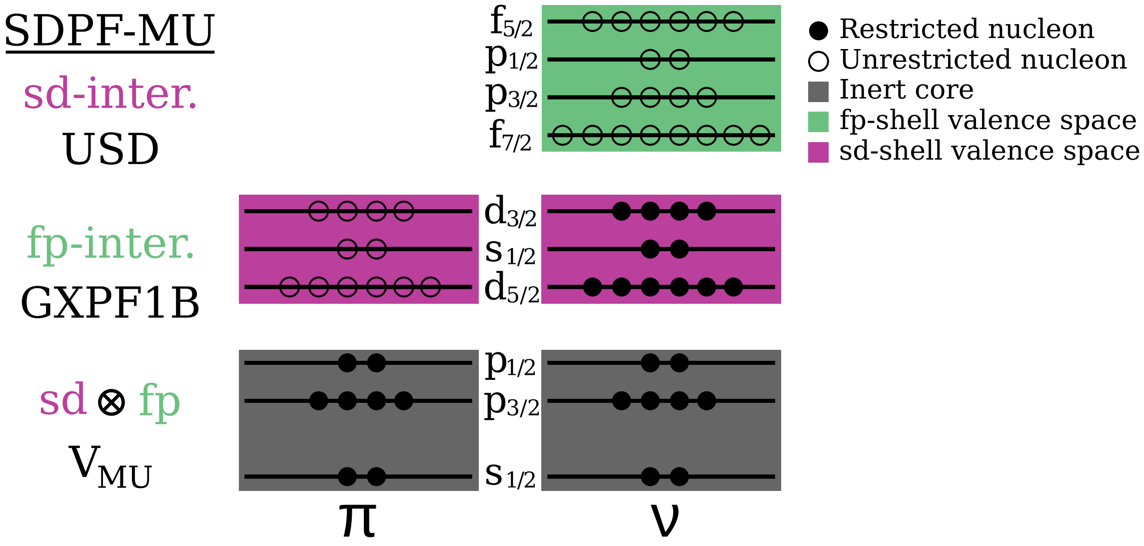

Figure 2.5: Simple diagram of the key features of the SDPF-MU Hamiltonian. Interactions included in the Hamiltonian are indicated on the left.

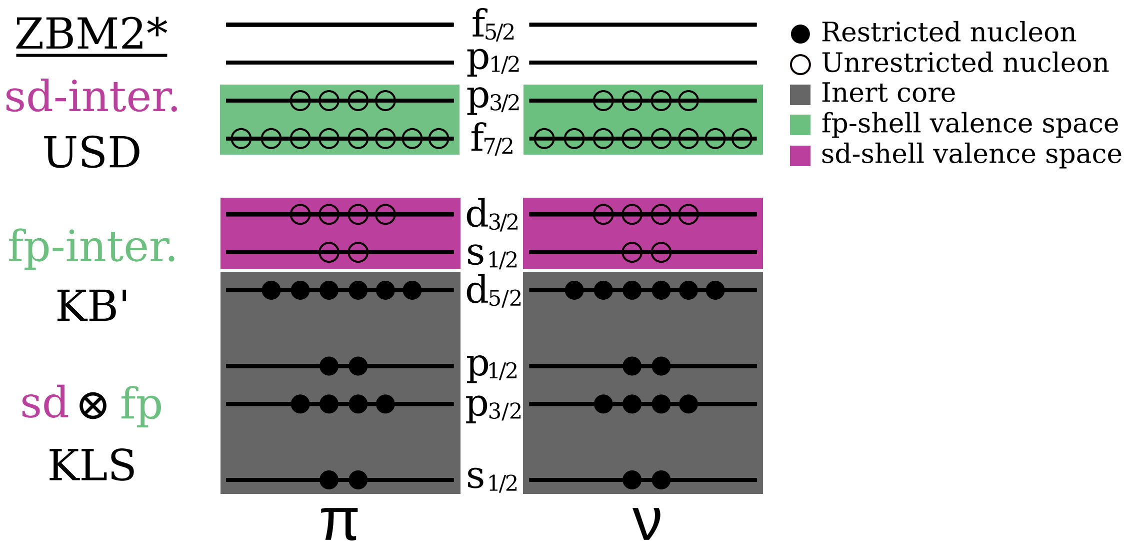

Figure 2.6: Simple diagram of the key features of the ZBM2* Hamiltonian. Interactions included in the Hamiltonian are indicated on the left.

2.3.3 ZBM2* Hamiltonian

While the two SDPF-based models previously discussed are excellent at modelling nuclei with $N \geq 28$, the calculations are restricted in the νsd shell. Alternatively, the ZBM2* Hamiltonian [56] is comprised of an inert core of ^{28}Si, with valence nucleons in $s_{1/2}$, $d_{3/2}$, $f_{7/2}$ and $p_{3/2}$ for both protons and neutrons (as shown in **Figure 2.6**).

The interactions employed are the same as those of SDPF-U, with different modifications: (1) the single-particle energies were adjusted to reflect the ^{29}Si spectrum [65], (2) the sd ⊗ fp monopoles were tuned to ^{39}K and ^{40,41}Ca [65], (3) the $d_{3/2}$ centroids were tuned to properly reproduce ^{38}K [66], and (4) the proton shell gap at $N = 20$ was increased to more accurately reflect their positions at $N = 28$ [56]. The version of ZMB2* used in this work was provided by B. A. Brown (personal communication).

2.4 Predictions from the shell model

2.4.1 ^{47}K(d,p)^{48}K

Calculations using the SDPF-U and SDPF-MU interactions for ^{47}K(d,p)^{48}K were performed using the NuShellX [67] shell model code. The predicted energy level structure, spectroscopic factor and nucleon orbital configurations can be seen in **Figure 2.7**. Considering the very different origins of the two models, described in the previous section, the two predictions are remarkably similar.

The most striking observation is the clear distinction between a region of p-wave states and

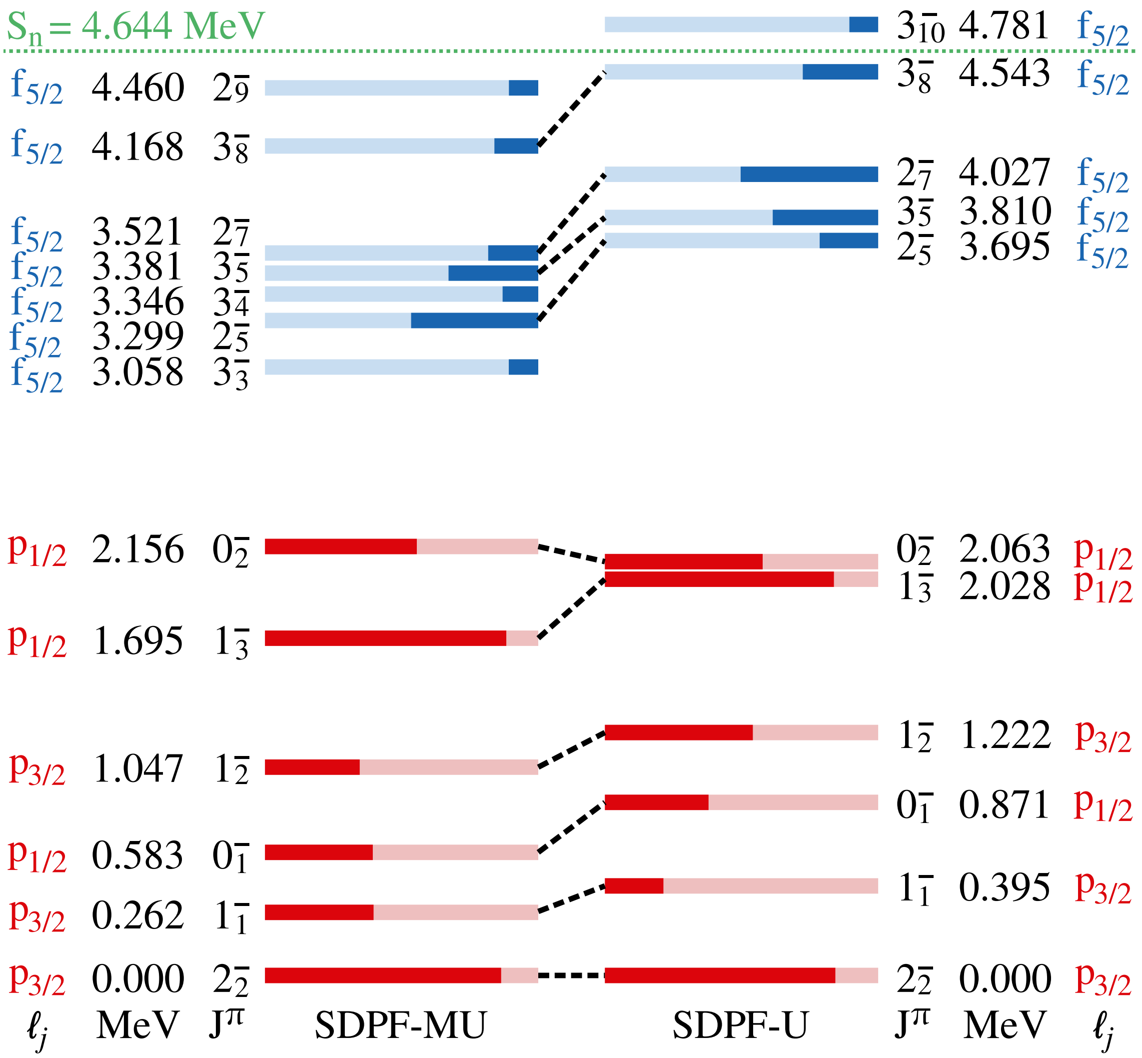

Figure 2.7: Comparison of SDPF-U and SDPF-MU shell model predictions for ^{47}K(d,p). Here, all states with a predicted spectroscopic factor larger than 0.1 are shown, and the spectroscopic factor is represented as the filled length of each bar, where a full bar equals 1. The $\ell = 1$ (p-wave) states fill from the left in red, and the $\ell = 3$ (f-wave) states fill from the right in blue.

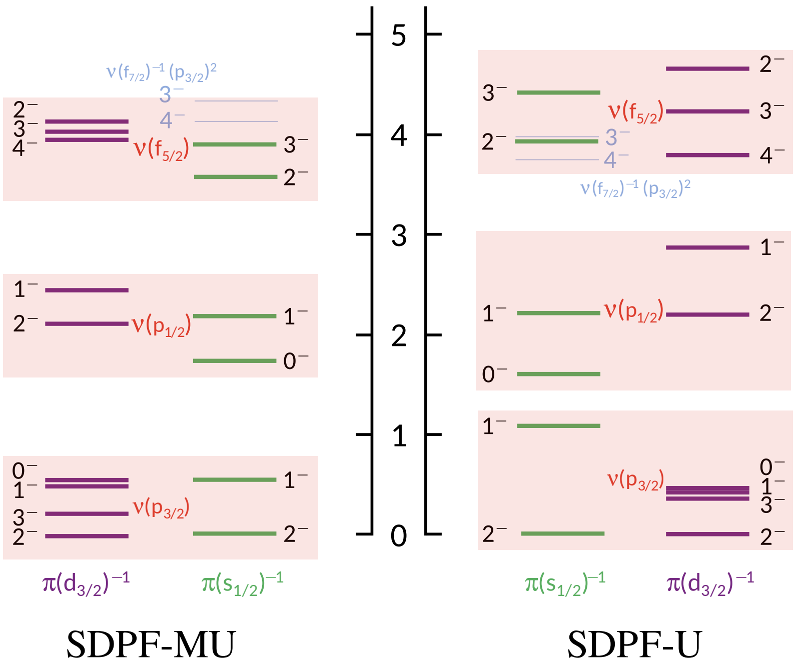

Figure 2.8: Diagram of the 'pure' $\pi s_{1/2}^{1} d_{3/2}^{4}$ (green) and $\pi s_{1/2}^{2} d_{3/2}^{3}$ (purple) coupling to the neutron orbitals. Note that, due to the near-degeneracy of the proton orbitals, the two families of states are very close in energy, and as such, identical spin-parities with different proton structures can mix.

a region of f-wave states in both models. This results from the expected $f_{5/2}$ single particle energy being higher than the $p_{1/2}$ and $p_{3/2}$, as discussed in Section 1.3.1. Both models have the same ordering of states, and broadly agree on spectroscopic factors of those states – note, however, that there are a greater number of strongly populated ($S > 0.1$) f-wave states in SDPF-MU than SDPF-U. This is due to different mixing between the states built upon the $\pi s_{1/2}^{1} d_{3/2}^{4}$ configuration, and their neighbouring states (of identical spin-parity) with $\pi s_{1/2}^{2} d_{3/2}^{3}$ structure, shown in **Figure 2.8**.

Additionally, both of these models have the same major pitfall; they predict a 2^- ground state in ^{48}K. This is contrary to the experimentally observed 1^- ground state [34]. This is a significant failing of the theory – further highlighting our poor understanding of this region, even for a close isobar of doubly-magic ^{48}Ca.

Some key differences between the models are:

- SDPF-U states are located at higher energies than SDPF-MU, with a larger gap between p-wave and f-wave states.
- The highest energy state with strong population is a bound 2^- in SDPF-MU, but an unbound 3^- state in SDPF-U.
- The 2^-_5 state is stronger in SDPF-MU than SDPF-U; the opposite is true for 2^-_7.

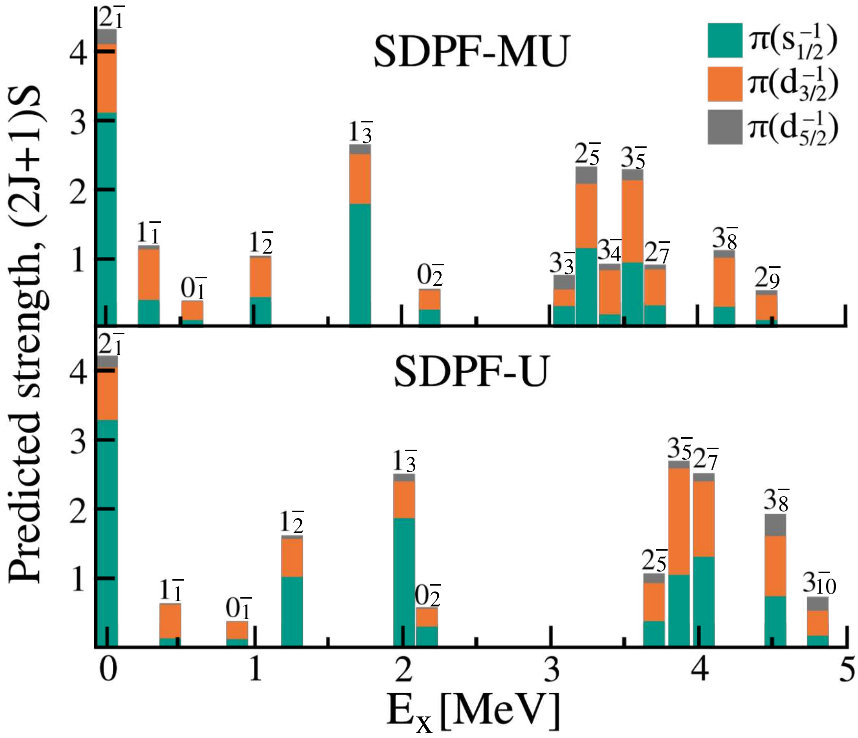

Figure 2.9: Shell model predicted ^{48}K state population strength by ^{47}K(d,p) based on shell-model calculation using the effective interactions SDPF-MU (top) and SDPF-U (bottom). Colours indicate the mixed proportion of each proton configuration in that state.

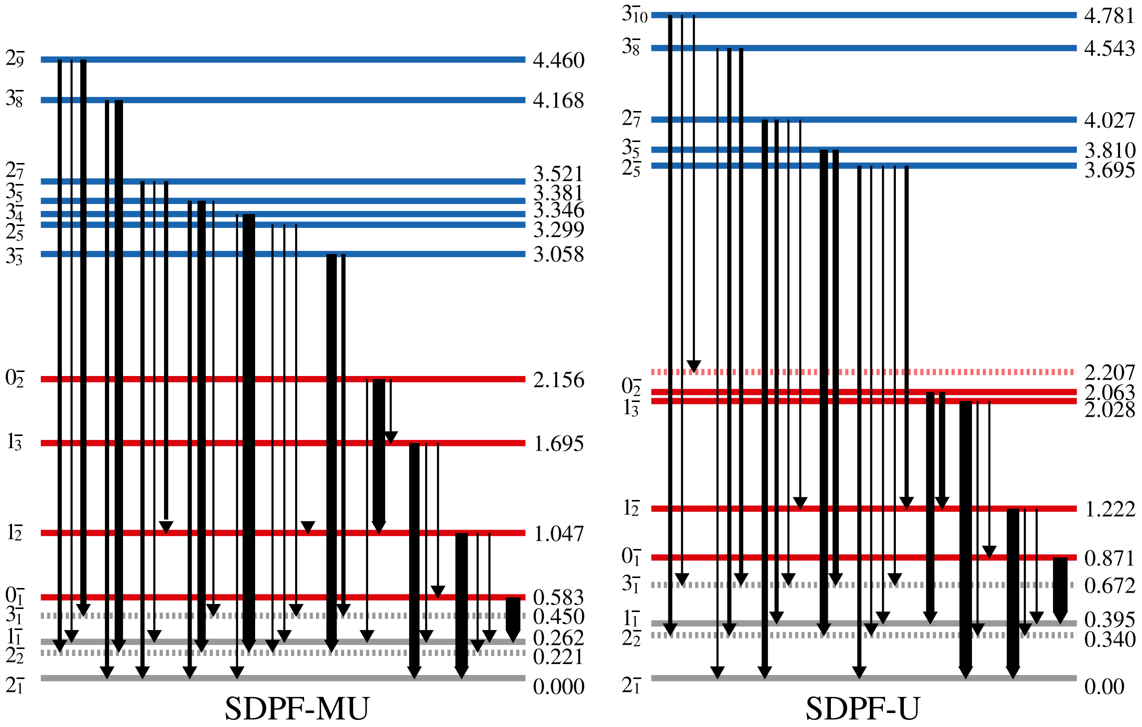

Figure 2.10: Shell model predictions of γ-ray transitions from strongly populated states in ^{48}K, with branching ratios represented by the thickness of the arrow. Here, dotted lines indicate states that are not directly populated by (d,p) transfer. Note that, in this diagram, no transitions are shown from the 1_1^-, 2_1^-, 2_2^- and 3_1^- states, in grey.

Using these shell model calculations, predicted ^{48}K excitation spectra and level schemes can be constructed, which have been distilled into **Figures 2.9** and **2.10**. In **Figure 2.9**, the predicted strength of population is very similar between the models, as would be expected given the similar spectroscopic factors observed in **Figure 2.7**. Interestingly, however, the relative weighting of the different proton configurations for states in the two models are also quite similar, with the notable exception of the 1^-_2 state, which is primarily $\pi s^1_{1/2} d^4_{3/2}$ in SDPF-U, but primarily $\pi s^2_{1/2} d^3_{3/2}$ in SDPF-MU.

To inspect the calculated branching ratios of γ-ray decays from the strongly populated states, it must first be acknowledged that the poor arrangement of the ground state and first excited state in the shell model calculations leads to spurious decays between the 1^-_1, 2^-_1, 2^-_2 and 3^-_1 states, which are certain to be inconsistent with experimental measurement. As such, these decays are omitted from the following discussion, and from **Figure 2.10**. Additionally, the difference in transition energy due to this poor arrangement may lead to some differences in the predicted branching ratios between different states. With this in mind, some key observations from the predicted transitions are given:

- In accordance with selection rules, the 0^- states only decay to lower-energy 1^-_1 with any significant strength, which makes these states especially unique amongst their neighbouring states.
- The 1^-_2 and 1^-_3 states both decay to the two low-lying 2^- states, however, both show a preference for 2^-_1 (primarily $\pi s^1_{1/2} d^4_{3/2}$ configuration) over 2^-_2 (primarily $\pi s^2_{1/2} d^3_{3/2}$ configuration).
- This trend is broadly reversed for the states at higher energies, which generally preferentially decay to 2^-_2 over 2^-_1. This is consistent with the large $\pi s^2_{1/2} d^3_{3/2}$ proportion seen in higher energy states in **Figure 2.9**.
- The exception to this trend is the 2^-_7 state, which – in both models – prefers 2^-_1.
- In the SDPF-U model, the highest energy state, 3^-_{10}, is expected to have a non-negligible decay to a state at 2.207 MeV which is not directly populated by transfer.

2.4.2 ^{47}K(d,t)^{46}K

Due to the complexity and computational expense of nucleon-removal calculations, the calculations for ^{47}K(d,t)^{46}K were performed under the advice of B. A. Brown – a preeminent expert in shell model theory, and creator of NuShellX – using the ZBM2* Hamiltonian. Note that in this region, there are no possible $\ell = 1$ and $\ell = 3$ mixed states; instead, there is a possibility of mixing between $\ell = 0$ and $\ell = 2$ configurations for 1^+ states. The results of this calculation are distilled into **Figure 2.11**. The interesting observations of this work are:

- The 2^- ground state is expected to be weakly populated by the removal of a neutron from $\nu p_{3/2}$. This is from the small component of $\nu f_{7/2}^{-2} p_{3/2}^{2}$ in the ^{47}K ground state (approximately 9% in ZBM2* calculations) due to the softness of the N = 28 closure.
- Each 1^+ state is predicted to have fairly significant mixing; this in opposition to the ^{47}K(d,p) shell model calculations that do not expect any state to be significantly mixed.

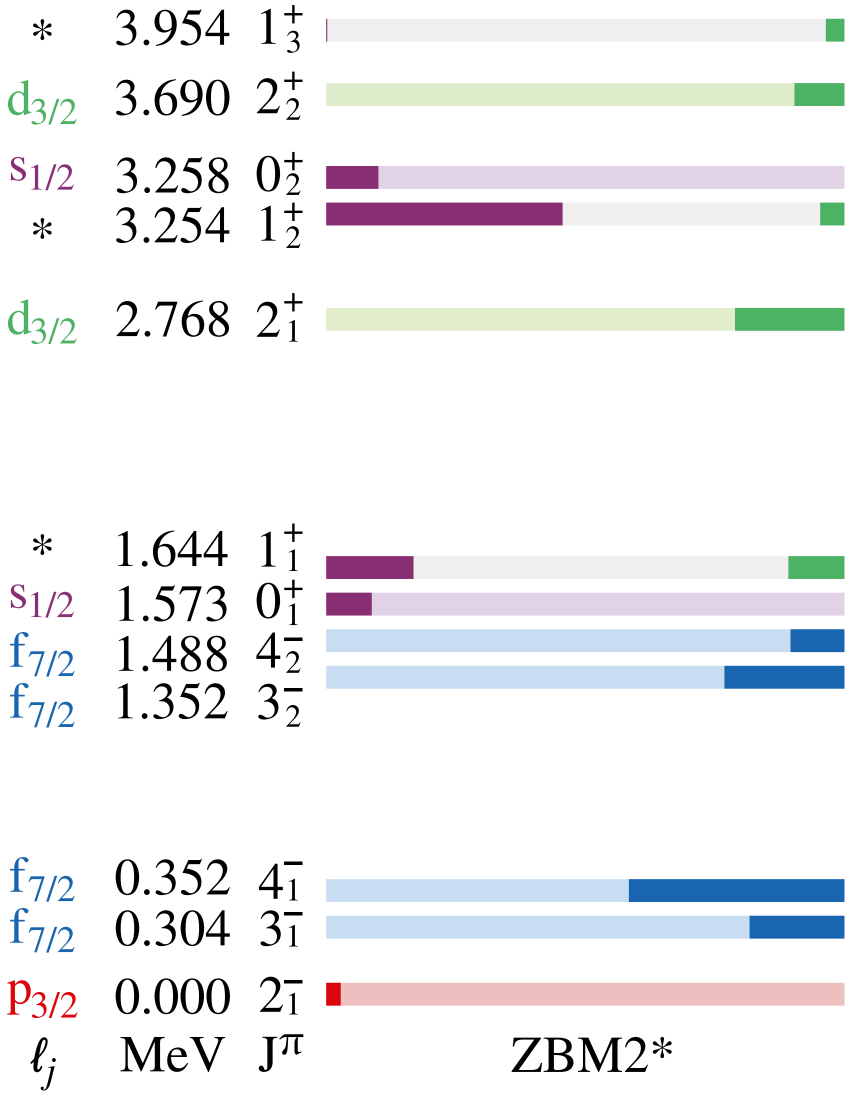

Figure 2.11: ZBM2* spectroscopic factor predictions for 47K(d,t). Here, all states with a predicted spectroscopic factor larger than 0.1 are shown, and the spectroscopic factor is represented as the filled length of each bar, where a full bar equals the maximum occupation of that orbital. The $\ell = 0, 1$ states fill from the left in purple and red, and the $\ell = 2, 3$ states fill from the right in green and blue. States marked with an asterisk are mixed configuration.

Chapter 3

Experiment

This thesis is based on an experiment performed in March 2021 at the *Grand Accélérateur National d'Ions Lourds* (GANIL) in Caen, France, for the study of the neutron pick-up and stripping reactions ^{47}K(d,p)^{48}K and ^{47}K(d,t)^{46}K. This experiment[1] was part of a campaign [68] of experiments coupling the γ-ray tracking array AGATA [69] and the particle detector array MUGAST [70] to the magnetic spectrometer VAMOS++ [71]. A radioactive beam of ^{47}K was provided by the SPIRAL1+ facility and was of exceptional quality, in terms of both intensity and purity. This beam then impinged upon a target of deuterated carbon (CD$_2$) at an energy of 7.7 MeV/u, and the transfer reactions were studied through triple coincidence detection of the light ejectile particle, heavy recoil nucleus and nuclear de-excitation γ-ray transitions.

This chapter begins by reviewing the two-body kinematics of transfer reactions, as this dictates several aspects of the experimental design, such as the placement of light ejectile detectors and the data required from a zero-degree heavy recoil apparatus. This is discussed in Section 3.1. Then, the method used to produce the radioactive isotope beam is reviewed in Section 3.2. Section 3.3 discusses semiconductors and their use as nuclear detectors, specifically silicon and germanium-based detectors. This is followed by an overview of magnetic spectrometers in Section 3.4. Then, the specific apparatus used in this work is discussed: the MUGAST charged particle detector (Section 3.5); the AGATA γ-ray detector (Section 3.6) and the VAMOS++ magnetic spectrometer (Section 3.7). The chapter concludes with an overview of the data acquisition system in Section 3.9.

3.1 Experimental overview

3.1.1 Two-body kinematics

The kinematics of transfer reactions – being, in essence, a two-body problem – can be well-described by simple conservation of energy and momentum arguments. For the experimental method employed in this work, it is ideal for the system in the centre-of-

---

[1] Experiment reference: *e793s*.

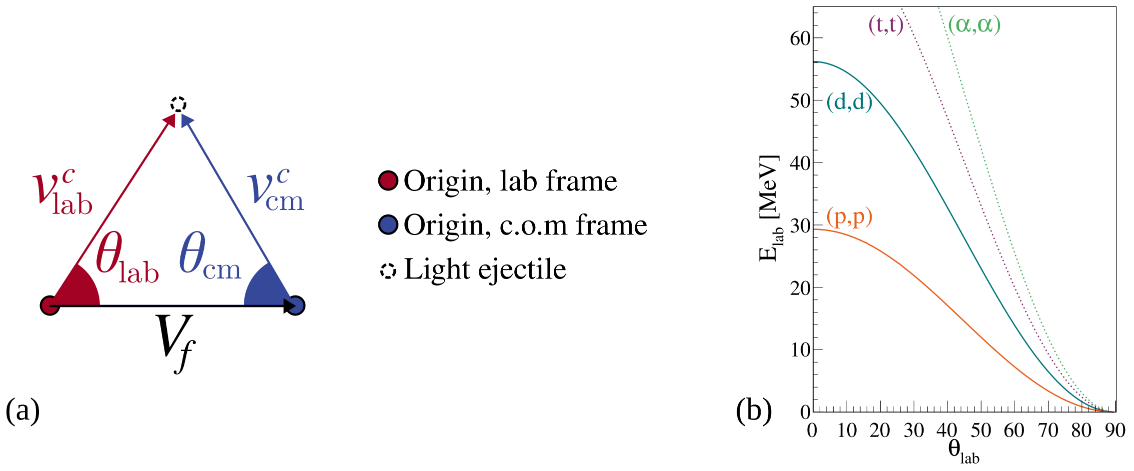

Figure 3.1: Simple diagrams exploring elastic scattering kinematics. (a) Vector diagram relating the light ejectile velocity in the laboratory and centre-of-mass frames. (b) $\mathrm{E_{lab}}$-θ_{lab} kinematic lines of different scattering particles. Dashed lines indicate scattering that is not relevant to the current work.

mass frame to be fully described using only measurements of the light ejectile that can be made in the laboratory frame of reference. Key points of this process are detailed here, but a more complete formalism can be found in Ref. [72].

Consider the transfer reaction $A(b,c)D$, in inverse kinematics. In the laboratory frame, a heavy beam particle A (with momentum $p^A_{\mathrm{lab}} = m^A v^A_{\mathrm{lab}}$) bombards a stationary, light target particle b (with momentum $p^b_{\mathrm{lab}} = m^b v^b_{\mathrm{lab}} = 0$). The initial velocity of the centre-of-mass frame relative to the laboratory frame (V_i) can be shown to be [72]

$$(m^A + m^b)V_i = m^A v^A_{\mathrm{lab}}, \quad \text{or} \quad V_i = \frac{m^A}{m^A + m^b} v^A_{\mathrm{lab}}. \tag{3.1}$$

In inverse kinematic transfer reactions, it is often the case that $m^A >> m^b$, so the centre-of-mass frame is moving relative to the laboratory frame at almost the beam velocity.

After the reaction, momentum must be conserved in both the laboratory and centre-of-mass frames. As such, it can be said that the final relative velocity of the centre-of-mass frame V_f is $(m^A + m^b)V_i = (m^c + m^D)V_f$. Using the previous definition of V_i in Equation 3.1, it can be found that $V_f = \frac{(m^A+m^b)}{m^c+m^D} V_i = \frac{m^A}{m^c+m^D} v^A_{\mathrm{lab}}$, and hence V_f can be simply derived from the incident beam velocity in the laboratory frame and the masses of the particles. With V_f now known, simple vector addition (see **Figure 3.1a**) reveals that measuring v^c_{lab} allows for v^c_{cm} to be determined. This simple configuration is used to demonstrate several key concepts in inverse kinematic transfer reactions.

Whilst in the laboratory frame, the target particle b is initially at rest, it is critical to note that in the centre of mass frame, $v^b_{\mathrm{cm}} = V_i$. In the simplest case of elastic scattering, $b = c$ and $A = D$, therefore $V_i = V_f$. As the light ejectile c has the same magnitude of velocity in

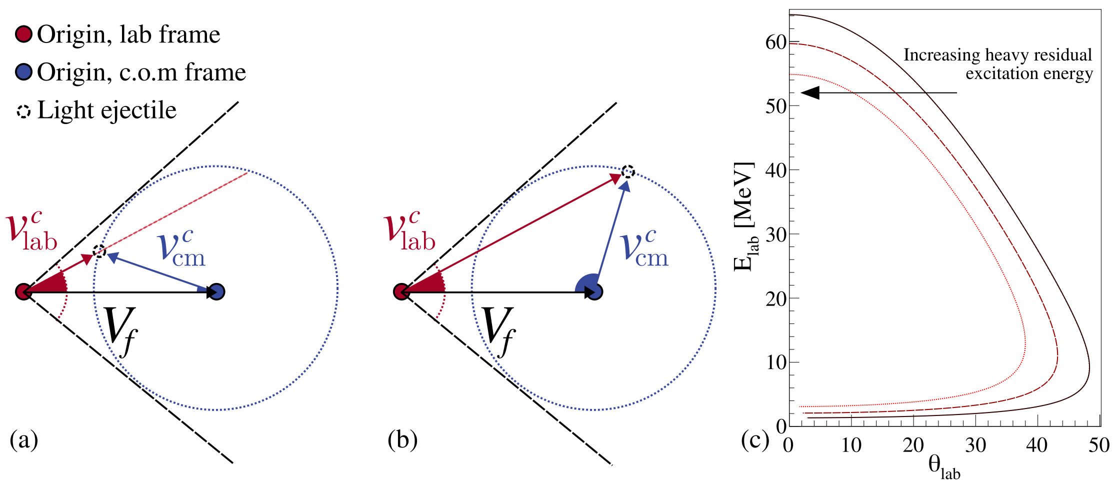

Figure 3.2: Simple diagrams exploring the (d,t) transfer reaction kinematics for (a) small θ_{cm}, (b) large θ_{cm}, and (c) the E_{lab}-θ_{lab} kinematic lines of different excitation energies.

the centre-of-mass frame as the target b [44], $|v^c_{\text{cm}}| = |v^b_{\text{cm}}| = |V_i| = |V_f|$. It is then trivial to see, with reference to **Figure 3.1**, that the ejectile from an elastic scattering reaction *must* always have $\theta_{\text{lab}} \leq 90°$.

In the case of the neutron pickup and stripping reactions, the target and ejectile are no longer equivalent particles. To conserve momentum in the centre-of-mass frame before and after the reaction, v^c_{cm} must vary in accordance with the change in mass between target b and ejectile c. For instance, in the case of the (d,t) reaction, the mass can be written as $m^c = \frac{3}{2}m^b$. As such,

$$|v^c_{\text{cm}}| = \frac{2}{3}|v^b_{\text{cm}}| \therefore |v^c_{\text{cm}}| = \frac{2}{3}|V_f|.$$

The vector diagrams in **Figure 3.2a** and **b** show this case, with two key features to note. Firstly, no matter the value of θ_{cm}, θ_{lab} is always forward-focused. Secondly, every θ_{lab} value (except the tangent) has two θ_{cm} solutions. These two solutions are only distinguishable by the magnitude of the velocity vector v^c_{lab}. This effect is clear when the kinematic line of the reaction is plotted, for E_{lab} against θ_{lab}, as in **Figure 3.2c**. While the recoil nucleus has so far been considered to remain in the ground state (g.s.), it is critical to note that, for cases where the heavy recoil nucleus is in an excited state E_x, the Q-value of the reaction is reduced by $Q = Q_{\text{g.s.}} - E_x$. As such, the ejectile particle carries less kinetic energy, $|v^c_{\text{cm}}|$ is reduced, and the range of laboratory angles available is restricted. Consequentially, excited states populated by the (d,t) reaction appear "inside" the ground state line in **Figure 3.2c**. For the lower ejectile energies that tend to be measured experimentally, the effect is that kinematic lines from excited states appear at higher E_{lab}.

For the case of the (d,p) reaction, the kinematics are very different:

$$m^c = \frac{1}{2}m^b \therefore |v^c_{\text{cm}}| = 2|v^b_{\text{cm}}| \therefore |v^c_{\text{cm}}| = 2|V_f|.$$

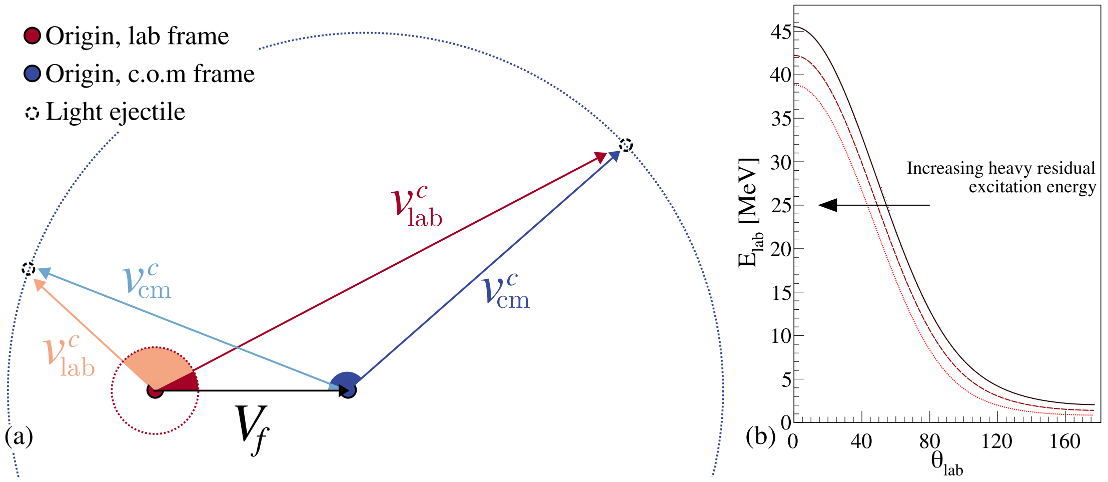

Figure 3.3: Simple diagrams exploring the (d,p) transfer reaction kinematics for (a) large and small θ_{com}, and (b) the $\mathrm{E}_{\mathrm{lab}}$-$\theta_{\mathrm{lab}}$ kinematic lines of different excitation energies

The vector diagram in **Figure 3.3a** shows this case. Note here that θ_{lab} is not restricted, as in previous cases; in fact, the light ejectile can be emitted in any direction in the laboratory frame. Critically, the energy of the ejectile varies significantly with θ_{cm}. For large values of θ_{cm} (i.e. small θ_{lab}), the magnitude of v^c_{lab} is large, but becomes much smaller for small θ_{cm} (i.e. large θ_{lab}). As such, the ejectile only has low energy, preferable for experimental measurements, at backwards laboratory angles, as shown in **Figure 3.3b**. In the case of (d,p), if the heavy recoil nucleus is in an excited state, there is less kinetic energy available for v^c_{cm}, which also reduces the magnitude of v^c_{lab}. For all θ_{lab} angles, this corresponds to a lower ejectile energy $\mathrm{E}_{\mathrm{lab}}$.

3.1.2 Observables of interest

For each excited state that is observed, certain measurements are required for the determination of the excitation energy, the magnitude and shape of the differential cross section, and the γ-ray transitions within the product nucleus. The measurements performed will determine:

- Direction (θ_{lab}, ϕ_{lab}) of the light ejectile, to distinguish between reaction channels, and to determine the excitation of the associated heavy recoil nucleus.
- Energy ($\mathrm{E}_{\mathrm{lab}}$) of the light ejectile, to determine the excitation of the associated heavy recoil nucleus.
- Distribution of the light ejectiles in θ_{lab} for a given state in the recoil nucleus, to extract the experimental differential cross section.
- Energy of coincident γ-rays in the de-excitation cascade of an excited nucleus, to determine the spin of the excited state by selection rules, and to isolate specific states

by their coincidences.

- Direction of coincident γ-rays relative to the beam direction, to correct for the Doppler effect due to the fast-moving recoil nucleus.
- Coincident heavy recoil signal, to distinguish the measured light ejectile and γ-rays from sources of background.
- Total number of incident beam particles over the course of the experiment, for the normalisation of the results when extracting spectroscopic factors.

The detectors of the MUGAST-AGATA-VAMOS++ campaign, shown in **Figure 3.4**, are specialised to measure all of these experimental observables. The detector systems used were:

MUGAST	A highly-segmented array of double-sided silicon strip detectors to measure E_{lab}, θ_{lab} and ϕ_{lab} of light ejectiles with high precision.
AGATA	An array of state-of-the-art high-purity germanium tracking detectors to measure the energy and interaction position of emitted γ-rays with high precision.
VAMOS++	A magnetic spectrometer to provide a coincidence timing signal for ^{46,47,48}K heavy recoils resulting from nucleon transfer or elastic scattering, resulting in clean spectra with minimal background.
CATS	A fast-counting multi-wire parallel plate avalanche counter to monitor the number of incident beam particles.

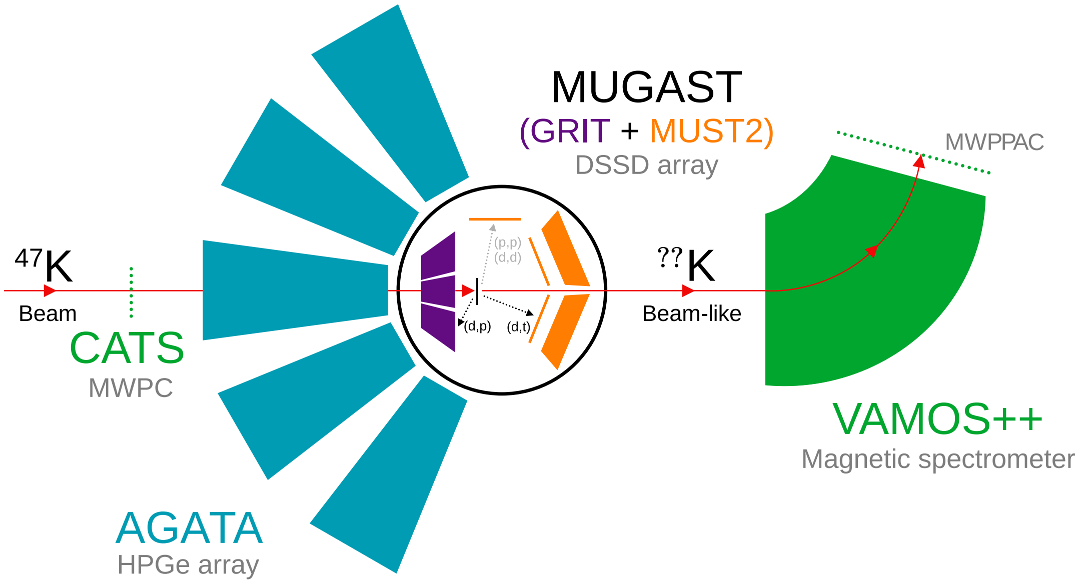

Figure 3.4: Conceptual design of the MUGAST-AGATA-VAMOS++ coupled system.

3.2 Radioactive beam production

The operational team of the SPIRAL1+ cyclotron system provided a high-purity, intense beam of ^{47}K for this experiment, using the isotope separation on-line (ISOL) method of producing a radioactive isotope beam. Details of this system are available from Refs. [73–75], with the general stages of the process distilled here.

3.2.1 Primary beam and fragmentation

A compact injector cyclotron (C01/C02) containing an ion source (in the case of this work, ^{48}Ca) accelerated a primary beam of stable nuclei. This primary beam was initially slow-moving, and so the beam was accelerated through the two separated sector cyclotrons (CSS1 and CSS2) to a velocity of $0.3c$. This acceleration was required to reach the requisite energy for fragmentation reactions to take place in the production target.

The fast primary beam was then directed to the target ion source and impinged on a thick target of BeO, where the beam nuclei fragmented. These fragments (including the intended beam isotope) diffused out of the hot target as neutral atoms and into a forced electron beam induced arc discharge (FEBIAD) ion source (see **Figure 3.5a**), which was used here in surface ionisation mode. Here, a cathode at approximately 2000°C emitted thermal electrons, which were accelerated by an anode grid to bombard the fragment atoms. These fragments were then ionised into a 1^+ charge state and extracted from the FEBIAD [76].

3.2.2 Charge breeding and reacceleration

For a given acceleration voltage, it is more effective to reaccelerate isotopes in a higher charge state than 1^+ [77] – as a result, charge breeding techniques are often employed at ISOL facilities. At SPIRAL1+, the slow radioactive beam extracted from the FEBIAD was directed into an electron cyclotron resonance ion source (ECRIS) charge breeder [78] where the 1^+ beam was stopped in a plasma. These isotopes were contained in the Phoenix ECRIS [75, 79] by confining magnetic fields, ionised into a higher charge state by multiple Coulomb collisions with thermally excited electrons, and extracted after a particular confinement time which determined their charge state.

The cocktail beam, now in a 10^+ charge state, was then sent to the *Cyclotron pour Ions de Moyenne Energie*, CIME. Here, the beam was reaccelerated to $\approx 0.1c$; the appropriate energy for the transfer reaction studied in this experiment. The use of a cyclotron to accelerate the beam, as opposed to the linear accelerators used by many other facilities, has the advantage of also separating out beam contaminants with a mass resolution of 10^{-4}.

3.2.3 Radioactive beam produced for this work

In March 2021, a primary beam of stable ^{48}Ca was used to deliver a radioactive beam of ^{47}K in the 10^{+} charge state to the VAMOS++ spectrometer with SPIRAL1+. The beam had an energy of 7.7 MeV/nucleon and an average intensity on the order of 5×10^{5} pps. An overall integrated beam of 1.842×10^{11} particles was incident upon the CD_2 target during this experiment, as measured just before the target position (see Section 3.8). For a beam of ^{47}K, the most likely contaminant was determined to be ^{47}Ca, which has a mass difference from ^{47}K of 1.6×10^{-4}. This is resolvable by the CIME cyclotron, and as such, there is great confidence that the reaccelerated beam of ^{47}K delivered to the experimental hall was > 99.99% pure. This beam purity determination is supported by the experimentally observed reaction products, as presented in Section 4.1.6.

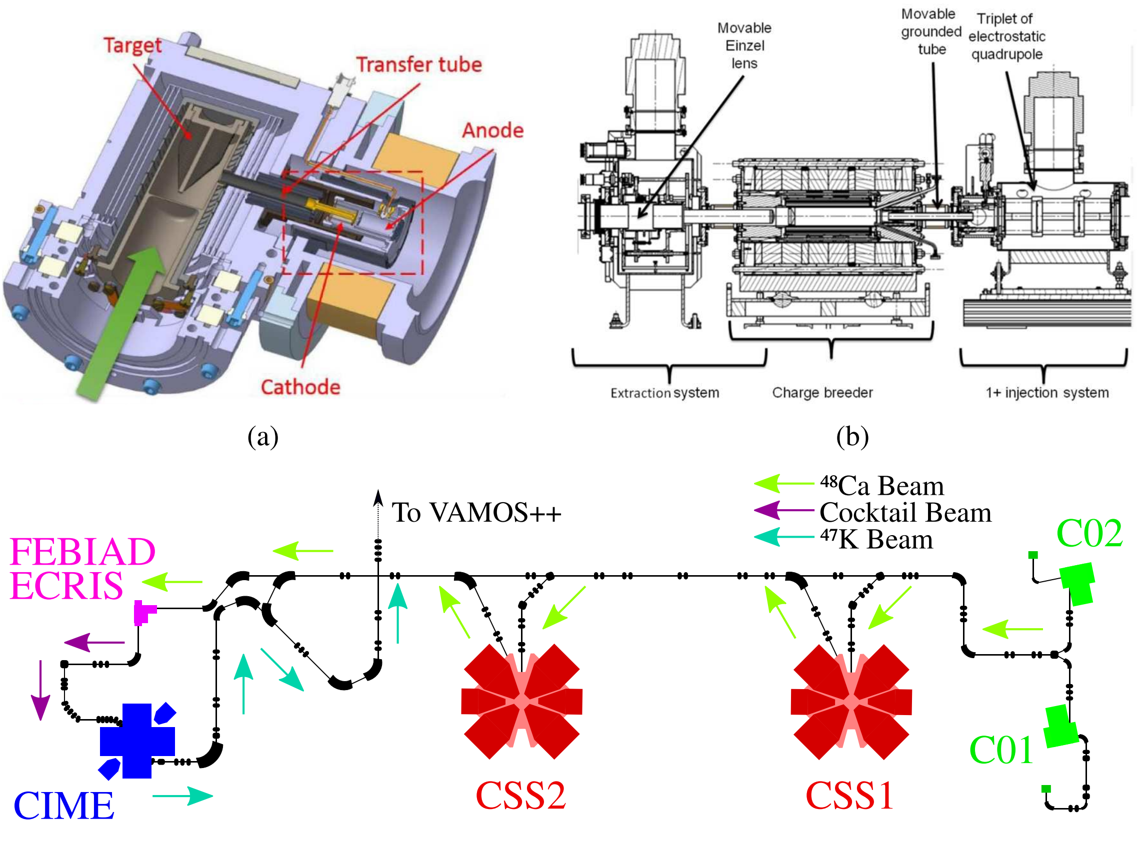

(a) (b)

(c)

Figure 3.5: Schematics of the SPIRAL1+ radioactive ion beam facility, and constituent components. (a) Schematic of the target arrangement and FEBIAD ion source (red dashed box). Figure from Ref. [76]. (b) Schematic of the Phoenix ECRIS charge breeder (beam injected from right). Figure from Ref. [79]. (c) Diagram of the GANIL-SPIRAL1+ accelerator facility, with each progressive stage of the beam production process represented by coloured arrows.

3.3 Semiconductor detectors

3.3.1 Principles of semiconductor detectors

Semiconductors are very effective detection materials, due to their characteristic band gap energies, intermediate between insulators and conductors. As opposed to the large, often insurmountable band gaps in insulators, or the free-flowing movement of electrons in conductors, semiconductors only allow the excitation of electrons into the conduction band via the application of a small external stimulus, leaving a hole in the valence band.

The passage of ionising radiation through a semiconductor detector would provide just such a stimulus, producing a number of electron-hole pairs directly related[2] to the energy of the incident radiation, and the band gap the electron was excited across [80, p. 348] These electron-hole pairs will move under the influence of an applied electrical field. The movement of these electrons and holes towards the electrical contacts at the boundary of the detector induces an electrical signal [81, p. 102].

In silicon and germanium semiconducting materials, the energy required to induce one electron-hole pair is on the order of a few eV; for a point of comparison, an industry-standard gas-filled detector would more likely have an ionisation energy on the order of several tens of eV. For any given particle detection, this order of magnitude increase in the number of charge carriers produced in a semiconductor detector means that the statistical error is much reduced, and so the detector resolution is greatly improved. Additionally, the higher density of these materials (relative to a gas) means that a thin detector is capable of stopping incident radiation completely within its volume, whereas a gas-filled detector requires significant thickness to achieve the same result [81, p. 79].

3.3.2 Neutron transmutation doping of silicon

While silicon is an intrinsic semiconductor, the electrical properties of a semiconducting material can be improved by doping, i.e. the intentional inclusion of impurities of an element with one more outer shell electron (n-type) or hole (p-type) than the semiconductor element – usually aluminium or phosphorus, in the case of silicon. At the boundary between a p-type and n-type semiconductor, a depletion zone is formed[3], which contains reduced numbers of charge carriers. As such, very little leakage current passes across the semiconductor, and hence the electron-hole shower from ionising radiation produces a pulse with a better signal-to-noise ratio.

---

[2] This assumption holds, provided the incident particle is stopped within the detector, and does not *punch through* the active volume.

[3] The size of this depletion zone is usually increased by reverse-biasing the semiconductor.

For some of the detectors used in this work, an unusual doping method was implemented; neutron transmutation doping (nTD) [82]. This specialist method of producing n-type bulk material is unique in that it relies on nuclear decays to form the doping elements [83]. This method takes advantage of the small natural abundance of ^{30}Si, creating a monocrystal of ^{nat}Si (92% ^{28}Si and 3% ^{30}Si) and exposing the lattice to a large neutron flux. The resulting neutron capture reaction ^{30}Si(n,γ) results in the unstable isotope ^{31}Si, which then β^- decays to stable ^{31}P, creating the n-type dopant extremely uniformly within the lattice.

Due to the uniform doping (and therefore low resistance variability[4]) across the whole bulk, the shape of the observed signal has very little dependence on the position in the wafer. This is critical for pulse shape analysis techniques (Section 3.6.1), that will eventually be applied in concert with nTD silicon detectors in the GRIT array [85].

3.3.3 Double-sided silicon strip detectors

Silicon strip detectors are a form of semiconductor detector whereby a thin diode wafer (generally on the order of hundreds of microns to millimetres thick) is electrically divided into many strip-like regions, which are each read separately. In such detectors, the p^+ wafer surface is divided by the controlled growth of SiO_2 to form isolating strip divisions. The charge carriers are collected on a thin aluminium layer deposited on the surface of the detector [86]. This design provides a one-dimensional positional measurement alongside the energy measurement.

An advance upon this design is the creation of double-sided silicon strip detectors (DSSDs), which utilise the fact that electrons and holes are driven to opposite sides of the silicon wafer by the bias voltage, and measure both of them. In such detectors, the direction of the back strips is orthogonal to the front strips, creating a grid. A single particle entering the detector will therefore induce two electrical signals; electrons on the ohmic (n-type) surface, and holes on the junction (p-type) surface. These two signals can be correlated to provide a two-dimensional position measurement by locating a single pixel on the grid [81, p. 116] .

The construction of the backside of the wafer is slightly more complicated than the front side due to the requirement for $n+$ implantation. In such cases, electrons can accumulate below the SiO_2 layers separating $n+$ strips, and this build-up of negative charge can screen the electric field, disrupting charge collection [81, pp. 117-119]. An industry-standard method of combating this issue is interleaving $p+$ implant strips between the $n+$ strips [87].

---

[4] Variations in nTD wafers are on the order of 2% across 200 mm, as opposed to alternative gas-doped wafers with variations on the order of 8% over the same range [84].

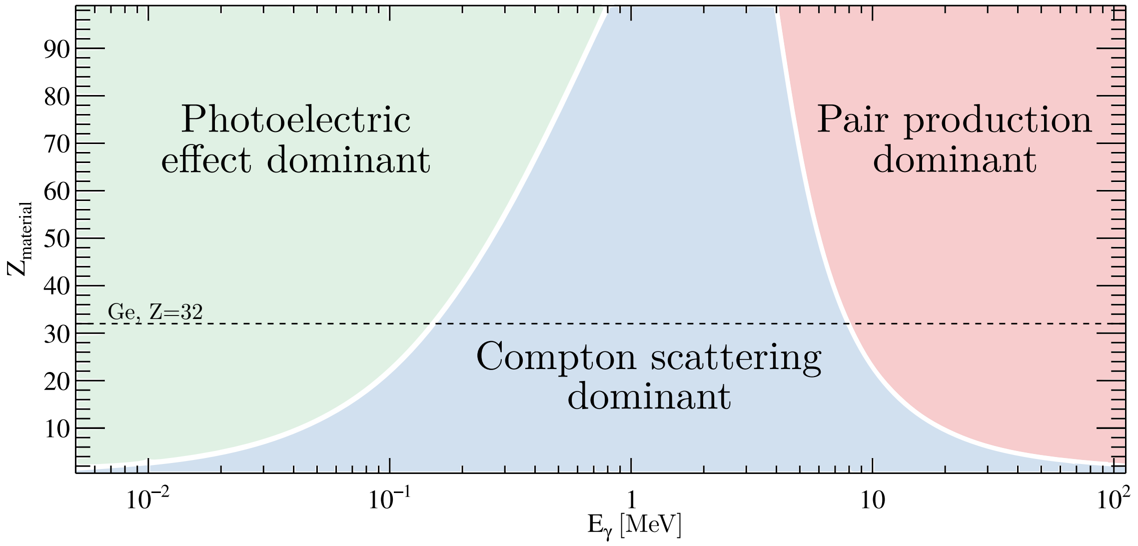

Figure 3.6: Dominant γ-ray interactions with matter at different energies and material Z. Note that, in the region of $_{32}$Ge, marked with a dashed line, Compton scattering is the dominant form of interaction for γ-rays in the approximate region of $10^{-1} - 10^{1}$ MeV.

3.3.4 High-purity germanium detectors

Germanium is a semiconducting material well-suited for γ-ray detection. Firstly, the small band gap energy (0.7 eV) allows for very high-resolution spectroscopy. Additionally, germanium ($Z = 32$) is a high-Z material, and as such has a high stopping power for γ-rays relative to, say, silicon ($Z = 14$).

As the depletion depth of a germanium crystal detector is inversely related to the net impurities in the crystal [80, Eq. 12-1], there is a point at which the only way to produce a detector with a large enough depletion region to both fully stop and fully measure a γ-ray is for the crystal to be ultrapure. This is the motivation for the development of high-purity germanium (HPGe) detectors, which have impurities on the order of 10^{-10} atoms cm^{-3} [88].

Additionally, the detection volume can be maximised through the choice of detector shape. A closed-end coaxial detector allows for a large crystal volume whilst minimising the distance from any given point to an electrical contact [80, p. 390]. In these cases, one electrode is on the outer surface, and the other on the inner surface – usually, the rectifying contact is placed outside, as this reduces the bias voltage required to form a depletion region through the whole detector [88], i.e. an n-type closed-end coaxial HPGe detector will have the $p+$ contact on the outer surface.

Unfortunately, HPGe detectors cannot be used at room temperature, as the size of the band gap in germanium is so small that electrons can be thermally excited into the conduction band. As such, HPGe detectors must be cooled during operation in order to reduce the noise from thermal excitation [80, p. 395]. This is typically achieved through the combined use of liquid N_2 cooling and an insulating vacuum cryostat.

The method by which a γ-ray interacts with a material depends on both the energy of the photon, and the properties of the material itself, as shown in **Figure 3.6**. Note that, for ${}_{32}$Ge, the primary method of interaction is Compton scattering, particularly in the 10^{-1} MeV to 10^{2} MeV energy range that is most relevant for nuclear structure studies. As these events only deposit some part of their energy each time they scatter, they must either be filtered out of the data, or recovered by rebuilding the total incident energy.

3.4 Magnetic spectrometers

3.4.1 Principles of magnetic spectrometers

In fast-beam experiments, many different reactions and interactions can occur between the beam isotope and the target nucleus. Single-nucleon transfer, elastic and inelastic scattering, fusion-evaporation and Coulomb excitation are all examples of interactions that could occur, some of which can occur at similar incident beam energies and therefore within the same experiment. As such, it is necessary to isolate particular reaction channels, often by distinguishing between the heavy nuclei that result from the different reactions.

Magnetic spectrometers exploit the behaviour of charged particles in magnetic fields to distinguish between nuclei with different magnetic rigidities, $B\rho$, using ion optical devices (Section 3.4.2). These dispersed nuclei then impinge on detectors positioned at the focal plane of the spectrometer (Section 3.4.3) for further measurements, as required.

3.4.2 Ion optics

3.4.2.1 Dipole magnets

A charged particle moving in a uniform magnetic field, such as that provided by a magnetic dipole, experiences a force $F_m = qvB$ perpendicular to the direction of motion, inducing a circular motion of the particle. As the magnetic force is the centripetal force F_c of this circular motion, and given that $F_c = \frac{mv^2}{\rho}$, where ρ is the radius of the curvature, the magnetic rigidity, $B\rho$, can be trivially derived:

$$B\rho = \frac{mv}{q}.$$

In a direct reaction experiment in inverse kinematics, it can be generally assumed that the velocity of the heavy beam-like recoil nucleus will continue with approximately the same velocity as the incident beam nucleus. As such, the velocity of different species of nuclei will be approximately equal, and they can be distinguished instead by their value of $\frac{m}{q}$, where q is the charge state of the nucleus.

As a result, nuclei passing through the dipole magnet of a magnetic spectrometer will be bent by different curvature radii, and exit the spectrometer at a different position along the dispersive axis. Some nuclei, which are far from the desired $\frac{m}{q}$ value, will not reach the focal plane at all, and will instead impinge the inner or outer edge of the nuclear spectrometer. This is often an effective method to exclude nuclei that arise from parasitic reactions in the target.

3.4.2.2 Quadrupole magnet

In order for different $\frac{m}{q}$ positions on the focal plane detectors to be well-resolved, the beam of reaction products entering the dipole should be of the highest achievable quality. As such, the reaction products often need to be focused into the dispersive dipole magnet. Quadrupole magnets are used for this purpose.

The magnetic field produced by a quadrupole is symmetric but not uniform. The strength of the field is strongest at the edges, and weaker towards the central axis. This has the effect of funnelling any divergent nuclei back onto the central path [89, p. 22]. Quadrupoles focus along one axis but defocus along the perpendicular axis. As such, they are often used in pairs, with the second quadrupole rotated 90° relative to the first, resulting in a net focusing in both directions.

3.4.3 Focal plane detectors

With nuclei of different magnetic rigidities spatially separated by the dispersive elements of the magnetic spectrometer, various types of detectors can be implemented at the focal plane to measure variables such as the position, time of flight, energy loss in a known medium and total energy of the nucleus, which can be used in combination to fully identify the isotope [71]. However, in this work, the focal plane detectors were bombarded by the full incident beam (see Section 3.7.2) which presents problems for many varieties of detectors. As only the detection of *some* nucleus at the focal plane position was absolutely required, and identification of the isotope was not critical, only the fast-counting gas multiplication detector type – capable of tolerating high counting rates on the order of 10^6 – will be detailed.

3.4.3.1 Gas multiplication detectors

Gas multiplication detectors are high-voltage gas-filled detectors that are capable of producing a large output signal from a single incident particle. Heavy ions entering the detector ionise the gas molecules and release electrons from the atoms, which are then accelerated by the electrical field towards the anode. If the electrical field is strong enough to accelerate the electrons such that their kinetic energy is greater than the ionisation energy of the gas, then each free electron can then go on to collide with and ionise another molecule in the detector [80]. This is the process of gas multiplication, which can cause a cascade of ionisation, or Townsend avalanche, which exponentially multiplies the collected charge from each impact.

If the applied voltage is within a given range of voltages – the ‘true proportionality’ region – then the number of secondary avalanche ions is proportional to the initial number of ions formed by the heavy nucleus. Therefore, the original signal strength is recoverable, and the overall signal detected has been amplified significantly. Detectors operating in this mode are referred to as *proportional counters*.

If, however, this range of proportional voltages is exceeded, then the detector enters the region of limited proportionality, where the concentration of secondary avalanche ions is sufficient to alter the shape of the detector’s electrical field [80, p. 162]. While the signal strength can be amplified even further in this higher voltage region, the relationship between the energy deposited by an incident heavy ion and the size of the signal produced is no longer linear, so energy measurements are not typically possible. Detectors operating in this mode are referred to as *avalanche counters*.

3.4.3.2 Multi-wire parallel plate avalanche counters

Various shapes of gas multiplication detectors have been developed, which are specialised for different purposes. For example, cylindrical shapes with axially symmetric fields have good energy resolution, but their timing properties are poor. Conversely, a parallel plate avalanche counter (PPAC) is designed for the purpose of fast timing.

PPACs are constructed of closely spaced anode and cathode plates, with their planes perpendicular to the expected path of incident radiation. As such, a heavy ion will pass through the plates, traversing the small gap and only depositing a small amount of its energy in the fill gas. As the distance for the electrons and ions to traverse is minimised, time resolutions of this type of detector can be on the order of hundreds of picoseconds [90].

A limitation of this method is that the heavy ion will lose some energy in passing through the two parallel plates, not just in the gas. Additionally, as the anode and cathode have large surface areas, no positional data is collected. To iterate upon this design, the multi-wire parallel plate avalanche counter (MWPPAC) was developed. MWPPACs replace the plates with sets of parallel wires. In general, one cathode grid will be positioned between two anode grids, with anode and cathode wires running in perpendicular directions. This allows for a two-dimensional position measurement with minimal interference to the heavy ion energy.

3.4.3.3 Multi-wire proportional counters

Similar in construction to a MWPPAC, multi-wire proportional counters (MWPCs) are also gas multiplication detectors consisting of closely spaced grids of anode and cathode wires. The key difference between the two types of detector is that, while MWPPACs are operated at a voltage in the region of limited proportionality, MWPCs are true proportional counters.

3.5 MUGAST

The MUGAST array [70] is a primarily DSSD-based array used for the detection of light emitted particles such as protons, deuterons, tritons and α-particles. MUGAST is a transitional phase of the GRIT project [85], which combines the well-established MUST2 array [91] detectors with next-generation GRIT trapezoidal detectors. The specifics of the two detector types are detailed below.

3.5.1 GRIT

The conceptual design for GRIT (Granularity, Resolution, Identification, Transparency) is a 4π array of DSSDs in a ball-like configuration, with annular detectors at both ends, plus lampshade arrangements of trapezoidal detectors in the upstream and downstream directions, and square detectors covering near-perpendicular angles. The array is designed to be compatible with both the HPGe AGATA array and the $LaBr_3$ PARIS array, and as such, transparency to γ-rays is critical. The mechanical structure, cooling system and front-end electronics of GRIT have all been carefully designed to limit the impedance on a 4π γ-ray array.

The array will have a thin, finely-segmented first stage, backed by thicker, more coarsely segmented second and third stages positioned immediately behind. The n-type silicon wafer is neutron transmutation doped (Section 3.3.2) and reverse mounted [68]. Mounting the detector such that the particle enters through the ohmic side produces a pulse shape that

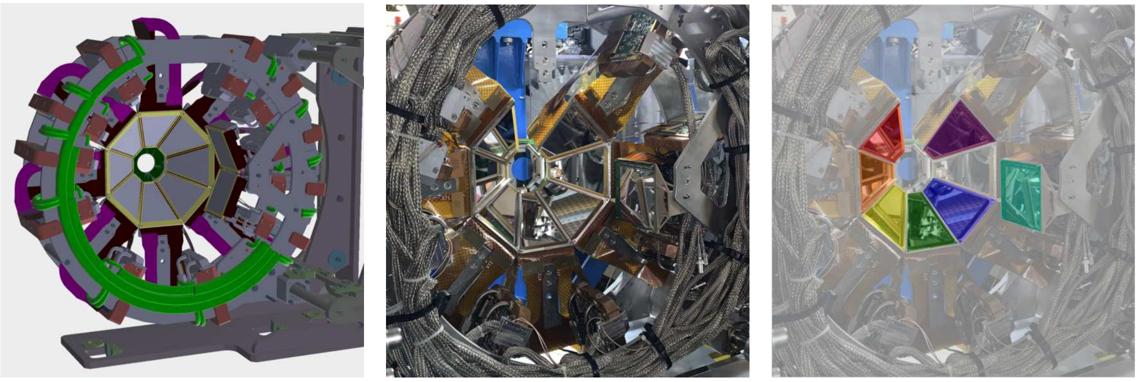

(a) (b) (c)

Figure 3.7: The GRIT upstream lampshade, as (a) a CAD diagram showing the full arrangement [68], (b) a photograph of the lampshade as installed for this experiment, and (c) a photograph with the detectors highlighted for clarity. The trapezoid at the twelve o'clock position is physically absent. The trapezoid at three o'clock, as seen from this perspective, was physically installed but not used. Additionally, one MUST2 DSSD was installed perpendicularly, as in (b) and (c), rather than the two GRIT square DSSDs shown in (a).

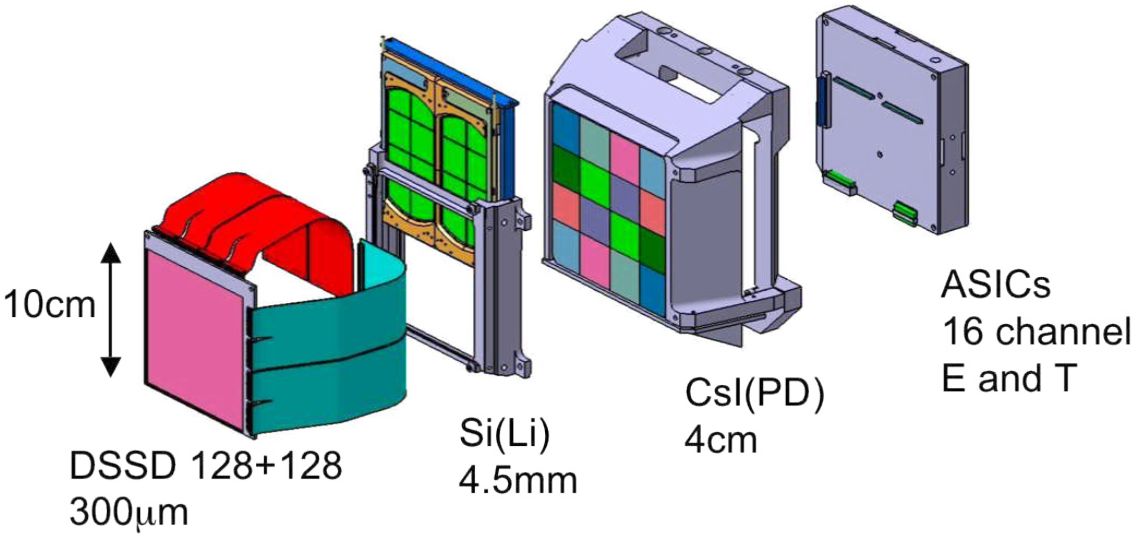

Figure 3.8: Exploded view of a single MUST2 detector, showing the various stages of detection. Note that, during the current work, the Si(Li) stage was absent from the detectors. Figure from Ref. [92].

is dominated by the hole propagation [93], and the charge collection time is related to the (Z,A) of the incident particle [94]. This will allow the GRIT detector to use pulse-shape discrimination to discern the species of charged particle detected on an event-by-event basis.

At the time of the experiment, six trapezoidal DSSDs were used in the upstream lampshade, as seen in **Figure 3.7**. A seventh trapezoid was installed, but non-functional. The trapezoidal detectors that had been fabricated as of the time of this experiment were stage one detectors; that is, they were 500 μm thick DSSDs with 128 strips on each side, with a pitch of 710 μm and 760 μm for the front and rear sides, respectively [68].

3.5.2 MUST2

The detectors of the MUST2 (Mur à Strips 2) array are multi-staged, and specialised for the detection of high-energy downstream ejectiles. The various stages, pictured in **Figure 3.8**, are:

DSSD A highly-segmented semiconductor detector for the precise measurement of charged particle position and energy. Each square detector is 100 cm^2 in area, 300 μm thick and 128 strips per side [95]. This was the primary stage used in this work.

Si(Li) A segmented semiconductor detector for the detection of high-energy charged particles; these were not installed for this experiment.

CsI A scintillator detector for detection of high-energy charged particles that punch through the previous stages. This stage constitutes a 4×4 grid of 4 cm thick crystals, read by photodiodes [91]. In this work, it is used exclusively as a veto. For more details regarding scintillation detectors, the reader is directed to Ref. [80, Chapter 8].

In the downstream direction of the experiment, many high-energy background events were expected, though the particles of interest are relatively low energy. As such, the MUST2 detector was well suited to the downstream position, as the thick CsI detector could collect charge from very high-energy particles with good efficiency. This made it an effective veto on counts detected in the DSSD layer, efficiently eliminating background and punch-through events. This is discussed further in Section 4.1.5.

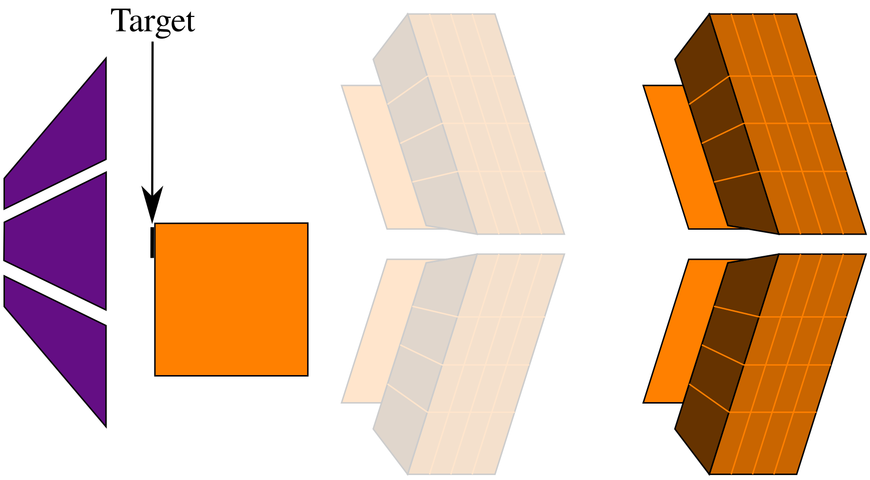

Figure 3.9: Perpendicular schematic of the detector arrangement during the experiment, with beam moving left to right. Additionally, the MUST2 close geometry position is shown in faded colours.

3.5.3 Arrangement of MUGAST during this work

In the MUGAST+AGATA+VAMOS experimental campaign, in March 2021, the arrangement of the detectors was:

Upstream Six trapezoidal GRIT detectors, at an average position from the target of 10 cm, covering the angular range 104° to 156° for the detection of ^{47}K(d,p) protons.

Perpendicular One MUST2 detector, consisting of only the DSSD face, was positioned 14 cm from the target, covering the angles 56° to 81° for ^{47}K(d,d) and ^{47}K(p,p) elastic scattering.

Downstream Four MUST2 detectors, with the DSSD faces backed by CsI scintillators, were positioned 36 cm from the target[5] for the detection of ^{47}K(d,t) tritons. These detectors covered the angular range 3° to 23°.

The high-precision energy and angle capabilities of MUGAST were critical for the reconstruction of the ^{46,48}K excitation, and eventual extraction of differential cross sections. The large angular coverage of the array, particularly in the upstream direction, allowed for a high degree of confidence in the assignment of ℓ-transfers.

---

[5] Note that the downstream MUST2 detectors were mounted in the maintenance position during the experiment, rather than the close geometry position, reducing the downstream angular coverage. See Section 4.1.4.

3.6 The Advanced Gamma Tracking Array (AGATA)

The Advanced Gamma Tracking Array (AGATA) [69] is a coaxial n-type HPGe semiconductor array, and one of only two next-generation tracking arrays in the world [96]. The array is constructed such that three HPGe crystals are grouped together into an AGATA Triple Cluster (ATC), which share a cryostat.

The salient feature of AGATA is the tracking capabilities afforded to it by the 36-fold electrical segmentation of each crystal (see **Figure 3.10a**). Fine crystal segmentation, when used in conjunction with the pulse shape analysis (PSA) techniques [97] and tracking algorithms [98] outlined in the following sections, allows for position and energy measurements for multiple interaction points from the Compton scattering of a single γ-ray, tracing its path.

Tracking arrays are an advancement on Compton-suppressed arrays, which reject any events that scatter out of the crystal, not depositing their full energy [99]. By instead reconstructing the path of the scattered events, the efficiency of the detector is greatly increased, the Doppler correction is significantly improved, and the solid angle coverage is increased (due to the elimination of escape-suppression veto detectors surrounding each crystal) [100].

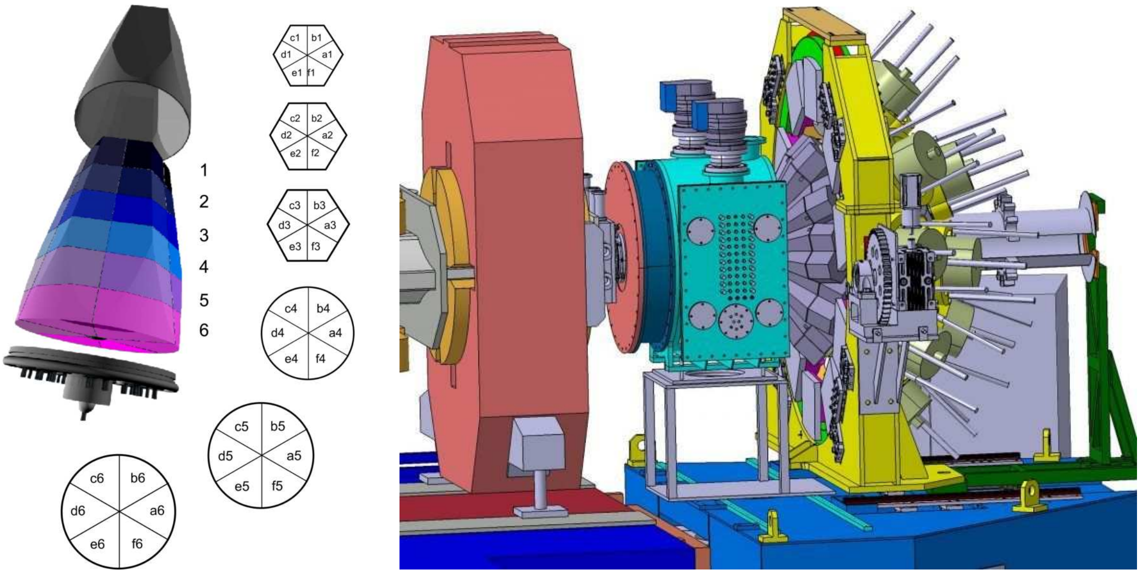

(a) (b)

Figure 3.10: Schematics of AGATA at GANIL. (a) Segmentation of a single AGATA crystal, showing the 36 segments and the taper from hexagonal end to circular base. Figure from Ref. [69]. (b) CAD diagram of AGATA detectors (right) arranged in the backwards hemisphere, coupled to MUGAST (centre) and VAMOS++ (left). Here, the beam direction is right to left. Figure from A. Matta, personal communication.

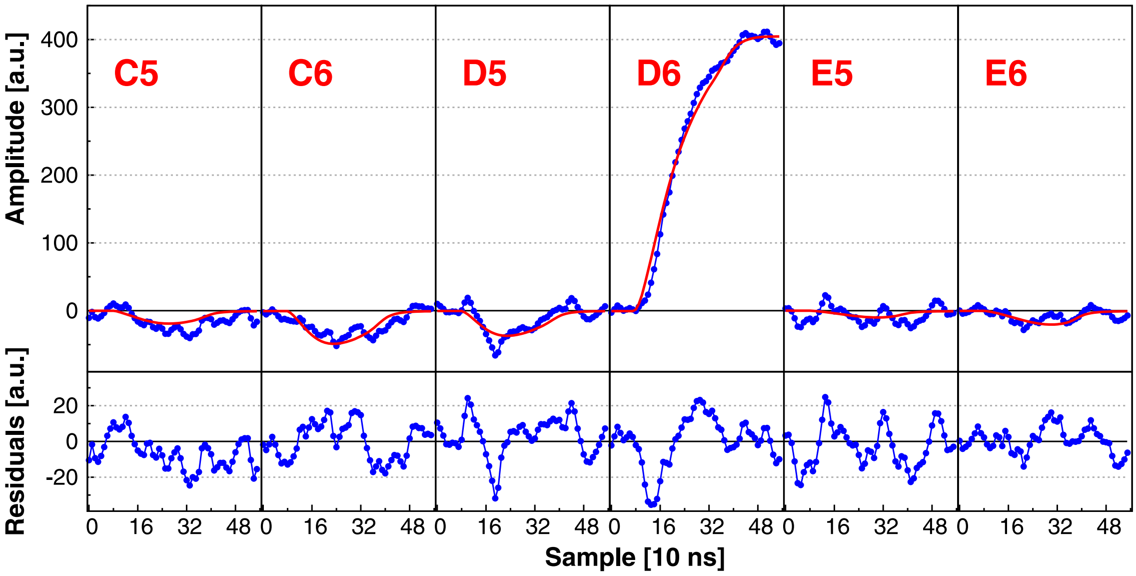

Figure 3.11: Comparison between a real signal (blue) and the simulated signal it is matched with (red). Figure from Ref. [97].

3.6.1 Gamma-ray pulse-shape analysis

As described in Section 3.3.1, when ionising radiation interacts with a semiconductor detector, the resulting particle-hole excitation causes a signal in both the anode and cathode. The shape of this pulse is dependent on the energy deposited by the interaction, and the position of the interaction relative to the anode and cathode [101]

This positional information can be extracted by comparing the experimental signal with a library [102] of simulated signals for interactions at many different positions. These simulations cover a 3D grid of possible interaction points, spaced at 2 mm intervals, for each individual detector. Detectors are treated as distinct due to slight variations between crystals (mass, electronic response, cross-talk properties etc.). For each comparison to a simulated point, a figure of merit is assigned based on the accuracy of the determined amplitude for each signal from both the detecting segment, and the segments surrounding it [97]. For example, in **Figure 3.11**, the pulse measured in the detecting segment (D6) and the surrounding segments is shown in blue, and has been matched via grid search minimisation to the simulated pulse shape in red, providing a determination of interaction position.

During the recent GANIL campaign, PSA position resolutions were found to vary between ATCs from 3.7 mm FWHM to 6.1 mm FWHM; for detectors positioned at 18 cm from the target, this can determine the emitted angle with an uncertainty of less than 2°. This is a five-fold improvement when compared to the smallest dimension of a typical AGATA segment (~ 30 mm), which instead covers an angle of approximately 10° [69].

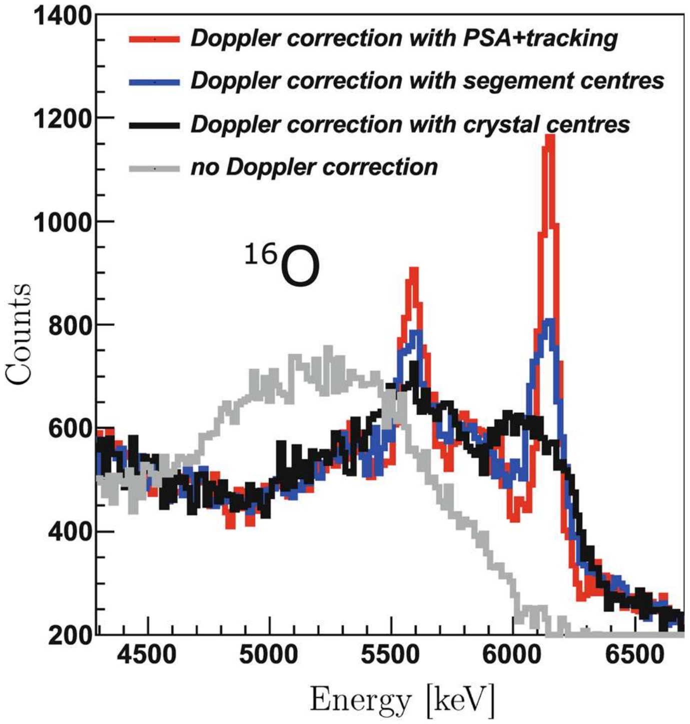

Figure 3.12: Demonstration of the improvement in resolution of a high-energy γ-ray due to various methods of Doppler correction position determination. Figure from Ref. [98], data from Ref. [103].

3.6.2 Gamma-ray tracking algorithm

The advantage of PSA becomes clear in the use of tracking algorithms. AGATA utilises the detection of clusters of partial energy depositions in the HPGe crystal to reconstruct the path of the γ-ray, with the aim of identifying the position of the first interaction. By finding the first interaction point, with the millimetre precision of PSA, the angle of γ-ray emission can be determined with unprecedented precision. This progressive increase of angular precision – from the angular coverage of a whole crystal, to a segment within that crystal, and now to a region of just a few millimetres within that segment – improves the Doppler correction of in-beam spectroscopy significantly (see **Figure 3.12**).

As noted in Section 3.3.4, for γ-rays in the energy range that is significant for nuclear structure physics, the dominant interaction process with HPGe is Compton scattering [80]. Tracking algorithms exploit the well-understood relationship between the energy of the incident γ-ray, $\mathrm{E}_{\mathrm{inc}}$, the scattered γ-ray, $\mathrm{E}_{\mathrm{scat}}$, and the angle of Compton scattering, θ [98]:

$$\cos(\theta) = 1 - m_e c^2 \left(\frac{1}{\mathrm{E}_{\mathrm{scat}}} - \frac{1}{\mathrm{E}_{\mathrm{inc}}} \right). \tag{3.2}$$

The algorithm determines every possible path through the cluster of points, and for each one, compares the measured energy deposition after scattering with the expected energy computed by Equation 3.2. As such, the most likely path can be determined, and the initial angle of incidence known to the high precision provided by PSA.

While there are some physical limitations to this method – such as the assumption implicit in Equation 3.2 that the electrons were stationary before scattering – the improvements in efficiency due to their use are significant. In the work of Ljungvall *et al.* (2020) [104], the singles efficiency of the array at 1322 keV was found to increase from 2.9%[6] when used as a standard multi-detector array, to 3.8% with the inclusion of γ-ray tracking.

3.6.3 Arrangement of AGATA during this work

For this experiment, 12 ATCs were used, at a distance of 18 cm from the target in the upstream hemisphere (see **Figure 3.10b**) covering angles $\theta_{\text{lab}} \sim 130° - 160°$ [106]. PSA and add-back (reconstructing events where γ-rays scatter between crystals) procedures were all performed on-line and sorted in coincidence with MUGAST. The use of AGATA in this experiment was vital for the establishment of decay schemes, for the isolation of specific states in ^{46,48}K and for the precise determination of the energies of said states.

3.7 VAMOS++

The VAriable MOde high-acceptance Spectrometer (VAMOS++) [71, 107] is a ray-tracing QQFD spectrometer, used to separate isotopes by their magnetic rigidity $B\rho$, which can then be identified using the focal plane detection systems [71]. VAMOS++ refers specifically to the upgraded version of VAMOS, where the large momentum acceptance of the spectrometer was further utilised by expanding the area of the detection systems from 400 x 110 mm to 1000 x 150 mm.

The ion-optical components consist of:

Quadrupole A doublet of magnetic quadrupoles for beam focusing. The first is 300 mm in diameter and focuses in the y-direction. The second focuses in the x-direction (i.e. the plane of dispersion) and as such is elliptical [107], with a width in the dispersive axis of 1000 mm to maximise angular acceptance.

Filter A velocity filter immediately following the quadrupole. This system was not used in the current work.

---

[6] This is in line with a 1π arrangement of the segmented shield-suppressed EXOGAM array, positioned at 14.6 cm from the target, which would have an efficiency of approximately 3% at 1.3 MeV [105]

Dipole A magnetic dipole to separate species by their magnetic rigidity. The magnet has a vertical gap of 150 mm and a variable angle of deflection between 0° and 60°.

The focal plane detection systems consist of:

MWPPAC A pair of MWPPACs – one positioned near the target, one positioned at the entry to the focal plane – to measure of time of flight of the particle. This system is critical for the current work, and is discussed in further detail below.

DC A pair of drift chambers to measure the vertical and horizontal position of the particle. This system was not used in the current work.

IC A segmented ionisation chamber to measure the energy loss of the particle for determination of Z. This system was not used in the current work.

Si wall A flat array of silicon detectors at the very end of the focal plane to measure the residual particle energy, for the determination of Z. This system was not used in the current work.

3.7.1 Focal Plane MWPPAC

The fast-timing focal plane MWPPAC consists of three planes; a central plane of 150 mm vertical cathode wires with a pitch of 500 μm, and two outer planes of 1000 mm horizontal anode wires with a pitch of 1000 μm. The planes are spaced 2.2 mm apart from each other. To ensure a fast timing signal, the long horizontal wires are segmented 20-fold [71]. The fill gas of the MWPPAC is 6 mbar of isobutane [68], isolated from the beam line vacuum by a thin Mylar window.

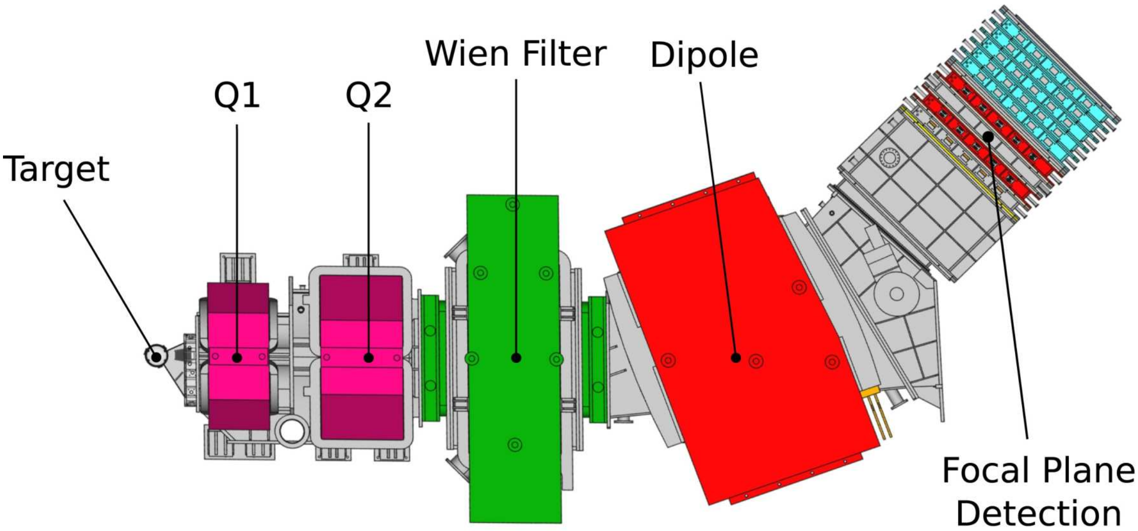

Figure 3.13: Schematic of the VAMOS++ magnetic spectrometer, as seen from above, showing the various optical elements. Figure from Ref. [108]

3.7.2 Arrangement of VAMOS++ during this work

VAMOS++ is mounted on a system of rails and can be rotated from 0° to 60° relative to the beam, depending on the particular requirements of the experiment [107]. In this experiment, as the beam particle (^{47}K) and the isotopes of interest (^{46}K, ^{48}K) are only one mass unit apart, VAMOS++ was positioned at 0° and was receiving the whole beam.

This imposed several limitations; the maximum beam intensity that could be received from the SPIRAL1+ cyclotron was limited to approximately 10^6 pps at any given time. Additionally, the DCs, ICs and Si wall would not be able to count at beam rates, and so were not utilised in this experiment. Instead, only the timing signal from the MWPPAC was recorded.

While VAMOS++ would not be able to spatially discriminate between ^{46}K, ^{47}K and ^{48}K at 0°, it was able to fully eliminate fusion-evaporation reactions on the carbon substrate of the CD_2 target – a common source of background in transfer reaction studies – as these nuclei would not have the correct Bρ to reach the focal plane. This, given the very pure beam (Section 3.2), ensured that so long as there was a coincident signal in VAMOS++, all transfer reaction channels could be fully distinguished, with minimal background, using the angle and species of particles detected in MUGAST. In such a situation, the MWPPAC alone is sufficient.

3.8 CATS

The Chambre À Trajectoires de Saclay (CATS) detector system [109] is an in-beam tracking detector, installed upstream of the target, for beam monitoring purposes. Each CATS detector is a MWPC, with one 70 mm anode plane between two 70 mm cathode planes. The cathode planes are constructed of 1.5 μm Mylar foils supporting 28 thin gold strips, with an interstrip region of 0.2 mm. The wires of the anode plane are 10 μm in diameter, with a pitch of 1 mm. The three planes are spaced 3.2 mm away from each other. Additionally, the two cathode planes run perpendicularly to each other, so that the cathodes alone can provide a two-dimensional position measurement by processing the positive ion signals in individual strips with a charge centroid determination algorithm [109]. The anode is therefore used exclusively for a timing signal from the fast electrons, and all wires are connected in parallel.

3.8.1 Arrangement of CATS during this work

The CATS detector system is specialised for the determination of the beam trajectory as it impinges on the target, which requires the use of two CATS detectors in sequence. While this is critical for highly-divergent fragmentation beams, it is not usually of much concern for ISOL beams, such as the one used in this work. Additionally, multiple scattering of the relatively low-energy 7.7 MeV/nucleon beam would greatly hinder any trajectory reconstruction. As such, a single CATS detector was installed during this work, for the purposes of recording the integrated beam over the course of the experiment and providing a timing signal relative to MUGAST and VAMOS++. This lead to an ambiguity in the interaction position of the beam on the target, which will be addressed in Section 4.1.3.

3.9 Data acquisition system

Each of the three major detectors has its own data acquisition system (DAQ), which were coupled during the MUGAST-AGATA-VAMOS++ campaign in order to provide correlated data with common time stamps. For more details about this system, the reader is referred to Refs [68, 69, 104].

AGATA The AGATA electronics are fully digital, and each event in a crystal produces 36 segment signals and two core signals of different gains [104]. These 38 waveforms are then digitised by 14 bit analogue-to-digital converters and passed to a preprocessing filter which reduces the data volume by approximately two orders of magnitude [69]. The data is then passed through the PSA algorithm (Section 3.6.1) to return the interaction position; from this point, the waveforms are stored and removed from the data stream. During this campaign, the data was then passed to the AGATA Event Builder, and a timestamp from each event was passed to the MUGAST data stream.

VAMOS++ As has been established, for this experiment the only required signal from the VAMOS++ focal plane was the coincidence timing signal. Timing between the VAMOS++ MWPPAC and various other reference timings (such the cyclotron radiofrequency, CATS timing trigger, or the MUGAST array) were determined by passing analogue signals to a discriminator, producing a logic signal. These logic signals were then passed to time-to-amplitude converters (TACs) [68].

MUGAST During this campaign, the MUGAST data – from both the GRIT and MUST2 detectors – was read out using the established MUST2 electronics system, in which the

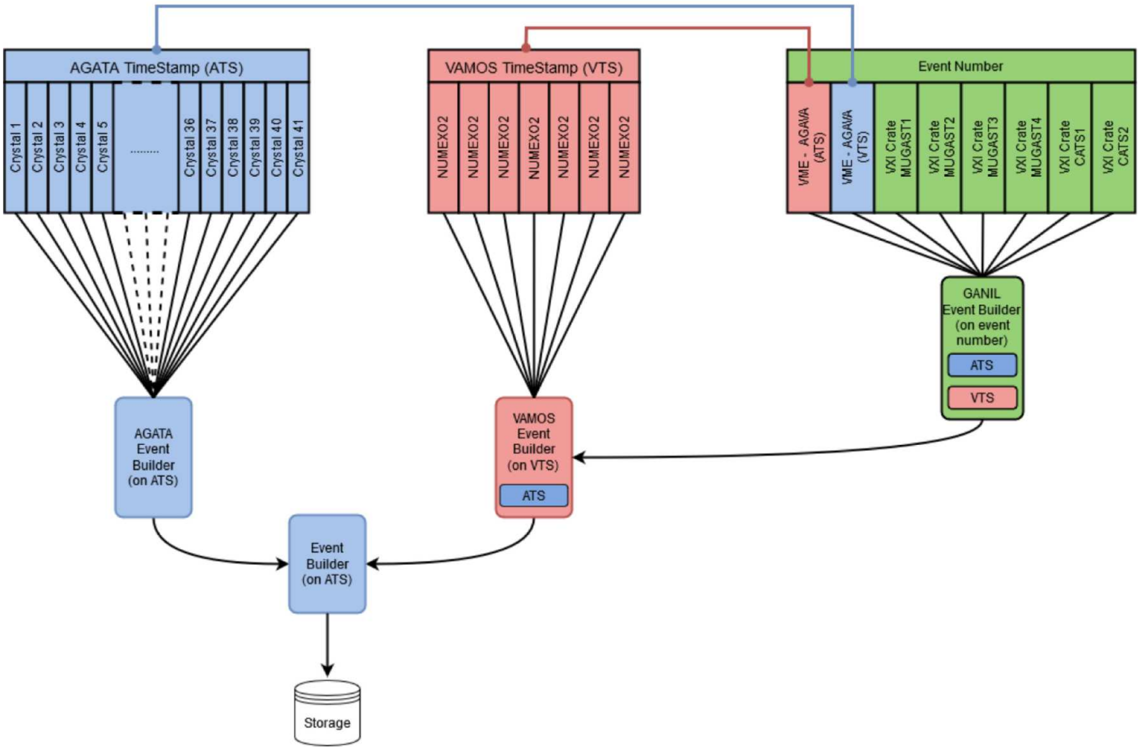

Figure 3.14: Flowchart of the MUGAST-AGTATA-VAMOS++ data acquisition process, showing the order of event building and time stamping. Figure from [68].

application-specific integrated circuits (ASICs) purpose-built chips read the strip signals and transferred the energy, time and leading edge discrimination information to ASICs on the MUFEE front-end data boards. Each board held 9 ASICs, which could read 144 channels, i.e. one face of a GRIT or MUST2 DSSD (128 strips), plus 16 MUST2 CsI crystals. The front-end data was then delivered to back-end MUVI crated boards, which could each take data from eight front-end MUFEE boards, or four telescopes. Four MUVI boards were used to read data from all 11 MUGAST detectors [68]. The MUGAST data stream also accepted the AGATA and VAMOS++ timestamps, which were encoded into the event in the GANIL Event Builder stage, using the CENTRUM module to correlate the GANIL crates in a common dead time triggered DAQ.

Merging With events from all three systems collected, the global event was then built by merging the three events. First, the MUGAST and VAMOS++ events were merged in the VAMOS event builder, based on their shared VAMOS++ timestamp. Then, the MUGAST-VAMOS++ event and AGATA event were merged based on their shared AGATA timestamp. Both of these building stages had a 1μs window.

Chapter 4

Data Analysis

In this chapter, the various analytical methods and data processing procedures used to extract the experimental observables from the raw data are discussed. In Section 4.1, the MUGAST data analysis is discussed, and particular attention is paid to corrections regarding the target thickness and beam position. In Section 4.2, the γ-ray data processing, i.e. the Doppler correction, is examined. Finally, the timing signals of VAMOS++ and CATS2 are discussed in Section 4.3.

All analysis presented in this thesis has been performed using the ROOT data analysis framework (v. 6.22/02) [110, 111] and NPTOOL (v. 3) [112].

4.1 MUGAST

4.1.1 Calibrations

Time Time calibration runs were performed for each of the six GRIT and five MUST2 detectors. Data from two directions of the strips in the DSSDs – X (junction) and Y (ohmic) – were fed to two separate MUFEE front-end electronic boards [70], and each MUFEE board was time-calibrated separately. One MUFEE, receiving the ohmic direction in MG5, did not have time calibration data. As such, the pre-existing time calibration was used for this set of strips. The data taken in these calibration runs was fed into in a sophisticated, automated timing calibration code.

Energy The energy calibrations of the MUGAST detectors were performed using a triple-α source; ^{239}Pu, ^{241}Am and ^{244}Cm. This source was mounted on the target ladder along with the CD_2 targets. The three primary peaks from these α emitters – 5.157 MeV, 5.486 MeV and 5.805 MeV, respectively – were automatically located and fit for each strip. Strips with unusual responses were flagged in the auto-generated report document; these strips were excluded from all data analysis and simulations. A calibration file was written, containing the calibration coefficients for each strip in that detector. Again, the X (junction) and Y (ohmic) strip directions were calibrated separately.

Position A survey of the positions of the MUGAST detectors was performed after the experimental campaign concluded, in July 2021. These measurements were conducted using a portable six-axis arm, which gave a three-dimensional coordinate for each corner of each detector. The array geometry was then included in the analytical code, for determining the physical position of each particle detection. While the position survey provided very precise positional data for each detector in its mechanical mount, this did not account for the position of the mount along the rails it moves upon. This position is usually well-constrained, but due to a mistake during the period of this experiment, the position of the downstream detector mount was non-standard. This is discussed further, and satisfactorily characterised, in Section 4.1.4.

4.1.2 Solid angle coverage

At various points in this analysis, the solid angle coverage of the MUGAST detectors was required in order to correct measured numbers of particles by the geometric efficiency of the array. In all cases, the solid angle was determined using realistic Monte Carlo simulations, performed using GEANT4 [113] via the NPSIMULATION package of NPTOOL. These simulations used the same detector geometry and reaction physics as the experimental data analysis, and both sets of data were processed by the same NPANALYSIS sorting code to maintain consistency between the two.

The solid angle covered by the MUGAST detectors, as simulated using ^{47}K(d,p)^{48}K$_{\text{g.s.}}$ for upstream GRIT detectors, ^{47}K(d,d)^{47}K$_{\text{g.s.}}$ for the perpendicular MUST2 detector, and

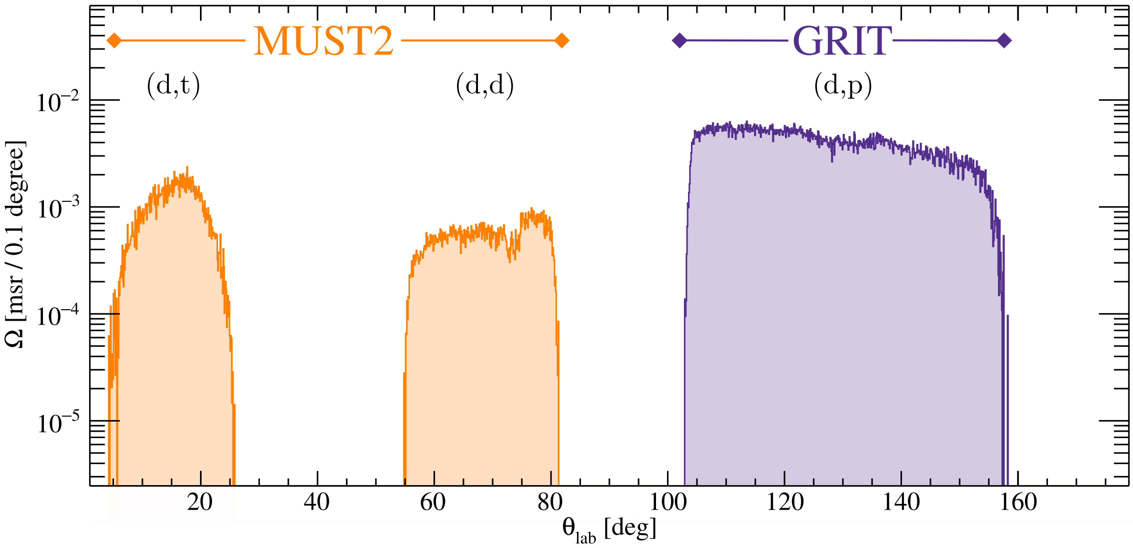

Figure 4.1: Solid angle coverage of the various MUGAST detectors, in θ_{lab}. Simulations were performed using the ^{47}K(d,t), ^{47}K(d,d) and ^{47}K(d,p) direct reactions.

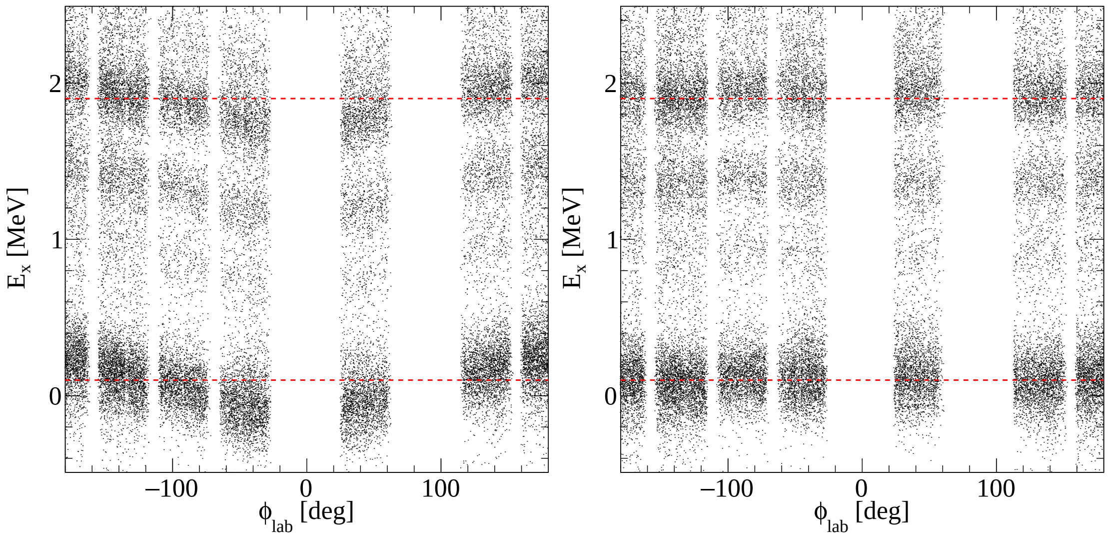

(a) $(X_B, Y_B) = (0.0\text{ mm}, 0.0\text{ mm})$ (b) $(X_B, Y_B) = (-4.2\text{ mm}, 0.5\text{ mm})$

Figure 4.2: Reconstructed excitation energy against ϕ_{lab}, (a) before and (b) after the beam spot position correction. The sinusoidal artefact is no longer present after the corrections.

^{47}K(d,t)^{46}K* for the downstream MUST2 detectors[1], is shown in **Figure 4.1**. Note the large θ_{lab} coverage of the GRIT detectors, and the large solid angle due to the high ϕ_{lab} coverage of 66%. The perpendicular MUST2 solid angle is lower, as the single MUST2 telescope had fractional ϕ_{lab} coverage, 8%. The large ϕ_{lab} coverage of the downstream MUST2 detectors, 84%, provided good solid angle coverage of the (d,t) reaction[2].

4.1.3 Beam spot position and target thickness

During this experiment, the position of the radioactive beam on the target persistently drifted towards the negative x direction, despite efforts to use steering dipoles to recentre the beam. This presented a significant problem, because an uncharacterised deviation in beam position would affect the calculation of the particle angle of emission, θ_{lab}, which would in turn affect the reconstruction of the product isotope excitation energy, E$_x$.

This effect is most obvious when comparing the reconstructed energy E$_x$ against ϕ_{lab}, where each trapezoidal MUGAST detector occupies a distinct region of ϕ_{lab} space, as in **Figure 4.2a**. This sinusoidal wave across the detectors is characteristic of a significant beam offset.

Additionally, the number of counts detected during the experimental run was significantly lower than was anticipated given the high beam intensity, suggesting that the target may

---

[1] Note that the ^{47}K(d,t) reaction was simulated for the population of a 3 MeV excited state so as to exclude threshold effects that reduce the angular coverage of ^{47}K(d,t)^{46}K$_{\text{g.s.}}$, providing a fairer representation of the detector solid angle.

[2] This is true for realistic differential cross sections, where the high-energy θ_{lab} solution is negligible. Were it equally weighted, punch through reduces the solid angle by an order of magnitude.

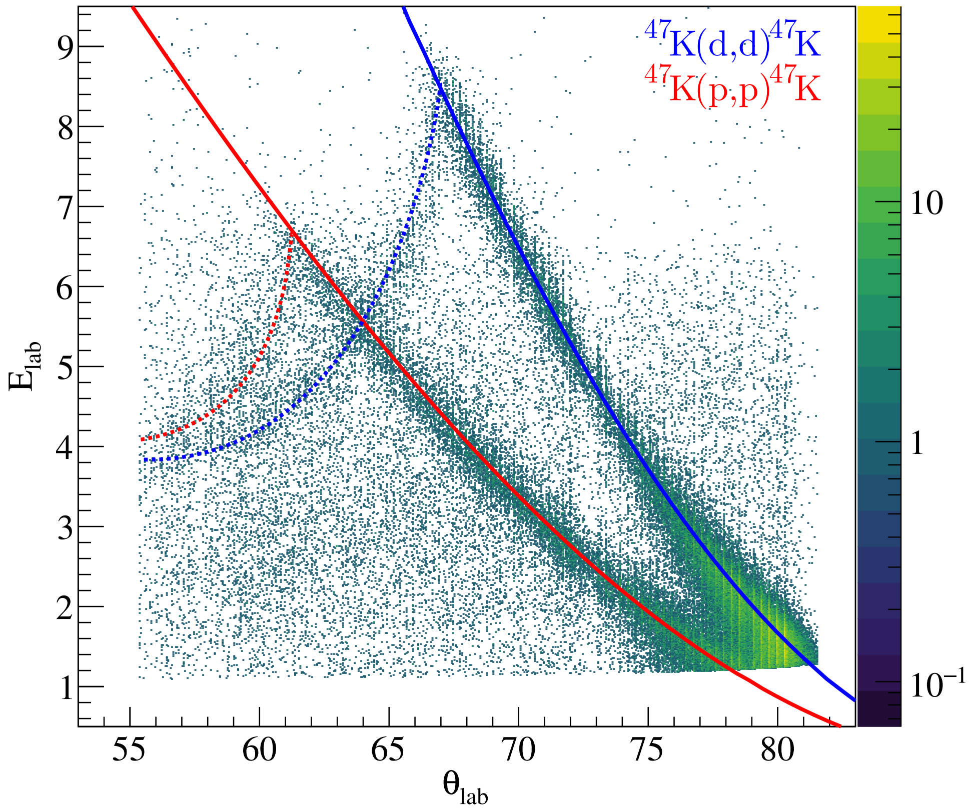

Figure 4.3: Elastically scattered protons and deuterons, as seen in the MUST2 detector at 90°. The shallower left-hand kinematic line is from ^{47}K(p,p), and the steeper right-hand line is from ^{47}K(d,d). Dashed lines indicate punch-through events.

have been thinner than the 0.5 mg/cm^2 nominal thickness. As the distance travelled through the target varies depending on the angle of emission, an incorrect target thickness could lead to a significant energy offset for states with differential cross sections with larger weightings towards smaller θ_{lab} angles.

As a result, there was a clear need to determine the true position of the beam spot and the thickness of the target. Two methods – one analytical, the other numerical – were developed, which together produced highly satisfactory corrections, as can be seen in **Figure 4.2b**. These methods are detailed in the following sections.

4.1.3.1 T_T from elastic scattering

The thickness of the target can be determined most accurately by analysing the elastically scattered protons and deuterons detected just forwards of 90° in θ_{lab} (see **Figure 4.3**) and comparing these to theoretical cross sections from optical models. There are three distinct phases of this process; measuring the particles detected in each angular bin, determining the solid angle of the angular bins, and then comparing the experimental elastic scattering cross sections to optical models.

First, the two-body kinematic calculator CatKIN [114] was used to determine the equation relating the light particle angle of emission in the centre-of-mass frame (θ_{CM} [deg]) to the energy of the light particle ($\mathrm{E}_{\mathrm{lab}}$ [MeV]) for the reactions ^{47}K(p,p) and ^{47}K(d,d). These were found to be:

$$^{47}\mathrm{K(p,p)}: \ \mathrm{E}_{\mathrm{lab}} = 14.51\ [\mathrm{MeV}] \cos(\theta_{\mathrm{CM}}) + 14.51\ [\mathrm{MeV}] \tag{4.1}$$

$$^{47}\mathrm{K(d,d)}: \ \mathrm{E}_{\mathrm{lab}} = 27.77\ [\mathrm{MeV}] \cos(\theta_{\mathrm{CM}}) + 27.77\ [\mathrm{MeV}] \tag{4.2}$$

Using these equations, the values of $\mathrm{E}_{\mathrm{lab}}$ that would correspond to integer values of θ_{CM} were calculated. This allowed for projections onto the x-axis of **Figure 4.3** with precise energy gates, which corresponded exactly to the particles detected in one-degree slices of θ_{CM}.

From these projections, the areas, A, of the proton and deuteron scattering peaks were determined. Due to the difference in Equation 4.1 and Equation 4.2, different energy gating is required for the two reactions, so measurements of the area of ^{47}K(p,p) and ^{47}K(d,d) peaks were taken separately.

Next, the solid angle of these θ_{CM} bins was determined, using realistic Monte Carlo simulations of isotropic sources at the target position, with the same geometry input files as the experimental analysis. From these, the solid angle of each θ_{CM} bin could be determined through the relationship,

$$\Omega(\theta_{\mathrm{CM}}) = \frac{A_{\mathrm{det.}}}{A_{\mathrm{emit.}}} \cdot 2\pi \sin\left(\theta_{\mathrm{CM}}\right) \cdot \mathrm{binwidth}. \tag{4.3}$$

This produced solid angles for ^{47}K(p,p) and ^{47}K(d,d) as shown in **Figure 4.4**. The area of the elastic scattering peaks was then divided by the solid angle, Ω [sr], for the corresponding range of θ_{CM}. This set of experimental data y_i, now represented in units of sr^{-1}, is related to the differential cross section, $\frac{\delta\sigma}{\delta\Omega}\left[\frac{\mathrm{mb}}{\mathrm{sr}}\right]$, by

$$\hat{y}_i = B f_{\frac{\delta\sigma}{\delta\Omega}}(x_i), \tag{4.4}$$

where $\hat{y}_i$ is the expectation value of y_i and B [mb] is some normalising factor.

The target thickness can now be derived. First, Equation 11.13 in Ref. [15] was rearranged to give

$$\frac{N_c}{\Omega}\left[\frac{1}{\mathrm{sr}}\right] = N_i \cdot \frac{\sigma}{\Omega}\left[\frac{\mathrm{mb}}{\mathrm{sr}}\right] \cdot \frac{N_{\mathrm{target}}}{\mathrm{area}}\left[\frac{1}{\mathrm{cm}^2}\right], \tag{4.5}$$

where N_i is the number of incident particles, and N_c is the number of counts detected. The number of target particles per unit area was determined through the knowledge that

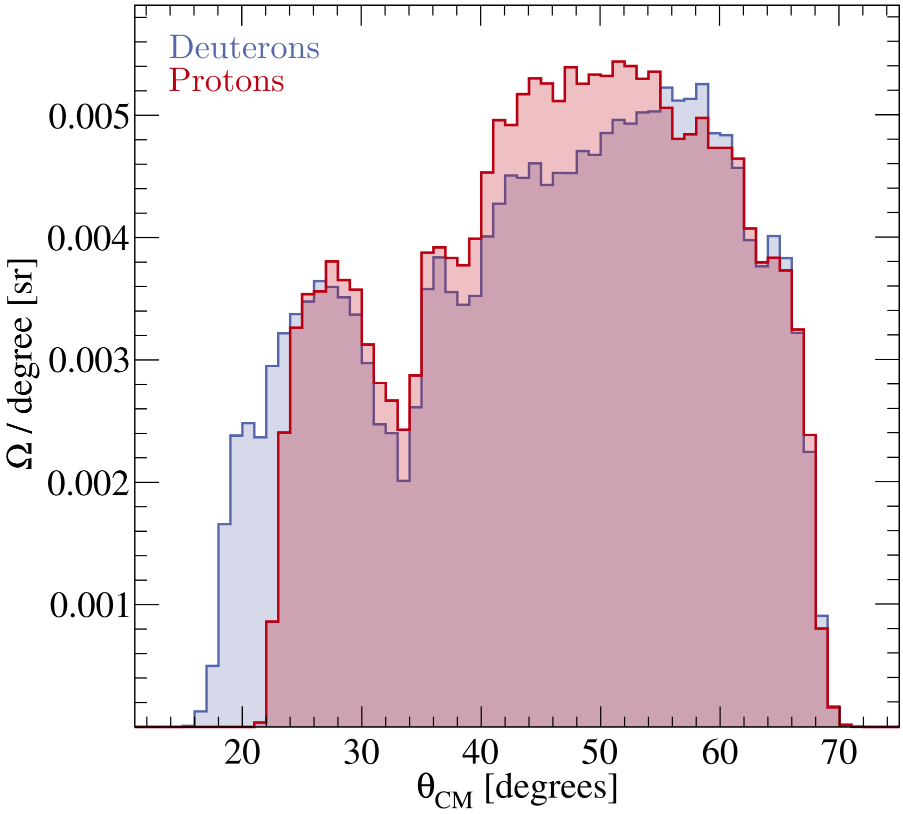

Figure 4.4: Comparison of the solid angle of the perpendicular MUST2 detector, as seen by isotropically emitted protons (red) and deuterons (blue), in the centre-of-mass frame.

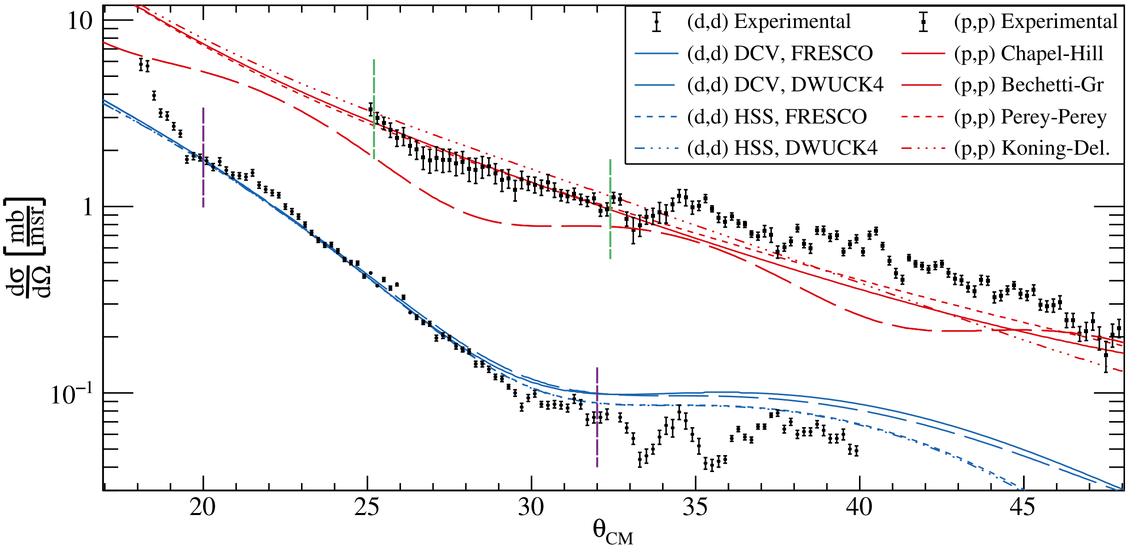

Figure 4.5: Differential cross sections of experimental elastic scattering data, compared to various optical models. ^{47}K(d,d) optical models are shown in blue, and ^{47}K(p,p) optical models shown in red. The range of experimental data used in the fitting is marked out by purple and green dashed lines, respectively. Optical models are from Refs. [49, 115–119]

an Avogadro's number, N_A, of particles with mass A weighs A grams, therefore,

$$\frac{N_{\text{target}}}{\text{area}} = \frac{T}{1000 * A} * N_A, \tag{4.6}$$

where T is the target thickness in mg/cm^2. Substituting Equation 4.6 into Equation 4.5 gives the relationship,

$$\frac{N_c}{\Omega} = \frac{\sigma}{\Omega} * N_i * \frac{T}{1000 * A} * N_A \quad \rightarrow \quad T = \frac{N_c/\Omega}{\sigma/\Omega} * \frac{1000 * A}{N_i N_A}. \tag{4.7}$$

Recalling $y_i \left[\text{sr}^{-1}\right]$ and $f_{\frac{\delta\sigma}{\delta\Omega}} \left[\frac{\text{mb}}{\text{sr}}\right]$, it can be found from Equation 4.4 that $1/B = y_i / f_{\frac{\delta\sigma}{\delta\Omega}} = \frac{N_c/\Omega}{\sigma/\Omega}$, therefore,

$$T = \frac{1}{B} * \frac{1000 * A}{N_i N_A}. \tag{4.8}$$

Hence, the target thickness was determined using only known constants A and N_A, the measured incident integrated beam N_i, and the previously determined normalisation factor B. This method was applied to find the thickness of protons and deuterons, and in turn the thickness of CH_2 and CD_2, in the experimental target.

Through an error-weighted minimisation, shown in **Figure 4.5**, the normalisation factors were found to be 0.003(1) for protons, and 0.00023(2) for deuterons. Here, protons are normalised to the Chapel-Hill '89 (CH89) [117] optical model and deuterons are normalised to the Daehnick-Childs-Vrcelj (DCV) [115] optical model. This corresponds to CH_2 and CD_2 thicknesses of 0.02 ± 0.01 mg/cm^2 and 0.32 ± 0.03 mg/cm^2, respectively, for a total target thickness of 0.34 ± 0.04 mg/cm^2.

As this is much thinner than the expected 0.5 mg/cm^2 target that was believed to be in use during the experiment, this methodology has been thoroughly examined for inaccuracies. Any mistake would be propagated to the eventual determination of spectroscopic factors; as such, this analytical process is key. A common point of failure is the inclusion or exclusion of a factor of two in the optical model calculations; as such, a thorough examination and testing of this methodology can be found in Appendix A.1. This analysis found agreement between the DWUCK4 [120] and FRESCO [121] elastic scattering calculations, which were both additionally in agreement with the comprehensive deuteron elastic scattering observations of Childs *et al.* (1974) [122]. No factor-of-two discrepancy was found, instilling confidence in this analytical determination of target thickness.

4.1.3.2 X_B, Y_B, Z_T and T_T from numerical minimisation

In addition, a numerical method was developed, using the large volume of ^{47}K(d,p) data. This method has the additional advantage of determining all four relevant variables, rather than just the target thickness. First, the following data was extracted for each particle detection:

- Position of the detected particle in real space, (X_D, Y_D, Z_D).
- Energy of detected proton, E_p.
- Detector number of the MUGAST trapezoid that the event was detected in.
- Time difference between MUGAST and VAMOS++ event detection.
- Energy of coincident γ-ray, E_γ.

Then, all events that satisfied the criteria of (a) being within the MUGAST-VAMOS++ coincidence window, and (b) being coincident with a 0.143 MeV γ-ray in AGATA, were retained (approximately 3300 particle events). This ensured that any protons detected had, in fact, been emitted from the ^{47}K(d,p) reaction, and that the ground state peak was eliminated from beneath the 0.143 MeV state in the excitation spectrum. Two strongly populated and energetically separated states were chosen for the following minimisation; 0.143 MeV and 1.978 MeV. The latter state has been observed for the first time in this work, and so the precise energy was determined by the γ-ray de-excitation of the state, as detected by AGATA.

Following this, iteration and minimisation processes were performed. The values of the beam spot on the target (X_B, Y_B), the target position (Z_T) and target thicknesses (T_T) were set as limited variables in a MINUIT minimisation. In each iteration, the particle vector for every event was calculated by (X_D, Y_D, Z_D) − (X_B, Y_B, Z_T), and from this an angle of emission, θ, was determined. Using this angle and T_T, the distance travelled through the target was determined, and the energy loss in the target was calculated. With the initial energy of the proton emitted from the reaction known, the energy of the ^{48}K isotope E_x could be trivially derived. This calculation was performed for every particle detection event, and E_x spectra were produced for individual MUGAST trapezoids, as seen in **Figures 4.6a** and **c**, and high and low θ_{lab} gates, as seen in **Figures 4.6b** and **d**.

When all events had been processed, the resulting E_x peaks were fit with Gaussian peaks to determine the centroid energies E_{peak} and widths of the peaks, σ_{peak}. This was used to determine a metric, $|E_{peak1} - 0.143| + |E_{peak2} - 1.978| + 0.1(\sigma_{peak1} + \sigma_{peak2})$, which was then minimised to determine the values of X_B, Y_B, Z_T and T_T that produced peaks as narrow and as accurate to 0.143 MeV and 1.978 MeV as possible, across all trapezoids.

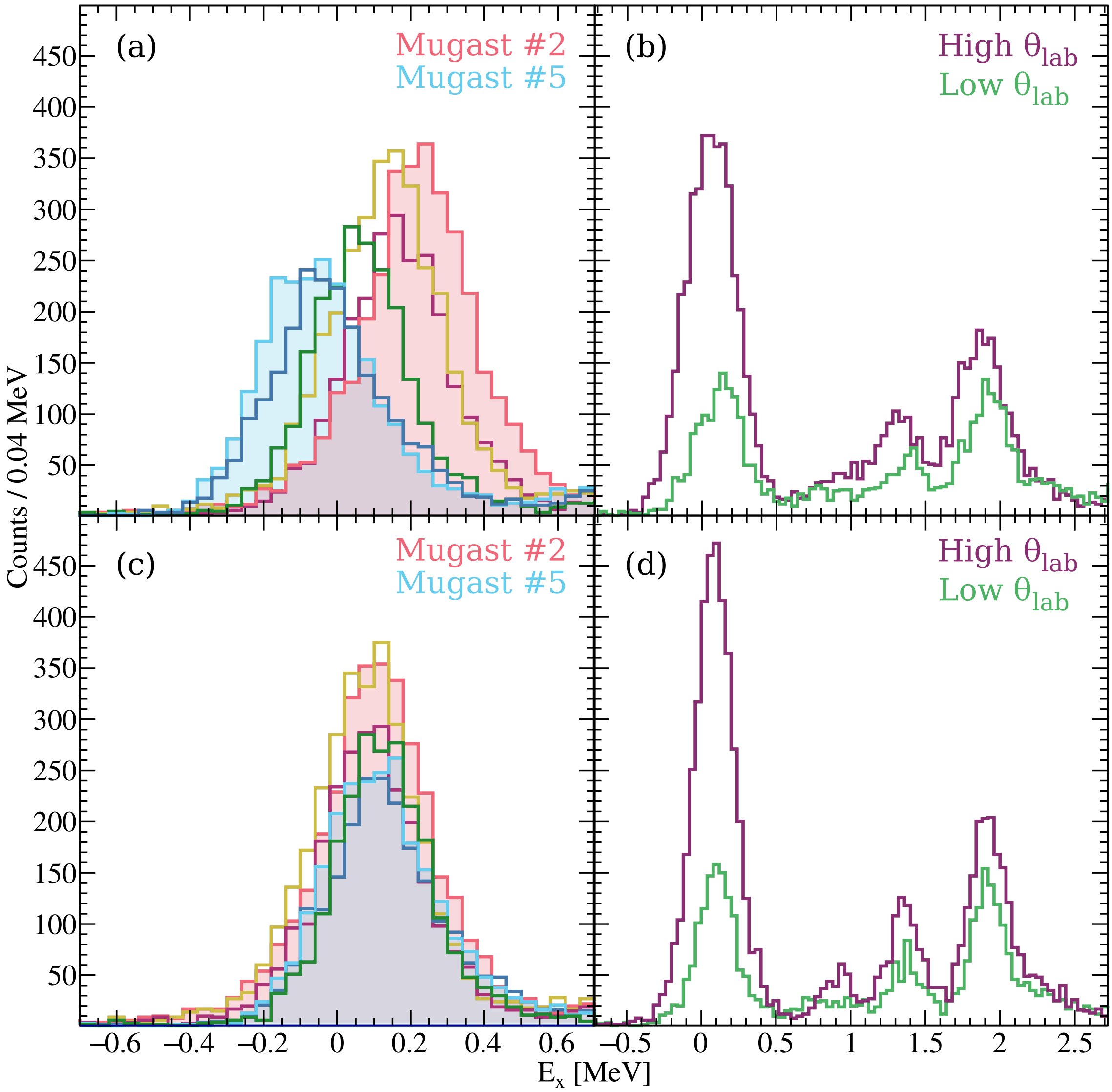

Figure 4.6: Improvement from numerical minimisation of X_B, Y_B, Z_T and T_T. (a) ^{48}K excitation as seen by individual MUGAST detectors, before correction. (b) ^{48}K excitation at the highest (145 – 155°) and lowest (105 – 115°) angles of θ_{lab}, before correction. (c) and (d) are the equivalent of (a) and (b), after corrections were applied.

This method was heavily reliant on two transitions, which both happened to have differential cross sections that favoured large values of θ_{lab}, where the influence of the target thickness was smallest. As the reconstructed energy had a complex dependency on both Z_T and T_T, for any value of T_T there was a corresponding value of Z_T that would produce a local minimum. This was rectified by restricting the thickness in the numerical minimisation based on the analytical result (Section 4.1.3.1). Additionally, the outputs were verified by confirming that there was minimal variation in reconstructed excitation energy across θ_{lab}. That is, **Figures 4.6a** and **c** were used for minimisation, and **Figures 4.6b** and **d** were used for verification.

4.1.3.3 Post-hoc gradient

Using these two methods, the set of variables that produced the best results were found to be

$$X_B = -4.16\text{ mm} \qquad Y_B = +0.47\text{ mm} \qquad Z_T = +0.22\text{ mm} \qquad T_T = +3.00\ \mu\text{m}$$

It is critical to note that, while there was a set of values that produced a more accurate[3] reconstructed excitation spectrum for the strongest states, that value set was biased towards high θ_{lab} angles and had a significant shift in energy at low θ_{lab}. As the consistency of excitation across angles is more critical for this work than absolute accuracy – especially in regards to the target thickness – the value set with greater consistency across angles was selected, and a post-hoc correction gradient of $x_{\text{observed}} = 0.989 x_{\text{true}}$ was applied.

4.1.4 Position of downstream detectors

It was noted in Section 3.5.2 and Section 4.1.1 that the downstream MUST2 detectors were not in the usual operational position during this experiment. This is evidenced by the significant variation between the calculated kinematic line and the measured tritons in E_{lab} against θ_{lab}, when the target-to-detector distance is assumed to be the standard operational position, shown in **Figure 4.7a**.

It was found that applying a downstream shift of approximately 200 mm produced a strong agreement between the expected and observed kinematic lines. During discussions with MUST2 experts, it was found that this corresponds to the maintenance position of MUST2. Helpfully, the detector apparatus is pinned to a fixed position during maintenance, as shown in **Figure 4.8**. Applying this known downstream shift of 200 mm to the detector positions produced **Figure 4.7b**, in agreement with expectation.

---

[3] Accuracy, here, being measured relative to the expected energies of these states determined through the high-precision γ-ray energies

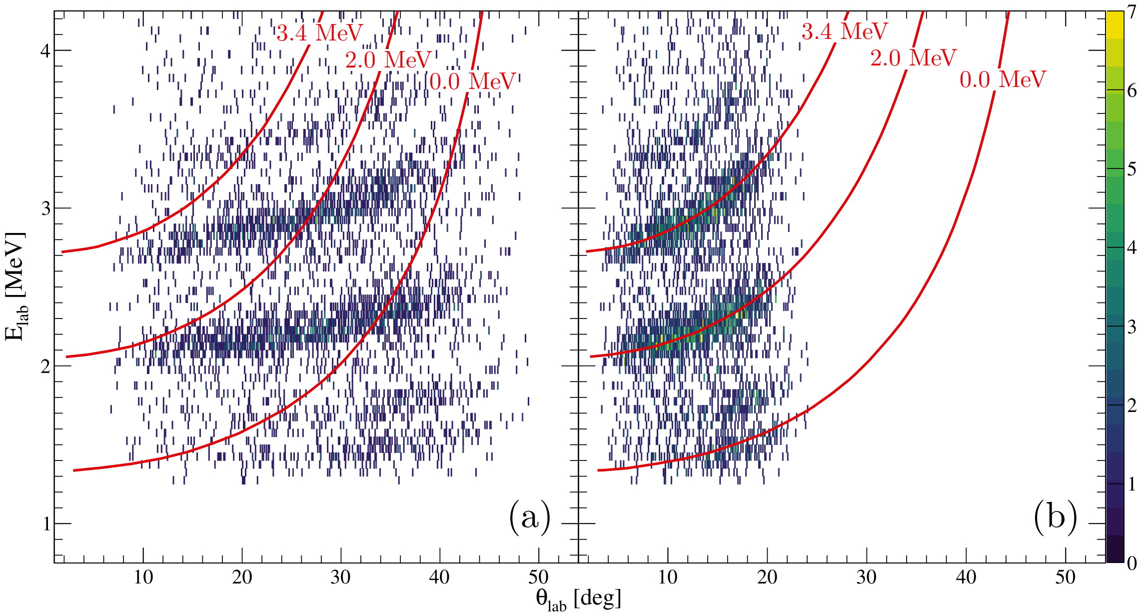

Figure 4.7: Comparison of expected kinematic lines for ^{47}K(d,t)^{46}K tritons at different ^{46}K excitation energies. (a) Assuming MUST2 is in the operating position. (b) Assuming MUST2 is in the maintenance position.

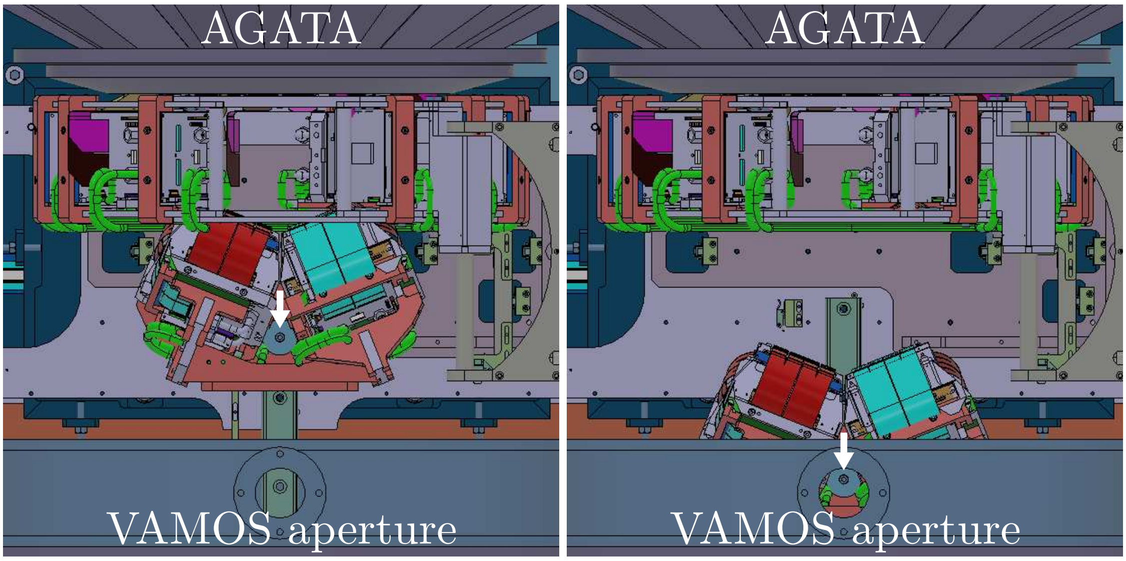

(a) Operating position

(b) Maintenance position

Figure 4.8: Diagrams of the MUGAST+AGATA+VAMOS++ connective mechanical structure, in (a) the standard operating position and (b) the retracted maintenance position. The two pin points of the MUST2 downstream apparatus are marked with arrows.

4.1.5 Identification of tritons

While the protons and deuterons detected in the upstream and perpendicular detectors were fully identifiable by their energy and angle, this was not the case for tritons. There is a large background in the spectra from the MUST2 detectors, simply by virtue of them being in the downstream direction, which necessitated further particle identification procedures to extract the triton detections.

During this experiment, the MUST2 array had two detecting components; the DSSD stage and the CsI stage. Any particle with a high enough energy to punch through the DSSD layer into the CsI detectors is inherently too high in energy to be a triton from the ^{47}K(d,t)^{46}K reaction, so background in the high-energy region was removed by placing a veto condition on a coincident CsI hit.

Further to this, the species of particle can be identified using the kinematic separation

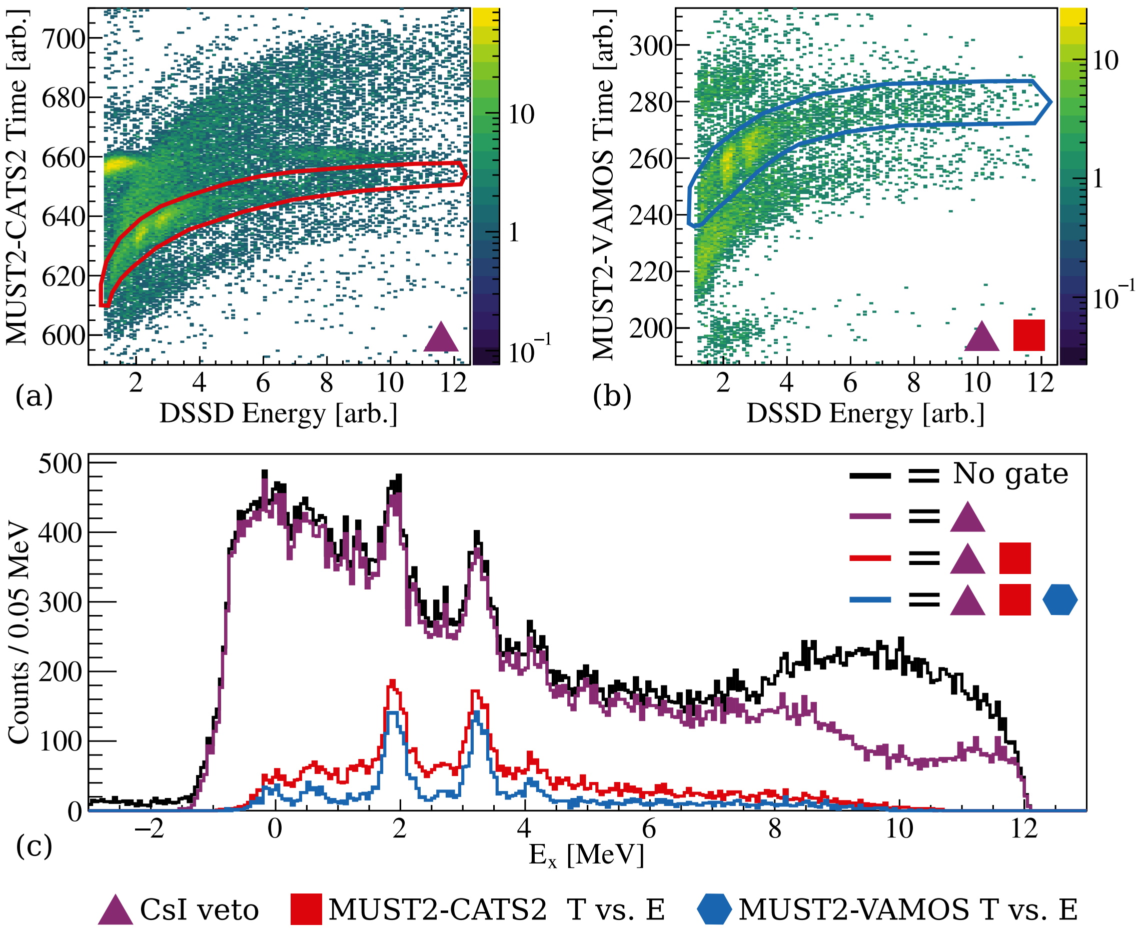

Figure 4.9: Demonstration of the various gates used to isolate (d,t) triton detections in MUST2. Symbols indicate the gates that are applied. (a) Charge-energy locum of tritons, indicated with the red gate. (b) Additional timing gate, relative to VAMOS++, indicated with the blue gate. (c) Reconstructed ^{46}K excitation spectrum with the various gates applied, showing the improvement with each additional condition.

based on mass. The time of flight, t, and energy, E, of a particle are related to its mass, m by the equation:

$$t = d\sqrt{1 - \frac{m^2}{E^2}} \tag{4.9}$$

Therefore, by plotting the energy detected in the MUST2 DSSDs against time of flight, the different masses of light ejectiles were separated into different loci. Two visual gates were made, one using the time between MUST2 and CATS (**Figure 4.9a**) and one using the time between MUST2 and VAMOS++ (**Figure 4.9b**). In both cases, the triton locum – identified by known γ-ray coincidences – is indicated with a visual gate.

Using these three requirements, a clean reconstructed ^{47}K(d,t)^{46}K excitation spectrum was produced with minimal background, as shown in **Figure 4.9c**.

4.1.6 Assessment of the quality of post-processed data

Having applied the various calibrations, target thickness corrections and coincidence requirements outlined in this section, the experimental observables of interest have been attained, as shown in **Figure 4.10**. Here, the quality of the observed data is clear in **Figure 4.10a**, where the large angular coverage and high-statistics measurement of ^{47}K(d,p) reveals several clear, well-defined states. Also revealed in this figure is the challenge presented by the ^{47}K(d,t) data, which has far fewer total measured events. Note that kinematic lines associated with (d,p) transfer on likely beam contaminants are also marked. There is no discernible population of these regions, supporting the belief that the radioactive isotope beam provided during this experiment was extremely pure. In addition, these kinematic lines are all well-separated from the ^{47}K(d,p) region, making contamination of this data unlikely even in the case of some fractional beam impurity.

The importance of the $\mathrm{X_B}$, $\mathrm{Y_B}$, $\mathrm{Z_T}$ and $\mathrm{T_T}$ corrections are clear in **Figure 4.10b**, as the missing-mass relativistic reconstruction [123] of the heavy recoil nucleus excitation, $\mathrm{E_x}$, is constant with regards to θ_{lab} for both reactions. If the energy loss of the light ejectile through the target was poorly defined, the reconstructed excitation energy would have an erroneous angular dependence, potentially impacting the eventual differential cross section evaluations.

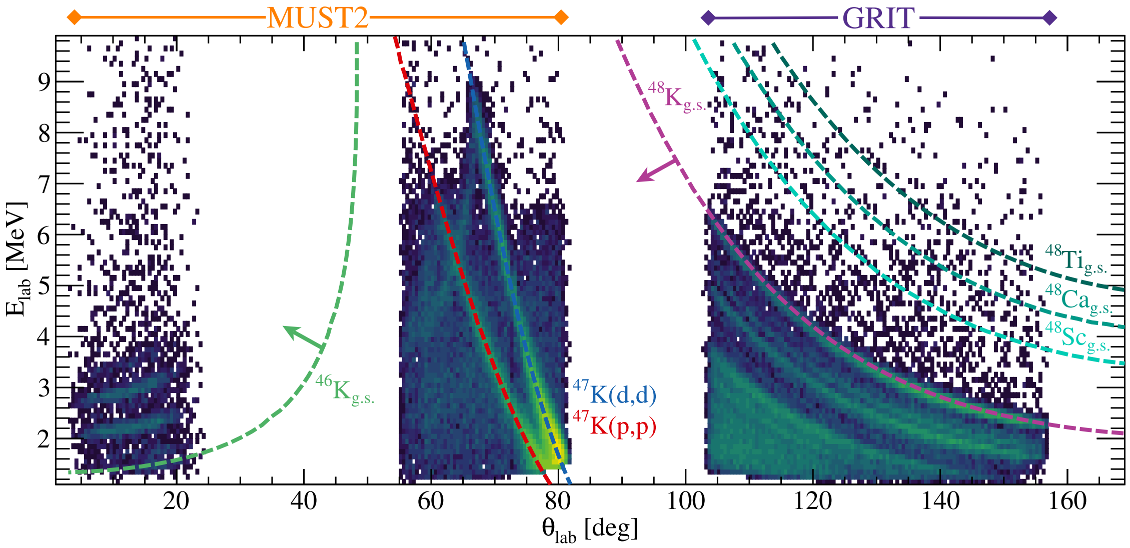

(a) E_{lab} against θ_{lab}

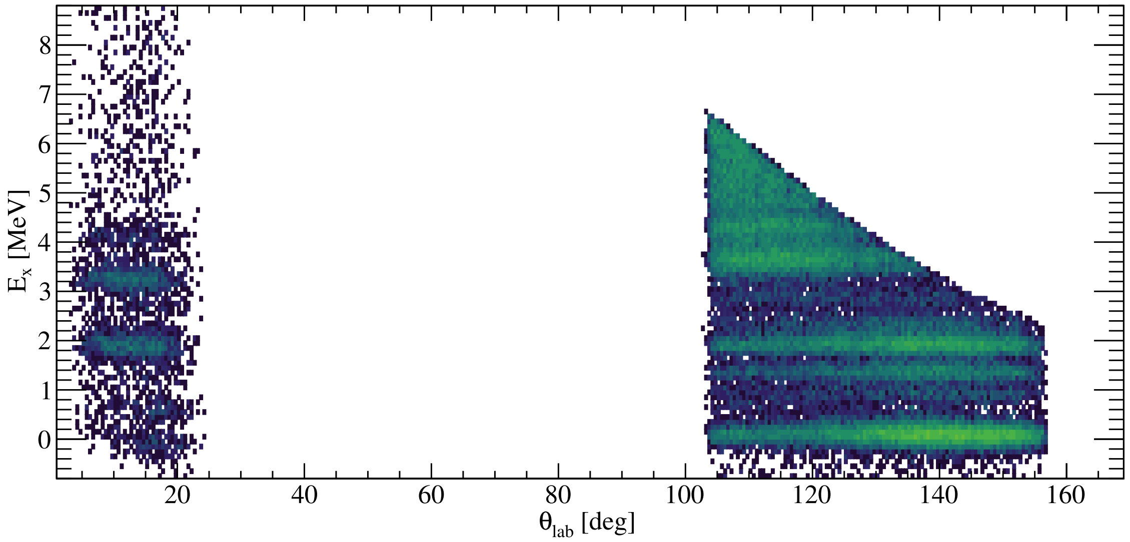

(b) E_x against θ_{lab}

Figure 4.10: Variance with lab angle of (a) the detected light ejectile energy (b) the reconstructed heavy ejectile excitation energy, showing the quality of the ^{47}K(d,p) and ^{47}K(d,t) data after the processing and calibration outlined in Section 4.1. For the transfer reactions, the direction of increasing heavy recoil excitation energy is marked with an arrow. Kinematic lines for the (d,p) transfer of other A = 47 isobars are also marked.

4.2 AGATA

4.2.1 Preprocessing of data

4.2.1.1 Tracking and Calibrations

As the AGATA collaboration is a large, international group, the initial data processing is standardised and well-automated. The local AGATA team performed the calibrations for this experiment, and sorted all AGATA data on-line. Pulse shape analysis and add-back were performed during this on-line sort.

4.2.1.2 Efficiency curve

Understanding how the efficiency of the AGATA array varies with energy is critical, as it allows for the comparison of relative γ-ray transition strengths across the whole energy range. For this experiment[4], the efficiency was initially measured using a ^{152}Eu source, which has strong decays in the range of 0.1 MeV to 1.4 MeV. Unfortunately, there was no source measurement for higher energies, so the response in this region was less well-defined.

In order to constrain the high-energy response of the AGATA array during this experiment, a realistic Monte Carlo simulation of a 3.5 MeV γ-ray source was performed. This simulation included the real AGATA geometry, any missing channels during this experiment, and the known inefficiencies in each crystal. A simulation was also performed for 1.408 MeV, and was found to agree with the experimentally measured value, confirming the validity of the simulation.

These experimental and simulated data points were then fit with a function of the form given by Equation 1 in Ref. [106];

$$\epsilon_{\gamma}(E) = \exp\left(\sum_{i=0}^{4} P_i(\ln(E))^i\right). \tag{4.10}$$

This efficiency function, fit to the data with and without the inclusion of the simulated data point, can be seen in **Figure 4.11**. Including the simulated efficiency in the fitting produced an efficiency curve that was more in line with expectations at high energies, whilst remaining consistent with experimental measurement. This corrected efficiency curve was used throughout this work.

---

[4] The procedure to determine the AGATA efficiency was performed by E. Clément (personal communication).

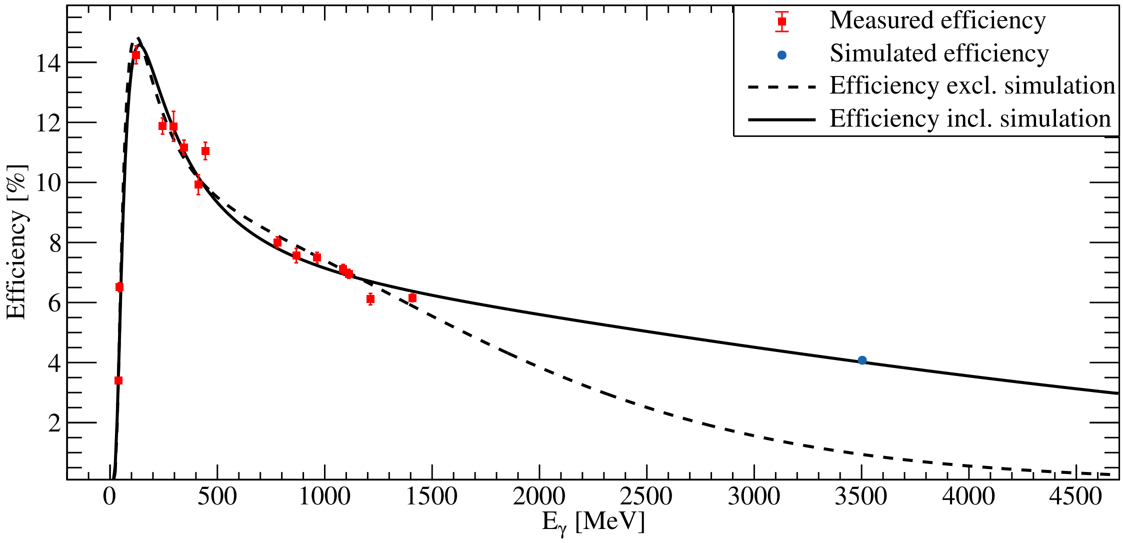

Figure 4.11: Efficiency of the AGATA array, as measured with a ^{152}Eu source (red squares) and a realistic Monte Carlo simulation (blue circle). The fitted efficiency curves, both with (solid line) and without (dashed line) the simulated point, are shown.

4.2.2 Doppler correction

As γ-rays are emitted from the de-exciting nucleus, which is travelling at a speed relative to AGATA approximating the incoming beam velocity, $0.126c$, the wavelength (and therefore, energy) of the emitted photon is shifted by the Doppler effect. The energy detected by AGATA, positioned in the backwards angle, is therefore lower than the "true" transition energy by some margin. In this analysis, the true energy was reconstructed using the following method.

Firstly, the initial speed of the radioactive isotope beam β_{initial} was slowed by the calculated energy loss of the beam passing through half of the target material.[5] The new average beam velocity, β_{target}, was then adjusted to account for the recoiling effect of a transfer reaction. This adjustment was made event-by-event, using the energy and angle of the light ejectile measured in MUGAST, to give β_{event}.

Given two frames of reference – that of the de-exciting nucleus, and that of the detection apparatus – moving at a constant velocity β_{event} relative to each other, the proper mathematical framework to move between frames is a Lorentz transformation. The energy and momentum of a particle – or the frequency and wave vector of a photon – form a four-vector, which was transformed by a non-rotational Lorentz transformation (also known as a Lorentz boost) between frames of reference. More details of this method can be found in Ref. [124, pp. 43-49].

---

[5] This method assumes that all reactions occur at the centre of the target, and that the lifetime of excited states is negligible. While there will be some broadening of the γ-ray peaks due to the spatial distribution of transfer reactions, the assumption is appropriate for a thin target.

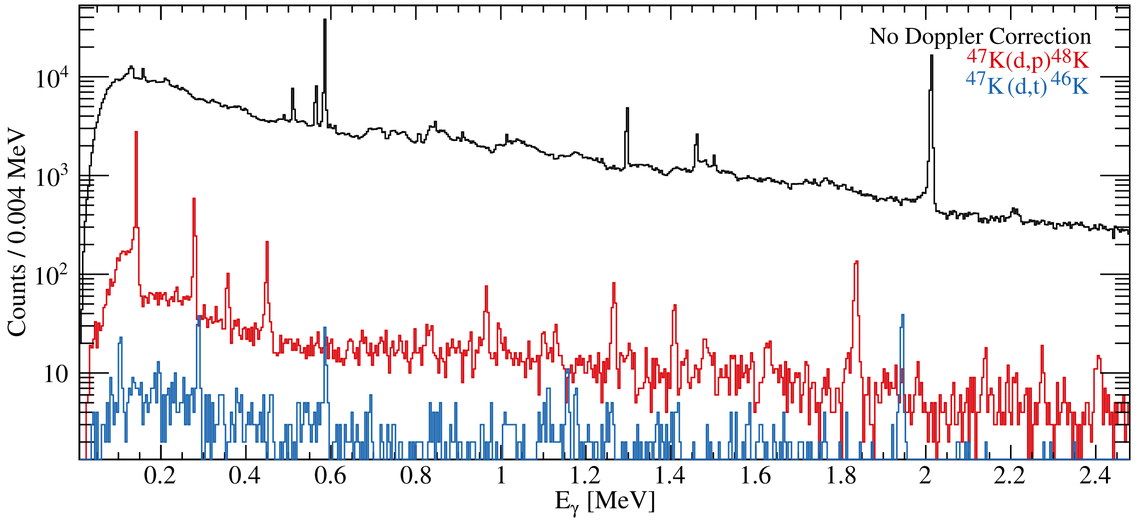

Figure 4.12: Comparison of the non-Doppler corrected and ungated γ-ray excitation spectrum (in black) to the Doppler-corrected and particle-gated (d,p) and (d,t) transfer reaction γ-ray spectra (red and blue, respectively).

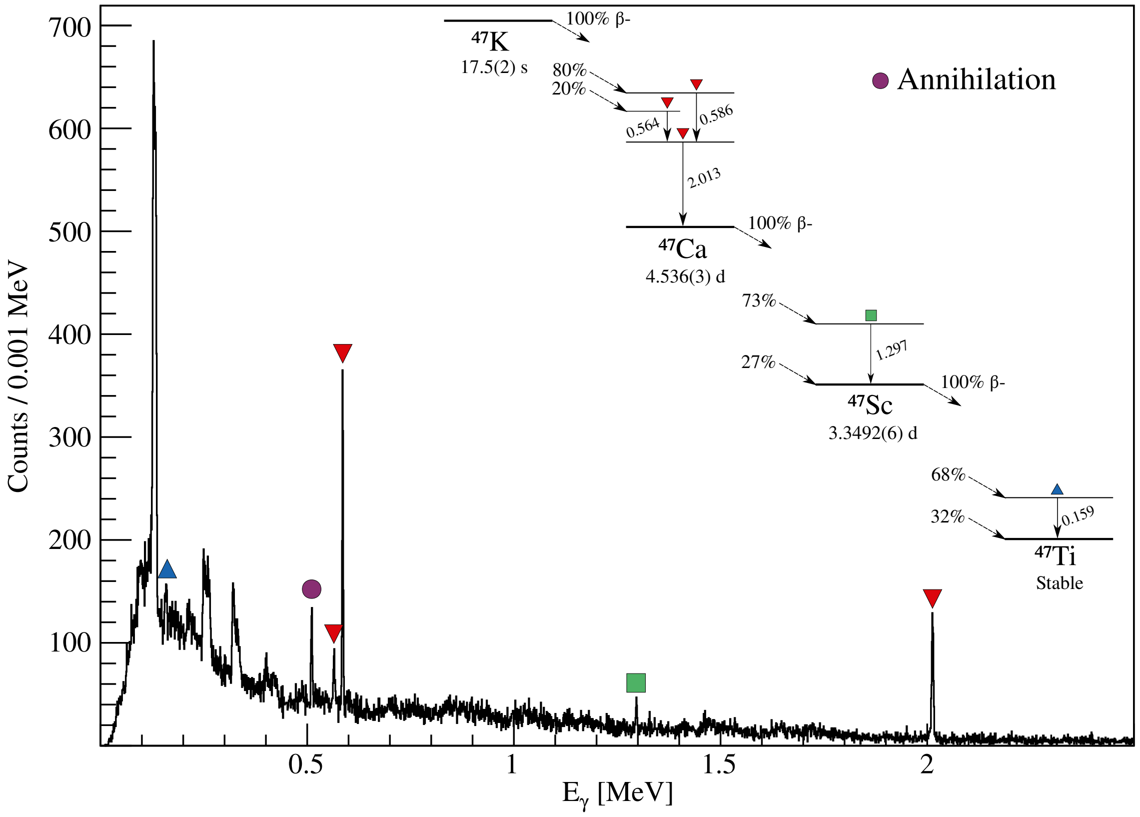

Figure 4.13: Identification of background γ-rays associated with the β^- decay of implanted beam. De-excitations within different isotopes are identified by coloured markers. The whole chain, to stable ^{47}Ti, is observed.

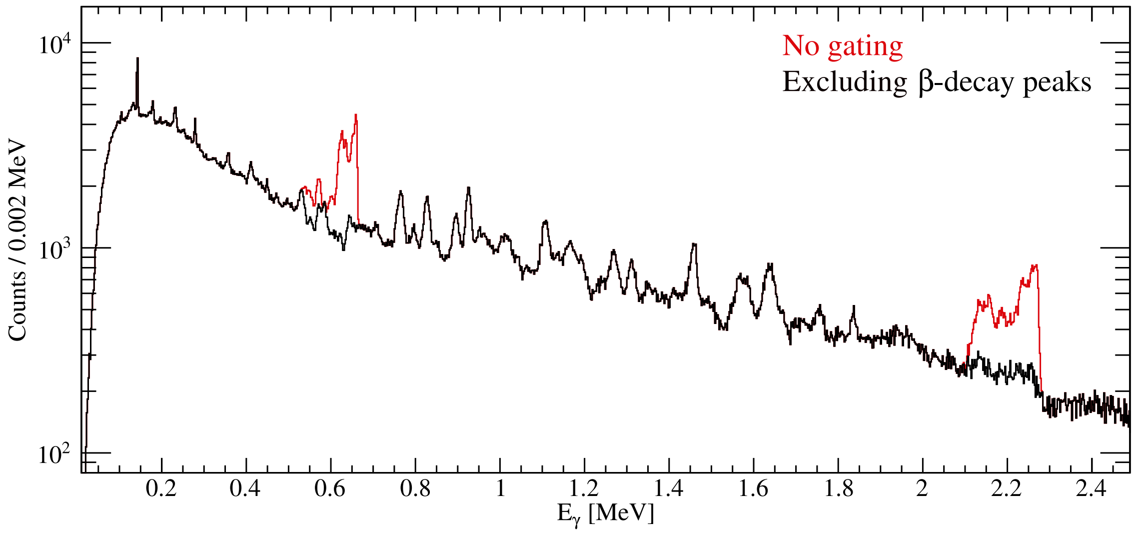

Figure 4.14: Demonstration of the effective removal of background γ-rays from the β^- decay of ^{47}K implanted in the beam pipe. The γ-ray spectrum, Doppler corrected for ^{48}K, is shown in red. The same spectrum, with exclusionary gates placed on the marked peaks in non-Doppler corrected data, is shown in black.

Following this, the corrected energy of the emitted γ-ray was found. A comparison of E_γ spectra can be seen in **Figure 4.12**. Here, the uncorrected spectrum is shown, alongside the Doppler-corrected and gated spectra associated with ^{47}K(d,p) and ^{47}K(d,t) transfer reactions. Some interesting features can be noted here; firstly, the non-Doppler corrected spectrum contains a variety of peaks that are not standard background peaks. These are associated with the decay of implanted ^{47}K in the beam pipe, as identified in **Figure 4.13**. Additionally, the effectiveness of the event-by-event Doppler correction is demonstrated by the comparable resolutions of the stationary β^- decay peaks (σ = 2 keV at 2.0 MeV) and the transfer reaction peaks (σ = 3 keV at 1.8 MeV).

In order to ensure no random background events from implanted beam are present in Doppler-corrected γ-ray spectra, all results include an exclusion gate on each of the β-decay peaks before Doppler correction is applied. The effect on the Doppler-corrected spectrum can be seen in **Figure 4.14**. This is only critical for γ-ray spectra without a particle coincidence gate, as random coincidences are excluded by the requirement of a valid light ejectile coincidence.

4.2.2.1 Inconsistency in (d,t) γ-ray peaks

During the analysis of the ^{47}K(d,t)^{46}K data, it was found that the 1.944 MeV γ-ray exhibited unusual behaviour, in that gating on the high or low energy sides of the single peak produced different coincident particle spectra. This can be seen in **Figures 4.15** and **4.16**. This could indicate a doublet (two γ-rays with unresolvable transition energies), a

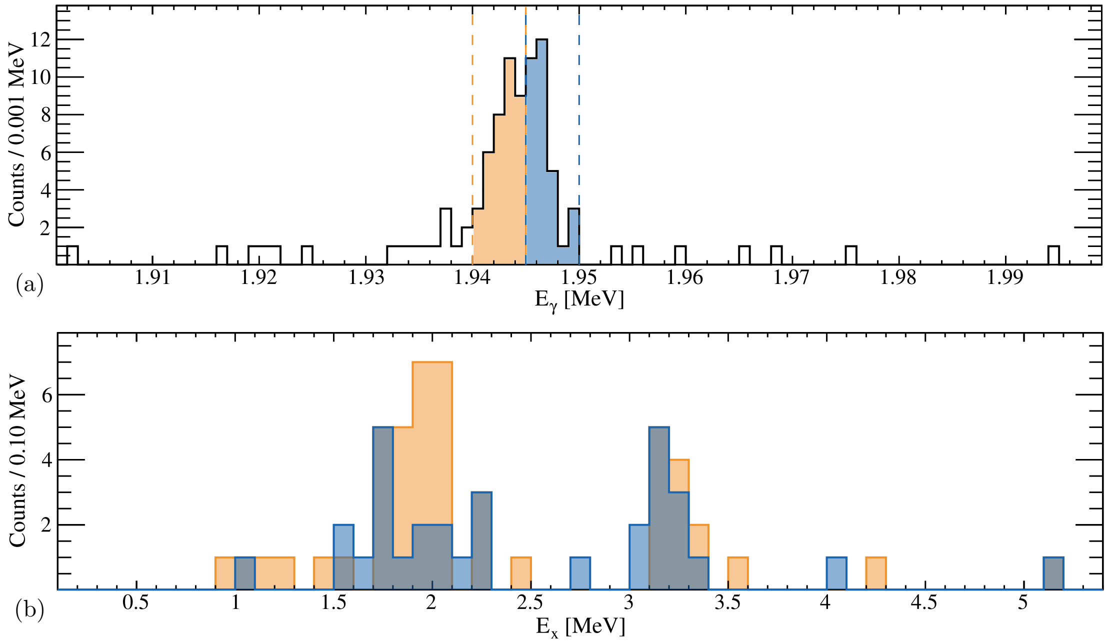

Figure 4.15: Demonstration of poor Doppler correction, by looking at the difference in excitation spectra (b) observed in coincidence with different halves of the 1.944 MeV γ-ray peak (a).

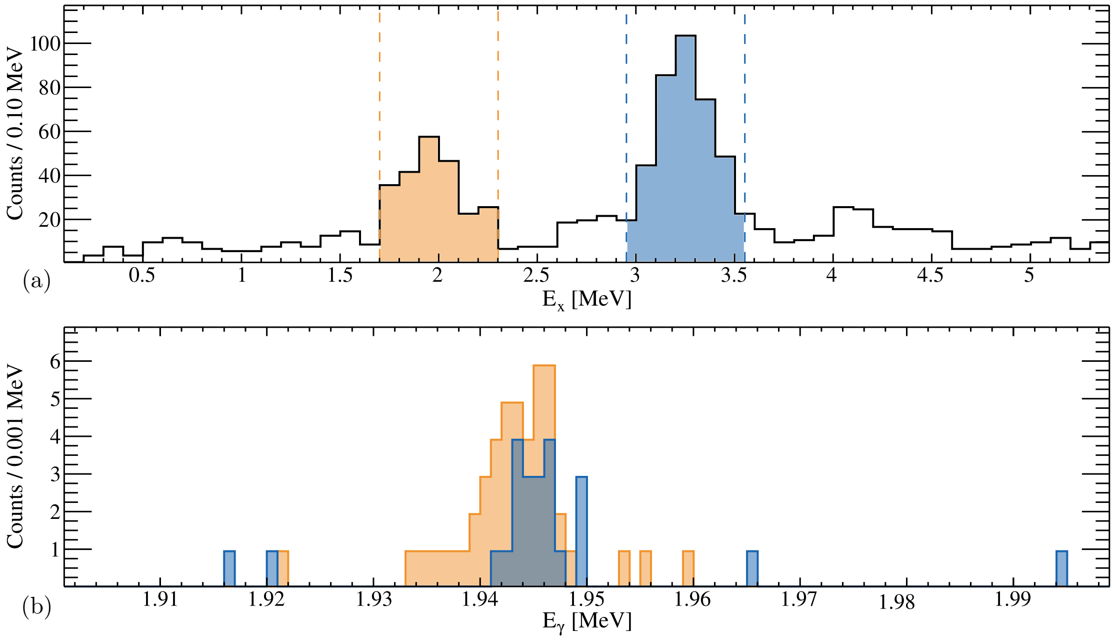

Figure 4.16: Demonstration of poor Doppler correction, by looking at the difference in the 1.944 MeV γ-ray peak (b) observed in coincidence with two different excited states (a).

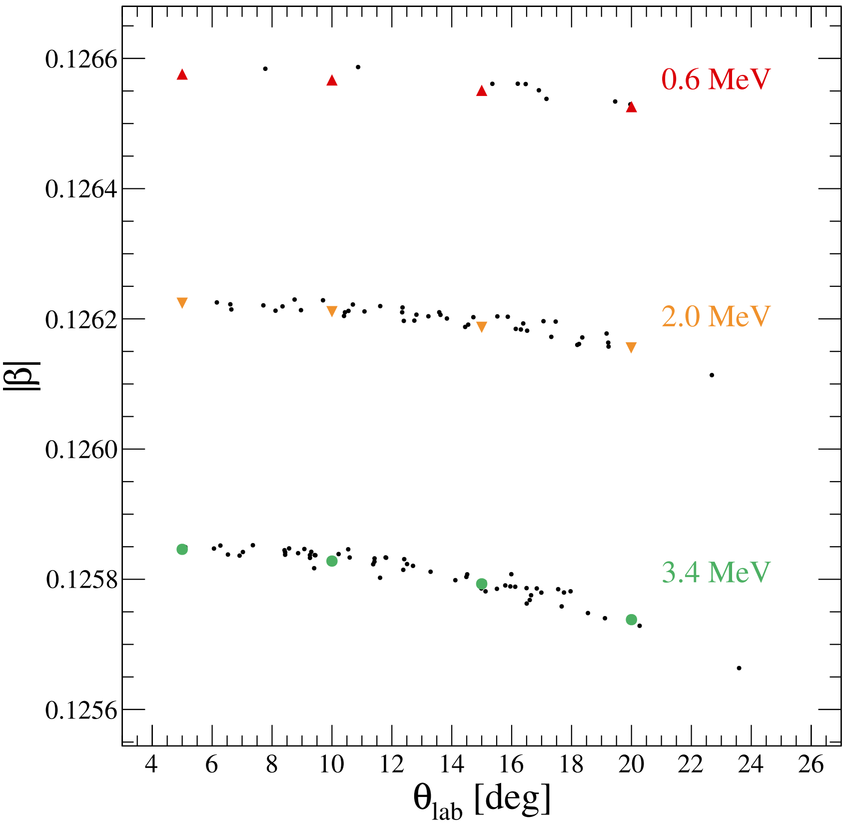

Figure 4.17: Ejectile-adjusted beam velocity β, compared to the angle of light ejectile detection θ_{lab}. Three energetically-distributed regions are isolated. Experimental results for these three regions are in black, and kinematic calculations are coloured triangles/circles.

non-negligible lifetime in the higher-energy feeding state, or an issue with the Doppler correction. Ideally, the same comparison of low and high energy sides of a peak would be performed for another strong transition in the ^{46}K data, but no appropriate candidate was identified.

Given the sparse nature of the γ-ray spectrum, the restrictive method of population, and the lack of other supporting evidence for a doublet of states, it was believed that a doublet was unlikely. This was further supported by an unpublished[6] high-statistic measurement of the β^- decay of ^{46}Ar to ^{46}K using AGATA – this work found no evidence to support a doublet of states. The same data set showed no evidence to suggest that the higher-energy feeding states exhibited any non-negligible lifetime. As such, a more detailed examination of the Doppler correction was performed.

The value of $|\beta_{\text{event}}|$ calculated in the analytical code was compared for several energetically disparate, strongly populated states in ^{46}K. As expected, the higher the energy of the excited state, the larger the effect of the recoil, and the smaller the $|\beta_{\text{event}}|$. Due to the variation of ejectile energy with angle for a single excitation state, $|\beta_{\text{event}}|$ was plotted against a further parameter, the detection angle θ_{lab}, as shown in in **Figure 4.17**.

---

[6] E. Clément (personal communication).

The experimental values were then compared to the expected $|\beta_{\text{event}}|$ calculated using the CatKin [114] kinematics program, which used the same value of β_{target} and excitation energy as the experimental analysis. These results, as a function of θ_{lab}, are shown as coloured markers in **Figure 4.17**. The remarkably close agreement between the experimental data and CatKin indicates that the analytical process is highly accurate, given the limitations of target thickness and MUGAST energy resolution. This inaccuracy in the Doppler correction, evaluated to be less than 1%, is acknowledged moving forwards.

It is important to note that this inaccuracy is not detectable in the ^{48}K γ-ray spectra, as the effect of the recoiling proton is approximately $1/3$ that of the triton.

4.3 VAMOS++ and CATS2

The operation and calibration of both the VAMOS++ magnetic spectrometer and the CATS2 in-beam detector are well-standardised, due to their many years of successful use by the local team. In this work, the VAMOS++ magnetic spectrometer was used exclusively for heavy recoil fast timing coincidence with light ejectiles detected in MUGAST, with no additional mass selection or particle identification. As such, only the MUGAST-VAMOS++ timing signal is discussed in depth in this section. Further analysis of detections at the VAMOS++ focal plane can be found in Appendix A.2.

4.3.1 Erroneous timing signals of true reaction products

Ideally, the transfer reaction products could be separated from the non-transfer background by the time-of-flight difference between a light ejectile detection in MUGAST and a heavy recoil in VAMOS++. The timing spectrum in **Figure 4.18a** shows this relative timing value, with a clear and distinct peak of reaction products (henceforth referred to as the ‘major’ peak, marked in blue) amongst the consistent background of CIME frequency beam pulses (‘minor’ peaks, marked in red).

Unfortunately, upon closer inspection[7], it becomes clear that some true reaction products are erroneously present in the minor peaks, as is shown in **Figure 4.18b**. By comparing the number of particle-γ coincidence events in the major timing peak versus events with an erroneous timing signal – that is, either in a minor peak, or with no timing signal at all – it was determined that $\approx$ 38% of the reaction events fell into the latter category. This presents a significant issue, as the unaccounted loss of transferred particles would lead to reduced measured spectroscopic factors. Conversely, the coincidence requirement is crit-

---

[7] Note that the following work has been verified for each trapezoid individually as well as the collective, and therefore the poor MG5 timing calibration is not the cause of the issues discussed.

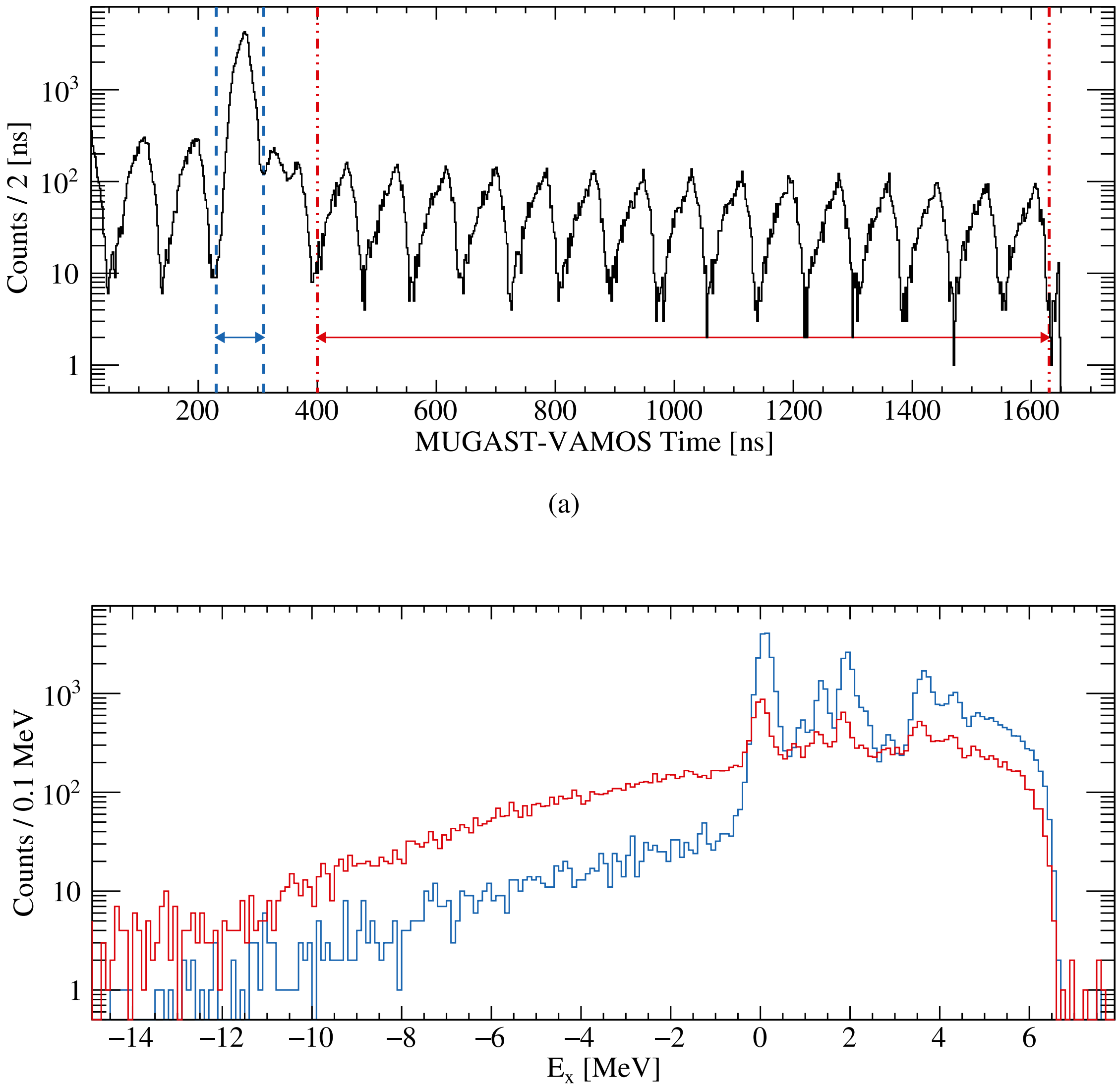

(a)

(b)

Figure 4.18: True transfer reaction events – demonstrated here using (d,p) transfer – are present both in the major timing peak (blue) and erroneously in the minor timing peaks (red). (a) The timing signal between the upstream MUGAST detectors and VAMOS++, with gates marked. (b) The ^{48}K excitation spectrum found in coincidence with the two marked timing gates.

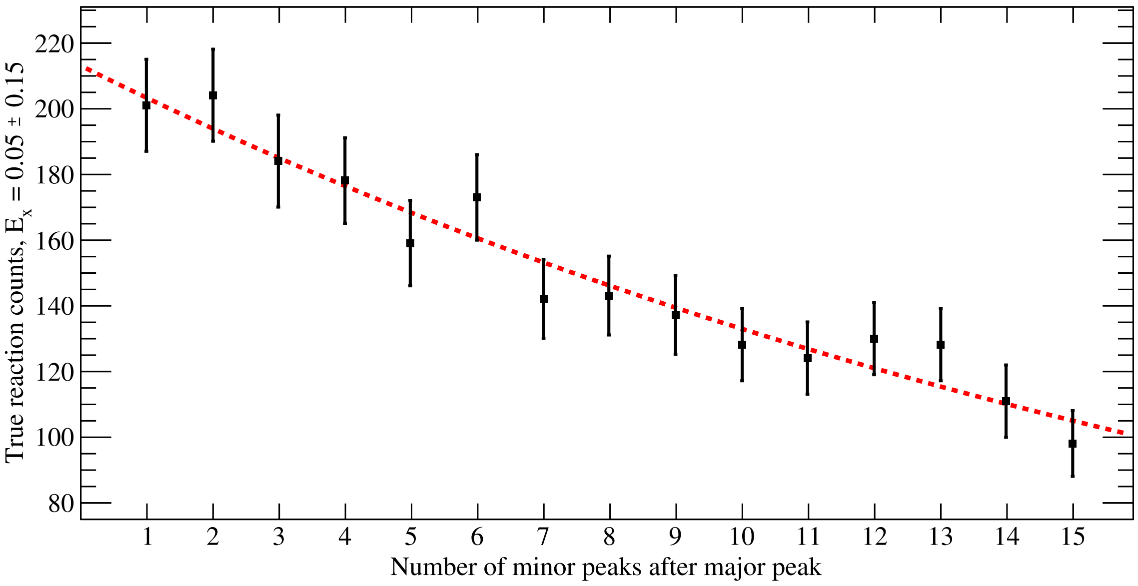

Figure 4.19: Exponential decay of the number of true reaction counts present in subsequent minor timing peaks after the major timing coincidence peak. Here, the timing signal is the MUGAST-VAMOS++ time. The fit is of the form $y = ae^{bx}$, and the fitted parameters determined were $a = 5.36(4)$ and $b = 0.047(5)$. This exponential decay is consistent with a malfunctioning CATS2 STOP timing signal.

ical for background reduction – particularly for tritons (see Section 4.1.5 and **Figure 4.9**). Excluding this requirement from the analysis produced an unacceptable degradation in the quality of experimental data. As such, a thorough investigation was performed to ensure that applying the timing coincidence did not bias the results.

While the hypothesis presented here cannot be proven unequivocally, several results are strongly indicative of an issue with the processing of the timing signal, which led to occasional random malfunctions wherein the STOP signal was not sent. The problem was found to occur in many different timing signals, all of which had a delayed CATS2 signal as the STOP, identifying this as the likely cause.

To support this conclusion, a falsifiable test was conducted. Were this to be true, the distribution of counts in the minor peaks would decay exponentially, because the STOP signal is generated by the next beam pulse that contains a particle. To a first approximation, the probability of a pulse containing a particle is near 4% per pulse[8] and the probability of detecting a true STOP signal in a given pulse can be determined, using Poisson statistics[9], to be an exponentially decaying distribution proportional to $e^{-\mu n}$, where μ is the probability of a pulse containing a particle, and n is the number of beam pulses. Indeed, such a distribution is observed in **Figure 4.19**, where the number of true reaction events in coincidence with each subsequent minor peak is fit with an exponential function proportional

---

[8] The CIME cyclotron frequency was approximately 12.5 MHz, but CATS2 recorded average incoming particles on the order of 0.5 MHz.

[9] See Appendix. A.3 for this derivation

to $e^{-0.047(5)n}$, suggesting a probability of a pulse containing a particle of approximately 5%. This strongly supports our interpretation of the data.

With this in mind, it becomes critical to determine if any biases would be introduced to the transfer differential cross sections by excluding the data with erroneous timing signals. To do this, it was established that the elastic scattering differential cross sections were affected by the same relative loss factor of ≈ 38% over the range of angles used in the normalisation of transfer data, within statistical error. Applying the major peak coincidence requirement did lead to a slight drop in yield at the very largest centre-of-mass scattering angles for ^{47}K(d,d), appearing to be related to the larger recoil momentum of these particles. A detailed examination of the VAMOS++ entrance window and focal plane – detailed in Appendix A.2 – ensured that all heavy recoil events were within the VAMOS++ acceptance, and reached the focal plane, implying some slight timing measurement effect for this limited range of events. In any case, the affected angles are already outside of the normalisation region – theoretical calculations of ^{47}K(d,d) scattering diverge at such large θ_{cm}, as seen in **Figure 4.5** – and hence do not introduce bias.

Thus, with a plausible explanation established and no suggestion of bias or error, the results presented in this work all require a MUGAST-VAMOS++ timing coincidence in the major peak. Despite sacrificing a significant portion of the events, the statistical accuracy is far greater due to the substantial background removal.

Chapter 5

Results

Using the analytical methods described in the previous chapter, the experimental observables – E_{lab}, θ_{lab}, θ_{CM}, E_x, E_γ, etc. – have been extracted. In this chapter, those observables are used to determine the structure of ^{46,48}K; that is, the energies, γ-ray transitions, spin-parities, ℓ-transfers and spectroscopic factors of the various states populated by single particle transfer reaction.

Certain states – labelled *simple* in **Figure 5.1** – could be identified in a straightforward manner, due to good energetic separation, strong population and clear γ-ray coincidences. Other states, such as unresolved doublets or regions of unbound strength, required additional detailed analysis. In each section of this chapter, the simple states are discussed collectively, followed by individual discussions of the complex states.

In Section 5.1.1, the excitation energies and γ-ray transitions of ^{48}K states are determined, followed in Section 5.1.2 by the differential cross sections of those states. The majority of

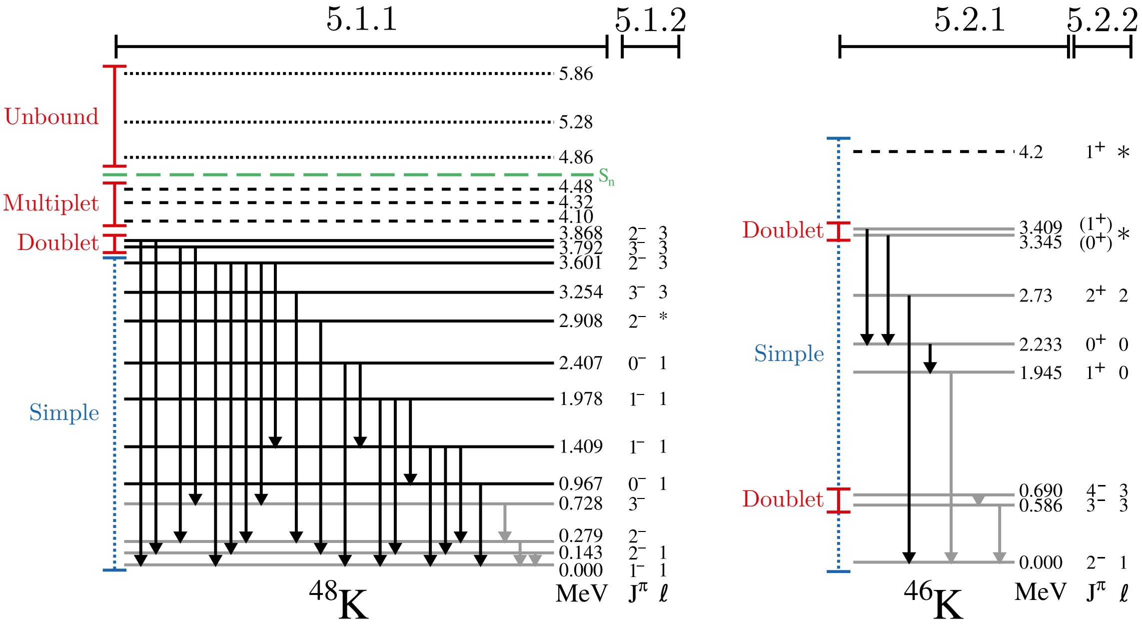

Figure 5.1: Simplified level schemes of ^{46,48}K, outlining the structure of this chapter, as described in-text. Novel states and transitions are in black, with established structure in light grey. Dashed lines indicate states with unknown γ-decay structure, and dotted lines indicate unbound states.

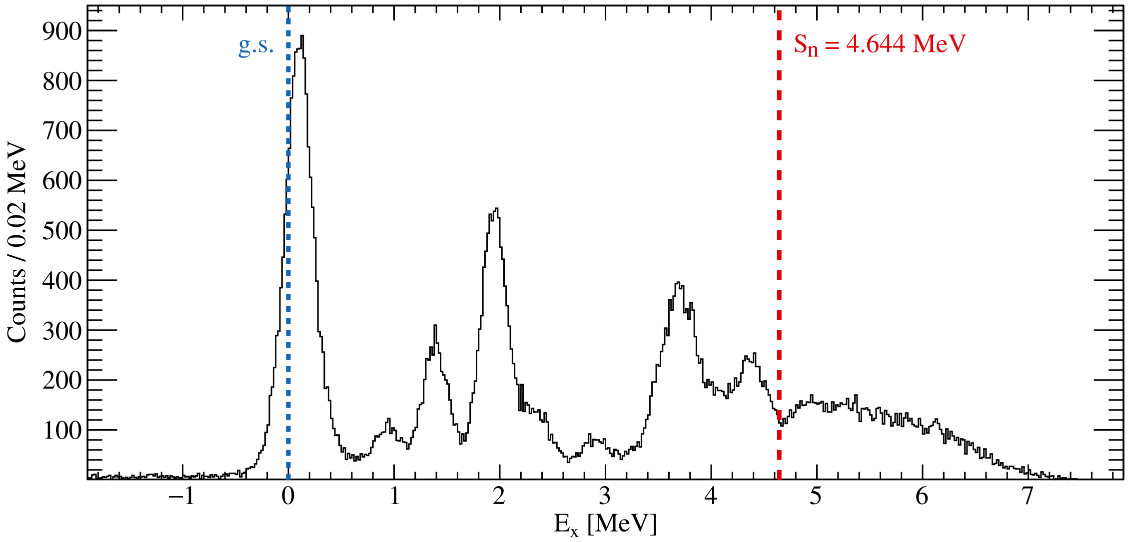

Figure 5.2: Reconstructed excitation spectrum of ^{47}K(d,p)^{48}K. The position of the ground state and the neutron separation threshold – the limited region of bound nuclear states – are marked in blue and red, respectively.

this chapter is dedicated to the extraction of these results, as they are the core motivation of this work.

Following this, attention turns to the complementary reaction, ^{47}K(d,t)^{46}K. Again, the identification of excited states and transitions is tackled first, in Section 5.2.1, followed by the differential cross sections in Section 5.2.2. These additional results use many of the same techniques as the primary data set, and as such are described in less exacting detail.

5.1 ^{47}K(d,p)^{48}K

5.1.1 Excited states and transitions

In the reconstructed heavy recoil excitation spectrum of ^{48}K, shown in **Figure 5.2**, there are several key features to note. Firstly, the signal to background ratio is excellent, evidenced by the near total lack of events below the ground state peak. Conversely, there is a relatively smooth continuum of events above the ^{48}K neutron separation threshold, S_n. These are mostly[1] attributed to the three-body deuteron break up channel ^{47}K + d $\rightarrow$ ^{47}K + p + n, which has a sloping shape in this spectrum due to the encroaching E_{lab} threshold.

The key advantage of the experimental setup used in this work is the inclusion of coincident γ-ray spectroscopy, which allows for a two-dimensional comparison of the energy of the ^{48}K state and the de-exciting γ-ray transitions out of that state. This is shown in **Figure 5.3**.

---

[1] Three weak unbound states have been identified in this region - they will be discussed in more detail in Section 5.1.1.3.

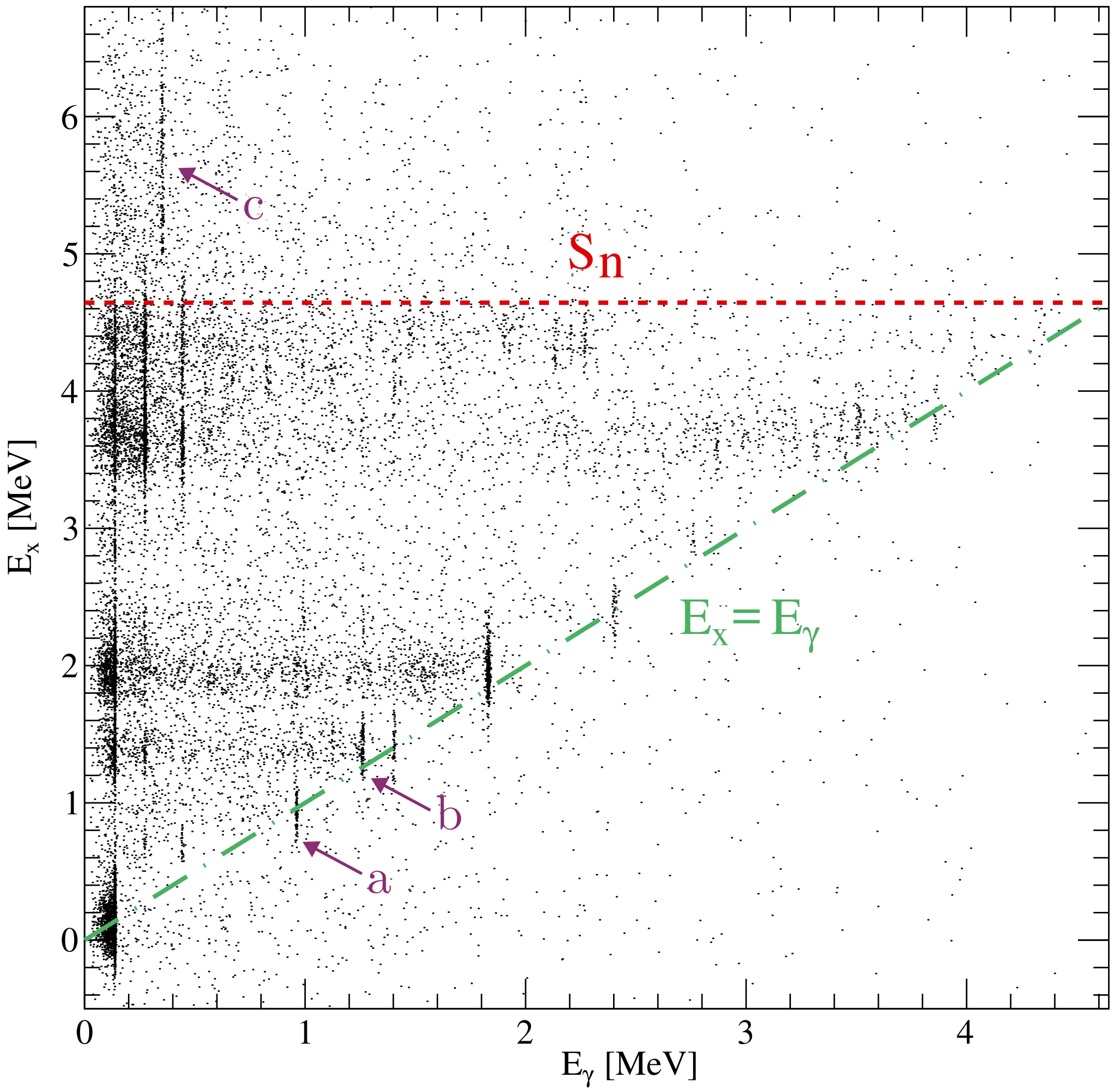

Figure 5.3: Observed ^{47}K(d,p)^{48}K excitation and γ-ray transition coincidences, with the three indicated features discussed in-text. The neutron separation energy is indicated in red, and the line of excitation-decay unity is indicated in green. Labels indicate (a) a decay directly to the ground state, (b) a decay to the first excited state, and (c) unbound coincidences with a known ^{47}K γ-ray.

The spectrum in **Figure 5.3** can be divided into four 'regions':

$E_\gamma > E_x$ Trivially, no true transfer reaction event can appear in this region.

$E_\gamma = E_x$ Features in this region are the result of a bound excited state decaying directly to the ^{48}K ground state in a single transition. These features may cross into the $E_\gamma > E_x$ region due to the finite resolution of MUGAST. Label *a* in **Figure 5.3** indicates a state that decays in this way.

$E_\gamma < E_x$ Features in this region are the result of a bound excited state decaying to the ^{48}K ground state via one or more intermediate states. Label *b* in **Figure 5.3** indicates a state that decays both straight to the ground state, and via an intermediate state.

$E_x > S_n$ Features in this region are the result of an unbound excited state decaying to some other excited state. Label *c* in **Figure 5.3** indicates such a feature in this work.

Focusing initially on events below the neutron separation energy, specific excited states can be isolated by requiring a coincidence with observed γ-rays, as seen in **Figure 5.4**. This not only allows otherwise inextricable states to be resolved, but by summing the energies of successive transitions, the energy of the initial state is determined. As such, the excitation energy can be measured with the much finer γ-ray resolution (7 keV at 1.8 MeV), rather than the more coarse reconstructed excitation resolution (330 keV in ^{48}K).

Spectra can also be produced by looking at γ-rays in coincidence with specific excitation energies. Whilst gating on a γ-ray reveals all of the populated states that decay via that transition, gating on an excitation peak instead reveals only the decay pathways that the specific state takes.

For the majority of states observed in this work – that is, all states up to 3.601 MeV – these simple comparisons are sufficient to construct a clear decay scheme.[2] There are, however, three regions of states that require a more detailed inspection. These will be explored in the following sections.

5.1.1.1 Doublet at 3.8 MeV

When examining high-energy γ-ray transitions of E_γ = 3.0 MeV to 4.0 MeV, three particular transitions present a compelling argument for a doublet of states. Looking first to the E_x spectra in coincidence with these three transitions – **Figure 5.5** – the transitions all

---

[2] Spectra relating to the analysis of these simple states can be found in Appendix B.1

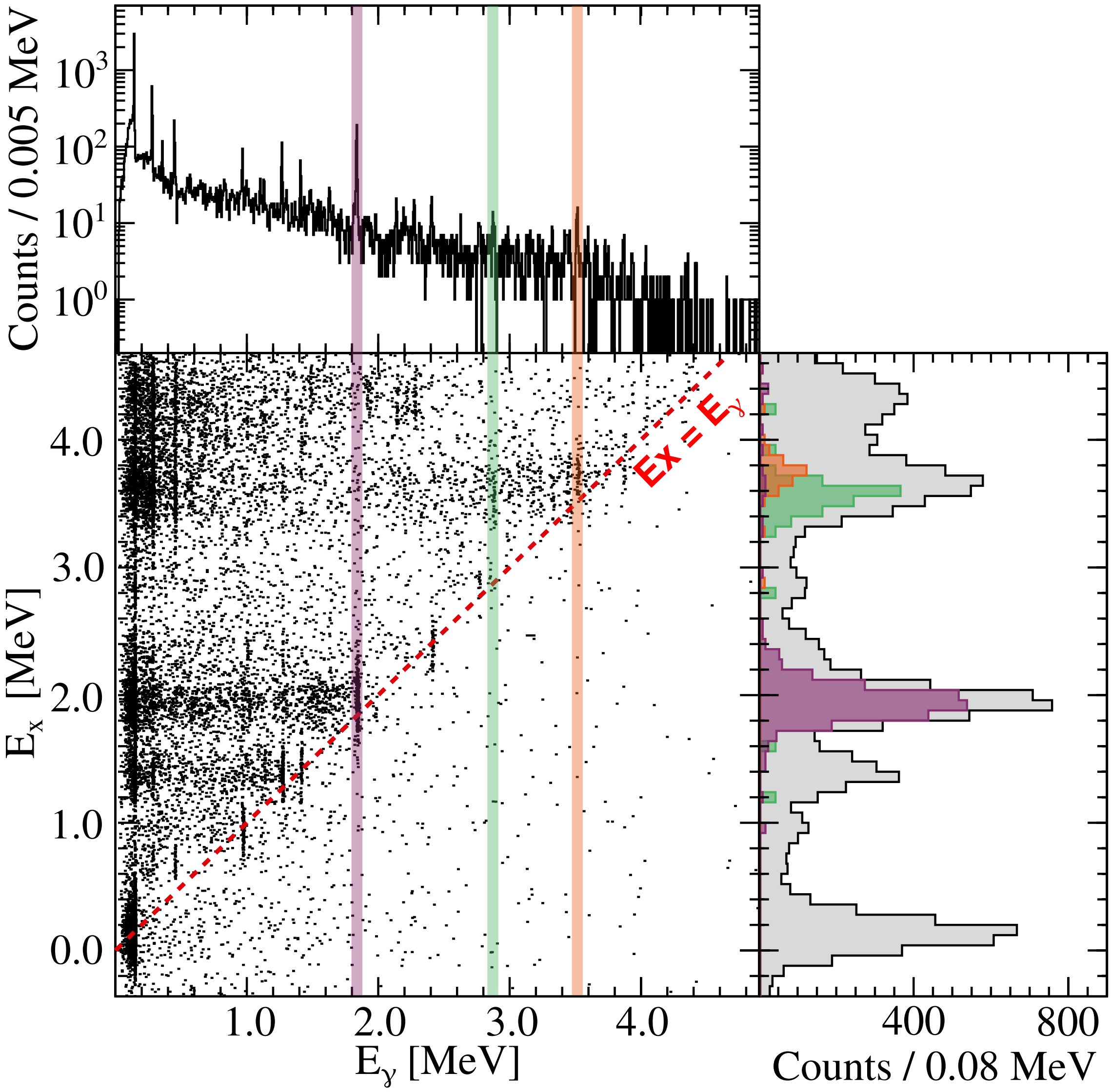

Figure 5.4: Observed coincidences between reconstructed ^{48}K excitation energy, E_x, and prompt γ-ray energy, E_γ. Full one-dimensional projections are shown in black on the relevant axes. Projections based on selecting specific γ-ray transitions are shown in colour (scaled relative to branching ratio and detection efficiency), highlighting the ability to isolate states that would otherwise be unresolved.

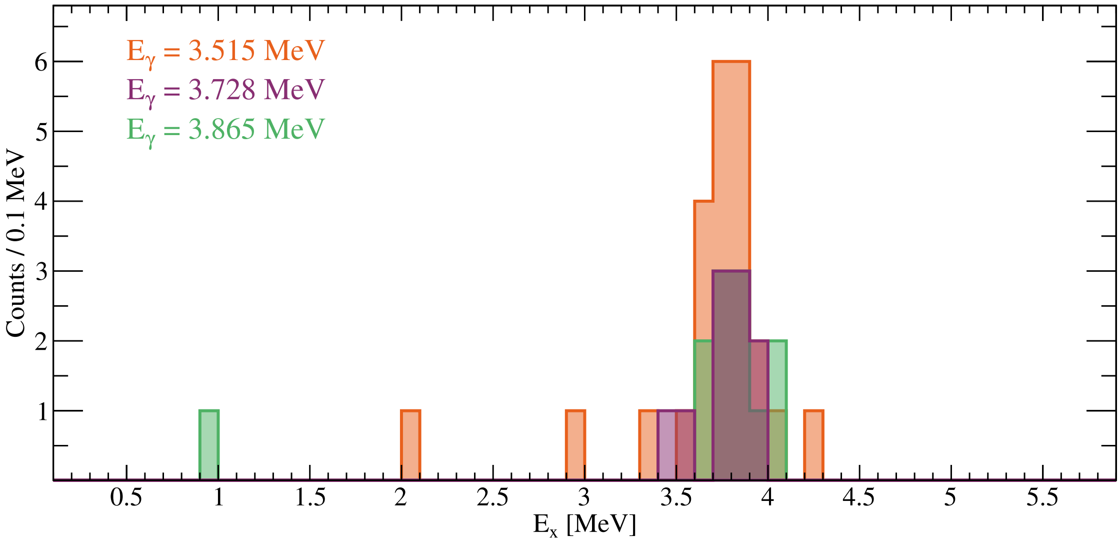

Figure 5.5: Observed excitation spectra in coincidence with three different γ-ray transitions; 3.515 MeV, 3.728 MeV and 3.865 MeV. Note that each of the three spectra have only one populated state, and in each, $E_x \approx 3.8$ MeV.

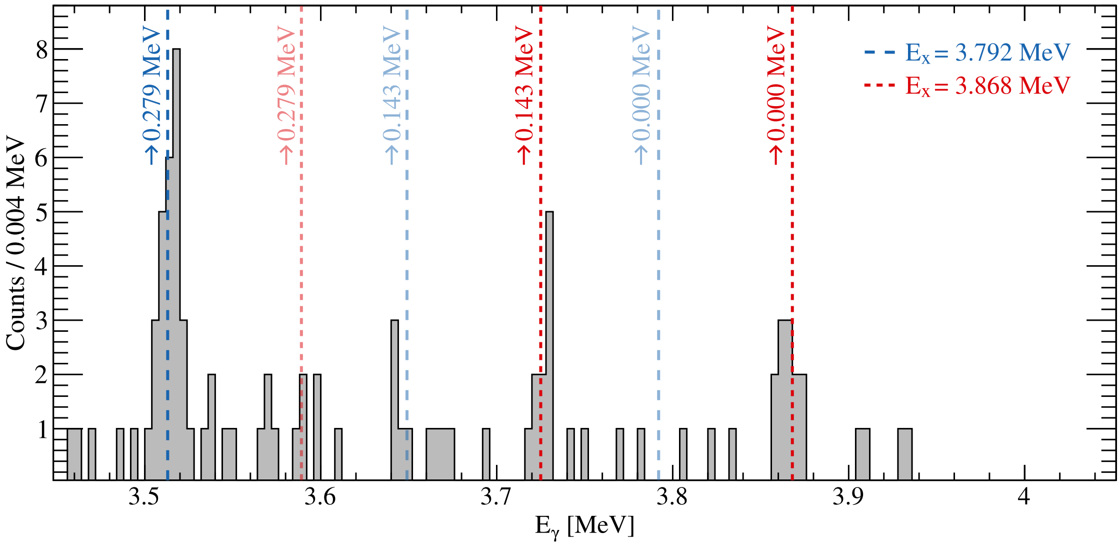

Figure 5.6: High-energy γ-ray spectrum, requiring coincidence with the $E_x = 3.8$ MeV region. Three clear γ-ray transitions can be seen, at 3.515 MeV, 3.728 MeV and 3.865 MeV. Dashed lines indicate the expected energy of a transition from the indicated state energy to one of the three lowest-energy states. Critically, no single state energy is correlated with all three transitions, indicating a doublet of states.

isolate only one state, at $E_x \approx 3.8$ MeV. This would, usually, suggest that all three decays originate from the same state.

Interestingly, the excitation-gated γ-ray spectrum, in **Figure 5.6**, does not support this interpretation. In this figure, the dashed lines indicate the expected energies of transitions out of a state into one of the lowest-energy states in ^{48}K. This illustrates that the difference in energy between 3.515 MeV and the other two transitions is not consistent with the established level scheme, instead requiring two different initial energies.

While this could in theory be the result of a decay from 3.868 MeV to some heretofore unknown low-energy state, a detailed examination of the experimental data showed no reason to believe that such a state exists. Instead, this is more plausibly explained by a doublet of excited states; 3.792 MeV and 3.868 MeV.

As these two states are irresolvable in the reconstructed excitation spectrum, they are fit together with one Gaussian peak for the remainder of this analysis.

5.1.1.2 States in the 4-4.6 MeV region

When considering the highest bound energies in ^{48}K, in the region of E_γ = 4.0 MeV to 4.6 MeV, there is an additional complication due to the much reduced γ-ray detection efficiency at high energies. As such, transitions to one of the lower-lying states are much harder to detect, and have far larger errors in their energy measurements.

We can instead turn to the lower energy multi-step transitions originating from these states. Somewhat uniquely amongst the observed transitions, these very high-energy states appear to have a rather fractured decay pattern, with many transitions through multiple intermediate states. This can be seen in the two-dimensional plot in **Figure 5.3**, where the $E_x > 4$ MeV region is quite barren above E_γ = 2.4 MeV, but a myriad of transitions can be found below this point. In **Figure 5.7**, three particularly strong transitions – observed with good efficiency – are selected to isolate three states at $E_x > 4$ MeV.

Unfortunately, despite detailed investigation, no candidate intermediate states could be identified for these transitions. There are many possible reasons for this; one could imagine that the intermediate states could have some non-negligible lifetime, meaning that the subsequent disintegration occurs outside of our detection region, or; the weakly populated states have some fractured decay into many states, making each onwards transition hard to discern. Nevertheless, the analysis only supports measurements of the state energy with the resolution of the isolated E_x spectra, rather than the γ-ray precision. As such, the three states observed in this region are E_x = 4.10(3) MeV, 4.30(5) MeV, and 4.48(3) MeV.

Due to the imprecise energy determination, and the possibility of additional populated states with primarily high-energy decay schema, the states above 4 MeV are treated as

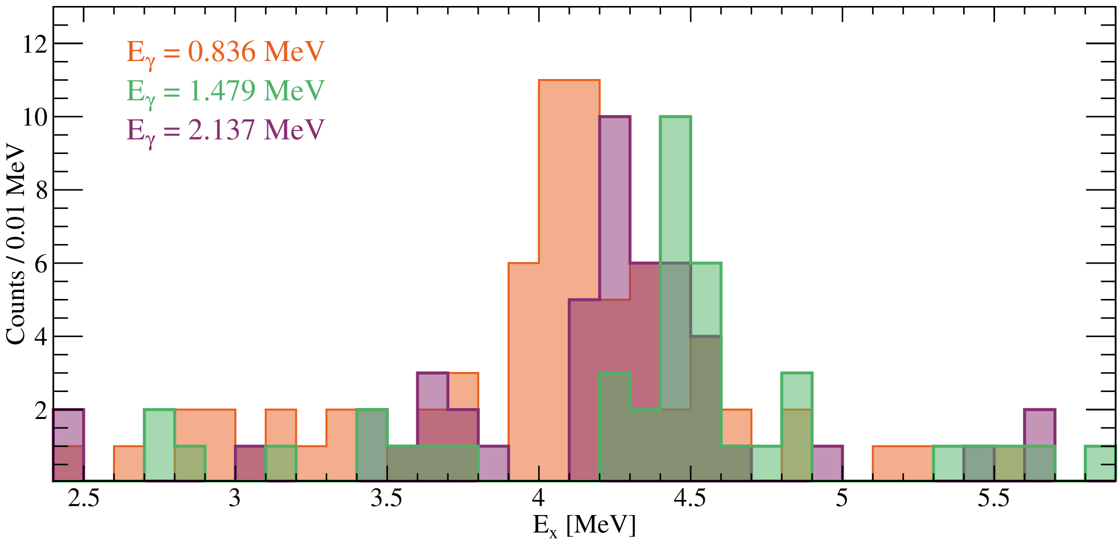

Figure 5.7: Observed excitation spectra in coincidence with three different γ-ray transitions; 0.836 MeV, 1.479 MeV and 2.137 MeV. Note that each transition isolates a different excited state in the 4 MeV region.

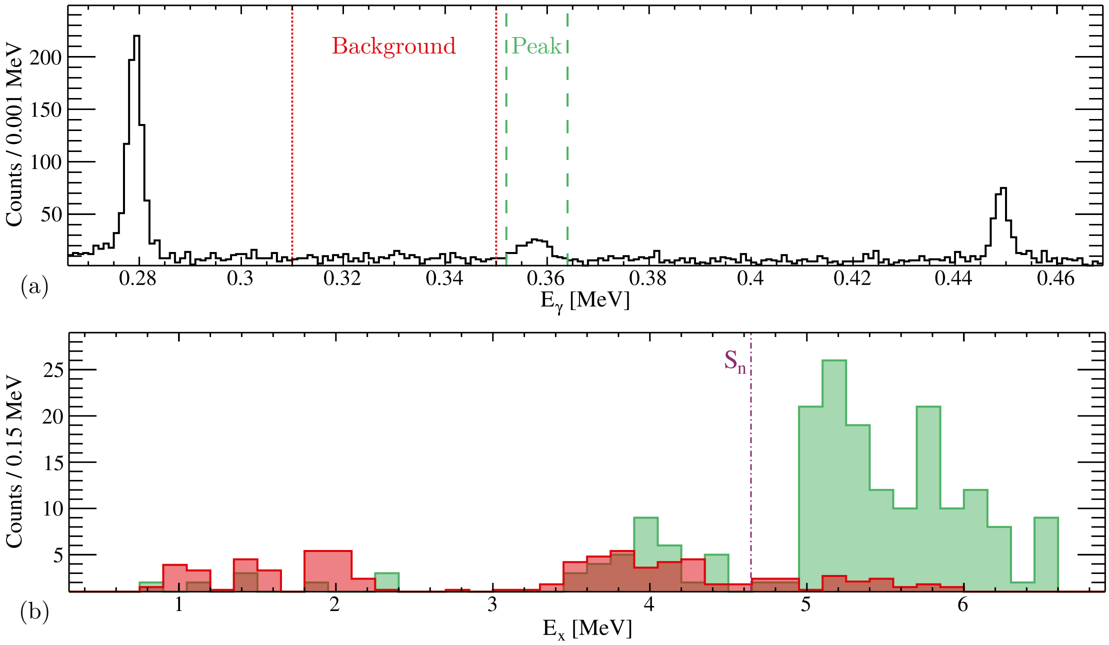

Figure 5.8: Particle-γ coincidence spectra of unbound states in ^{48}K. (a) γ-ray spectrum, showing the ^{47}K transition at 0.36 MeV, which is broadened relative to true ^{48}K transitions due to the difference in Doppler correction. (b) Excitation spectra in coincidence with the selected peak region (green) and scaled background region (red), showing significant strength above the neutron separation threshold S_n.

one region of strength. It was found that the region is well approximated by one broad Gaussian peak.

5.1.1.3 Unbound states

The feature marked *c* in **Figure 5.3** is particularly interesting, as these particle-γ coincidence events are occurring above the ^{48}K neutron separation threshold. Further, the γ-ray energy that these coincidences occur at is approximately 0.360 MeV, which is known to be the energy of the first excited state in ^{47}K [125]. Taken together, this indicates that the ^{47}K(d,p) transfer reaction is populating relatively narrow unbound states in ^{48}K, which are then decaying by neutron emission to ^{47}K. At least some of these unbound states have a decay branch to the first excited state, but there could be additional decay branches to the ground state that are not present in this E_x - E_γ plot.

In **Figure 5.8**, it is clear that the ~0.360 MeV γ-ray coincidence requirement isolates unbound strength far above background levels. Due to the reduction in statistics when this requirement is applied, the shape of the strength is indistinct, and it is not trivial to determine how many states are present.

Having confirmed the presence of unbound strength, we look to the E_x spectrum without any γ-coincidence requirement. The shape of this high-energy region is dominated by the deuteron breakup phase space, which must be well-defined in order to extract unbound states with any confidence. To do this, Geant4 Monte Carlo simulations of the deuteron breakup process were performed, using realistic geometry and responses of the MUGAST array. In order to remove any possible threshold effects, ensuring consistency between simulated and experimental data, gating was applied to the data as shown in **Figure 5.9a**, where cuts were taken parallel to the line of increasing E_x. An additional cutoff is applied at E_x = 6 MeV. These requirements are henceforth referred to as the *parallel gates*.

Now, two forms of background subtraction are performed on the parallel-gated experimental data. First, the known bound states are fit and subtracted, as the tail of the highest energy bound states could alter the shape of the low-energy unbound region. Then, the simulated deuteron breakup background is maximally subtracted. The remaining events are hence attributed to unbound states. As the detected peak shape of unbound states is not trivially Gaussian, further simulations were performed in order to find the expected shape of states with different excitation energies. A χ^2 minimisation was performed, using simulated energies from 4.64 MeV to 6.20 MeV, in steps of 0.02 MeV. The best fit to the data was found using three peaks of 4.86 MeV, 5.28 MeV and 5.86 MeV – see **Figure 5.10**. Interestingly, note that the 4.86 MeV state does not seem to be present in the γ-gated spectrum – this is consistent with expectation, as this energy is lower than S_n(^{48}K) plus 0.360 MeV, suggesting it would likely decay directly to the ground state of ^{47}K.

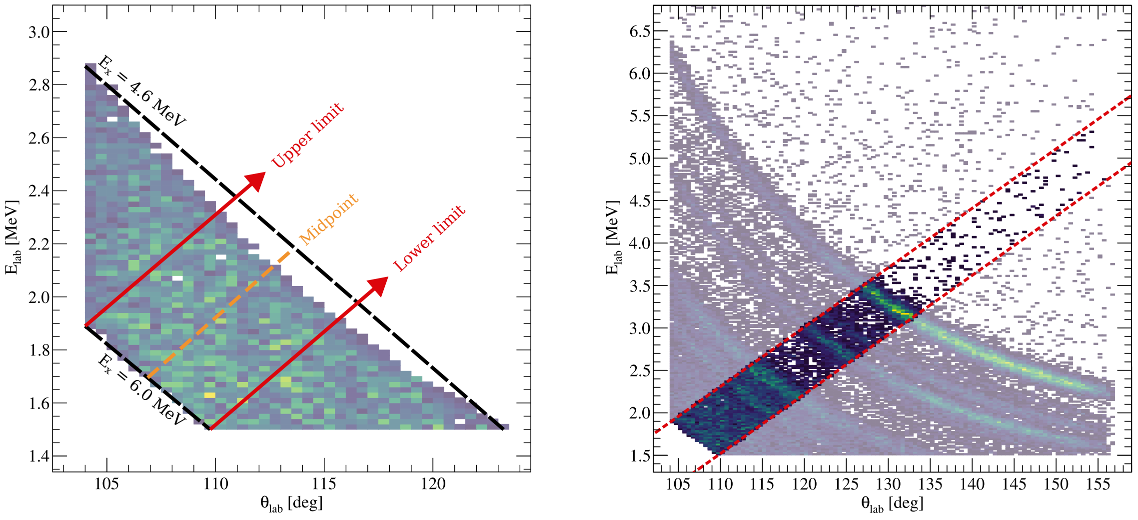

(a) Gradient of limits determined from the midpoint of lines connecting vertices of gated experimental data.

(b) Parallel gating requirements, as applied to the full data set.

Figure 5.9: Determination (a) and implementation (b) of the parallel gating requirements for unbound states. Here, the data shown requires E$_{\text{lab}}$>1.5, θ_{lab}>104, and E$_x$ < 6.0 MeV. Additionally, (a) requires E$_x$ > 4.6 MeV.

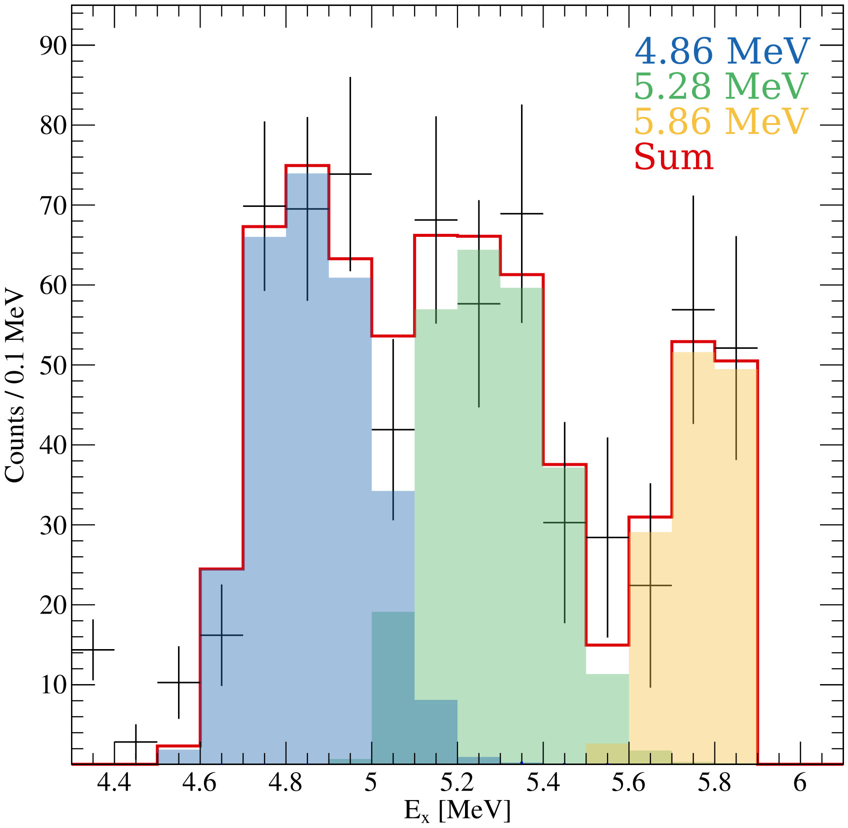

Figure 5.10: Results of the χ^2 minimisation of simulated peaks to the unbound region of strength, indicating three states at 4.86 MeV, 5.28 MeV and 5.86 MeV. Note that a hard high-energy cutoff has been applied to both the experimental and simulated data.

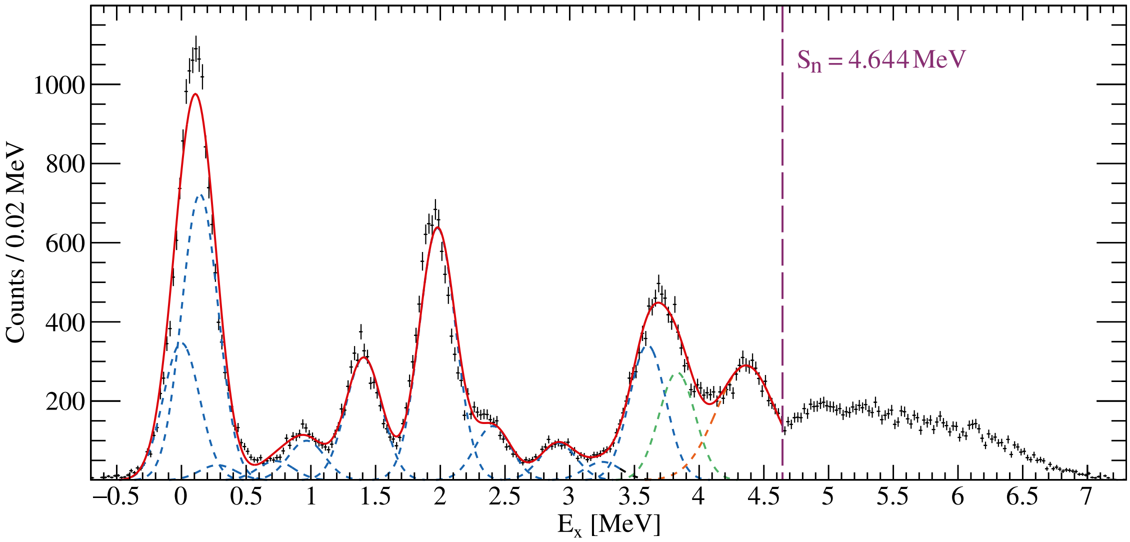

Figure 5.11: Reconstructed excitation of populated states in ^{48}K, fit with the function f_{all} using the state energies established in this work. Here, f_{all} is shown by the solid red line, with individual peaks shown with blue dashed peaks. The green dashed peak indicates the 3.8 MeV doublet, and the broad orange dashed peak indicates the fit to the > 4 MeV region.

5.1.2 Differential cross sections

With the energies of the populated states established, the full bound E_x spectrum, without γ-ray coincidence requirement, can be fit simultaneously. This is done by constructing a function of the form;

$$f_{\mathrm{all}} = \sum_{i=1}^{N_{\mathrm{states}}} h_i \exp\left(-0.5 * \left(\frac{x-\mu_i}{\sigma_i}\right)^2\right) \tag{5.1}$$

Here, each state (of which there are N_{states}) is fit by a Gaussian peak, with mean μ, height h and standard deviation σ. All values of μ are fixed to their measured value of E_x. The standard deviation of most peaks is fixed to 0.14 MeV, determined to be appropriate across the full energy range through γ-coincidence E_x spectra. The notable exception to this is the region above 4.0 MeV, which fits three states with a single Gaussian of $\sigma = 0.23$ MeV. When performing fits using this function, only the height h of the peaks is allowed to vary freely.

The function f_{all} reproduces the experimental spectrum very well[3] – as shown in **Figure 5.11** – allowing each state to be deconvoluted from the total signal. The extracted value of h for each peak i is then used to find the total area A by the standard relationship

$$A_i = \frac{h_i \sigma_i \sqrt{2\pi}}{w} \tag{5.2}$$

---

[3] Note that the signals are not necessarily perfectly Gaussian, due to various physical effects such as the finite target thickness, summing of signals from multiple detectors, etc. As the data are well-reproduced in this case, there was no need for further modification.

where w is the bin width of the histogram being fit. By this method, the total number of observed ^{47}K(d,p)^{48}K transfer events populating each of the states is measured, which indicates the total cross section σ_{meas}. Recalling Equation 2.1, this is sufficient to determine the spectroscopic factor, S, but a more revealing formulation is the *differential* cross section $\left(\frac{d\sigma}{d\Omega}\right)_{\text{meas}}$. For this, the same fitting is performed for E_x spectra with a range of θ_{lab} angle ranges.

For each bound state[4], the area of the E_x peak is found for every 2° section from θ_{lab} = 106 up to 154 degrees. Note that, for the higher energy states, large θ_{lab} angles intersect with the E_{lab} threshold, limiting the number of available angular bins. These areas are then divided by the solid angle Ω of that angular range to produce $\frac{\text{dA}}{\text{d}\Omega}$. The solid angle is determined using realistic Monte Carlo GEANT4 simulations which include the true inefficiencies in the experiment (geometry, missing strips etc) as detailed in Section 4.1.2. These simulations are performed for each populated state.

Recall Equation 4.4, which relates the differential cross section of elastic scattering to the efficiency-corrected counts by a normalising factor B [mb]. The elastic scattering data was used in that case to extract B_d and B_p for deuterons and protons respectively, encompassing the integrated incoming beam and the number of target particles. This same value of B_d is used now in order to normalise the ^{47}K(d,p) transfer reaction measurements in a wholly consistent and self-contained manner, extracting the differential cross section;

$$\frac{d\sigma}{d\Omega} = \mathrm{B_d}\frac{dA}{d\Omega} \tag{5.3}$$

This experimental differential cross section is then compared to ADWA calculations, performed with TWOFNR [48]. For each state, transfer of a neutron into the $p_{1/2}$, $p_{3/2}$ and $f_{5/2}$ orbital[5] are calculated using the Johnson-Tandy adiabatic model [50, 126] and the Koning-Delaroche [49] proton optical potential. In all cases, a qualitative visual comparison between the experimental and theoretical differential cross sections discriminates between $\ell = 1$ and $\ell = 3$ transfer unquestionably. Quantitatively, the theoretical function is scaled by a simple multiplying factor, determined by a χ^2 minimisation fit to the experimental data. This scaling factor is, by definition, the spectroscopic factor S.

$$\left(\frac{d\sigma}{d\Omega}\right)_{\text{meas}} = S\left(\frac{d\sigma}{d\Omega}\right)_{\text{calc}} \tag{2.2, revisited}$$

This process was performed for every Gaussian peak in f_{all}, and the results are shown in

---

[4] As the unbound states require a very different methodology to properly extract and fit the experimental data, the differential cross sections are determined separately from the rest of the states.

[5] Note that the differential cross sections of $p_{1/2}$ and $p_{3/2}$ transfer vary only by their magnitude, and can therefore only be distinguished by J^{π} and/or comparison to shell model calculations.

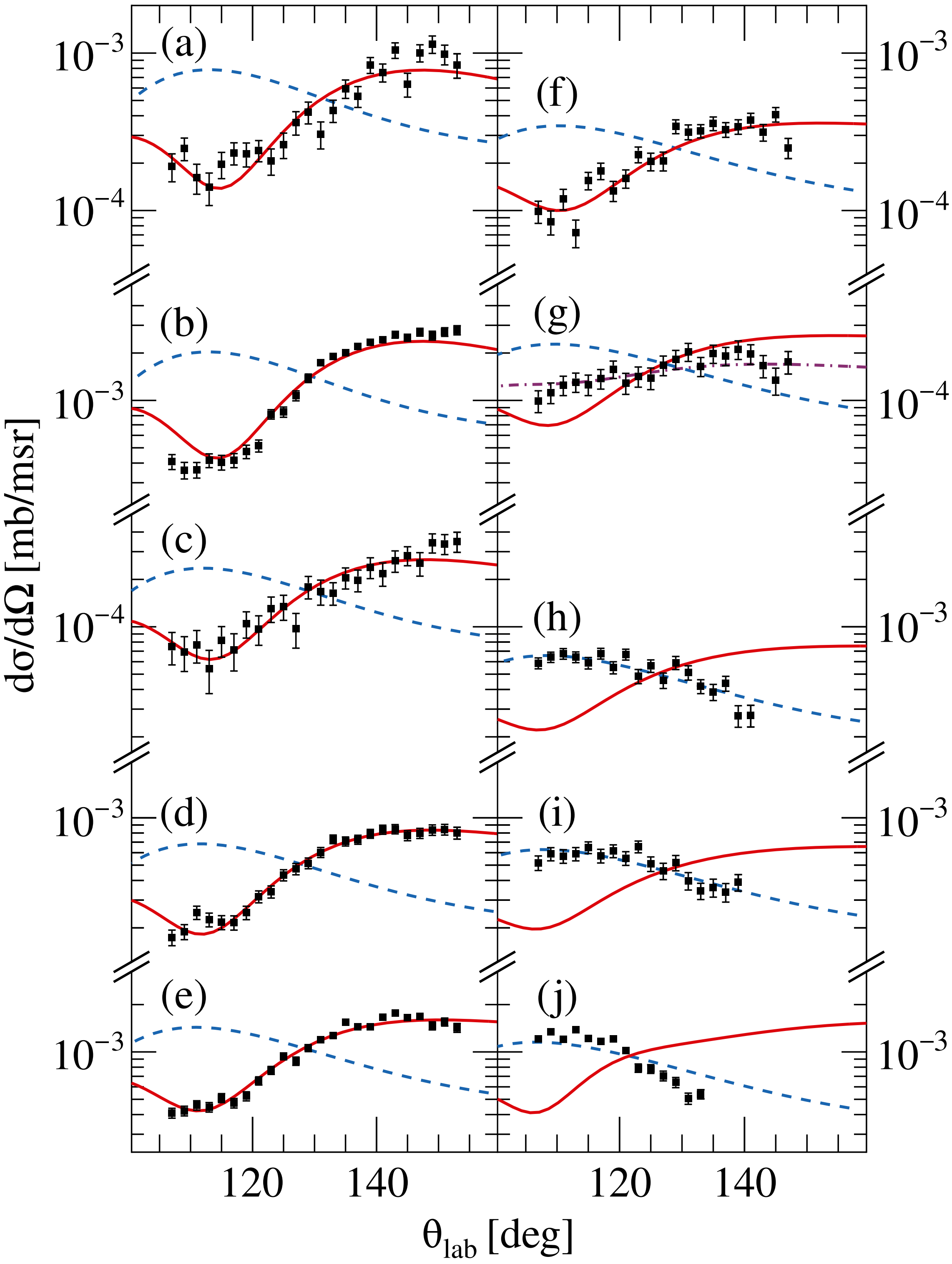

Figure 5.12: Experimental differential cross sections for ^{48}K states observed in this work, as well as the scaled theoretical differential cross sections for an ℓ = 1 (ℓ = 3) state at that energy in red (blue). Additionally, for the mixed state, 2.901 MeV, the best-fit mixing function is shown in purple. (a) 0.000 MeV, (b) 0.143 MeV, (c) 0.967 MeV, (d) 1.409 MeV, (e) 1.978 MeV, (f) 2.407 MeV, (g) 2.909 MeV, (h) 3.601 MeV, (i) 3.792 & 3.868 MeV, (j) >4 MeV region.

Figure 5.12. For the simple states, up to 3.601 MeV, this is the extent of the analysis required to determine the spectroscopic factor. The 3.8 MeV doublet and the > 4 MeV region required additional data processing to extract the spectroscopic factors, detailed in the following sections.

5.1.2.1 Non-trivial bound states

As there are two unresolvable states – 3.792 MeV and 3.868 MeV – that are fit with the same Gaussian peak, the differential cross section extracted is the sum of both states. In order to properly divide the observed strength between the two, the relative population and J^π of each state must be determined.

Both of these questions can be answered by looking to the γ-rays. First, the number of detected γ-ray events, N_{det}, in each assigned transition out of the states is found, and scaled by the AGATA efficiency, ϵ_{AGATA}, at that energy in order to determine the true number of emitted events, N_{emit}. The relative fraction of strength can then be found, as demonstrated in **Table 5.1**.

Additionally, the final states of these transitions indicate likely J^π assignments. Firstly, the undeniable f-wave nature of the transfer into these states, as shown in **Figure 5.12i**, limits the states to $J^\pi = 2^-$ or 3^-. The 3.868 MeV state decays to both the 1^-_1 ground state and 2^-_1 excited state with roughly equal branching ratios, presenting a strong argument for 2^- assignment. The 3.792 MeV state, however, decays primarily to the 2^-_2 state, with a small branch to the 3^-_1. This does not conclusively rule out either possible J^π, but the absence of a decay to the energetically-preferable 1^-_1 ground state is notable – especially as the ground state shares its predominantly $\pi s^2_{1/2} d^3_{3/2}$ structure with the two states that 3.792 MeV *is* seen to decay to [34]. This, in addition to the greater density of 3^- states in the energy region in the shell model calculations, is sufficient to assign the 3.792 MeV state to 3^-.

With these points established, the observed differential cross section can be divided by the relative fraction determined in **Table 5.1**, and properly calculated for a 2^- or 3^- state,

Table 5.1: Division of strength between 3.8 MeV doublet states in ^{48}K.

State [MeV]	Transition [MeV]	N_{det}	ϵ_{AGATA} [%]	N_{emit}	ΣN_{emit}	Rel. Frac. [%]
3.792	3.063	7 ± 3	4.45	160 ± 60	1290 ± 230	60(10)
	3.515	45 ± 7	4.00	1130 ± 170		
3.868	3.728	14 ± 4	3.80	370 ± 100	890 ± 220	40(10)
	3.868	19 ± 4	3.67	520 ± 120		

respectively. Hence, the spectroscopic factors of the 3.8 MeV doublet states have been determined.

As can be seen in **Figure 5.12j**, the 4 MeV region of states has a clear f-wave character, with no suggestion of p-wave mixing. This region is unfortunately unable to be deconvoluted in the same way as the 3.8 MeV doublet. Instead, this region is treated as a unit, with the spectroscopic factor of the region evaluated for different possible ratios of 2^- and 3^- states. If the region had purely 2^- (3^-) states, the combined spectroscopic factor of the region would be 0.45 (0.32), from which a mathematical relationship can be trivially established. This indefinite strength impacts the discussion of the $f_{5/2}$ neutron orbital, and is explored further in Section 6.3.1.

5.1.2.2 Unbound states

As established in Section 5.1.1.3, three narrow states above the neutron separation threshold have been identified through the application of two-dimensional gating requirements in E_{lab}–θ_{lab}. By taking this selective region of the data, the states are far easier to extract from the deuteron break-up phase space, but at the cost of a much restricted angular range. As such, attempts to determine the shape of the differential cross sections of these states – that is, through the use of multiple angular ranges for each state – have been unsuccessful. Instead, the whole angular range is taken for each state to provide an average determination of the spectroscopic factor. The area of each peak has already been determined in Section 5.1.1.3. An error of 10% is applied to the peak areas, owing to the uncertainty in the peak centroid energies. This was evaluated by varying the fitted peak energies by ±0.4 MeV. The solid angle coverage was determined using realistic Monte Carlo simulations with the same additional gating requirements applied, to ensure consistency between experimental and simulated data. The cross section determined for each peak is presented in **Table 5.2**.

This value must then be compared to an optical model result. While TWOFNR is unable to produce differential cross sections for unbound states, a common method is adopted

Table 5.2: Spectroscopic factors of three unbound states ^{48}K, comparing to WBNA $\ell = 3$ theoretical cross sections. Due to various significant approximations, detailed in the text, an error of 40% is applied to the spectroscopic factors.

	4.86 MeV	5.28 MeV	5.86 MeV
Area of peak	270(30)	250(30)	130(10)
$(\frac{d\sigma}{d\Omega})_{\mathrm{exp.}}$ [mb/msr]	$1.8(2) \times 10^{-4}$	$1.6(2) \times 10^{-4}$	$1.4(1) \times 10^{-4}$
S, assuming 2^-	0.07(3)	0.07(3)	0.06(2)
S, assuming 3^-	0.05(2)	0.05(2)	0.04(2)

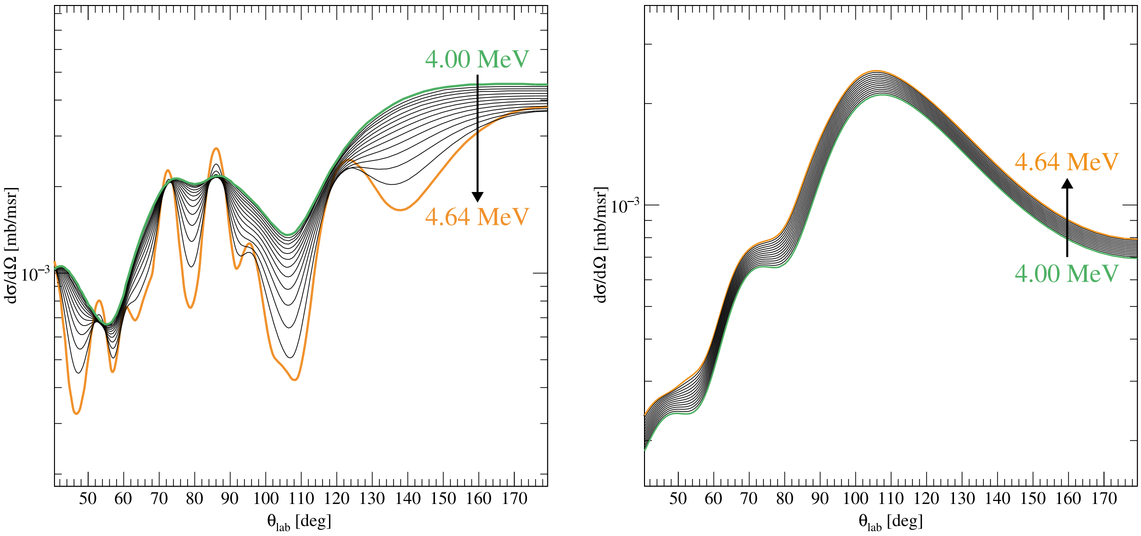

(a) Evolution of $p_{3/2}$.

(b) Evolution of $f_{5/2}$.

Figure 5.13: Evolution of the theoretical differential cross sections as E_x approaches S_n. Calculated every 0.05 MeV.

wherein the differential cross section is estimated by approximating the unbound state as bound by 1 keV. While this method, referred to as the weakly-bound neutron approximation (WBNA), is not as rigorous as the method of Vincent and Fortune (1970) [127], the comparative study of Sen *et al.* (1974) [128] found that that narrow unbound states lying close to the neutron separation threshold (in the case of their work, less than 2 MeV above S_n) are well-approximated by weakly bound states. As the three states in ^{48}K are unbound by between 0.2 MeV and 1.2 MeV, the WBNA method is deemed appropriate.

The differential cross sections determined using this method are shown in **Figure 5.13**. While the $\ell = 3$ differential cross section is consistent with the shape of the other states investigated in this work, the $\ell = 1$ calculation shows extreme sensitivity to the binding energy. The severe change in shape between a 4.00 MeV state and a 4.64 MeV state, shown in **Figure 5.13a**, results in such a small cross section in the $\theta_{\text{lab}} = 104°$ to $115°$ region that the spectroscopic factor for each unbound state would be approximately 0.5; this is not a credible result. Given the rapid variation with excitation energy, and the significant gradient in the region of experimental interest, any results extracted from these $\ell = 1$ differential cross sections would likely be spurious.

While there is no discrimination between $\ell = 1$ or $\ell = 3$ for the unbound states, recalling the shell model calculations presented in Section 2.4.1, it can be said that states in this high-energy region are most likely $f_{5/2}$ in character.[6] It is fortuitous, therefore, that the $\ell = 3$ WBNA predictions do not suffer from the same volatility as $\ell = 1$, as shown in **Figure 5.13b**. Additionally, the spectroscopic factors derived from the WBNA, assuming $\ell = 3$, are of a more reasonable order of magnitude; see **Table 5.2**. An error of 40% has

---

[6] This assertion is further supported by detailed discussions in Section 6.2.2

been placed on these spectroscopic factors, owing to the peak areas (10%, as previously mentioned), the phase space subtraction (5%), the variation of $\ell = 3$ differential cross sections due to excitation energy (5%), and the error associated with the choice of optical model (20%). While the analysis of these states is limited, the possible influence of these unbound states is addressed in Section 6.3.2.

5.1.3 Excited structure of ^{48}K

Through this experimental analysis, a comprehensive level scheme of ^{48}K, as populated by ^{47}K(d,p), has been determined. This can be seen in **Figure 5.14**, and is detailed in **Table 5.3**. In this work, 12 new bound states and three unbound states have been identified, with 21 new transitions. Critically, this work has also firmly determined the ℓ-transfer assignment and spectroscopic factors for each of the observed states. As such, arguments for spin-parity assignments – using the combined knowledge of ℓ-transfer and decay spectroscopy – are made for the simple states. Outcomes of the previous detailed

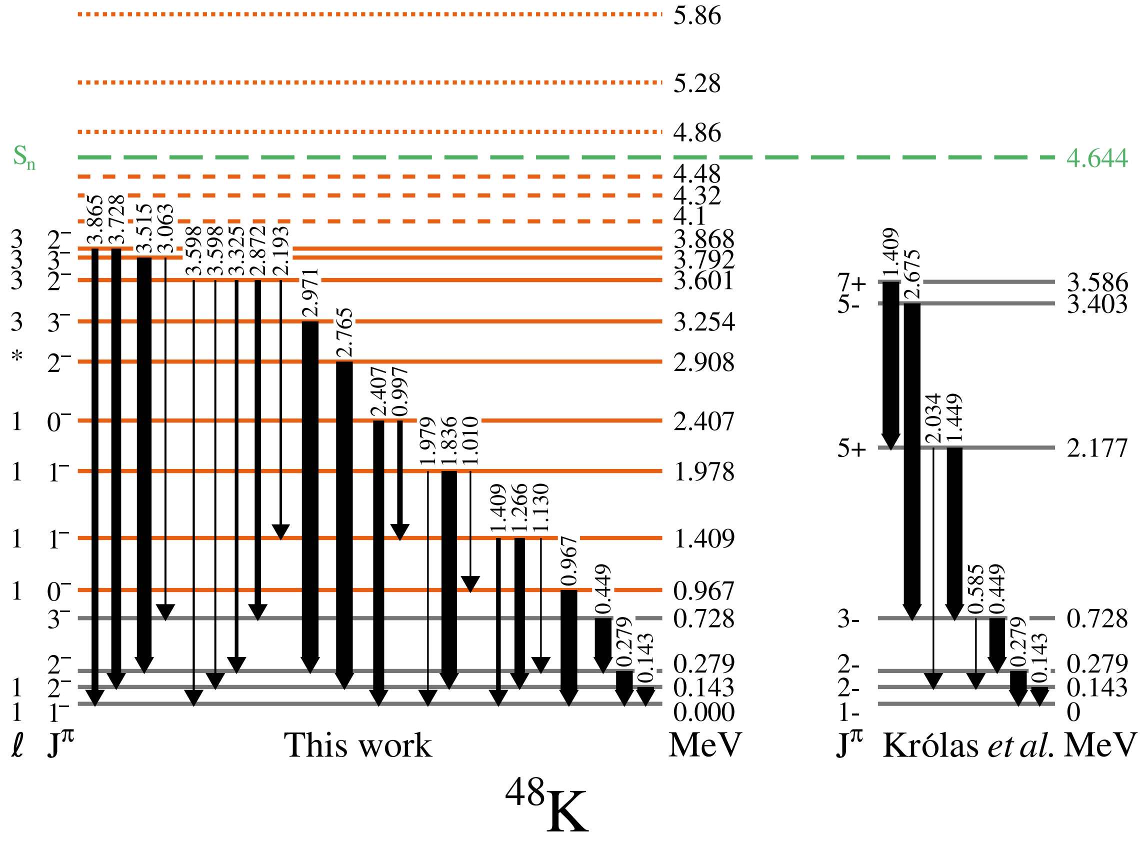

Figure 5.14: Level scheme of ^{48}K as determined in this work, compared to literature [34]. Previously known states are in black, with new states in orange; solid lines indicate states with energy derived from γ-rays, dashed lines indicate energy taken directly from E$_x$ spectra, and dotted lines indicate unbound states. The γ-ray transitions are labelled with their energy, with the thickness of the arrow indicating their branching ratio. The state marked with an asterisk is mixed $\ell = 1 + 3$ configuration.

arguments relating to the complex states are summarised.

Recall that the three orbitals that the transferred neutron may enter can produce only two spins when coupled to the $s_{1/2}$ proton; $\nu p_{1/2}$ can produce 0^- and 1^- states, $\nu p_{3/2}$ can produce 1^- and 2^-, and $\nu f_{5/2}$ can produce 2^- and 3^-. Notably, only 2^- states have the capability to have both p-wave ($\ell = 1$) and f-wave ($\ell = 3$) strength.

Of the previously observed states, only the 1^-_1 ground state and the first excited 2^-_1 state at 0.143 MeV are populated with significant intensity in this reaction. Both states have strong $\ell = 1$ character, consistent with their known J^π assignments. Upper limits have been placed on the spectroscopic factors of other previously observed states, 0.279 MeV ($S < 0.03$) and 0.728 MeV ($S < 0.04$), by comparison of their maximum possible cross section to states measured in this work.

The 0.967 MeV, 1.409 MeV, 1.978 MeV and 2.407 MeV states all exhibit $\ell = 1$ character, limiting their possible assignments to 0^-, 1^- or 2^-. The 0.967 MeV and 2.407 MeV states decay exclusively only to the 1^- ground state, characteristic of 0^- states. The 1.409 MeV state decays primarily to the 2^-_1, with weaker decays to the 2^-_2 and 1^-_1, indicative of a 1^- state. The 1.978 MeV state decays almost entirely to the 2^-_1, with weaker decays to 0^-_1 and 1^-_1, providing a confident 1^- assignment. The 2.908 MeV state is unique amongst this data, in that it exhibits a mixed character. As only 2^- states can exhibit mixed character, a firm spin-parity assignment is made.

The remaining states all show clear $\ell = 3$ character, and as such can only be 2^- or 3^-. Only one transition was observed from the weakly-populated 3.254 MeV state, decaying to the 2^-_2 state, making a 3^- assignment likely. The 3.601 state is the most strongly populated $\ell = 3$ state, and decays primarily to 1^-, 2^- and 3^- states, indicating a 2^- assignment to be most probable. Arguments for the remaining “complex” states have already been discussed; that is, 3.792 MeV seems to be 3^-, 3.868 MeV is convincingly 2^-, and the distribution of 2^- and 3^- states in the high-energy multiplet is ambiguous.

Table 5.3: Details of the ^{48}K states observed in this work, including γ-ray transitions, neutron orbital occupation and spectroscopic factors.

E_x [MeV]	J^π	E_γ [MeV]	BR [%]	J^π_f	nl_j	S^{stat}_{syst}
0.000	1^-_1	—	—	—	$2p_{3/2}$	0.237^{8}_{47}
0.143(1)	2^-_1	0.143(1)	~100	1^-_1	$2p_{3/2}$	0.418^{6}_{84}
0.279(1)	2^-_2	0.279(1)	~100	1^-_1	$2p_{3/2}$	< 0.03
0.728(2)	3^-_1	0.449(1)	~100	2^-_1	$1f_{7/2}$	< 0.04
0.967(2)	0^-_1	0.967(2)	~100	1^-_1	$2p_{1/2}$	0.257^{10}_{51}
1.409(2)	1^-_2	1.130(3)	10(2)	2^-_2	$2p_{3/2}$	0.241^{4}_{48}
		1.266(2)	63(2)	2^-_1		
		1.409(3)	28(1)	1^-_1		
1.978(2)	1^-_3	1.010(4)	5(1)	0^-_1	$2p_{1/2}$	0.499^{6}_{100}
		1.836(3)	93(2)	2^-_1		
		1.979(3)	2(1)	1^-_1		
2.407(4)	0^-_2	0.997(4)	33(2)	1^-_2	$2p_{1/2}$	0.344^{9}_{69}
		2.407(5)	67(7)	1^-_1		
2.908(7)	2^-_3	2.765(7)	~100	2^-_1	$2p_{3/2}$	0.023^{2}_{5}
					$1f_{5/2}$	0.062^{6}_{12}
3.250(4)	3^-_2	2.971(4)	~100	2^-_2	$1f_{5/2}$	0.058^{6}_{12}
3.601(3)	2^-_4	2.193(3)	15(4)	1^-_2	$1f_{5/2}$	0.341^{8}_{68}
		2.872(7)	38(7)	3^-_1		
		3.325(4)	22(5)	2^-_2		
		3.458(7)	12(4)	2^-_1		
		3.598(7)	12(4)	1^-_1		
3.792(4)	3^-_3	3.063(2)	12(4)	3^-_1	$1f_{5/2}$	0.164^{4}_{33}
		3.516(7)	88(4)	2^-_2		
3.868(6)	2^-_5	3.727(6)	59(9)	2^-_1	$1f_{5/2}$	0.140^{4}_{28}
		3.865(8)	41(9)	1^-_1		
Multiplet	(2^-)	—	—	—	$1f_{5/2}$	0.452^{8}_{90}
	(3^-)	—	—	—		0.323^{6}_{65}

5.2 ^{47}K(d,t)^{46}K

5.2.1 Excited states and transitions

Once the additional requirements for triton selection are applied, the results of ^{47}K(d,t) are treated in much the same way as ^{47}K(d,p). The reconstructed excitation spectrum – seen in **Figure 5.15** – shows the ^{46}K states that were observed in this work, fit using the same methodology described in the previous section with only two notable changes:

Background While every effort has been made to remove random background events from this spectrum, some still remain. This is treated as a flat background, fit to the region above 5 MeV where no significant strength is observed.

Resolution While the states in the (d,p) excitation spectrum had peaks of width σ = 0.14 MeV, the (d,t) resolution is slightly larger, measured to be σ = 0.18 MeV.

The states were isolated through γ-ray coincidence, as discussed previously. The particle-γ coincidence matrix for ^{46}K can be found in **Figure 5.16**. While most states were trivial to extract using this method[7], there are two pairs of unresolved doublet states, and a pair of weak states that are treated uniquely.

The first pair – 0.587 MeV and 0.691 MeV – were already known to exist in the literature [42], and have been well-resolved in the past when studied via multi-nucleon transfer in normal kinematics [36, 39, 129]. Both states appear to be populated in this work, as the high-energy side of the E_x peak has γ-ray coincidences consistent with the known decays of 0.691 MeV, and the low-energy side of the peak is similarly consistent with 0.587 MeV.

A second pair of states – observed here at 3.344 MeV and 3.410 MeV – were also expected from the literature, but no γ-ray transitions from these states had previously been observed. The 3.4 MeV region is strongly populated, however, and two clear transitions out of this state can be seen at 1.111 MeV and 1.177 MeV. Both transitions present only one E_x coincidence peak, at 3.4 MeV. Using the same summation arguments as in Section 5.1.1.1, the presence of only one state in the region of 2.2 MeV as a viable final state for these transitions suggests there may be a doublet. This is confirmed by turning to the unpublished[8] results of a high-statistics γ-ray study of ^{46}Ar β^{-} decay. In that study, the 1.111 MeV and 1.177 MeV γ-rays were indeed found to be coincident with the known 0.288 MeV transition out of the 2.232 MeV state. As such, a doublet is established.

---

[7] Spectra relating to the analysis of these simple states can be found in Appendix B.2

[8] E. Clément (personal communication).

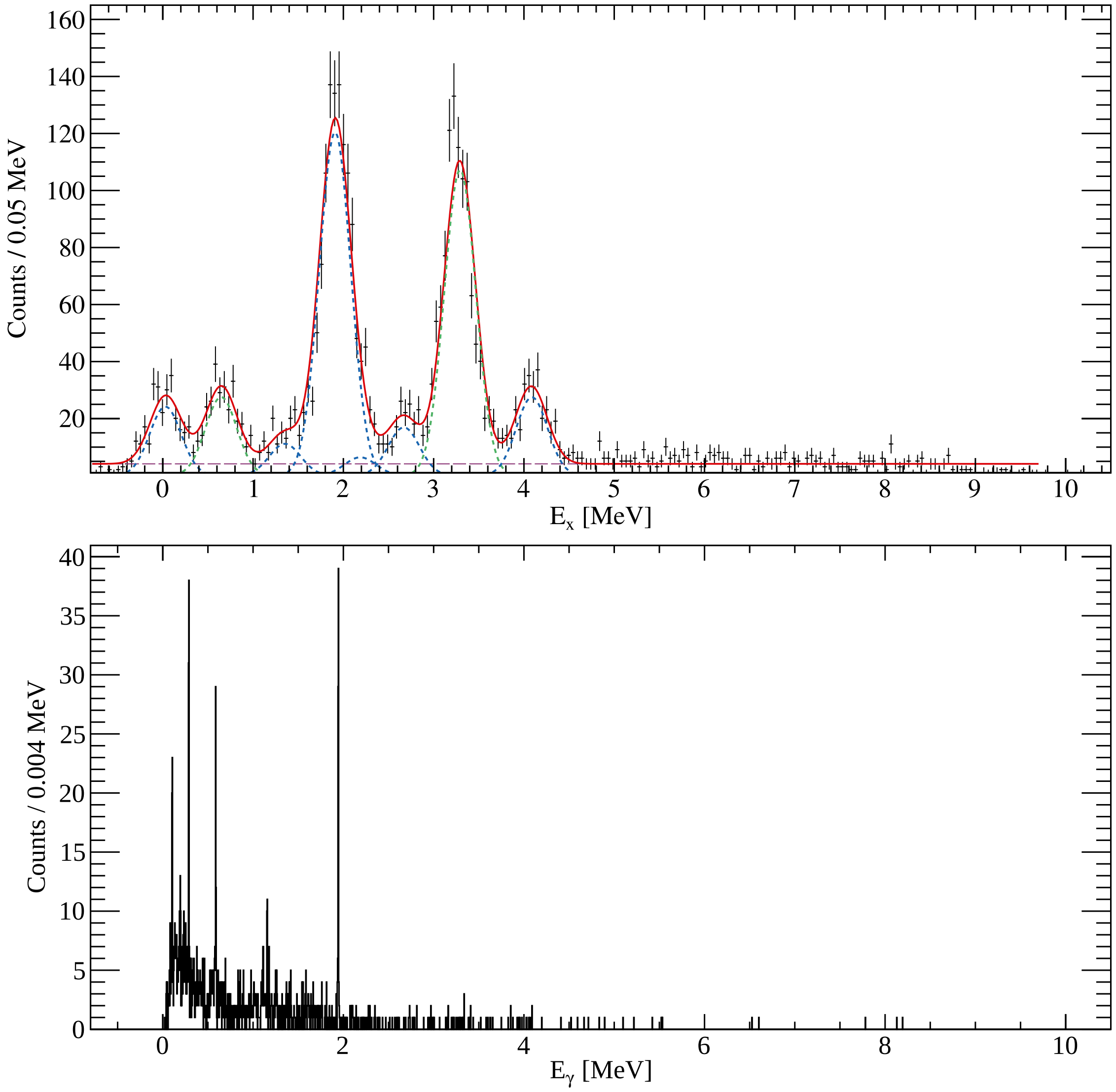

Figure 5.15: Reconstructed excitation of populated states (top) and coincident γ-rays (bottom) in ^{46}K. The E_x spectrum is fit with the function f_{all} (solid red line) and a flat background (dashed purple line) which has been fit to the high-energy region. Individual states are shown with blue dashed peaks. The green dashed peaks indicate irresolvable doublets at 0.6 MeV and 3.4 MeV.

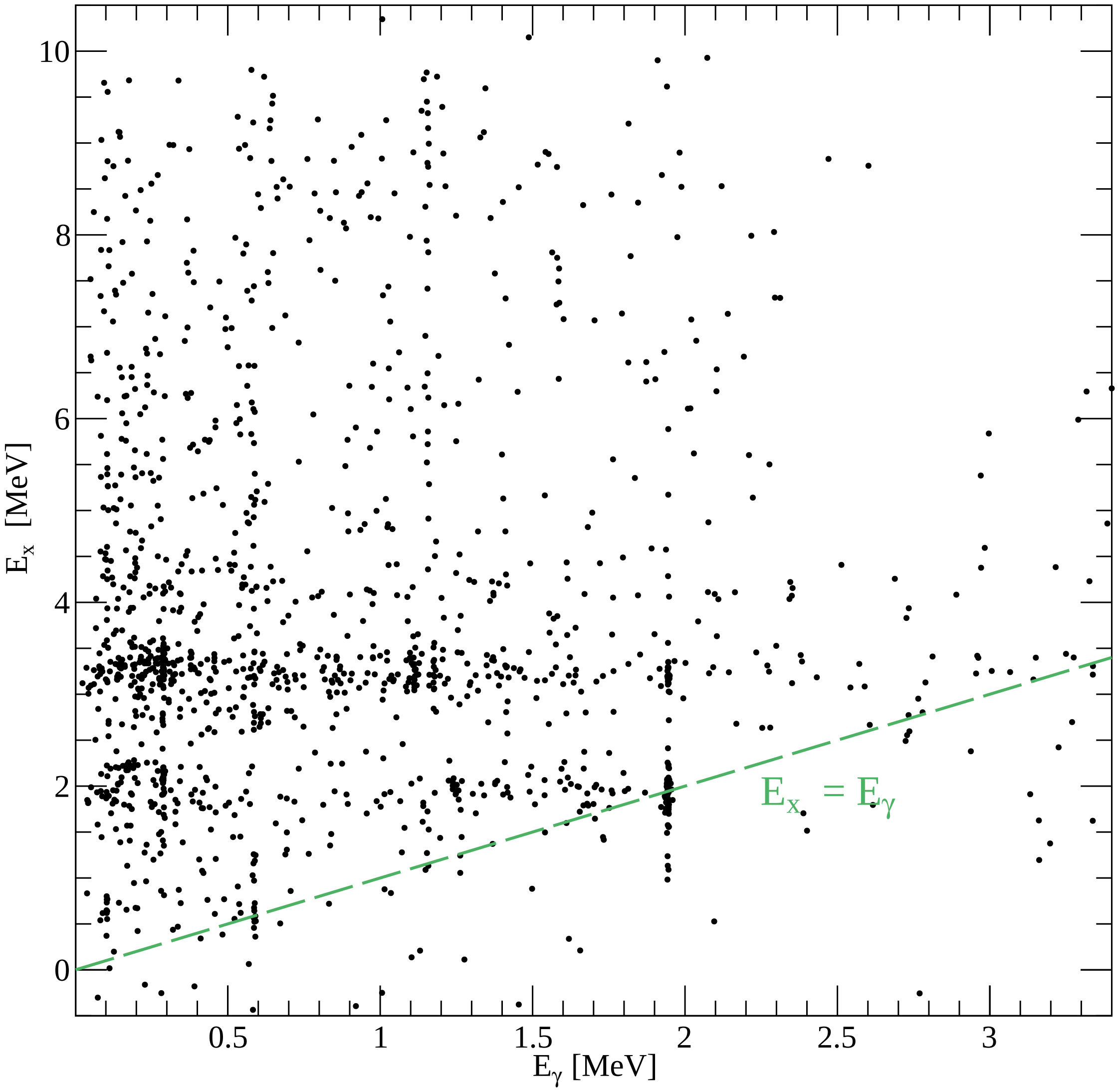

Figure 5.16: Observed ^{47}K(d,t)^{46}K excitation and γ-ray transition coincidences. The line of excitation-decay unity is indicated in green. Note that there is no neutron separation energy imposing an 'upper limit' on the excitation populated by this reaction. Interestingly, there appear to be γ-ray coincidences in the region of E$_x$>5 MeV, however the strength is very broad. No states were able to be identified in the region.

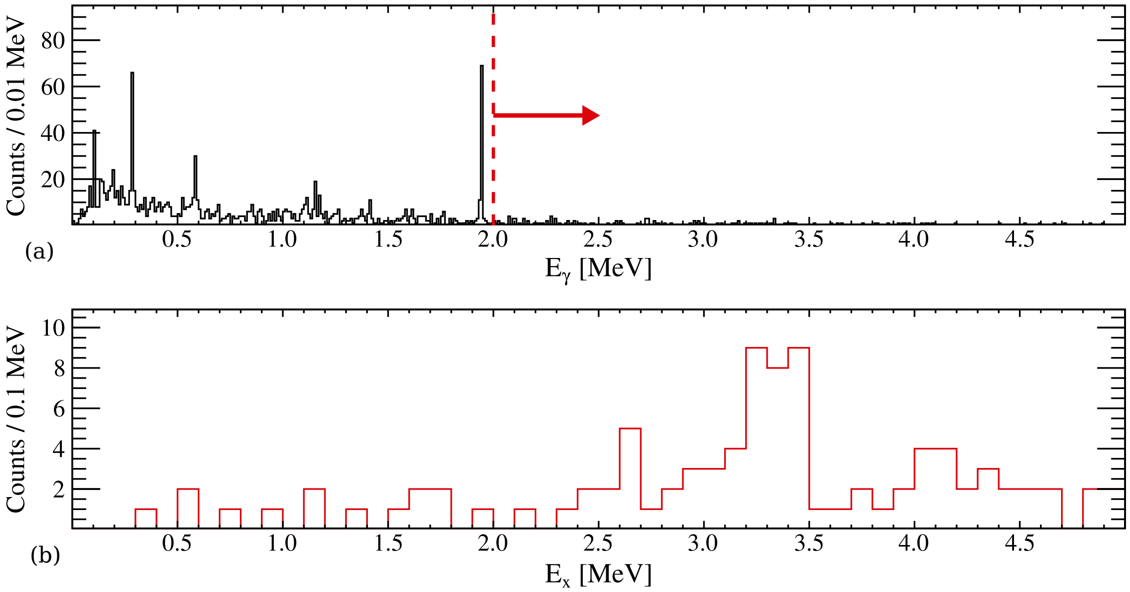

Figure 5.17: Particle-γ coincidence spectrum of high-energy γ-ray transitions in ^{46}K. (a) γ-ray spectrum, showing the gating region $E_\gamma > 2.0$ MeV. (b) Excitation spectrum, showing some coincidences with the 3.4 MeV doublet and the 4.2 MeV state.

Finally, possible high-energy decays are investigated. As the γ-ray spectrum of ^{46}K has very few counts above 2 MeV, as shown in **Figure 5.15**, a broad coincidence requirement of $E_\gamma > 2.0$ MeV is applied. This requirement, shown in **Figure 5.17**, reveals what appear to be coincidences with the 3.4 MeV doublet and the 4.2 MeV peak. As there is no definite γ-ray energy, it is unclear whether one or both of the doublet states is decaying via some high-energy transition, so no tentative transition is assigned from this analysis. The possible 4.2 MeV transition is more revealing, as this peak does not have any clear coincidences with the established low-energy γ-ray transitions. If the 4.2 MeV state decays via a transition of more than 2 MeV, then it must be to a state below 2.2 MeV. As the 4.2 MeV state is not in coincidence with any of the known transitions from 2.233 MeV or below, this suggests that this state may primarily decay directly to the ground state. As such, a tentative transition is established.

With the state energies and transitions determined, the focus turns again to the differential cross sections of each populated state.

5.2.2 Differential cross sections

The experimental and calculated differential cross sections were determined using the same methodology used for ^{47}K(d,p) (described in detail in Section 5.1.2) and are shown in **Figure 5.18**. There are additional complicating factors for the ^{47}K(d,t) cross sections, however, such as the overall lower number of counts, the reduced angular coverage of downstream detectors, and the wider variety of possible ℓ-transfers. The combination of these challenges means that these neutron orbital determinations are less obviously clear-cut than their ^{47}K(d,p) counterparts.

Take, for example, the 0.6 MeV doublet; **Figure 5.18b**. Here, the data does not lie wholly along one theoretical curve, and appears close to both p-wave (red) and f-wave (blue). Nevertheless, there are three checks that are performed;

Experiment Comparing the experimental and theoretical curves is, as always, the first step. In the case of the 0.6 MeV doublet, the data is most akin to the $\ell = 1$ and $\ell = 3$ curves.

Literature The existing literature provides a useful guide for this work, as J^{π} assignments restrict the possible ℓ-transfer to only one option, in many cases. This is the case for the 0.6 MeV doublet, as the 3^- and tentative 4^- assignments limit the possible configuration to $f_{7/2}$ character *only*.

Shell model Finally, the tentative ℓ-transfer derived from the previous steps is compared to the shell model calculations – is there a clear candidate for a state at this energy, with this structure? In this example, the shell model does predict two low-lying states with $f_{7/2}$ character.

With these three steps completed, and their results in concordance, the 0.6 MeV doublet is assigned as $f_{7/2}$ character. This process is repeated for each observed state.

5.2.2.1 Mixed configuration states

In this reaction, the only configuration mixing available is between $s_{1/2}$ and $d_{3/2}$ to form 1^+ states. As such, the tentative 1^+ state 1.944 MeV was investigated for this possibility. The state has very clear $s_{1/2}$ character, as seen in **Figure 5.18d**, with no indication of $d_{3/2}$ contribution at large θ_{CM}, where an effect would be most noticeable. For the 3 MeV doublet in **Figure 5.18g**, however, a small deviation from the $s_{1/2}$ character can be seen at the largest angles, consistent with a mixed configuration for one of the states. The 4.2 MeV state (**Figure 5.18h**) also exhibits a convincing mixed character, as none of the four possible unmixed calculated lines provides a satisfactory agreement with the experimental data at high θ_{CM} angles. As this 4.2 MeV state is observed for the first time in this work, there is no literature spin-parity – this result, however, is strong evidence to support a 1^+ assignment.

Critically, the relatively flat shape of the $d_{3/2}$ differential cross section leads to imprecise determination of the contribution of $\ell = 2$ to mixed configuration differential cross sections. As such, there is an additional 25% error on the $d_{3/2}$ spectroscopic factors in mixed states.

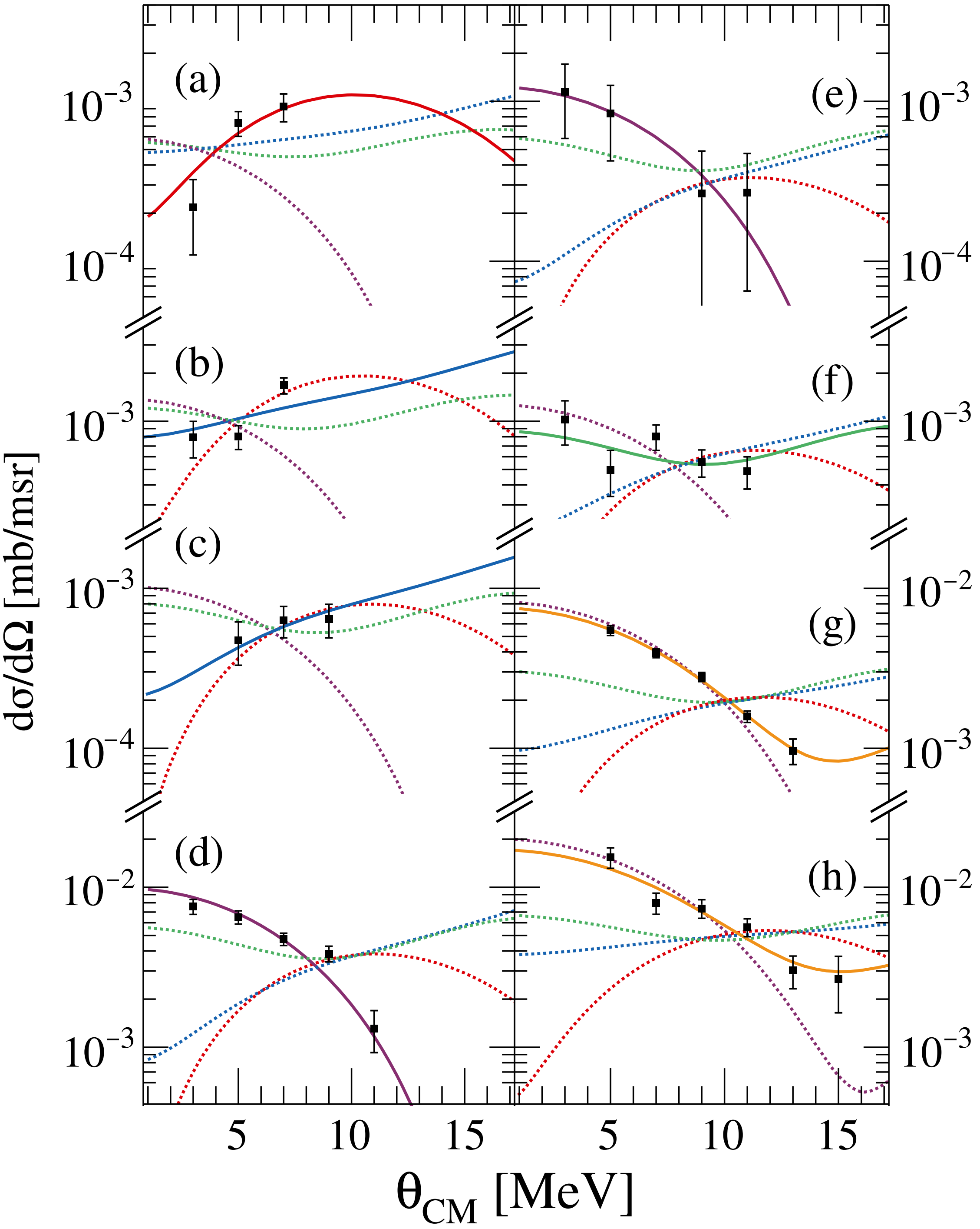

Figure 5.18: Experimental differential cross sections for ^{46}K states observed in this work, as well as the scaled theoretical differential cross sections fora state at that energy with $\ell = 0$ (purple), $\ell = 1$ (red), $\ell = 2$ (green) or $\ell = 3$ (blue). Additionally, for the mixed states, the best-fit $\ell = 0 + 2$ mixing function is shown in orange. (a) 0.000 MeV, (b) 0.587 & 0.691 MeV, (c) 1.0 to 1.8 MeV region, (d) 1.944 MeV, (e) 2.232 MeV, (f) 2.732 MeV, (g) 3.344 MeV & 3.410 MeV, (h) 4.20 MeV.

5.2.2.2 Doublet states

As with ^{48}K, γ-ray spectroscopy can provide a window into the division of strength for doublet states in ^{46}K. For the 0.587 MeV and 0.691 MeV doublet, the only decays observed in this experiment are 0.691 MeV to 0.587 MeV, and then 0.587 MeV to the ground state, however the small number of observed γ-ray counts places a severe limitation on this process. Several approaches were taken: (i) by gating on the E_x spectrum and looking at γ-ray coincidences, (ii) by gating on E_γ and looking at particle coincidences, and finally (iii) by looking only at the E_γ spectrum without E_x gating. The first two methods produced relative fractions with very large errors, where the 0.587 MeV state took 50(40)% and 60(40)% of the strength, respectively. The final method is more precise, with the 0.587 MeV state taking 70(20)% of the strength. Critically, however, neither the first nor last method cannot account for possible strength 'lost' to the alternative 0.691 MeV ground-state decay, which is present in the literature but is not observed in this experiment. As such, division of the $\ell = 3$ strength between 0.587 MeV and 0.691 MeV remains undetermined in this work.

The 3.4 MeV doublet also present a challenge, as the spectroscopic factor is mixed, with $S(s_{1/2}) = 0.94(7)$ and $S(d_{3/2}) = 3(1)$. As the shell model predicts one 0^+ and one 1^+ state in this region, it can be assumed that the $\nu d_{3/2}$ strength lies solely in the 1^+ state, with the remaining $\nu s_{1/2}$ strength divided between the two. The relative contributions of the two configurations to the mixed differential cross section were determined, by integrating the theoretical curves in the experimental θ_{CM} range, to be 81.5% and 18.5% for $s_{1/2}$ and $d_{3/2}$, respectively, and the ratio of 3.344 MeV strength to 3.410 MeV strength was determined, by the usual γ-ray comparison, to be 50(20)% for both states. Unfortunately, the results of this experiment cannot determine which of the two states is the 1^+ state. While the shell model predicts the 0^+ state to be higher in energy, it incorrectly predicts the ordering of the other 0^+ - 1^+ pair, 2.232 MeV and 1.944 MeV, and hence cannot be used to firmly discriminate between the two. Attempts to compare the γ-gated differential cross sections of the two states failed due to limited statistics. As such, the distribution of strength between these states is also undetermined, but could be resolved by future work to determine the spin-parities of the two states.

5.2.3 Excited structure of ^{46}K

The level scheme established through this work is compared to the established literature in **Figure 5.19**. While several new transitions have been observed, there are some established transitions that are not present in the current work.

Two of the known states, 1.370 MeV and 1.738 MeV, present a challenge in this work.

While these states have been previously observed, and we would expect to populate 3^- and 4^- states such as these, there is no conclusive evidence that they are populated in this work. There is a small excess of counts, above background, in the excitation energy region between 0.7 MeV and 1.9 MeV, but the γ-ray transitions in coincidence with this region do not correlate with the known decays of 1.370 MeV and 1.738 MeV states[9]. In addition, if peaks in this region are included in the fitting, the differential cross section – shown in **Figure 5.18c** – has a shape consistent with $\ell = 3$ assignment (i.e. 3^- or 4^-), but not exclusive of $\ell = 1, 2$. The spectroscopic factor of this region, if taken to be $\ell = 3$, is $\mathrm{S} = 6(1)$. It should be noted that this reaction is unlikely to populate new low-lying states that were not observed in the many extensive ^{48}Ca(d,α) and ^{48}Ca(p,^{3}He) studies performed in the 1970's [36–39, 41, 129]. Despite this, as there is no conclusive evidence of population, this region is excluded from the analysis and discussion of this work.

The remaining observed states are far clearer in their interpretation. All differential cross sections are consistent with the literature spin-parities, and ℓ-transfer assignments are largely in agreement with previous transfer reaction studies. The exception to this is the 1.945 MeV state, which is consistent with a pure $\ell = 0$ transfer in this experiment, but has been assigned as a mixed $\ell = 0 + 2$ state in previous multi-nucleon removal experiments, most convincingly by Daehnick *et al.* (1974) [129]. This could be due to the limited angular range of the ^{46}K measurement, as the $\ell = 0$ and $\ell = 2$ theoretical differential cross sections become increasingly divergent at θ_{CM} angles just larger than the experimental range.

The two most critical results of this ^{46}K analysis are;

Ground state The spectroscopic factor for $\ell = 1$ transfer into the ^{46}K ground state is found to be small, as predicted by the shell model. This suggests that the beam nucleus, $^{47}\mathrm{K}_{\mathrm{g.s.}}$, has a small population of the $\nu(\mathrm{p}_{3/2})$ orbital across the $N = 28$ shell gap, but one which is consistent with expectation. This result is significant in the following chapter.

4.2 MeV state A new state has been observed at 4.2 MeV. While no firm transitions can be established, there is sufficient evidence to suggest that this state decays primarily to the ground state. The differential cross section is convincingly $\ell = 0 + 2$, which sufficiently defines the spin-parity of the state as 1^+. This is consistent with a possible dominant decay to the 2^- ground state.

---

[9] That is, there are some coincident counts around $\mathrm{E}_\gamma = 1.151$ MeV and 0.679 MeV, the two established transitions from these states, but there are no coincident counts around 0.587 MeV, which should be fed by these decays.

Table 5.4: Details of the ^{46}K states observed in this work, such as γ-ray transitions and spectroscopic factors. The tentative transition from 4.2 MeV is italicised. Note that the mixed $d_{3/2}$ spectroscopic factors have an additional 25% error.

E_x [MeV]	J^π	E_γ [MeV]	BR [%]	J^π_f	nl_j	S ± syst
0.000	2^-_1	—	—	—	$2p_{3/2}$	0.13 ± 0.03
0.586(3)	3^-_1	0.586(3)	~100	2^-_1	$1f_{7/2}$	8 ± 2
0.690(5)	4^-_1	0.104(2)	~100	3^-_1		
1.945(3)	1^+_1	1.945(3)	~100	2^-_1	$2s_{1/2}$	0.5 ± 0.1
2.233(5)	0^+_1	0.288(2)	~100	1^+_1	$2s_{1/2}$	0.11 ± 0.02
2.730(6)	2^+_1	2.730(6)	~100	2^-_1	$1d_{3/2}$	2.7 ± 0.5
3.345(8)	—	1.112(3)	~100	0^+_1	†	
3.409(7)	—	1.176(2)	~100	0^+_1		
4.2(2)	1^+_3	*4.2(2)*	—	2^-_1	$2s_{1/2}$	0.33 ± 0.07
					$1d_{3/2}$	1.6 ± 0.7

†$2s_{1/2} = 0.94 \pm 0.07$ and $1d_{3/2} = 3 \pm 1$, analysed as an unresolved doublet.

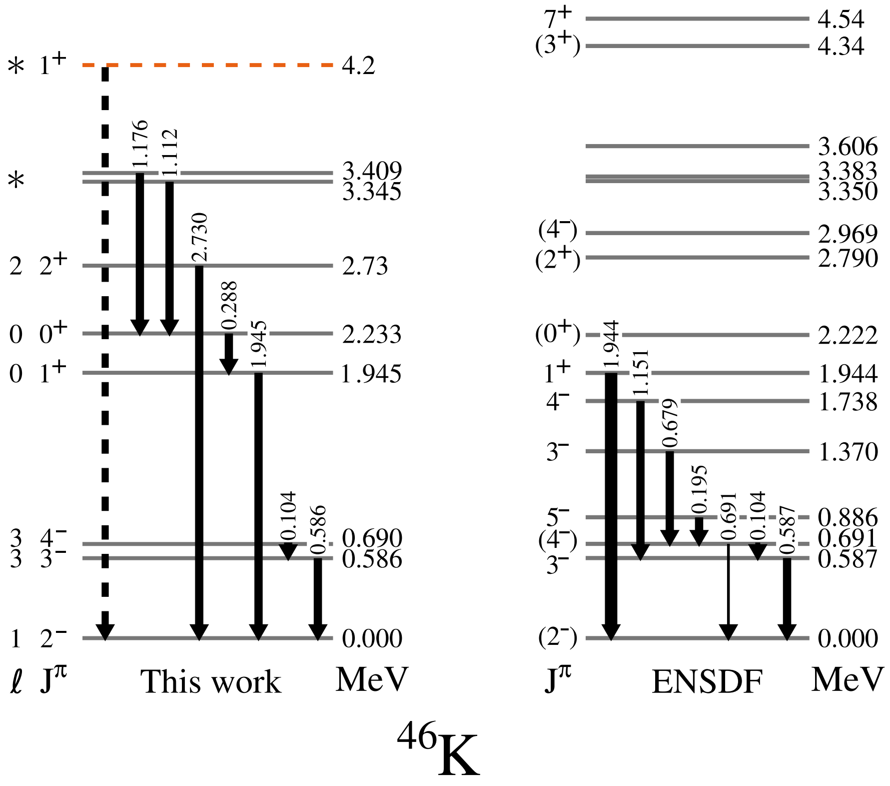

Figure 5.19: Level scheme of ^{46}K as determined in this work to literature [42]. New states are in orange, solid lines indicate states with energy derived from γ-rays, and dashed lines indicate energy taken directly from E_x spectra. The γ-ray transitions are labelled with their energy, with the thickness of the arrow indicating their branching ratio. Dashed transitions are tentative. States marked with an asterisk are mixed $\ell = 0 + 2$ configuration.

Chapter 6

Discussion

The outcomes and implications of the ^{47}K(d,p)^{48}K and ^{47}K(d,t)^{46}K results determined through this work are presented in this chapter. This chapter begins by comparing the experimental results of each transfer reaction to the shell model calculations in Section 6.1. This comparison raises an issue, in that the ^{47}K(d,p) experimental spectroscopic factors are significantly reduced relative to the shell model predictions. This issue is then discussed in more detail in Section 6.2, and an apparent relationship between the reduced spectroscopic factors and the calculated proton configuration is explored. In Section 6.3, the weighted average energies of the neutron orbitals are discussed, and the experimental results are used to indicate specific failings in the shell model predictions. The implications of these relative neutron orbital energies, in the context of shell evolution in the region 'southeast' of ^{48}Ca, are discussed in Section 6.4. Finally, possible directions for future works are presented in Section 6.5.

6.1 Comparison to shell model calculations

6.1.1 Interpretation of ^{48}K results

In this work, a comprehensive level scheme of ^{48}K, as populated by ^{47}K(d,p), has been determined. More critically, this work has also firmly determined the ℓ-wave transfer assignment and spectroscopic factors for each of the observed states. These results are compared to the SDFP-U and SDPF-MU shell model calculations in **Figure 6.1**. This comparison reveals several key successes and failures of the shell model.

$\ell = 1$ states Consistent with previous shell model calculations [30, 34], both SDPF-MU [55, 63] and SDPF-U [32] incorrectly predict a 1^- ground state in ^{48}K. The failure of the shell model to correctly reproduce ground state properties of a nucleus so close to doubly-magic ^{48}Ca is striking. This serves to reiterate the importance of theoretical improvements in this region, where πsd orbitals are degenerate. Beyond this, both models successfully describe the ordering of the remaining $\ell = 1$ states. Both predict that the

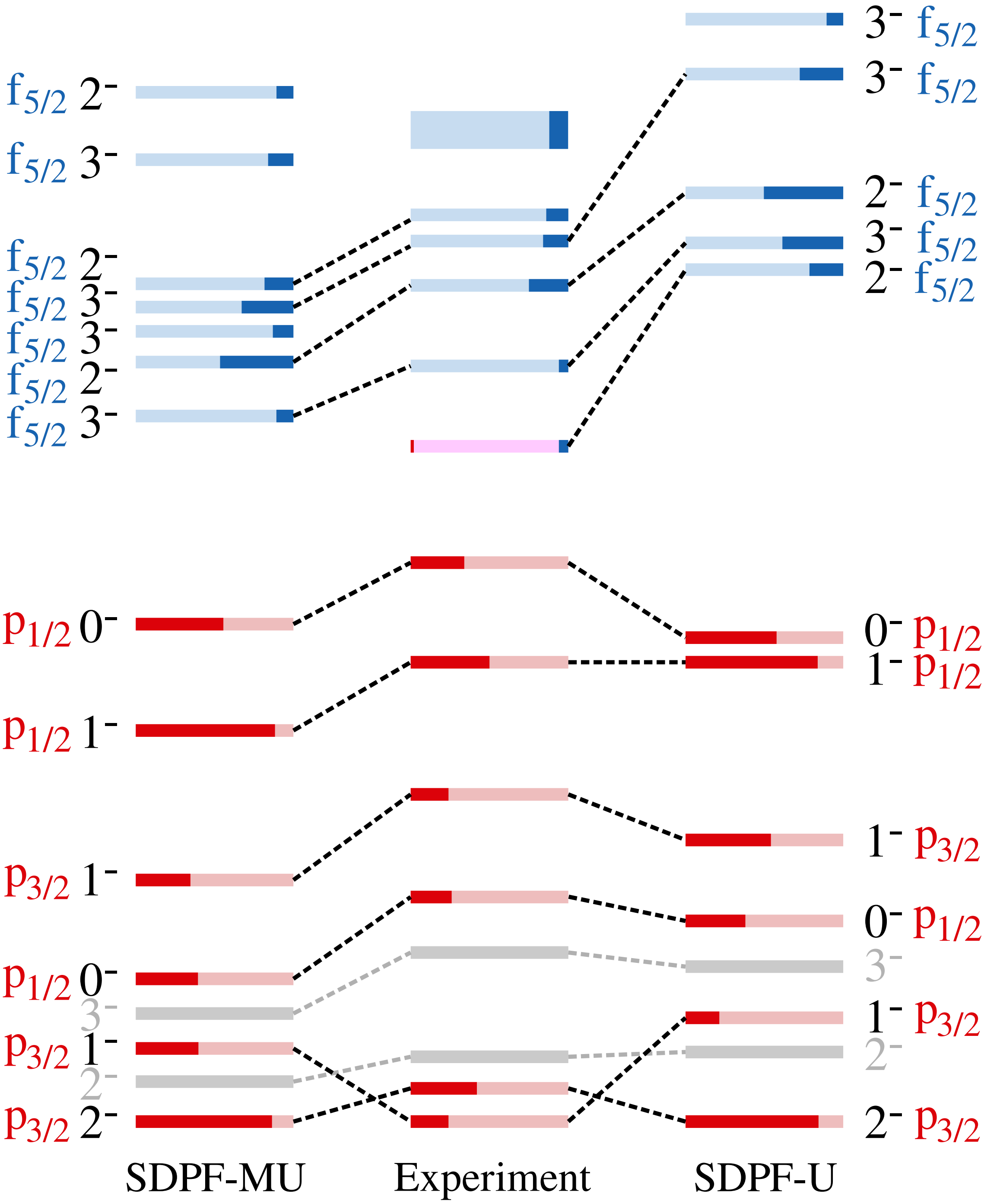

Figure 6.1: Comparison of spectroscopic factors in SDPF-MU (left) and SDPF-U (right) shell model calculations, and those measured in this work (centre). The filled length of each state line represents the spectroscopic factor, where each state has a maximum spectroscopic factor of 1. The p-wave states (red) fill from the left, and the f-wave states (blue) fill from the right. The mixed $p_{3/2}$-$f_{5/2}$ state fills from both directions.

Table 6.1: Comparison of ^{47}K(d,p) experimental results with SDPF-MU and SDPF-U shell model calculations (labelled MU and U, respectively). Experimental spectroscopic factors are presented with both the statistical error, due to fitting, and the systematic error, due to the choice of optical potential. See also **Table 5.3** in Section 5.1.3.

J^π	$E_{exp.}$	E_{MU}	E_U	$n\ell_j$	$(S_{exp})^{stat}_{sys}$	S_{MU}	S_U
1^-	0.000	0.262	0.395	$2p_{3/2}$	0.237^{8}_{47}	0.397	0.214
2^-	0.143	0.000	0.000	$2p_{3/2}$	0.418^{6}_{84}	0.864	0.843
2^-	0.279	0.220	0.340	$2p_{3/2}$	< 0.03	0.011	0.046
3^-	0.728	0.450	0.672	$1f_{7/2}$	< 0.04	0.060	0.048
0^-	0.967	0.583	0.870	$2p_{1/2}$	0.257^{10}_{51}	0.394	0.379
1^-	1.409	1.047	1.221	$2p_{3/2}$	0.241^{4}_{48}	0.347	0.541
1^-	1.978	1.695	2.027	$2p_{1/2}$	0.499^{6}_{100}	0.883	0.838
0^-	2.407	2.156	2.063	$2p_{1/2}$	0.344^{9}_{69}	0.556	0.577
2^-	2.908	—	3.694	$2p_{3/2}$	0.023^{2}_{5}	—	—
				$1f_{5/2}$	0.062^{6}_{12}	—	0.214
3^-	3.250	3.058	3.810	$1f_{5/2}$	0.058^{6}_{12}	0.108	0.386
2^-	3.601	3.300	4.027	$1f_{5/2}$	0.341^{8}_{68}	0.466	0.503
3^-	3.792	3.381	4.542	$1f_{5/2}$	0.164^{4}_{33}	0.327	0.276
2^-	3.868	3.521	—	$1f_{5/2}$	0.140^{4}_{28}	0.183	—

strongest states are the first 2^- and third 1^- states, which is supported by the experimental measurement. Additionally, both calculations predict $\ell = 1$ excitation energies that are consistently too low.

ℓ = 3 states Here, the two shell model calculations are quite different; while SDPF-U produces excitation energies that are systematically too high, SDPF-MU excitation energies are systematically low. The number of strong states calculated by each model varies, and neither correctly reproduces the mixed $\ell = 1 + 3$ state.

Separation in energy of p- and f-wave states The experimental results and the shell model calculations all have a distinct separation of $\ell = 1$ and $\ell = 3$. This is consistent with the known shell structure in this region of the nuclear chart, as the $f_{5/2}$ neutron orbital is expected to be outside of the p-shell, opening up a shell gap at $N = 34$. Critically, these experimental results can shed light on the magnitude of this gap. To demonstrate this, take the energy difference between the highest energy 0^- state and the strongest f-wave 2^- state as a convenient benchmark. Experimentally, this spacing is 1.2 MeV, and while SDPF-MU is quite accurate at 1.1 MeV, SDPF-U significantly over-predicts this spacing, producing a value of 1.9 MeV. Qualitatively, this suggests that SDPF-U may over-predict the robustness of the $N = 34$ shell gap in this case.

Reduced spectroscopic factors There is an additional complication in the comparisons made thus far, wherein the experimentally measured spectroscopic factors are *significantly* reduced relative to the shell model; S_{exp} values are, on average, approximately two-thirds of their S_{MU} or S_{U} counterparts. A variety of possible experimental causes – such as poor VAMOS geometric efficiency, or the incorrect determination of normalisation factor, B_{d} – have been explored in detail in Chapter 4, and each has been ruled out. As such, the experimentally measured spectroscopic factors are indeed correct, and the values are reduced relative to the shell model calculations.

Here, the complementary ^{47}K(d,t)^{46}K reaction channel becomes a valuable tool, as neutron removal is a probe of the *initial* neutron orbital population. The ^{46}K ground state has a structure predicted by the shell model to be predominantly $\pi d_{3/2}^{-1}$ coupled to $\nu f_{7/2}^{-1}$, and has the spin parity 2^{-}. As the ^{47}K(d,t) reaction is selectively populating the $\pi s_{1/2}^{-1}$ component of the final state, which cannot couple to $\nu f_{7/2}^{-1}$ to form a 2^{-} state, the ^{46}K ground state is instead accessed via the small component of $^{47}K_{g.s.}$ in which a neutron pair is excited from $\nu f_{7/2}$ to $\nu p_{3/2}$, across the soft $N=28$ shell gap. The presence of $\nu p_{3/2}$ neutrons in ^{47}K would, in effect, "block" the transfer of a neutron into these states, resulting in reduced $\nu p_{3/2}$ spectroscopic factors for ^{47}K(d,p). Therefore, if the spectroscopic factor of $^{46}K_{g.s.}$ measured in this work is large, then this would imply some unexpectedly large pair excitation component of $^{47}K_{g.s.}$. While significant pair excitation into $\nu p_{1/2}$ or $\nu f_{5/2}$ in $^{47}K_{g.s.}$ is improbable – and hence, it is unlikely that blocking would resolve the small ^{47}K(d,p) spectroscopic factors for states arising from these orbitals – measuring the spectroscopic factor of ^{47}K(d,t) transfer into $^{46}K_{g.s.}$ would provide some measure of the most likely pair excitation in ^{47}K; $\nu f_{7/2}^{-2} p_{3/2}^{2}$.

Therefore, to provide additional clarity on the ^{47}K(d,p)^{48}K reaction, discussion turns to the ^{47}K(d,t)^{46}K results.

6.1.2 Interpretation of ^{46}K results

Experimental results relating to the ^{47}K(d,t)^{46}K reaction are compared to ZBM2* [56] shell model calculations in **Figure 6.2**.[1] As opposed to the ^{48}K results, ℓ-transfer in ^{47}K(d,t) is less easy to assign, owing in part to reduced statistics. The results of neutron removal from each orbital are now discussed in turn:

1 $f_{7/2}$ states As shown in **Figure 6.2**, the shell model expects the $f_{7/2}$ strength to be spread between two pairs of 3^{-} and 4^{-} states, however the experimental measurement places all

---

[1] Recall that the model space of the ZMB2* shell model interaction is more appropriate for the ^{47}K(d,t) reaction, as detailed in Section 2.3.3.

Table 6.2: Comparison of ^{47}K(d,t) experimental results with ZBM2* shell model calculations. J^π values of the unresolved doublet states, 3.345 MeV and 3.409 MeV, are undetermined, and the spectroscopic factors of the doublet are $2s_{1/2} = 0.94 \pm 0.07$ and $1d_{3/2} = 3 \pm 1$.

J^π	$E_{exp.}$	E_{ZBM2*}	$n\ell_j$	$S_{exp.}$	S_{ZMB2*}
2^-	0.000	0.000	$2p_{3/2}$	0.13 ± 0.03	0.11
3^-	0.586	0.303	$1f_{7/2}$	8 ± 2	1.46
4^-	0.690	0.352	$1f_{7/2}$		3.33
3^-	—	1.375	$1f_{7/2}$	—	1.85
4^-	—	1.488	$1f_{7/2}$	—	0.83
1^+	1.945	1.664	$2s_{1/2}$	0.5 ± 0.1	0.34
			$1d_{3/2}$	—	0.65
0^+	2.233	1.573	$2s_{1/2}$	0.11 ± 0.02	0.18
2^+	2.730	2.768	$1d_{3/2}$	2.7 ± 0.5	1.27
1^+	†	3.254	$2s_{1/2}$	†	0.91
			$1d_{3/2}$		0.28
0^+		3.258	$2s_{1/2}$		0.20
2^+	—	3.690	$1d_{3/2}$	—	0.58
1^+	4.2	3.954	$1d_{3/2}$	1.6 ± 0.7	0.22

† Analysed as an unresolved doublet – see caption.

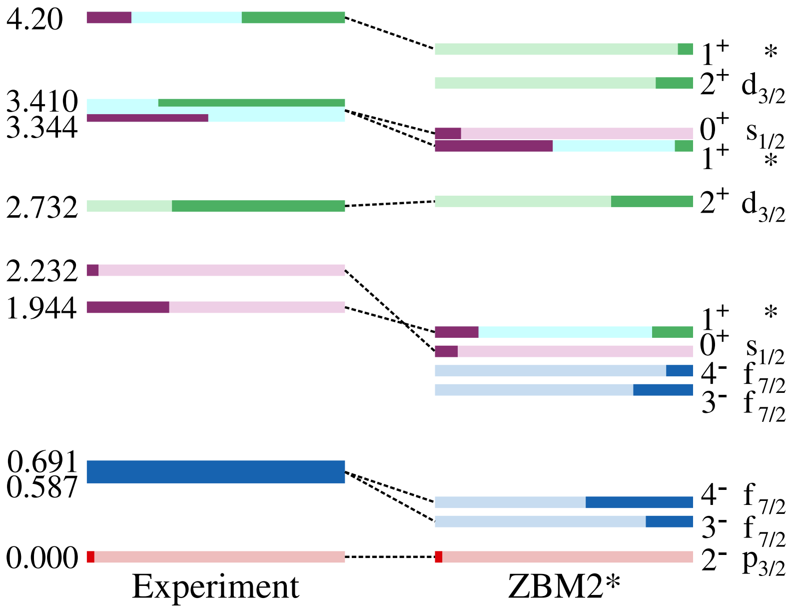

Figure 6.2: Comparison of states and spectroscopic factors measured in this work (left) and the ZBM2* shell model calculation (right). The filled length of each state line represents the spectroscopic factor. The s-wave (purple) and p-wave (red) states fill from the left, and the d-wave (green) and f-wave (blue) states fill from the right. Mixed $s_{1/2}$-$d_{3/2}$ states are marked with *, and fill from both sides.

of this strength ($\Sigma S_{exp} = 8 \pm 2$) into the lower energy couplet[2]. This result is interesting, as the shell model expects very similar neutron structures in all four states, but nearly opposite proton structures in the two 4^- states; that is, 70% $\pi s_{1/2}^1 d_{3/2}^4$ in the low energy 4^- state, and 70% $\pi s_{1/2}^2 d_{3/2}^3$ in the higher energy counterpart.

1 d$_{3/2}$ states The experimental strength of $d_{3/2}$ states are consistently higher than the shell model – in fact, the sum of the experimental spectroscopic factors is large, at $\Sigma S_{exp} = 7.2 \pm 2.5$ (compared to the shell model $\Sigma S_{ZMB2*} = 3.00$). Recall that, due to the relatively flat $d_{3/2}$ differential cross section, the experimental measurements failed to place a tight constraint on the mixed state $d_{3/2}$ spectroscopic factors. With this in mind, a result that is within 1.7σ of theoretical expectation is acceptable.

2 s$_{1/2}$ states The $s_{1/2}$ spectroscopic factors are relatively well-predicted by the shell model, and indeed the sum of spectroscopic factors for theory and experiment are in agreement, with $\Sigma S_{exp} = 1.6 \pm 0.2$, and $\Sigma S_{ZMB2*} = 1.63$.

2 p$_{3/2}$ ground state Most significantly, the spectroscopic factor of the ground state – the only state that probes the occupation of the $\nu p_{3/2}$ orbital in the ^{47}K beam isotope – is very small. A large spectroscopic factor here would indicate that the population of $\nu p_{3/2}$ is underestimated in ^{47}K, which could suggest a reason for reduced ^{47}K(d,p) spectroscopic factors. The small and theoretically consistent spectroscopic factor observed makes this explanation unlikely.

6.2 Reduced measured spectroscopic factors in ^{47}K(d,p)^{48}K

6.2.1 Dependence upon proton configuration

Having concluded that there are no systematic issues in the data analysis (Section 4.3.1) or elastic scattering normalisation (Section 4.1.3), and with no evidence of neutron transfer blocking by a significant population of the $\nu p_{3/2}$, $\nu p_{1/2}$ or $\nu f_{5/2}$ orbitals in the ground state of ^{47}K, further consideration is now given to the reduced ^{47}K(d,p)^{48}K spectroscopic factors observed, compared to the shell model prediction.

Here, it is suggested that the shell model spectroscopic factors are reproducing the neutron wavefunction overlap of the ^{47}K+n and ^{48}K systems well, but may not be correctly reproducing the poor *proton* wavefunction overlap of the two isotopes. While isotopes

---

[2] Recall that there was no conclusive evidence supporting the population of the higher energy $f_{7/2}$ couplet in this experiment

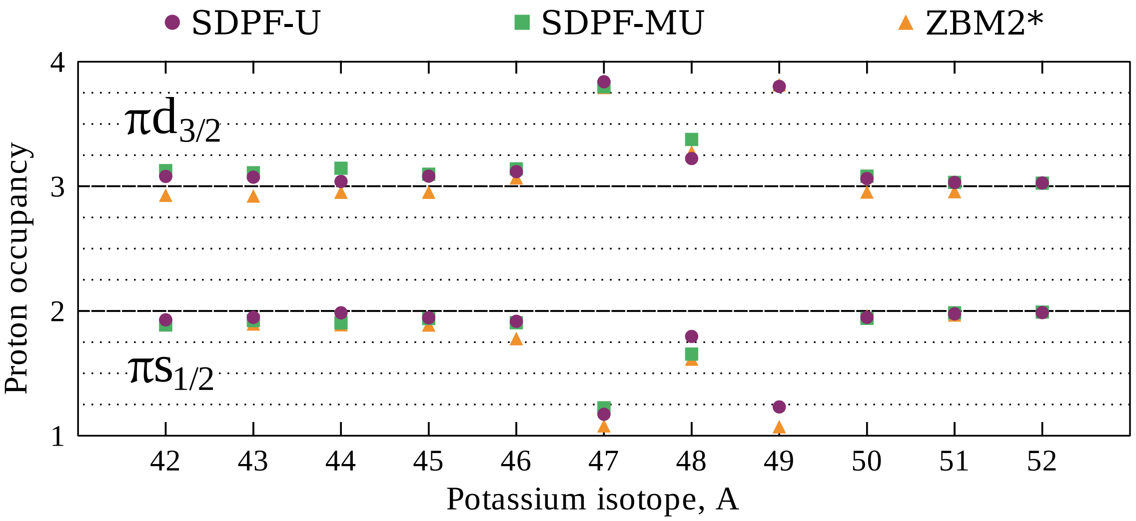

Figure 6.3: Ground state proton occupancies of potassium isotopes calculated with the three shell model Hamiltonians used in this work; SDPF-U (purple circles), SDPF-MU (green squares) and ZBM2* (orange triangles). Ground states were identified in Ref. [30]. Note that the ^{47}K ground state has the configuration $\pi s^{1}_{1/2} d^{4}_{3/2}$.

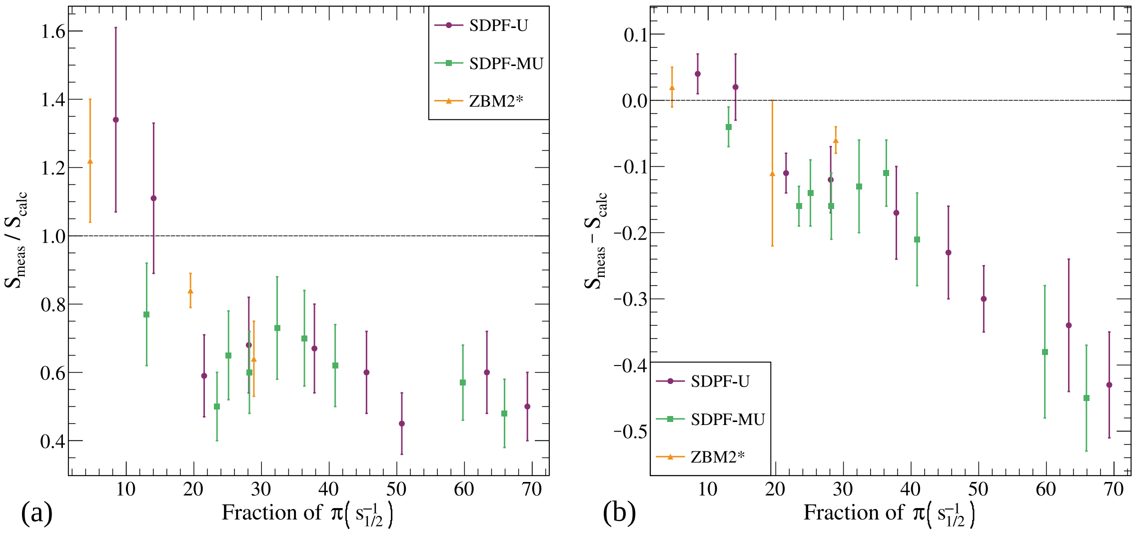

Figure 6.4: Accuracy of the three shell model calculations – SDPF-U (purple circles), SDPF-MU (green squares) and ZBM2* (orange triangles) – plotted against the fraction of $\pi s^{-1}_{1/2}$ configuration that the model calculates for that state. (a) Accuracy represented by the fraction S_{meas}/S_{calc}. (b) Accuracy represented by the difference $S_{meas} - S_{calc}$. Dashed line indicates $S_{meas} = S_{calc}$.

of the same element would usually share the same proton structure, it is clear from the existing literature [30] that the A = 47, 49 isotopes of potassium are unique in their inverted ground state proton structure, shown in **Figure 6.3**; indeed, that is what initially made ^{47}K an attractive candidate for this experiment.[3] As the ^{47}K(d,p) and ^{47}K(d,t) reactions are populating the $\pi s_{1/2}^{-1}$ components of the final states, the shell model calculations could produce incorrectly large spectroscopic factors for transfer if they were overestimating the $\pi s_{1/2}^{-1}$ configuration component of the populated states.

Support for this statement regarding the proton configuration is presented in **Figure 6.4**, which compares the accuracy of shell model calculations for states[4] populated in ^{46,48}K. Here, S_{meas}/S_{calc} and $S_{meas}-S_{calc}$ represent the agreement between experiment and theory, and are plotted against the fraction of $\pi s_{1/2}^{-1}$ present in the configuration of that state, according to the shell model calculations. An interesting relationship is apparent here, where states with larger predicted $\pi s_{1/2}^{-1}$ configurations have consistently low experimental spectroscopic factors relative to theory, whereas states with smaller $\pi s_{1/2}^{-1}$ configuration fractions are more accurately described by the shell model. While one could imagine that the shell model would poorly reproduce smaller spectroscopic factors, simply because a small wavefunction component is more likely to be poorly described in the calculation, what we observe is the opposite – the largest spectroscopic factors are the most suppressed, and the smallest spectroscopic factors are in agreement. Take, for example, the 0.143 MeV state; $S_{calc} = 0.85$, whereas $S_{meas} = 0.42(8)$. This is opposed to, for example, the ground state; $S_{calc} = 0.21$ in SDPF-U, which is in very close agreement with $S_{meas} = 0.24(5)$. If the 'accuracy' of the shell model were to be equally poor for each state, it would imply that the shell model is only poorly estimating the $^{47}K_{g.s.}$ configuration, but this variation suggests a dependence on the final state configuration, also. As such, it seems that the shell model calculations are poorly reproducing the proton wavefunctions of these nuclei.

It is interesting to note, in this context, that a recent study by Beck *et al.* (2023) [130] found that the ^{9}Be(^{38}Ca,^{36}Ca) two-neutron removal reaction gave experimental spectroscopic factors that were significantly suppressed (30% to 50%) relative to shell model calculations. They posit that the shell model was poorly estimating the proton cross-shell excitation component, $\pi(sd)^{-2}(fp)^{2}$, of the final state, it being too small in USD [57] and too large in ZBM2 [65] shell model calculations. This recent result is another example of the proton wavefunction influencing the spectroscopic factors of neutron transfer reactions, though in a different mass region (neutron-deficient Ca) and with a different microscopic mechanism driving the proton structure.

---

[3] This was discussed with reference to **Figure 1.6** in Section 1.3.1 – **Figure 6.3** is an updated version of this figure, with new calculations performed in this work using the SDPF-MU, SDPF-U and ZBM2* shell model interactions, which agree very well with **Figure 1.6**.

[4] To simplify this unusual comparison, certain states are excluded, namely those that are weakly populated, in doublets, or mixed.

Table 6.3: Total sum of spectroscopic factors, comparing experimental observation with the shell model. Shell model calculations were performed for 40 states of each spin.

	$\nu p_{1/2}$, 0^-	$\nu p_{1/2}$, 1^-	$\nu p_{3/2}$, 1^-	$\nu p_{3/2}$, 2^-	$\nu f_{5/2}$, 2^-	$\nu f_{5/2}$, 3^-
Exp. (±20%)	0.60	0.50	0.48	0.44	0.54 - 1.00	0.22 - 0.55
SDPF-MU	0.99	0.95	0.86	0.93	0.97	0.93
SDPF-U	0.98	0.96	0.88	0.93	0.96	0.91

6.2.2 Working with reduced spectroscopic factors

Generally, in order to make well-founded inferences about nuclear orbitals from experimental (d,p) transfer data, a significant fraction of the strength must be observed – that is, the sum of S_{meas} for each spin produced by each νfp orbital must approach unity. This ensures that any remaining unobserved strength is not significant, and would therefore have a reduced influence on the average energies and orbital splitting. Due to the non-negligible influence of the proton wavefunction in this work, the sum of observed strength is significantly below unity, as shown in **Table 6.3**. It is argued, however, that the measured spectroscopic factors are still a valid probe of the $\pi s^{-1}_{1/2} \otimes \nu fp$ interaction.

6.2.2.1 Unobserved bound states

The shell model calculations do not suggest the presence of strongly populated states in ^{48}K beyond those that have been observed in this experiment. In **Figure 6.1**, presented previously, every shell model state with a spectroscopic factor of greater than 0.1 was indicated. Note that every $\ell = 1$ state in both shell model calculations has an experimental counterpart. In addition, most of the $\ell = 3$ states have been accounted for, though this picture is muddied by the high-energy multiplet in the experimental data (discussed in Section 5.1.1.2), and the different numbers of strong states in the two shell models (discussed in Section 2.4.1). Despite this, there do not appear to be states with significant strength that have not been identified in this work, particularly not any that could carry the 'missing' 40% of the spectroscopic strength.

6.2.2.2 Unobserved high-energy states

It is often true that the bound states of a nucleus do not contain the whole spectroscopic factor of a transfer, and in fact, some strength can be spread amongst many high energy states, which each have some very small spectroscopic factor. To investigate this, shell model calculations were performed for (d,p) transfer on $^{47}K_{g.s.}$ (primarily $\pi s^{-1}_{1/2}$ configuration) and additionally on the *first excited state* of ^{47}K (primarily $\pi d^{-1}_{3/2}$ configuration) to

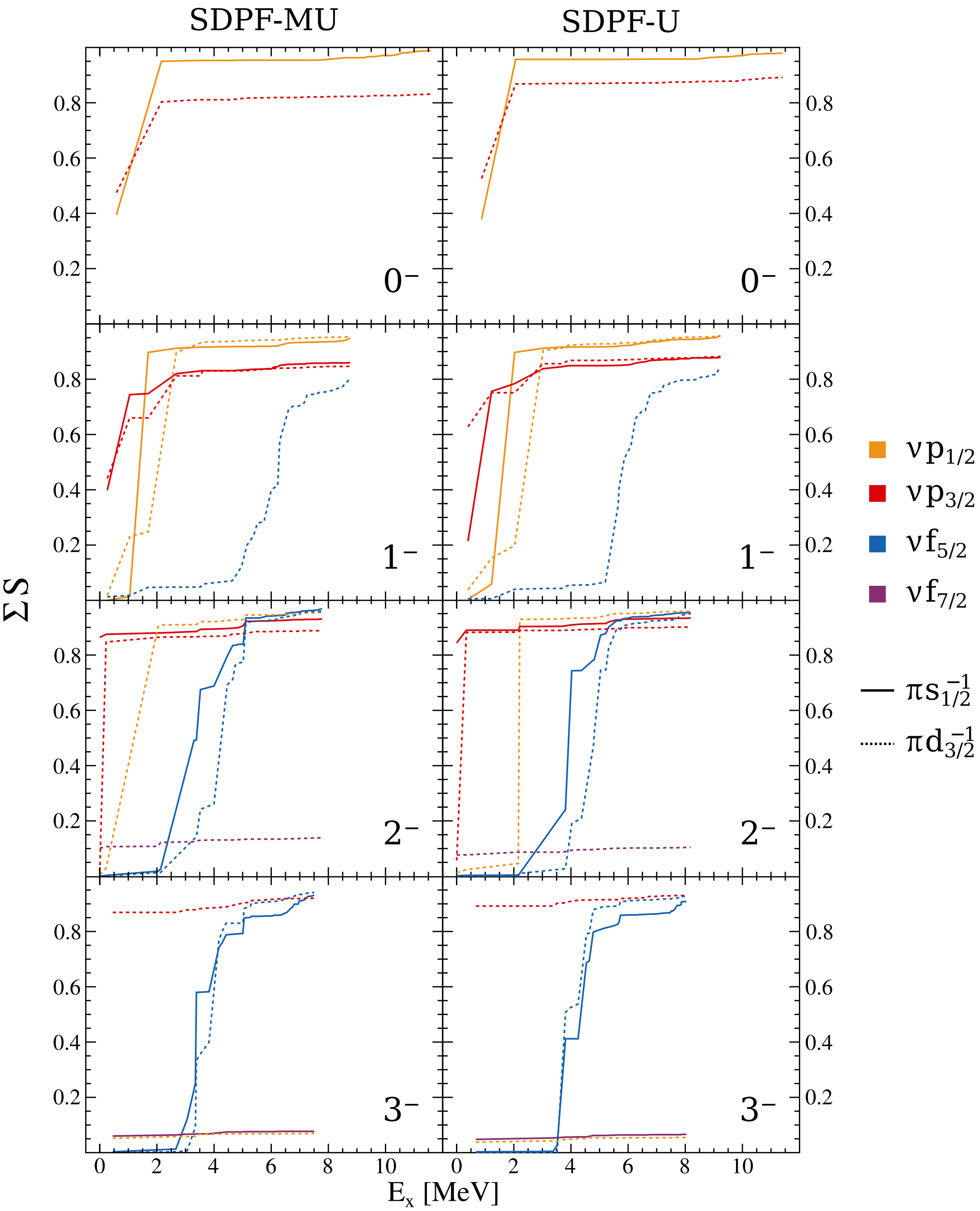

Figure 6.5: Cumulative sum of spectroscopic factors for each spin-parity and configuration, compared to the shell model excitation energy. The neutron configuration is indicated by the line colour, and the proton configuration (selected by the initial state of ^{47}K) is indicated by the line style, according to the key.

assess the accumulation of strength at high energies. This cumulative spectroscopic factor is plotted against energy in **Figure 6.5**, and from these calculations, it can be seen that:

$\nu p_{1/2}$ The $\nu p_{1/2}$ strength is saturated at very low excitation energies, for both $\pi s_{1/2}^{-1}$ and $\pi d_{3/2}^{-1}$ configurations. Comparing, for example, the 1^- states, both configurations reach a plateau below 3 MeV.

$\nu p_{3/2}$ While the $\nu p_{3/2}$ 1^- states begin to plateau at noticeably smaller values than other $\ell = 1$ states, this is consistent with the small $\nu f_{7/2}^{-2} p_{3/2}^{2}$ pair excitation expected in $^{47}K_{g.s.}$. Despite this suppression, the theoretical plateau is still significantly larger than the experimental observation. Again, the $\pi s_{1/2}^{-1}$ and $\pi d_{3/2}^{-1}$ configurations behave very similarly.

$\nu f_{5/2}$ The $f_{5/2}$ strength is spread across more states than the $\ell = 1$ strength, and is concentrated in the region of 3 MeV to 6 MeV in the two shell models. Comparing the $\pi s_{1/2}^{-1}$ and $\pi d_{3/2}^{-1}$ configurations, 2^- states seem to plateau at approximately the same point, with 3^- states having a slightly larger total spectroscopic factor in $\pi d_{3/2}^{-1}$ configuration. A steady rise in 3^- strength is seen at approximately 7 MeV in both models.

From this inspection of the shell model calculations, three main observations can be drawn. Firstly, the sum of spectroscopic strengths is between 0.70 and 0.95 for the different neutron orbitals when considering only the bound states (below approximately 5 MeV) suggesting that the majority of the strength should lie in the region studied in this experiment. Secondly, there are no apparent concentrations of significant strength at high energies, suggesting that the remaining strength in this high-energy region is very dispersed. Finally, the $\pi s_{1/2}^{-1}$ and $\pi d_{3/2}^{-1}$ configuration states behave in much the same way, rising at comparable rates and reaching similar plateaus, with only a slight offset in energy. This, critically, suggests that the high-energy states have structures more complex than either of the dominant proton configurations in potassium. Hence, an analysis of the neutron orbitals in ^{48}K based solely on the low-lying states observed in this work is justified.

6.2.2.3 Quantifying the proton contribution

From the previous section, it seems that the true single particle structure in ^{48}K is all found at excitation energies below approximately 5 MeV. It was noted in Section 6.1.1 that the measured spectroscopic factors are lower in most cases than the shell model predictions for what appear to be the corresponding states. These observations, plus the discussion in Section 6.2.1 regarding the dependence on proton configuration, suggest that the reduced

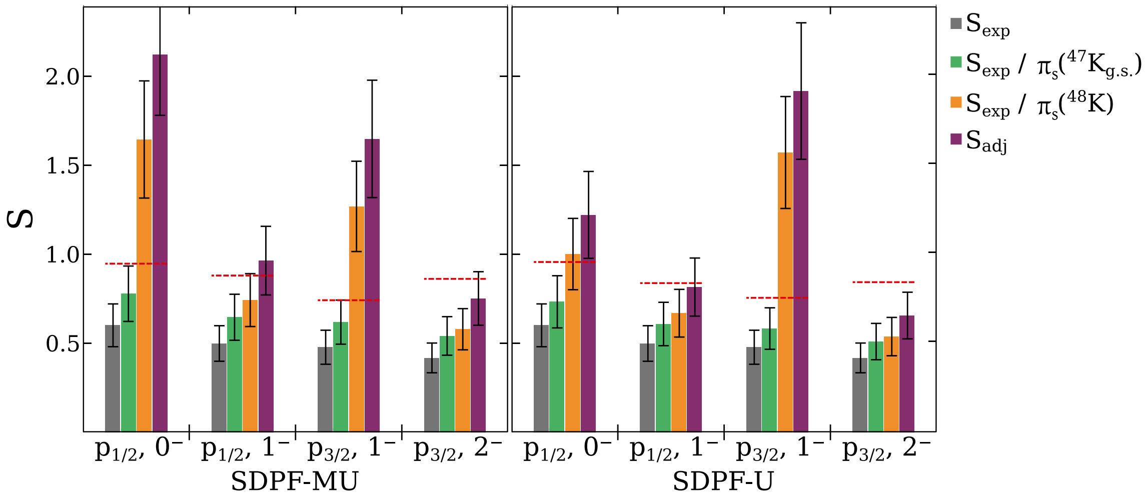

Figure 6.6: Adjusted spectroscopic factors, S_{adj}, when accounting for the calculated $\pi s_{1/2}$ configuration fraction of ^{48}K (orange), $^{47}K_{g.s.}$ (green), and both (purple). Red dashed line indicates the expected sum of spectroscopic factors, for the included states. Error bars of ±20% are applied. The $\ell = 3$ states are excluded from this analysis, as not every theoretical state has an experimental counterpart.

spectroscopic factors arise from a failure of the proton part of the wavefunction populated ^{48}K states to overlap with the proton configuration in the initial $^{47}K_{g.s.}$ nucleus. The shell model does attempt to predict the proton wavefunction overlap, but possibly fails. As such, a method has been developed to extricate the single particle structure in the neutron part of the wavefunction from this possible poor proton overlap. The method, presented in **Figure 6.6**, is to divide the measured spectroscopic factors, S_{exp}, by the fraction of the initial and final nucleus states that have $\pi s^{-1}_{1/2}$ configuration. This adjusted value, S_{adj}, is therefore,

$$S_{adj} = \frac{S_{meas}}{\pi_s(^{47}K_{g.s.})\ \pi_s(^{48}K)} \tag{6.1}$$

where $\pi_s(^{47}K_{g.s.})$ and $\pi_s(^{48}K)$ are the fraction of $\pi s^{-1}_{1/2}$ configuration in the initial and final nucleus, as deduced from the shell model calculations. The effects of adjusting the spectroscopic factors by only one of either $\pi_s(^{47}K_{g.s.})$ or $\pi_s(^{48}K)$ are also shown. Note that, in most cases, adjusting for $\pi_s(^{47}K_{g.s.})$ alone is not sufficient to rectify the small spectroscopic factors. For some categories, the final adjusted spectroscopic factors are an overestimation – in each of these cases, one of the states contributing to that category has a small calculated $\pi s^{-1}_{1/2}$ configuration; that is, there was already relatively good agreement between experiment and shell model.

While this is not a rigorous test, and no firm claims could be made on this evidence, the general improvement from the application of this method indicates that the reduced experimental spectroscopic factors are, in fact, capturing a large proportion of the $\pi s^{-1}_{1/2}\ \nu fp$ strength.

As such, having determined that it is appropriate to discuss the neutron structure of ^{48}K, despite the unusually reduced spectroscopic factors, a more standard discussion follows. Conclusions can now be reached regarding the ultimate motivation of this work; the single-particle energies and orbital splitting of $\nu p_{1/2}$, $\nu p_{3/2}$ and $\nu f_{5/2}$.

6.3 Inferences regarding the ν(fp) orbitals

While experimental excitation energies and spectroscopic factors are the key parameters used to anchor fits of shell model two-body matrix elements, further inspection of the results is warranted in order to contrast the SDPF-MU and SDPF-U shell model interactions more effectively. As such, the centroid single particle energy of the neutron orbitals are determined in each case, and compared with the values derived from the experimental results.

First, the weighted average energy (E_{WA}, or *barycentre*) of each spin which is produced by each orbital is calculated, by taking the sum of energies and spectroscopic factors of the states, i, of that spin and orbital configuration:

$$E_{WA} = \frac{\sum E_i S_i}{\sum S_i}. \tag{6.2}$$

The centroid single particle energy, $\langle E_{orb} \rangle$, for the originating orbitals can then be determined [131, 132] by taking a weighted sum of the two E_{WA} values for the two spins, j, produced by that orbital:

$$\langle E_{orb} \rangle = \frac{\sum (2J_j + 1)(E_{WA})_j}{\sum 2J_j + 1}. \tag{6.3}$$

These values can then be compared directly to the shell model E_{WA} and $\langle E_{orb} \rangle$ values, calculated in the same way. In order to quantify the influence of the many very weak states[5] in the plateau regions of **Figure 6.5**, the shell model E_{WA} values are calculated firstly for 10 states of each J^{π}, and again for 40 states of each J^{π}. This is effectively an evaluation of the convergence of E_{WA}.

Due to the importance of spin-parity in the deduction of E_{WA} and $\langle E_{orb} \rangle$, the ambiguous spin-parity assignments of ^{48}K states in the 4 MeV multiplet and the unbound region must now be addressed.

---

[5] Such states could not reasonably be observed in an inverse kinematic experiment using a radioactive isotope beam.

6.3.1 Influence of uncertain spin assignments in the 4 MeV region

As was alluded to in Section 5.1.2.1, the ill-defined spin-parity distribution of states in the 4 MeV region complicates the determination of the $f_{5/2}$ orbital barycentres. Rather than a single average value for each J^{π}, instead the variation in average orbital energies was established for various fractions of 2^{-} to 3^{-} strength. If all of the 4 MeV strength originated from 2^{-} states, then the centroid of the 4 MeV multiplet, 4.363 MeV, would carry a spectroscopic factor of $S^{\mathrm{stat}}_{\mathrm{sys}} = 0.452\,^{8}_{90}$. Conversely, if the region contained only 3^{-} states, $S^{\mathrm{stat}}_{\mathrm{sys}} = 0.323\,^{6}_{65}$. These extreme values can be used to place limits on the $f_{5/2}$ barycentres. Further to this, the smooth variation between these points can be seen in **Figure 6.7**. Note that the 3^{-} barycentre should, if all strength is measured, be at a higher energy than the 2^{-} barycentre,[6] which only occurs when the fraction of 2^{-} states is less than approximately two-thirds. Interestingly, the variation in $\langle E_{\mathrm{orb}} \rangle$ is quite small across the various possible spin fractions, creating the unusual position where $\langle E_{\mathrm{orb}} \rangle$ is much better constrained than the orbital splitting.

6.3.2 Influence of unbound strength

Until this point, the discussion has not included the weakly populated states in the unbound region. In this work, three possible unbound states have been identified at 4.86 MeV, 5.28 MeV and 5.86 MeV (Section 5.1.1.3). Unfortunately, attempts to determine the experimental angular distribution of this strength failed, and instead, only the magnitude could be determined (Section 5.1.2.2). While there is no experimental discrimination between $\ell = 1$ and $\ell = 3$, recall the shell model analysis shown in **Figure 6.5**, which revealed that the $\ell = 1$ strength in the unbound region was negligible, but some unbound $\ell = 3$ strength is anticipated. Quantitatively, the strength above the neutron separation threshold is between 0.02 and 0.04 for $\ell = 1$ states, whereas the different shell models expect total unbound $\ell = 3$ strength of between 0.1 and 0.2 – this is in fact in good agreement with the measured spectroscopic factors of the three unbound states. Using this argument, the three unbound states observed experimentally are assumed to be $f_{5/2}$ in nature.

Applying the same method to the unbound strength as was used for the 4 MeV region, the influence of these weak states on the $f_{5/2}$ barycentres can be characterised. Through this, it is determined that the inclusion of unbound states increases the maximum value of the 2^{-} (3^{-}) $f_{5/2}$ barycentre by 0.2 MeV (0.3 MeV).

---

[6] The 3^{-} states represent the anti-aligned $s_{\pi}s_{\nu}$ configuration, which should be higher in energy than the aligned 2^{-} arrangement.

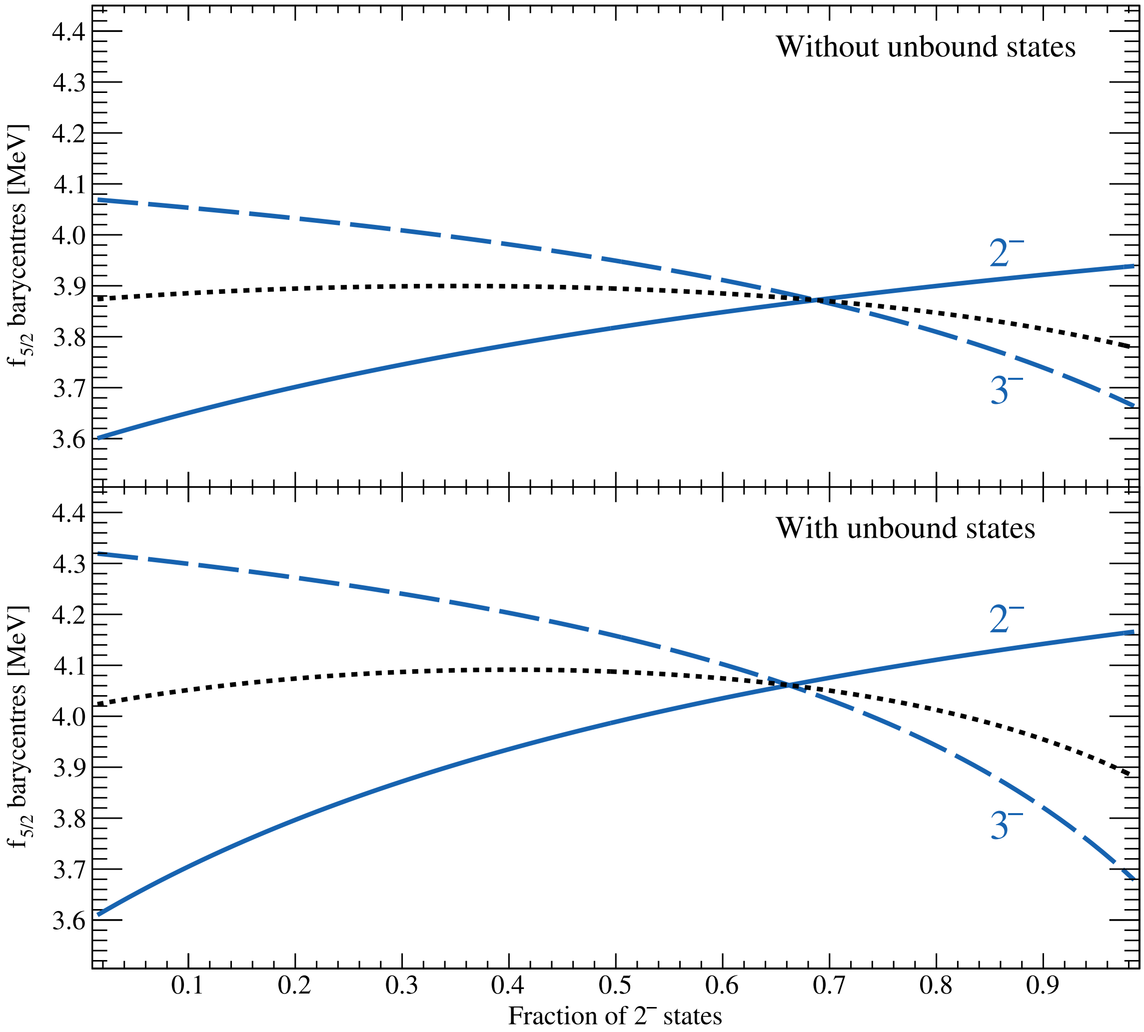

Figure 6.7: Range of possible $f_{7/2}$ weighted average energies, depending on the ratio of 2^- to 3^- states in the high-energy multiplet, with and without the inclusion of the unbound states. The black dotted line indicates $\langle E_{orb} \rangle$.

Table 6.4: Limits of the $f_{5/2}$ barycentre due to the ill-defined J^π of the 4 MeV region and unbound states. The limits are presented with and without the unbound states.

	Excluding unbound states				Including unbound states			
J^π	$f_{5/2}$, 2^- [MeV]	$f_{5/2}$, 3^- [MeV]	Splitting [MeV]	$\langle E_{orb} \rangle$ [MeV]	$f_{5/2}$, 2^- [MeV]	$f_{5/2}$, 3^- [MeV]	Splitting [MeV]	$\langle E_{orb} \rangle$ [MeV]
All 2^-	3.94	3.65	-0.29	3.84(7)	4.17	3.65	-0.52	4.0(1)
All 3^-	3.59	4.07	0.48		3.59	4.32	0.73	

6.3.3 Relative energies of shell model orbitals

The experimental and shell model barycentres are compared graphically in **Figure 6.8**, where the shell model results are truncated at 10 calculated states or at 40 calculated states. Here, the two expressions are included in order to indicate the influence of the very weak states; the 10-state expression encompasses every state with S > 0.1, whereas the 40-state expression includes the influence of the many weak states carrying strength on the order of 0.01. Comparing the properties of the 40-state truncation to the experimental observations (given in **Table 6.5**, as well as the aforementioned figure) reveals some interesting features:

$\nu p_{3/2}$ In both shell model calculations, the $p_{3/2}$ splitting is greatly overestimated – by nearly a factor of two in SDPF-MU and a nearly factor of three in SDPF-U. In **Figure 6.8**, this is shown by the spacing between the solid red and dashed red lines (1^- and 2^-, respectively) which show a much larger separation in theory than in the experiment. Conversely, both theoretical $\langle E_{orb} \rangle$ calculations, shown with dashed black lines, are in relative agreement with the experiment, being only 0.1 MeV and 0.2 MeV too high, respectively.

$\nu p_{1/2}$ Here, the splitting between 0^- (solid orange line) and 1^- (dashed orange line) is too small in the SDPF-MU calculation, and again too large in the SDPF-U calculation. The $\langle E_{orb} \rangle$ calculated by SDPF-MU is in exceptionally good agreement with the experimental value, whereas SDPF-U is once again too high.

$\nu f_{5/2}$ Here, the the large range of possible experimental $f_{5/2}$ barycentres – represented by labelled regions in **Figure 6.8** – makes comparison less straightforward. Again, the theoretical SDPF-MU is clearly exceeding its counterpart. While SDPF-U calculated energies are significantly higher than the maximum experimental range – even with the inclusion of the unbound states – both of the SDPF-MU spins (2^- and 3^-, represented by solid blue lines and dashed blue lines for theory results, and labelled regions for experimental results) are within range. Both models are within the upper limit placed on the spin-orbit splitting.

As such, SDPF-MU appears to be the more successful of the two shell model interactions.

Table 6.5: Comparison of νfp properties in the experimental data and those calculated by SDPF-MU and SDPF-U. The properties are; the weighted average energies of the high-spin, E^{+}_{WA}, and low-spin, E^{-}_{WA}, projections; the energy of the orbital, $\langle E_{\mathrm{orb}} \rangle$, and; the splitting of the orbital, ΔE. Experimental results include unbound states. Shell model calculations truncated at 40 states.

Energies	$p_{3/2}$			$p_{1/2}$			$f_{5/2}$		
[MeV]	Exp.	MU	U	Exp.	MU	U	Exp.	MU	U
E^{-}_{WA}	0.71(1)	1.03	1.38	1.79(1)	1.81	1.79	3.9(3)	3.80	4.21
E^{+}_{WA}	0.29(1)	0.27	0.22	1.98(1)	1.91	2.23	4.0(4)	3.91	4.45
$\langle E_{\mathrm{orb}} \rangle$	0.45(2)	0.56	0.66	1.93(2)	1.88	2.12	4.0(1)*	3.87	4.35
ΔE	0.42(2)	0.76	1.16	0.19(1)	0.10	0.44	<0.8	0.11	0.24

* Excluding the unbound states, $\langle E_{\mathrm{orb}} \rangle = 3.84(7)$.

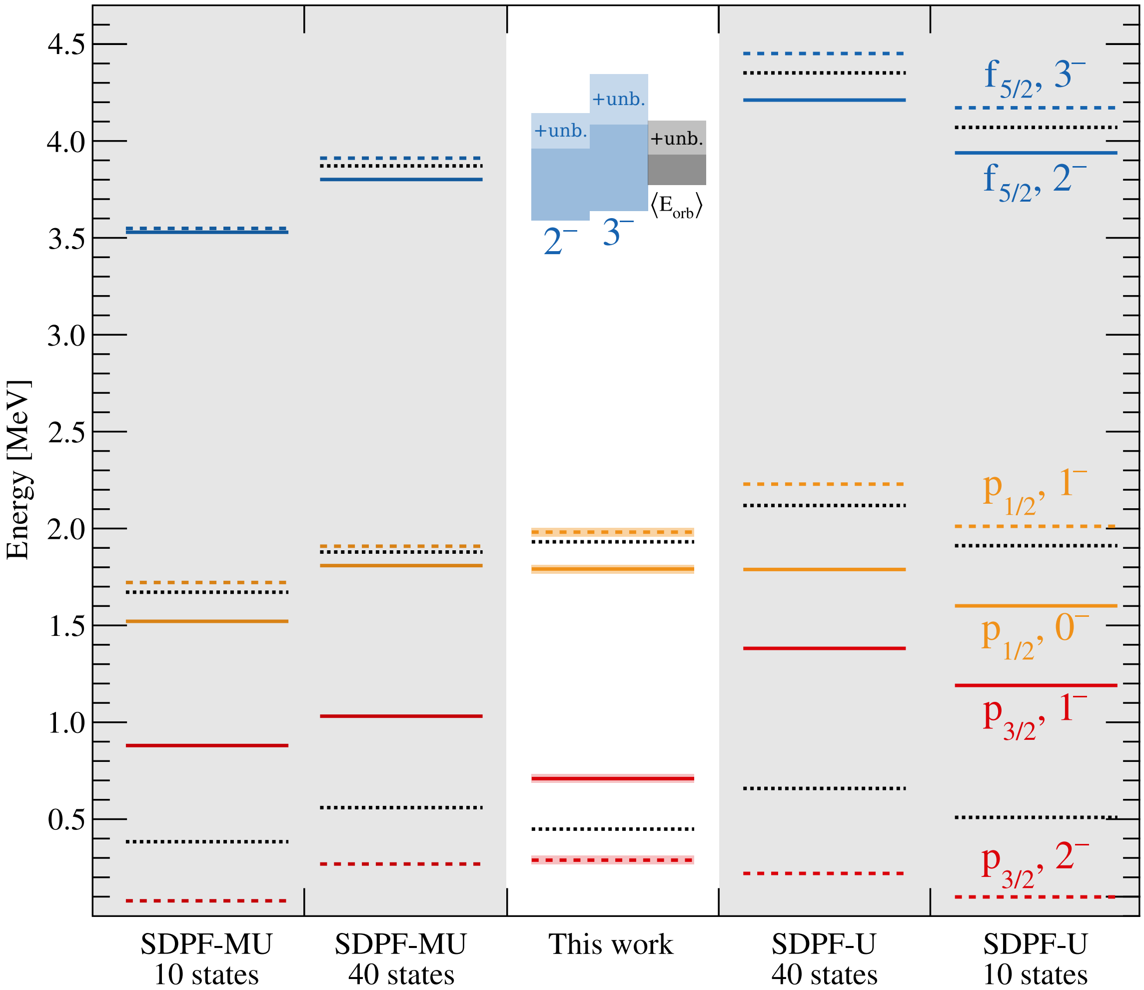

Figure 6.8: Visual comparison of νfp E_{WA} values observed in this work (centre) against SDPF-MU (left) and SDPF-U (right). $\langle E_{\mathrm{orb}} \rangle$ is indicated with dashed black lines. Shaded regions indicate experimental errors. Ambiguous $f_{5/2}$ energies, excluding and including unbound states ("+ unb."), are represented by shaded bars. See text for details.

6.4 Implications for N > 28, Z < 20 shell evolution

The initial motivation for this work was to expand our understanding of shell evolution near N = 28 in very proton-deficient nuclei. Previous works examining the N = 34 isotones have established that the weakening attractive interaction between $\pi f_{7/2}$ and $\nu f_{5/2}$ single-particle orbitals in more exotic nuclei causes a reordering of νfp neutron orbitals as protons are removed, moving from Z = 26 to Z = 20 nuclei [19]. This reordering, shown in **Figure 6.9**, is in turn responsible for the emergence of magicity in N = 32, 34. The goal of this work was to probe the deeper πsd proton shells and clarify the relative energies of these νfp neutron orbitals for more exotic nuclei.

Experimental measurements of the νfp orbital energies have been made in less exotic isotopes – through (d,p) transfer on the stable isotopes ^{48}Ca [137] and ^{30}Si [138], for example. Neither of these reactions has probed the $\pi s_{1/2}d_{3/2} \otimes \nu fp$ interactions, however, as the πsd shell is full in Ca, and the orbitals $\pi s_{1/2}d_{3/2}$ are empty in Si. Prior to this work, the only single particle transfer reaction investigation of $\pi s_{1/2}d_{3/2} \otimes \nu fp$ was ^{46}Ar(d,p)^{47}Ar [61], which probed $\pi d_{3/2} \otimes \nu fp$. The relative energies of the neutron orbitals derived from that work are also shown in **Figure 6.9**, and reveal a sharp decrease in the N = 32 spacing and a continued widening of the N = 34 gap, relative to ^{48}Ca.

The work presented in this thesis instead probes the heretofore unexamined $\pi s_{1/2} \otimes \nu fp$

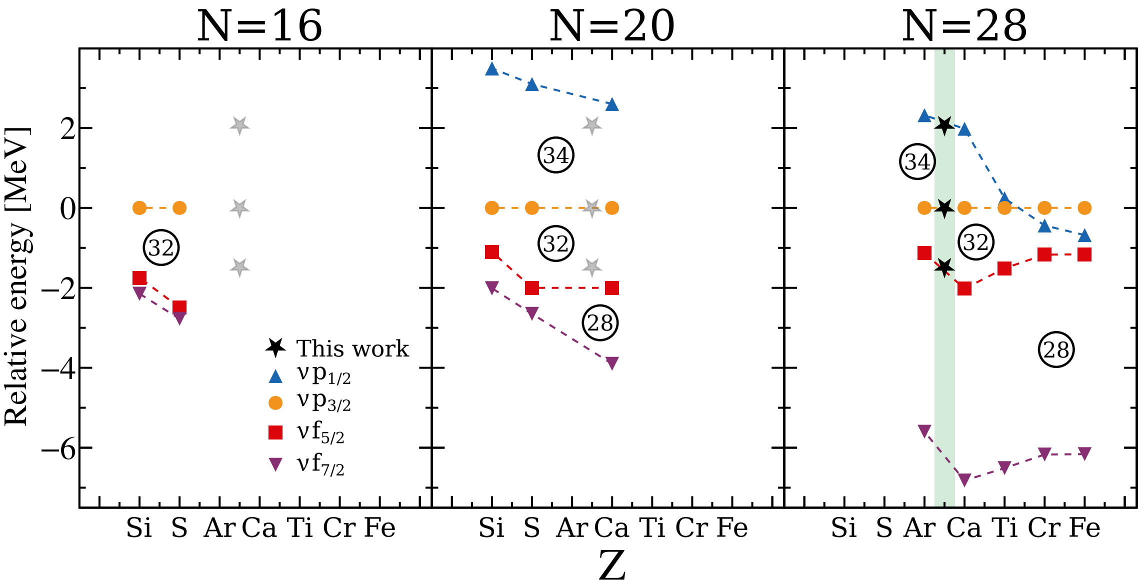

Figure 6.9: Systematic analysis of relative neutron orbital energies from experimental data. The results of this work are shown in black stars, and highlighted in green. Energies are presented relative to $\nu p_{1/2}$ in order to highlight the N = 32, 34 gaps. N = 16 data from Refs [133, 134]. N = 20: adapted from Figure 3 in Ref.[135]. N = 28: adapted from Figure 24 in Ref. [20], using results from Refs [61, 136].

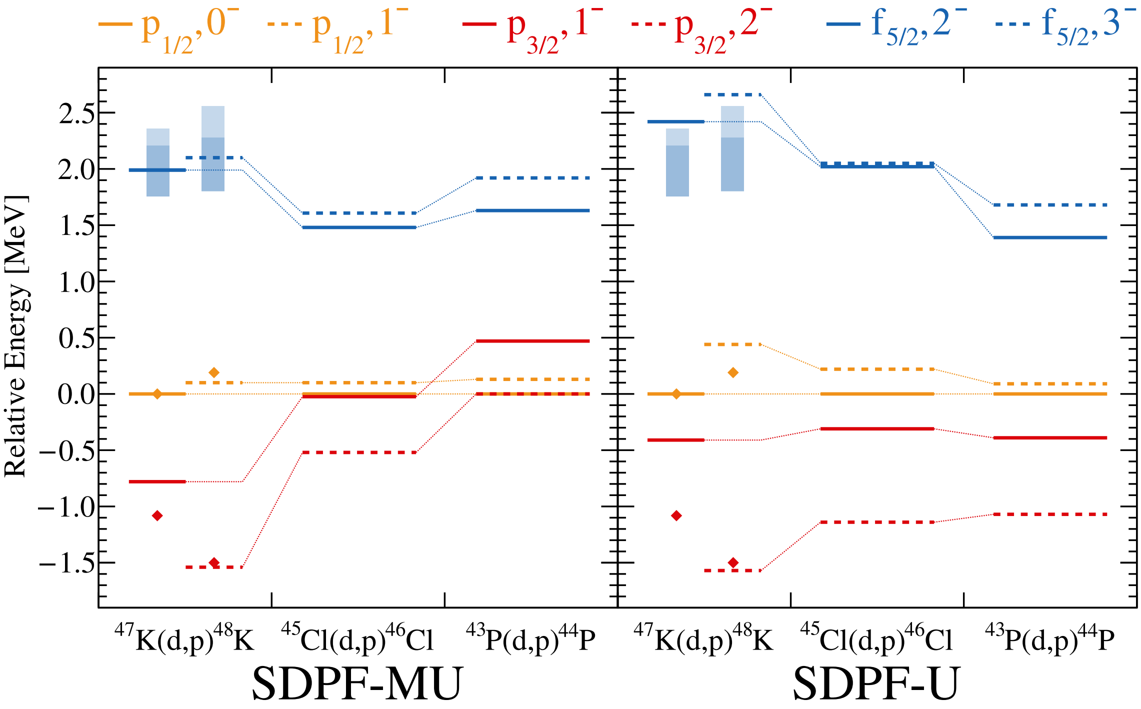

Figure 6.10: Systematic analysis of relative neutron orbital energies, E_{WA}, in different shell models. Calculated results are represented by lines as in **Figure 6.8**, and experimental results are represented by dots ($p_{1/2}$, $p_{3/2}$) or shaded regions ($f_{5/2}$). No experimental data is available for ^{45}Cl(d,p) or ^{43}P(d,p). Energies are presented relative to $p_{1/2}$ 0^- to highlight the $N = 32, 34$ gaps.

interaction, through the exotic ground state configuration of ^{47}K, $\pi s_{1/2}^{1} d_{3/2}^{4}$. These results are placed in a broader context by way of systematic comparison in **Figure 6.9**. Note that, although the unusual proton ground state configuration of ^{47}K is not shared by ^{48}Ca and ^{46}Ar, the average orbital energies derived in this work lie conveniently between those of its even-even neighbours. As well as providing some validation of the procedures applied in this interpretation, this consistency seems to suggest that the different proton configurations – Ar, $\pi(s_{1/2}d_{3/2})^4$; K, $\pi s_{1/2}^{1} d_{3/2}^{4}$ or $\pi s_{1/2}^{2} d_{3/2}^{3}$; Ca, $\pi\, s_{1/2}^{2} d_{3/2}^{4}$ – do not appear to have a strong influence on the neutron orbital energies; that is, there is a dependence on the number of protons, but not to any large extent on the specific proton configuration.

As the only current direct transfer measurement of states arising from the $\pi s_{1/2} \otimes \nu f_{5/2}$ interaction, the results of this work can help to improve theoretical modelling for nuclei as exotic as ${}^{>43}_{15}\mathrm{P}_{>28}$. Our results have indicated flaws in the current leading shell model calculations for this region, SDPF-MU and SDPF-U. Through comparison of the calculated and observed excitation energies of ^{48}K, shown at the beginning of the chapter in **Figure 6.1**, it can be seen that $\ell = 1$ states are systematically low in both models, and $\ell = 3$ states are low in SDPF-MU and high in SDPF-U. Further analysis, shown in **Figure 6.8**, revealed that the SDPF-MU model is in better agreement with the experimental weighted average energies and orbital energy of $\nu f_{5/2}$, though both models significantly over-predict the $\nu p_{3/2}$

splitting. As such, this experimental work shows a preference for SDPF-MU, in which the cross-shell πsd $\otimes$ νfp interaction is derived from the properties of monopole effective nucleon-nucleon interactions (Section 2.3.2), over SDPF-U, in which the cross-shell interaction is empirically derived – in part through fitting to the experimental measurement ^{46}Ar(d,p) [61] (Section 2.3.1).

With this distinction in mind, SDPF-MU and SDPF-U calculations for proton-deficient ^{45}Cl(d,p) and ^{43}P(d,p) have been performed. In extrapolating these shell models to such extreme nuclear systems, the two predictions have diverged significantly, as shown in **Figure 6.10**. While both models anticipate a reduction in the spacing between the neutron orbitals, SDPF-U maintains some spacing between the three, with the low-spin projections of the two $\ell = 1$ orbitals approaching each other due to the large $p_{3/2}$ splitting. This is in contrast to SDPF-MU, which predicts a degeneracy of the $\nu p_{3/2}$ and $\nu p_{1/2}$ orbitals in phosphorus, indicating a collapse of the $N = 32$ gap. Such a degeneracy could have significant structural implications, particularly as it could increase the collectivity of these nuclei [139].

The new experimental results presented in this thesis can be used to constrain the shell model, improving our understanding of these exotic cross-shell interactions, and hence producing more reliable predictions of nuclear structure in the region of $N < 28$, $Z > 20$. Greater understanding of the single particle structure in ^{44}P region would, in turn, help to provide a microscopic understanding of the known collective structure in ^{44}S [140] and ^{42}Si [28].

6.5 Future work

Theoretical Firstly, as has been discussed, further theoretical work is required to correctly reproduce the experimental energies of the single-particle states observed in this work. The $f_{5/2}$ states observed in this work may prove especially helpful to strongly phenomenological shell model interactions, such as the FSU interaction [141], for which the lack of experimental $f_{5/2}$ neutron orbital measurements is a significant hindrance.[7]

Experimental – N = 28 A logical next step for this work would be the next isotope with this unusual proton configuration, ^{45}Cl(d,p), as a stepping stone on the way to a future ^{43}P(d,p) experiment. ^{45}Cl(d,p) would probe the $\pi s_{1/2} \otimes \nu$fp interaction in the case of a half-filled $\pi d_{3/2}$ orbital, helping to determine the scale of the influence of $\pi d_{3/2}$ on the neutron orbital energies, allowing for improved predictive capabilities for ^{43}P, where the

---

[7] Calculations with the FSU interaction were performed during the course of this work, but the overall description of ^{48}K was poor.

$\pi d_{3/2}$ orbital is no longer occupied. A beam of ^{45}Cl of sufficient intensity for transfer reactions is expected to be possible at the new Facility for Rare Isotope Beams[8], and should be exploited for this purpose.

Experimental – $\pi s_{1/2}$ depletion Further to this, the shell model's apparent overestimation of $\pi s_{1/2}$ configuration contribution in ^{48}K states is a challenge that requires a more advanced investigation, outside of the scope of this work. This could take the form of additional experiments probing the proton occupation of N = 28 isotones, such as ^{47}K(d,^{3}He)^{46}Ar or ^{46}Ar(d,^{3}He)^{45}Cl.[9] The proton structure of ^{47}K and ^{46}Ar are of particular interest due to recent evidence [135, 142] of 'bubble' nuclei; that is, isotopes for which the $s_{1/2}$ orbital is empty. In the work of Mutschler *et al.* (2017) [142], it is argued that reduced occupation of $\pi s_{1/2}$ – which has a radial density peaked at the centre of the nucleus – is effectively a depletion of the central proton density. It is argued that this central density depletion leads to a weaker spin-orbit splitting force at the core of the nucleus, which is probed most effectively by low-ℓ nucleons. Though not a universally accepted explanation [143], proponents of bubble nuclei offer this as an explanation of the unusual structure of ^{35}Si, which presents a significant reduction in $\ell = 1$ spin-orbit splitting relative to other N = 21 isotones, whilst the $\ell = 3$ splitting appears unchanged [135]. This can be seen in **Figure 6.9**, where the $\ell = 1$ splitting is reduced between Z = 16 ($\pi d^{6}_{5/2}s^{2}_{1/2}$) and Z = 14 ($\pi d^{6}_{5/2}s^{0}_{1/2}$) for N = 16, 20 nuclei. A similar reduction is seen between Z = 20 and Z = 18 for N = 28 nuclei, hinting that nuclei in the region of $\pi s_{1/2}d_{3/2}$ degeneracy could also exhibit such bubble structure. Additionally, previous experimental measurements [61] have been interpreted with some reliance on the shell model – the results presented in this thesis suggest that the shell model may poorly reproduce experimental results in the N = 28 isotones below ^{48}Ca. As such, further experimental work is required to measure the proton occupation of these unique isotones.

---

[8] Approximately 10^5 particles per second of accelerated ^{45}Cl beam could be produced in PAC Two [29]

[9] Such works are already in discussion (O. Sorlin, private communication).

Chapter 7

Conclusions

In this work, the exotic cross-shell $\pi s_{1/2} \otimes \nu fp$ interaction has been probed by the single neutron transfer reaction ^{47}K(d,p)^{48}K. The unusual proton structure of ^{47}K allows for the selective population of states arising from this interaction, which is expected to dominate the structure of ^{44}P and influence magicity in $N = 32, 34$. This work serves as a stringent test of the predictive capabilities of the shell model, as we look towards future transfer experiments south-east of ^{48}Ca.

This experiment was conducted at the GANIL facility as part of the MUGAST-AGATA-VAMOS++ campaign, utilising state-of-the-art detectors to observe light ejectiles, heavy recoils and prompt γ-ray emissions for transfer and scattering reactions. A pure radioactive beam of ^{47}K was delivered by the SPIRAL1+ accelerator complex, and impinged on a thin solid CD_2 target. Simultaneous observation of ^{47}K(d,d) and ^{47}K(p,p) elastic scattering was critical to the success of this experiment, providing an internally consistent measure of the target thickness and integrated beam normalisation factor. In a procedure somewhat unique to this experiment, the target thickness was also determined by requiring the reconstructed ^{48}K excitation energy to agree across the full angular range. Critically, while requiring a coincident VAMOS++ heavy ejectile detection was found to reduce the total number of transfer reactions observed, the excellent background rejection provided by such a coincidence requirement was found to far outweigh the statistical reduction.

Through this work, nine new bound states were identified in ^{48}K, with transitions, branching ratios and J^π assignments. A further three bound states were observed with undetermined γ-ray transitions. Three likely unbound states have also been observed in ^{48}K. Additionally, the complementary ^{47}K(d,t)^{46}K transfer reaction was analysed, and found to be consistent with the literature – one new state has been identified, and an unambiguous J^π assignment achieved. For each bound state populated by ^{47}K(d,p)^{48}K, differential cross sections have been extracted, which reveal the ℓ-transfer without ambiguity. Spectroscopic factors of $\pi s_{1/2}^{-1}$ configuration states in ^{48}K have been measured, but their significant reduction relative to SDPF-MU and SDPF-U shell model calculations is not wholly explained. It is suggested that the shell model calculations are failing to predict the proton wavefunction overlap of ^{47}K and ^{48}K, and evidence to support this statement has been presented.

Through the comparison of experimental weighted average energies of the $\nu p_{3/2}$, $\nu p_{1/2}$ and $\nu f_{5/2}$ orbitals with those predicted by SDPF-MU and SDPF-U, it is found that SDPF-MU provides a better overall description of ^{48}K. The structure of proton-deficient ^{44}P, as calculated by the two shell model interactions, is then compared. Unlike SDPF-U, the SDPF-MU calculations predict a complete collapse of the $N = 32$ shell gap, owing to $\nu p_{3/2}p_{1/2}$ degeneracy in this isotope. Further experimental and theoretical work, such as ^{45}Cl(d,p)^{46}Cl, is now required to elucidate the rapidly evolving nuclear structure in proton-deficient $N = 28$ nuclei.

Bibliography

[1] H. Becquerel. “Sur les radiations émises par phosphorescence”. In: *Comptes rendus de l’Academie des Sciences Paris* 122 (1896), pp. 420–421.

[2] H. Becquerel. “Sur les radiations invisibles émises par les corps phosphorescents”. In: *Comptes rendus de l’Academie des Sciences Paris* 122 (1896), 501 – 503.

[3] H. Becquerel. “Sur quelques propriétés nouvelles des radiations invisibles émises par divers corps phosphorescents”. In: *Comptes rendus de l’Academie des Sciences Paris* 122 (1896), p. 559.

[4] H. Becquerel. “Sur les radiations invisibles émises par les sels d’uranium”. In: *Comptes rendus de l’Academie des Sciences Paris* 122 (1896), pp. 689–694.

[5] H. Becquerel. “Sur les propriétés différentes des radiations invisibles émises par les sels d’uranium, et du rayonnement de la paroi anticathodique d’un tube de Crookes”. In: *Comptes rendus de l’Academie des Sciences Paris* 122 (1896), p. 762.

[6] M. Curie. “Rayons émis par les composés de l’uranium et du thorium”. In: *Comptes rendus de l’Academie des Sciences Paris* 126 (1898).

[7] P. Curie and M. Sklodowska-Curie. “Sur une substance nouvelle radio-active, contenue dans la pechblende”. In: *Comptes rendus de l’Academie des Sciences Paris* 127 (1898), pp. 175–178.

[8] E. Rutherford. “VIII. Uranium radiation and the electrical conduction produced by it”. In: *The London, Edinburgh, and Dublin Philosophical Magazine and Journal of Science* 47.284 (1899), pp. 109–163.

[9] P. Villard. “Sur le rayonnement du radium”. In: *Comptes rendus de l’Academie des Sciences Paris* 130 (1900), p. 1178.

[10] E. Rutherford. “LXXIX. The scattering of α and β particles by matter and the structure of the atom”. In: *The London, Edinburgh, and Dublin Philosophical Magazine and Journal of Science* 21.125 (1911), pp. 669–688.

[11] N. Bohr. “I. On the constitution of atoms and molecules”. In: *The London, Edinburgh, and Dublin Philosophical Magazine and Journal of Science* 26.151 (1913), pp. 1–25.

[12] J. Chadwick. “The existence of a neutron”. In: *Proceedings of the Royal Society of London. Series A, Containing Papers of a Mathematical and Physical Character* 136.830 (1932), pp. 692–708.

[13] E. Simpson. *The Colourful Nuclide Chart.* URL: `https://people.physics.anu.edu.au/~ecs103/chart/`.

[14] Maria Goeppert Mayer. “On Closed Shells in Nuclei. II”. In: *Phys. Rev.* 75 (12 1949), pp. 1969–1970. DOI: `10.1103/PhysRev.75.1969`. URL: `https://link.aps.org/doi/10.1103/PhysRev.75.1969`.

[15] K.S. Krane. *Introductory nuclear physics*. New York, NY: Wiley, 1988.

[16] R.D. Woods and D.S. Saxon. “Diffuse Surface Optical Model for Nucleon-Nuclei Scattering”. In: *Phys. Rev.* 95 (2 July 1954), pp. 577–578. DOI: `10.1103/PhysRev.95.577`. URL: `https://link.aps.org/doi/10.1103/PhysRev.95.577`.

[17] Otto Haxel, J. Hans D. Jensen, and Hans E. Suess. “On the "Magic Numbers" in Nuclear Structure”. In: *Phys. Rev.* 75 (11 1949), pp. 1766–1766. DOI: `10.1103/PhysRev.75.1766.2`. URL: `https://link.aps.org/doi/10.1103/PhysRev.75.1766.2`.

[18] W.E. Burcham and M. Jobes. *Nuclear and Particle Physics*. Harlow, UK: Longman, 1995.

[19] D. Steppenbeck et al. “Evidence for a new nuclear ’magic number’ from the level structure of Ca-54”. In: *Nature* 502 (Oct. 2013), pp. 207–210. DOI: `10.1038/nature12522`.

[20] O. Sorlin and M.-G. Porquet. “Nuclear magic numbers: New features far from stability”. In: *Progress in Particle and Nuclear Physics* 61.2 (2008), pp. 602–673. ISSN: 0146-6410. DOI: `https://doi.org/10.1016/j.ppnp.2008.05.001`. URL: `https://www.sciencedirect.com/science/article/pii/S0146641008000380`.

[21] T. Baumann et al. “Discovery of 40Mg and 42Al suggests neutron drip-line slant towards heavier isotopes”. In: *Nature* 449 (Nov. 2007), pp. 1022–4. DOI: `10.1038/nature06213`.

[22] N. Tsunoda et al. “The impact of nuclear shape on the emergence of the neutron dripline”. In: *Nature* 587 (4 Nov. 2020), pp. 66–71. DOI: `10.1038/s41586-020-2848-x`. URL: `https://doi.org/10.1038/s41586-020-2848-x`.

[23] L. A. Riley et al. “Inverse-kinematics proton scattering from ^{42,44}S,^{41,43} P, and the collapse of the $N = 28$ major shell closure”. In: *Phys. Rev. C* 100 (4 Oct. 2019), p. 044312. DOI: `10.1103/PhysRevC.100.044312`. URL: `https://link.aps.org/doi/10.1103/PhysRevC.100.044312`.

[24] T. Otsuka et al. “Magic Numbers in Exotic Nuclei and Spin-Isospin Properties of the *NN* Interaction”. In: *Phys. Rev. Lett.* 87 (8 Aug. 2001), p. 082502. DOI: `10.1103/PhysRevLett.87.082502`. URL: `https://link.aps.org/doi/10.1103/PhysRevLett.87.082502`.

[25] Takaharu Otsuka et al. “Evolution of Nuclear Shells due to the Tensor Force”. In: *Phys. Rev. Lett.* 95 (23 2005), p. 232502. DOI: `10.1103/PhysRevLett.95.232502`. URL: `https://link.aps.org/doi/10.1103/PhysRevLett.95.232502`.

[26] T. Otsuka et al. “Evolution of shell structure in exotic nuclei”. In: *Rev. Mod. Phys.* 92 (1 Mar. 2020), p. 015002. DOI: `10.1103/RevModPhys.92.015002`. URL: `https://link.aps.org/doi/10.1103/RevModPhys.92.015002`.

[27] C. Wrede. “The 30P(p, γ)31S reaction in classical novae: progress and prospects”. In: *AIP Advances* 4.4 (2014), p. 041004. DOI: `10.1063/1.4864193`.

[28] S. Grévy et al. “Beta-decay half-lives at the N=28 shell closure”. In: *Physics Letters B* 594.3 (2004), pp. 252–259. ISSN: 0370-2693. DOI: `https://doi.org/10.1016/j.physletb.2004.06.005`. URL: `https://www.sciencedirect.com/science/article/pii/S0370269304007981`.

[29] Facility for Rare Isotope Beams. *FRIB Estimated Rates, Version 2.10*. Oct. 2022. URL: `https://groups.nscl.msu.edu/frib/rates/fribrates.html`.

[30] J. Papuga et al. “Shell structure of potassium isotopes deduced from their magnetic moments”. In: *Phys. Rev. C* 90 (3 Sept. 2014), p. 034321. DOI: `10.1103/PhysRevC.90.034321`. URL: `https://link.aps.org/doi/10.1103/PhysRevC.90.034321`.

[31] E. Caurier et al. “Shell model study of the neutron rich isotopes from oxygen to silicon”. In: *Phys. Rev. C* 58 (4 1998), pp. 2033–2040. DOI: `10.1103/PhysRevC.58.2033`. URL: `https://link.aps.org/doi/10.1103/PhysRevC.58.2033`.

[32] F. Nowacki and A. Poves. "New effective interaction for $0\hbar\omega$ shell-model calculations in the sd-pf valence space". In: *Phys. Rev. C* 79 (1 Jan. 2009), p. 014310. DOI: `10.1103/PhysRevC.79.014310`. URL: `https://link.aps.org/doi/10.1103/PhysRevC.79.014310`.

[33] T.W. Burrows. "Nuclear Data Sheets for A = 48". In: *Nuclear Data Sheets* 107.7 (2006), pp. 1754–1755. ISSN: 0090-3752. DOI: `https://doi.org/10.1016/j.nds.2006.05.005`. URL: `https://www.sciencedirect.com/science/article/pii/S0090375206000482`.

[34] W. Królas et al. "Coupling of the proton-hole and neutron-particle states in the neutron-rich ^{48}K isotope". In: *Phys. Rev. C* 84 (6 Dec. 2011), p. 064301. DOI: `10.1103/PhysRevC.84.064301`. URL: `https://link.aps.org/doi/10.1103/PhysRevC.84.064301`.

[35] A. Dewald, O. Möller, and P. Petkov. "Developing the Recoil Distance Doppler-Shift technique towards a versatile tool for lifetime measurements of excited nuclear states". In: *Progress in Particle and Nuclear Physics* 67.3 (2012), pp. 786–839. ISSN: 0146-6410. DOI: `https://doi.org/10.1016/j.ppnp.2012.03.003`. URL: `https://www.sciencedirect.com/science/article/pii/S0146641012000713`.

[36] M. Paul et al. "The level structure of 46K studied by comparison of the (d, α) reaction on 42Ca and 48Ca". In: *Nuclear Physics A* 168.2 (1971), pp. 267–272. ISSN: 0375-9474. DOI: `https://doi.org/10.1016/0375-9474(71)90793-7`. URL: `https://www.sciencedirect.com/science/article/pii/0375947471907937`.

[37] Y. Dupont, P. Martin, and M. Chabre. "Study of ^{42}K, ^{42}Ca and ^{46}K, ^{46}Ca by Pickup Reactions". In: *Phys. Rev. C* 7 (2 1973), pp. 637–650. DOI: `10.1103/PhysRevC.7.637`. URL: `https://link.aps.org/doi/10.1103/PhysRevC.7.637`.

[38] Y. Dupont, P. Martin, and M. Chabre. "Observation of T=4 states in ^{46}Ca and level structure of ^{46}K". In: *Physics Letters* 31B (2 1970).

[39] W. W. Daehnick and R. Sherr. "Investigation of ^{46}K and ^{46}Ca with $(p, {}^{3}\mathrm{He})$ and (p, t) Reactions at 42 MeV". In: *Phys. Rev. C* 7 (1 1973), pp. 150–160. DOI: `10.1103/PhysRevC.7.150`. URL: `https://link.aps.org/doi/10.1103/PhysRevC.7.150`.

[40] R. F. Petry et al. "Decay of neutron-rich ^{45}Ar and ^{46}Ar". In: *Phys. Rev. C* 17 (6 1978), pp. 2197–2204. DOI: `10.1103/PhysRevC.17.2197`. URL: `https://link.aps.org/doi/10.1103/PhysRevC.17.2197`.

[41] N. Frascaria et al. "Selective population of maximum-J states in the d, α reaction at 80 MeV". In: *Phys. Rev. C* 10 (4 1974), pp. 1422–1428. DOI: `10.1103/PhysRevC.10.1422`. URL: `https://link.aps.org/doi/10.1103/PhysRevC.10.1422`.

[42] S.-C. Wu. "Nuclear Data Sheets for A = 46". In: *Nuclear Data Sheets* 91.1 (2000), pp. 1–116. ISSN: 0090-3752. DOI: `https://doi.org/10.1006/ndsh.2000.0014`. URL: `https://www.sciencedirect.com/science/article/pii/S0090375200900140`.

[43] J.S. Lilley. *Nuclear Physics: Principles and Applications*. Wiley, 2001.

[44] W.N. Catford. "What Can We Learn from Transfer, and How Is Best to Do It?" In: *The Euroschool on Exotic Beams, Vol. IV Lecture Notes in Physics* (2014), 67–122. DOI: `10.1007/978-3-642-45141-6_3`.

[45] A. M. Moro Muñoz. *Quantum scattering theory and direct nuclear reactions*. ISOLDE Nuclear Reaction and Nuclear Structure Course. 2014.

[46] N.K. Timofeyuk and R.C. Johnson. “Theory of deuteron stripping and pick-up reactions for nuclear structure studies”. In: *Progress in Particle and Nuclear Physics* 111 (2020), p. 103738. ISSN: 0146-6410. DOI: `https://doi.org/10.1016/j.ppnp.2019.103738`. URL: `https://www.sciencedirect.com/science/article/pii/S0146641019300730`.

[47] I. J. Thompson. “Chapter 3.1.2 - Methods of Direct Reaction Theories”. In: *Scattering*. Ed. by Roy Pike and Pierre Sabatier. London: Academic Press, 2002, pp. 1360–1372. ISBN: 978-0-12-613760-6. DOI: `https://doi.org/10.1016/B978-012613760-6/50073-5`. URL: `https://www.sciencedirect.com/science/article/pii/B9780126137606500735`.

[48] J.A. Tostevin. *University of Surrey version of the code TWOFNR (of M. Toyama, M. Igarashi and N. Kishida) and code FRONT (private communication). v20*. 2021. URL: `http://nucleartheory.eps.surrey.ac.uk/NPG/code.htm`.

[49] A.J. Koning and J.P. Delaroche. “Local and global nucleon optical models from 1 keV to 200 MeV”. In: *Nuclear Physics A* 713.3 (2003), pp. 231–310. ISSN: 0375-9474. DOI: `https://doi.org/10.1016/S0375-9474(02)01321-0`. URL: `https://www.sciencedirect.com/science/article/pii/S0375947402013210`.

[50] R.C. Johnson and P.C. Tandy. “An approximate three-body theory of deuteron stripping”. In: *Nuclear Physics A* 235.1 (1974), pp. 56–74. ISSN: 0375-9474. DOI: `https://doi.org/10.1016/0375-9474(74)90178-X`. URL: `https://www.sciencedirect.com/science/article/pii/037594747490178X`.

[51] J.M. Lohr and W. Haeberli. “Elastic scattering of 9–13 MeV vector polarized deuterons”. In: *Nuclear Physics A* 232.2 (1974), pp. 381–397. ISSN: 0375-9474. DOI: `https://doi.org/10.1016/0375-9474(74)90627-7`. URL: `https://www.sciencedirect.com/science/article/pii/0375947474906277`.

[52] Xiao-Hua Li and Lie-Wen Chen. “Isospin dependent global neutron-nucleus optical model potential”. In: *Nucl. Phys. A* 874 (2012), pp. 62–80. DOI: `10.1016/j.nuclphysa.2011.10.008`. arXiv: `1108.4858 [nucl-th]`.

[53] B. Alex Brown. “The Nuclear Shell Model towards the Drip Lines”. In: *Physics* 4.2 (2022), pp. 525–547. ISSN: 2624-8174. DOI: `10.3390/physics4020035`. URL: `https://www.mdpi.com/2624-8174/4/2/35`.

[54] B.A. Brown. “The nuclear shell model towards the drip lines”. In: *Progress in Particle and Nuclear Physics* 47.2 (2001), pp. 517–599. ISSN: 0146-6410. DOI: `https://doi.org/10.1016/S0146-6410(01)00159-4`. URL: `https://www.sciencedirect.com/science/article/pii/S0146641001001594`.

[55] Y. Utsuno et al. “Shape transitions in exotic Si and S isotopes and tensor-force-driven Jahn-Teller effect”. In: *Phys. Rev. C* 86 (5 Nov. 2012), p. 051301. DOI: `10.1103/PhysRevC.86.051301`. URL: `https://link.aps.org/doi/10.1103/PhysRevC.86.051301`.

[56] B. Alex Brown and Kei Minamisono. “β^2 corrections to spherical energy-density functional calculations for root-mean-square charge radii”. In: *Phys. Rev. C* 106 (1 2022), p. L011304. DOI: `10.1103/PhysRevC.106.L011304`. URL: `https://link.aps.org/doi/10.1103/PhysRevC.106.L011304`.

[57] B.H. Wildenthal. “Empirical strengths of spin operators in nuclei”. In: *Progress in Particle and Nuclear Physics* 11 (1984), pp. 5–51. ISSN: 0146-6410. DOI: `https://doi.org/10.1016/0146-6410(84)90011-5`. URL: `https://www.sciencedirect.com/science/article/pii/0146641084900115`.

[58] A. Poves and A. Zuker. "Theoretical spectroscopy and the fp shell". In: *Physics Reports* 70.4 (1981), pp. 235–314. ISSN: 0370-1573. DOI: `https://doi.org/10.1016/0370-1573(81)90153-8`. URL: `https://www.sciencedirect.com/science/article/pii/0370157381901538`.

[59] S. Kahana, H. C. Lee, and C. K. Scott. "Effect of Woods-Saxon Wave Functions on the Calculation of $A = 18, 206, 210$ Spectra with a Realistic Interaction". In: *Phys. Rev.* 180 (4 1969), pp. 956–966. DOI: `10.1103/PhysRev.180.956`. URL: `https://link.aps.org/doi/10.1103/PhysRev.180.956`.

[60] S. Nummela et al. "Spectroscopy of ^{34,35}Si by β decay: $sd - fp$ shell gap and single-particle states". In: *Phys. Rev. C* 63 (4 2001), p. 044316. DOI: `10.1103/PhysRevC.63.044316`. URL: `https://link.aps.org/doi/10.1103/PhysRevC.63.044316`.

[61] L. Gaudefroy et al. "Reduction of the Spin-Orbit Splittings at the $N = 28$ Shell Closure". In: *Phys. Rev. Lett.* 97 (9 2006), p. 092501. DOI: `10.1103/PhysRevLett.97.092501`. URL: `https://link.aps.org/doi/10.1103/PhysRevLett.97.092501`.

[62] Y. Uozumi et al. "Shell-model study of ^{40}Ca with the 56-MeV (d→,p) reaction". In: *Phys. Rev. C* 50 (1 1994), pp. 263–274. DOI: `10.1103/PhysRevC.50.263`. URL: `https://link.aps.org/doi/10.1103/PhysRevC.50.263`.

[63] Takaharu Otsuka et al. "Novel Features of Nuclear Forces and Shell Evolution in Exotic Nuclei". In: *Phys. Rev. Lett.* 104 (1 2010), p. 012501. DOI: `10.1103/PhysRevLett.104.012501`. URL: `https://link.aps.org/doi/10.1103/PhysRevLett.104.012501`.

[64] M. Honma, T. Otsuka, and T. Mizusaki. "Shell-model description of neutron-rich Ca isotopes". In: *RIKEN Accelerator Progress Report* 41 (2008), p. 32.

[65] E Caurier et al. "Shell model description of isotope shifts in calcium". In: *Physics Letters B* 522.3 (2001), pp. 240–244. ISSN: 0370-2693. DOI: `https://doi.org/10.1016/S0370-2693(01)01246-1`. URL: `https://www.sciencedirect.com/science/article/pii/S0370269301012461`.

[66] M. L. Bissell et al. "Proton-Neutron Pairing Correlations in the Self-Conjugate Nucleus ^{38}K Probed via a Direct Measurement of the Isomer Shift". In: *Phys. Rev. Lett.* 113 (5 2014), p. 052502. DOI: `10.1103/PhysRevLett.113.052502`. URL: `https://link.aps.org/doi/10.1103/PhysRevLett.113.052502`.

[67] B.A. Brown and W.D.M. Rae. "The Shell-Model Code NuShellX@MSU". In: *Nuclear Data Sheets* 120 (2014), pp. 115–118. ISSN: 0090-3752. DOI: `https://doi.org/10.1016/j.nds.2014.07.022`. URL: `https://www.sciencedirect.com/science/article/pii/S0090375214004748`.

[68] M. Assié et al. "The MUGAST-AGATA-VAMOS campaign: Set-up and performances". In: *Nuclear Instruments and Methods in Physics Research Section A: Accelerators, Spectrometers, Detectors and Associated Equipment* 1014 (2021), p. 165743. ISSN: 0168-9002. DOI: `https://doi.org/10.1016/j.nima.2021.165743`. URL: `https://www.sciencedirect.com/science/article/pii/S0168900221007282`.

[69] S. Akkoyun et al. "AGATA — Advanced GAmma Tracking Array". In: *Nuclear Instruments and Methods in Physics Research Section A: Accelerators, Spectrometers, Detectors and Associated Equipment* 668 (2012), pp. 26–58. ISSN: 0168-9002. DOI: `https://doi.org/10.1016/j.nima.2011.11.081`. URL: `https://www.sciencedirect.com/science/article/pii/S0168900211021516`.

[70] M. Assié. “The MUGAST campaign at GANIL”. In: *Journal of Physics: Conference Series* 1643 (Dec. 2020), p. 012070. DOI: `10.1088/1742-6596/1643/1/012070`.

[71] M. Rejmund et al. “Performance of the improved larger acceptance spectrometer: VAMOS++”. In: *Nuclear Instruments and Methods in Physics Research Section A: Accelerators, Spectrometers, Detectors and Associated Equipment* 646.1 (2011), pp. 184–191. ISSN: 0168-9002. DOI: `https://doi.org/10.1016/j.nima.2011.05.007`. URL: `https://www.sciencedirect.com/science/article/pii/S0168900211008515`.

[72] Carl Wheldon. “Derivations for two-body kinematics (both relativistic and non-relativistic)”. In: (2015).

[73] P. Chauveau et al. “A new FEBIAD-type ion source for the upgrade of SPIRAL1 at GANIL”. In: *Nuclear Instruments and Methods in Physics Research Section B: Beam Interactions with Materials and Atoms* 376 (2016). Proceedings of the XVIIth International Conference on Electromagnetic Isotope Separators and Related Topics (EMIS2015), Grand Rapids, MI, U.S.A., 11-15 May 2015, pp. 35–38. ISSN: 0168-583X. DOI: `https://doi.org/10.1016/j.nimb.2016.01.039`. URL: `https://www.sciencedirect.com/science/article/pii/S0168583X16001002`.

[74] O. Kamalou et al. “Status Report on GANIL and Upgrade of SPIRAL1”. In: *22nd International Conference on Cyclotrons and their Applications (CYC2019)*. Cape Town, South Africa, Sept. 2019, MOA03. DOI: `10.18429/JACoW-Cyclotrons2019-MOA03`. URL: `https://hal.archives-ouvertes.fr/hal-02911937`.

[75] P. Chauveau et al. “Latest improvements of the SPIRAL1 facility at GANIL”. In: *Nuclear Instruments and Methods in Physics Research Section B: Beam Interactions with Materials and Atoms* 541 (2023), pp. 61–64. ISSN: 0168-583X. DOI: `https://doi.org/10.1016/j.nimb.2023.05.003`. URL: `https://www.sciencedirect.com/science/article/pii/S0168583X23002008`.

[76] P. Delahaye et al. “New exotic beams from the SPIRAL 1 upgrade”. In: *Nuclear Instruments and Methods in Physics Research Section B: Beam Interactions with Materials and Atoms* 463 (2020), pp. 339–344. ISSN: 0168-583X. DOI: `https://doi.org/10.1016/j.nimb.2019.04.063`. URL: `https://www.sciencedirect.com/science/article/pii/S0168583X19302472`.

[77] Pierre Delahaye. “ECRIS and EBIS charge state breeders: Present performances, future potentials”. In: *Nuclear Instruments and Methods in Physics Research Section B: Beam Interactions with Materials and Atoms* 317 (2013). XVIth International Conference on ElectroMagnetic Isotope Separators and Techniques Related to their Applications, December 2–7, 2012 at Matsue, Japan, pp. 389–394. ISSN: 0168-583X. DOI: `https://doi.org/10.1016/j.nimb.2013.04.070`. URL: `https://www.sciencedirect.com/science/article/pii/S0168583X13006216`.

[78] L. Maunoury et al. “Charge breeding at GANIL: Improvements, results, and comparison with the other facilities”. In: *Review of Scientific Instruments* 91.2 (2020), p. 023315. DOI: `10.1063/1.5128661`.

[79] P. Delahaye, L. Maunoury, and R. Vondrasek. “Charge breeding of light metallic ions: Prospects for SPIRAL”. In: *Nuclear Instruments and Methods in Physics Research Section A: Accelerators, Spectrometers, Detectors and Associated Equipment* 693 (2012), pp. 104–108. ISSN: 0168-9002. DOI: `https://doi.org/10.1016/j.nima.2012.07.016`. URL: `https://www.sciencedirect.com/science/article/pii/S0168900212007784`.

[80] Glenn F. Knoll. *Radiation Detection and Measurement*. 2nd. John Wiley and Sons, 1989.

[81] Gerhard Lutz. *Semiconductor Radiation Detectors*. 2nd ed. Springer, 2007.

[82] *Neutron Transmutation Doping of Silicon at Research Reactors*. TECDOC Series 1681. Vienna: INTERNATIONAL ATOMIC ENERGY AGENCY, 2012. ISBN: 978-92-0-130010-2. URL: `https://www.iaea.org/publications/8739/neutron-transmutation-doping-of-silicon-at-research-reactors`.

[83] *Neutron Transmission Doping of Silicon*. URL: `https://nrl.mit.edu/facilities/ntds`.

[84] Anders Lei, Martin Græsvænge, and Christian Hindrichsen. "Reduced radial resistivity variation of FZ Si wafers with Advanced NTD". In: *Journal of Crystal Growth* 512 (2019), pp. 65–68. ISSN: 0022-0248. DOI: `https://doi.org/10.1016/j.jcrysgro.2019.02.017`. URL: `https://www.sciencedirect.com/science/article/pii/S0022024819300910`.

[85] J.-J. Dormard et al. "Pulse shape discrimination for GRIT: Beam test of a new integrated charge and current preamplifier coupled with high granularity Silicon detectors". In: *Nuclear Instruments and Methods in Physics Research Section A: Accelerators, Spectrometers, Detectors and Associated Equipment* 1013 (2021), p. 165641. ISSN: 0168-9002. DOI: `https://doi.org/10.1016/j.nima.2021.165641`. URL: `https://www.sciencedirect.com/science/article/pii/S0168900221006264`.

[86] Y Blumenfeld et al. "MUST: A silicon strip detector array for radioactive beam experiments". In: *Nuclear Instruments and Methods in Physics Research Section A: Accelerators, Spectrometers, Detectors and Associated Equipment* 421.3 (1999), pp. 471–491. ISSN: 0168-9002. DOI: `https://doi.org/10.1016/S0168-9002(98)01178-4`. URL: `https://www.sciencedirect.com/science/article/pii/S0168900298011784`.

[87] R.H. Richter et al. "Strip detector design for ATLAS and HERA-B using two-dimensional device simulation". In: *Nuclear Instruments and Methods in Physics Research Section A: Accelerators, Spectrometers, Detectors and Associated Equipment* 377.2 (1996). Proceedings of the Seventh European Symposium on Semiconductor, pp. 412–421. ISSN: 0168-9002. DOI: `https://doi.org/10.1016/0168-9002(96)00257-4`. URL: `https://www.sciencedirect.com/science/article/pii/0168900296002574`.

[88] J. Eberth and J. Simpson. "From Ge(Li) detectors to gamma-ray tracking arrays–50 years of gamma spectroscopy with germanium detectors". In: *Progress in Particle and Nuclear Physics* 60.2 (2008), pp. 283–337. ISSN: 0146-6410. DOI: `https://doi.org/10.1016/j.ppnp.2007.09.001`. URL: `https://www.sciencedirect.com/science/article/pii/S0146641007000828`.

[89] E. Wilson and B. Holzer. *Accelerators, Colliders and Their Application*. May 2020. ISBN: 978-3-030-34244-9. DOI: `10.1007/978-3-030-34245-6_1`.

[90] S. Beghini et al. "The focal plane detector of the magnetic spectrometer PRISMA". In: *Nuclear Instruments and Methods in Physics Research Section A: Accelerators, Spectrometers, Detectors and Associated Equipment* 551.2 (2005), pp. 364–374. ISSN: 0168-9002. DOI: `https://doi.org/10.1016/j.nima.2005.06.058`. URL: `https://www.sciencedirect.com/science/article/pii/S0168900205013501`.

[91] E. Pollacco et al. "MUST2: A new generation array for direct reaction studies". In: *The European Physical Journal A* 25.S1 (2005), 287–288. DOI: `10.1140/epjad/i2005-06-162-5`.

[92] Adrien Matta. "Study of the very neutron-rich 10He by one-proton transfer reaction 11Li(d, 3He)". PhD thesis. Université Paris-Sud XI, 2012.

[93] D. Beaumel. “The GASPARD project”. In: *Nuclear Instruments and Methods in Physics Research Section B: Beam Interactions with Materials and Atoms* 317 (2013). XVIth International Conference on ElectroMagnetic Isotope Separators and Techniques Related to their Applications, December 2–7, 2012 at Matsue, Japan, pp. 661–663. ISSN: 0168-583X. DOI: `https://doi.org/10.1016/j.nimb.2013.05.047`. URL: `https://www.sciencedirect.com/science/article/pii/S0168583X13006113`.

[94] H. Hamrita et al. “Charge and current-sensitive preamplifiers for pulse shape discrimination techniques with silicon detectors”. In: *Nuclear Instruments and Methods in Physics Research Section A: Accelerators, Spectrometers, Detectors and Associated Equipment* 531.3 (2004), pp. 607–615. ISSN: 0168-9002. DOI: `https://doi.org/10.1016/j.nima.2004.05.112`. URL: `https://www.sciencedirect.com/science/article/pii/S0168900204011106`.

[95] Accessed: 28 July 2023. URL: `https://must2.cea.fr/index.php?id=5&ref=1`.

[96] M.A. Deleplanque et al. “GRETA: utilizing new concepts in γ-ray detection”. In: *Nuclear Instruments and Methods in Physics Research Section A: Accelerators, Spectrometers, Detectors and Associated Equipment* 430.2 (1999), pp. 292–310. ISSN: 0168-9002. DOI: `https://doi.org/10.1016/S0168-9002(99)00187-4`. URL: `https://www.sciencedirect.com/science/article/pii/S0168900299001874`.

[97] M. Siciliano et al. “Position uncertainties of AGATA pulse-shape analysis estimated via the bootstrapping method”. In: *The European Physical Journal A* 57.2 (2021). DOI: `10.1140/epja/s10050-021-00385-z`.

[98] F. C. Crespi et al. “Agata: Performance of γ-ray tracking and associated algorithms”. In: *The European Physical Journal A* 59.5 (2023). DOI: `10.1140/epja/s10050-023-01019-2`.

[99] J. Pakarinen et al. “The jurogam 3 spectrometer”. In: *The European Physical Journal A* 56.5 (2020). DOI: `10.1140/epja/s10050-020-00144-6`.

[100] I Y Lee, M A Deleplanque, and K Vetter. “Developments in large gamma-ray detector arrays”. In: *Reports on Progress in Physics* 66.7 (2003), p. 1095. DOI: `10.1088/0034-4885/66/7/201`. URL: `https://dx.doi.org/10.1088/0034-4885/66/7/201`.

[101] F.C.L. Crespi et al. “A pulse shape analysis algorithm for HPGe detectors”. In: *Nuclear Instruments and Methods in Physics Research Section A: Accelerators, Spectrometers, Detectors and Associated Equipment* 570 (Jan. 2007). Received 30 June 2006, Revised 4 October 2006, Accepted 5 October 2006, Available online 7 November 2006., p. 459. ISSN: 01689002. DOI: `10.1016/j.nima.2006.10.003`. URL: `https://linkinghub.elsevier.com/retrieve/pii/S0168900206017803`.

[102] B. Bruyneel, B. Birkenbach, and P. Reiter. “Pulse shape analysis and position determination in segmented HPGE detectors: The Agata Detector Library”. In: *The European Physical Journal A* 52.3 (2016). DOI: `10.1140/epja/i2016-16070-9`.

[103] A. Bracco, F. C. Crespi, and E. G. Lanza. “Gamma decay of pygmy states from inelastic scattering of ions”. In: *The European Physical Journal A* 51.8 (2015). DOI: `10.1140/epja/i2015-15099-6`.

[104] J. Ljungvall et al. “Performance of the Advanced GAmma Tracking Array at GANIL”. In: *Nuclear Instruments and Methods in Physics Research Section A: Accelerators, Spectrometers, Detectors and Associated Equipment* 955 (2020), p. 163297. ISSN: 0168-9002. DOI: `https://doi.org/10.1016/j.nima.2019.163297`. URL: `https://www.sciencedirect.com/science/article/pii/S0168900219315475`.

[105] F. Azaiez et al. “The EXOGAM array: A radioactive beam gamma-ray spectrometer”. In: *Acta Physica Hungarica A* 11 (May 2000), pp. 159–188.

[106] E. Clément et al. “Conceptual design of the AGATA 1π array at GANIL”. In: *Nuclear Instruments and Methods in Physics Research Section A: Accelerators, Spectrometers, Detectors and Associated Equipment* 855 (2017), pp. 1–12. ISSN: 0168-9002. DOI: `https://doi.org/10.1016/j.nima.2017.02.063`. URL: `https://www.sciencedirect.com/science/article/pii/S0168900217302590`.

[107] Hervé Savajols. “VAMOS: A variable mode high acceptance spectrometer for identifying reaction products induced by SPIRAL beams”. In: *Nuclear Instruments and Methods in Physics Research Section B: Beam Interactions with Materials and Atoms* 204 (2003). 14th International Conference on Electromagnetic Isotope Separators and Techniques Related to their Applications, pp. 146–153. ISSN: 0168-583X. DOI: `https://doi.org/10.1016/S0168-583X(02)01908-0`. URL: `https://www.sciencedirect.com/science/article/pii/S0168583X02019080`.

[108] A. Lemasson and M. Rejmund. “Fast trajectory reconstruction techniques for the large acceptance magnetic spectrometer VAMOS++”. In: *Nuclear Instruments and Methods in Physics Research Section A: Accelerators, Spectrometers, Detectors and Associated Equipment* 1054 (2023), p. 168407. ISSN: 0168-9002. DOI: `https://doi.org/10.1016/j.nima.2023.168407`. URL: `https://www.sciencedirect.com/science/article/pii/S0168900223003972`.

[109] S. Ottini-Hustache et al. “CATS, a low pressure multiwire proportionnal chamber for secondary beam tracking at GANIL”. In: *Nuclear Instruments and Methods in Physics Research Section A: Accelerators, Spectrometers, Detectors and Associated Equipment* 431.3 (1999), pp. 476–484. ISSN: 0168-9002. DOI: `https://doi.org/10.1016/S0168-9002(99)00380-0`. URL: `https://www.sciencedirect.com/science/article/pii/S0168900299003800`.

[110] Rene Brun and Fons Rademakers. “ROOT — An object oriented data analysis framework”. In: *Nuclear Instruments and Methods in Physics Research Section A: Accelerators, Spectrometers, Detectors and Associated Equipment* 389.1 (1997). New Computing Techniques in Physics Research V, pp. 81–86. ISSN: 0168-9002. DOI: `https://doi.org/10.1016/S0168-9002(97)00048-X`. URL: `https://www.sciencedirect.com/science/article/pii/S016890029700048X`.

[111] CERN. *ROOT*. Version 6.22/02. Aug. 17, 2020. URL: `https://github.com/root-project/root/tree/v6-22-02`.

[112] A. Matta et al. “NPTool: a simulation and analysis framework for low-energy nuclear physics experiments”. In: *Journal of Physics G: Nuclear and Particle Physics* 43.4 (Mar. 2016), p. 045113. DOI: `10.1088/0954-3899/43/4/045113`. URL: `https://doi.org/10.1088/0954-3899/43/4/045113`.

[113] S. Agostinelli et al. “Geant4—a simulation toolkit”. In: *Nuclear Instruments and Methods in Physics Research Section A: Accelerators, Spectrometers, Detectors and Associated Equipment* 506.3 (2003), pp. 250–303. ISSN: 0168-9002. DOI: `https://doi.org/10.1016/S0168-9002(03)01368-8`. URL: `https://www.sciencedirect.com/science/article/pii/S0168900203013688`.

[114] W.N. Catford. *CatKIN v2.03*. 2019. URL: `http://personal.ph.surrey.ac.uk/~phs1wc/kinematics/`.

[115] W. W. Daehnick, J. D. Childs, and Z. Vrcelj. “Global optical model potential for elastic deuteron scattering from 12 to 90 MeV”. In: *Physical Review C* 21.6 (1980), 2253–2274. DOI: `10.1103/physrevc.21.2253`.

[116] Yinlu Han, Yuyang Shi, and Qingbiao Shen. “Deuteron global optical model potential for energies up to 200 MeV”. In: *Phys. Rev. C* 74 (4 Oct. 2006), p. 044615. DOI: `10.1103/PhysRevC.74.044615`. URL: `https://link.aps.org/doi/10.1103/PhysRevC.74.044615`.

[117] "A global nucleon optical model potential". In: *Physics Reports* 201.2 (1991), pp. 57–119. ISSN: 0370-1573. DOI: `https://doi.org/10.1016/0370-1573(91)90039-O`. URL: `https://www.sciencedirect.com/science/article/pii/037015739190039O`.

[118] F. D. Becchetti and G. W. Greenlees. "Nucleon-Nucleus Optical-Model Parameters, $A > 40, E < 50$ MeV". In: *Phys. Rev.* 182 (4 1969), pp. 1190–1209. DOI: `10.1103/PhysRev.182.1190`. URL: `https://link.aps.org/doi/10.1103/PhysRev.182.1190`.

[119] F. G. Perey. "Optical-Model Analysis of Proton Elastic Scattering in the Range of 9 to 22 MeV". In: *Phys. Rev.* 131 (2 June 1963), pp. 745–763. DOI: `10.1103/PhysRev.131.745`. URL: `https://link.aps.org/doi/10.1103/PhysRev.131.745`.

[120] P.D. Kunz. *DWUCK4: Zero range DWBA*. 2002. URL: `www.oecd-nea.org/tools/abstract/detail/nesc9872`.

[121] Ian Thompson. *Fresco*. Version 3.1.1. URL: `www.fresco.org.uk`.

[122] J. D. Childs, W. W. Daehnick, and M. J. Spisak. "Accurate elastic scattering cross sections for 17-MeV deuterons". In: *Phys. Rev. C* 10 (1 1974), pp. 217–230. DOI: `10.1103/PhysRevC.10.217`. URL: `https://link.aps.org/doi/10.1103/PhysRevC.10.217`.

[123] A Obertelli. "Nuclear structure from direct reactions with rare isotopes: observables, methods and highlights". In: *Eur. Phys. J. Plus* 131.319 (2016). DOI: `https://doi.org/10.1140/epjp/i2016-16319-8`. URL: `https://link.springer.com/article/10.1140/epjp/i2016-16319-8`.

[124] Wolfgang. Rindler. *Relativity : Special, General, and Cosmological*. 2nd ed. Oxford University Press, 2006. ISBN: 9780198567325.

[125] T.W. Burrows. "Nuclear Data Sheets for A = 47". In: *Nuclear Data Sheets* 108.5 (2007), pp. 923–1056. ISSN: 0090-3752. DOI: `https://doi.org/10.1016/j.nds.2007.04.002`. URL: `https://www.sciencedirect.com/science/article/pii/S0090375207000403`.

[126] R. C. Johnson and P. J. R. Soper. "Contribution of Deuteron Breakup Channels to Deuteron Stripping and Elastic Scattering". In: *Phys. Rev. C* 1 (3 Mar. 1970), pp. 976–990. DOI: `10.1103/PhysRevC.1.976`. URL: `https://link.aps.org/doi/10.1103/PhysRevC.1.976`.

[127] C. M. Vincent and H. T. Fortune. "New Method for Distorted-Wave Analysis of Stripping to Unbound States". In: *Phys. Rev. C* 2 (3 1970), pp. 782–792. DOI: `10.1103/PhysRevC.2.782`. URL: `https://link.aps.org/doi/10.1103/PhysRevC.2.782`.

[128] S. Sen et al. "Study of the (d, p) reaction to bound and unbound states of 19O". In: *Nuclear Physics A* 219.3 (1974), pp. 429–449. ISSN: 0375-9474. DOI: `https://doi.org/10.1016/0375-9474(74)90110-9`. URL: `https://www.sciencedirect.com/science/article/pii/0375947474901109`.

[129] W. W. Daehnick et al. "Nuclear structure of ^{46}K: Studies with ^{48}Ca$(d, \alpha\gamma)^{46}$K and deuteron-transfer reactions". In: *Phys. Rev. C* 10 (1 1974), pp. 136–149. DOI: `10.1103/PhysRevC.10.136`. URL: `https://link.aps.org/doi/10.1103/PhysRevC.10.136`.

[130] T. Beck et al. "Probing proton cross-shell excitations through the two-neutron removal from ^{38}Ca". In: *Phys. Rev. C* 108 (6 2023), p. L061301. DOI: `10.1103/PhysRevC.108.L061301`. URL: `https://link.aps.org/doi/10.1103/PhysRevC.108.L061301`.

[131] C. H. Johnson and C. Mahaux. "Neutron–^{40}Ca mean field between -80 and +80 MeV from a dispersive optical-model analysis". In: *Phys. Rev. C* 38 (6 1988), pp. 2589–2609. DOI: `10.1103/PhysRevC.38.2589`. URL: `https://link.aps.org/doi/10.1103/PhysRevC.38.2589`.

[132] J. Chen et al. “Experimental study of the effective nucleon-nucleon interaction using the $^{21}\mathrm{F}(d,p)^{22}\mathrm{F}$ reaction”. In: *Phys. Rev. C* 98 (1 2018), p. 014325. DOI: `10.1103/PhysRevC.98.014325`. URL: `https://link.aps.org/doi/10.1103/PhysRevC.98.014325`.

[133] Jun Chen and Balraj Singh. “Nuclear Structure and Decay Data for A=31 Isobars”. In: *Nuclear Data Sheets* 184 (2022), pp. 29–405. ISSN: 0090-3752. DOI: `https://doi.org/10.1016/j.nds.2022.08.002`. URL: `https://www.sciencedirect.com/science/article/pii/S0090375222000394`.

[134] Jun Chen and Balraj Singh. “Nuclear Data Sheets for A = 33”. In: *Nuclear Data Sheets* 112.6 (2011), pp. 1393–1511. ISSN: 0090-3752. DOI: `https://doi.org/10.1016/j.nds.2011.04.003`. URL: `https://www.sciencedirect.com/science/article/pii/S0090375211000445`.

[135] G. Burgunder et al. “Experimental Study of the Two-Body Spin-Orbit Force in Nuclei”. In: *Phys. Rev. Lett.* 112 (4 2014), p. 042502. DOI: `10.1103/PhysRevLett.112.042502`. URL: `https://link.aps.org/doi/10.1103/PhysRevLett.112.042502`.

[136] D.C. Kocher and W. Haeberli. “Vector analysing power and cross section for (d, p) reactions on 40Ca, 46Ti, 48Ti, 50Ti, 52Cr and 54Fe”. In: *Nuclear Physics A* 196.2 (1972), pp. 225–268. ISSN: 0375-9474. DOI: `https://doi.org/10.1016/0375-9474(72)90963-3`. URL: `https://www.sciencedirect.com/science/article/pii/0375947472909633`.

[137] Y. Uozumi et al. “Single-particle strengths measured with 48Ca(d, p)49Ca reaction at 56 MeV”. In: *Nuclear Physics A* 576.1 (1994), pp. 123–137. ISSN: 0375-9474. DOI: `https://doi.org/10.1016/0375-9474(94)90740-4`. URL: `https://www.sciencedirect.com/science/article/pii/0375947494907404`.

[138] Š. Piskoř et al. “A study of the 30Si(d,p)31Si reaction”. In: *Nuclear Physics A* 662.1 (2000), pp. 112–124. ISSN: 0375-9474. DOI: `https://doi.org/10.1016/S0375-9474(99)00425-X`. URL: `https://www.sciencedirect.com/science/article/pii/S037594749900425X`.

[139] A. O. Macchiavelli et al. “Structure of ^{43}P and ^{42}Si in a two-level shape-coexistence model”. In: *Phys. Rev. C* 105 (1 2022), p. 014309. DOI: `10.1103/PhysRevC.105.014309`. URL: `https://link.aps.org/doi/10.1103/PhysRevC.105.014309`.

[140] L. Cáceres et al. “In-beam spectroscopic studies of the ^{44}S nucleus”. In: *Phys. Rev. C* 85 (2 2012), p. 024311. DOI: `10.1103/PhysRevC.85.024311`. URL: `https://link.aps.org/doi/10.1103/PhysRevC.85.024311`.

[141] R. S. Lubna et al. “Evolution of the $N = 20$ and 28 shell gaps and two-particle-two-hole states in the FSU interaction”. In: *Phys. Rev. Res.* 2 (4 2020), p. 043342. DOI: `10.1103/PhysRevResearch.2.043342`. URL: `https://link.aps.org/doi/10.1103/PhysRevResearch.2.043342`.

[142] A. Mutschler et al. “A proton density bubble in the doubly magic 34Si nucleus”. In: *Nature Physics* 13.2 (2017), pp. 152–156. ISSN: 1745-2481. DOI: `10.1038/nphys3916`. URL: `https://doi.org/10.1038/nphys3916`.

[143] B. P. Kay, C. R. Hoffman, and A. O. Macchiavelli. “Effect of Weak Binding on the Apparent Spin-Orbit Splitting in Nuclei”. In: *Phys. Rev. Lett.* 119 (18 2017), p. 182502. DOI: `10.1103/PhysRevLett.119.182502`. URL: `https://link.aps.org/doi/10.1103/PhysRevLett.119.182502`.

Appendix A

Checks and confirmations

A.1 Verification of elastic scattering calculations

While DWUCK4 [120] was eventually used for ^{47}K(d,d) and ^{47}K(p,p) elastic scattering analysis, the possibility of an errant scaling factor being the cause of the reduced ^{47}K(d,p) spectroscopic factors lead to the additional use of FRESCO [121], for validation. DWUCK4 uses zero-range adiabatic assumption, which reduces a 6-dimensional integral to a delta function, but introduces the need for a later corrective factor, D_0. It was not wholly clear whether the DWUCK4 output included this correction or not. FRESCO, however, performs the whole integral and therefore would reveal any discrepancy between codes.

To confirm that FRESCO and DWUCK4 – which are complex codes which rely on an adept user – were being properly used in these calculations, comparisons were made between the two codes, and to elastic scattering results in literature, using the optical potential of Ref. [115] (DCV) and Ref. [116] (HSS). Some of these results can be seen in **Figure A.1**.

In **Figure A.1a**, the ratio between the differential cross sections calculated by FRESCO and DWUCK4, for a given reaction and optical model, is shown to oscillate around one. As such, there does not seem to be any erroneous factor-of-two difference between the two outputs. While the variation does increase at large θ_{CM} angles, only the small θ_{CM} region is used for normalisation in this work. DWUCK4 is adopted for elastic scattering calculations in the body of this work. In **Figure A.1b**, the calculated elastic scattering differential cross sections of deuterons on various isotopes are compared to the work of Childs *et al.* (1974) [122]. Critically, the current calculations are in agreement with experimental results at small θ_{CM} angles, indicating again that the methodology is sound. Additionally, while the two optical models are similar in the important low-angle region, HSS consistently overestimates the depth of the minima after the first minimum. As such, the optical model of DCV is preferred for the deuteron elastic scattering.

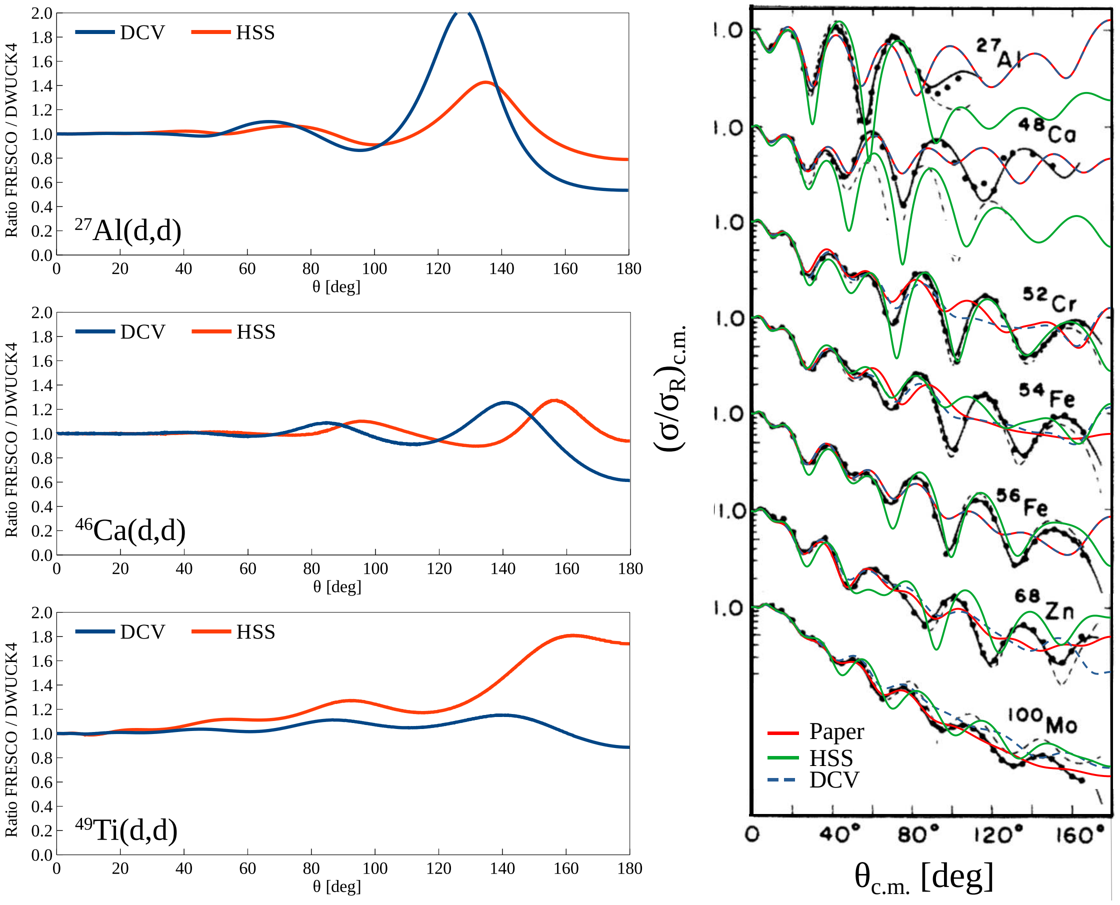

(a) (b)

Figure A.1: Verification of the elastic scattering methodologies. (a) Comparing the outputs of FRESCO [121] and DWUCK4 [120] for given reactions and models. (b) Comparing DWUCK4 calculations using HSS [116] and DCV [115] with literature [122].

A.2 VAMOS++ acceptance and focal plane detection

The erroneous timing signals discussed in Section 4.3.1 prompted a detailed investigation of the heavy recoil detection. It could have been possible that some inefficiency in VAMOS++ – either heavy recoils not entering the spectrometer, or not impinging on the focal plane detectors – could have lead to the $\approx 38\%$ reduction in particle detections when introducing a MUGAST-VAMOS timing gate. This was ultimately determined not to be the cause, but the results discussed here support the conclusion that there is no significant inefficiency in VAMOS++.

Firstly, it was confirmed that the heavy recoil particles were not impinging on the downstream MUST2 detectors. The heavy recoil ejection cone was found to be very small, and it was unlikely that any significant bombardment of the downstream detectors was occurring (see **Figure A.2a**). This also precludes any suggestion of the recoils missing the entrance window, as this cone is clearly within the exceptionally large acceptance of the VAMOS++ spectrometer (see **Figure A.2b**).

Secondly, it was confirmed that the heavy recoil particles were reaching the focal plane. It could in theory be possible for some heavy recoil events to be lost due to one or more of the final charge states of the heavy recoil having a significantly different $B\rho$ value than VAMOS++ had been tuned for. Looking to **Figure A.3**, the fully stripped charge state ($Q = 19$) is clearly identified, as there is no peak at lower rigidity (where rigidity is increasing with increasing VAMOS segment number). The spacing between charge states is consistent with the dispersion of the VAMOS spectrometer.[1] Four charge states – $Q = 19, 18, 17$ and 16 – are clear, and a fifth charge state, were it to be present, would still be impinging on the PPAC at segment 18. The rapidly decreasing population of charge states with increasing rigidity suggests that there is no significant loss of timing signal due to charge states failing to reach the focal plane.

With these checks performed, we are satisfied that no real transfer events are being lost due to inefficiency in the VAMOS spectrometer.

---

[1] To first order, each 50 mm VAMOS segment covers 2.1% dispersion in momentum [107] and the percentage difference in charge between the different charge states is $1/19 = 5.3\% = 2.5$ segments, $1/18 = 5.6\% = 2.7$ segments, etc.

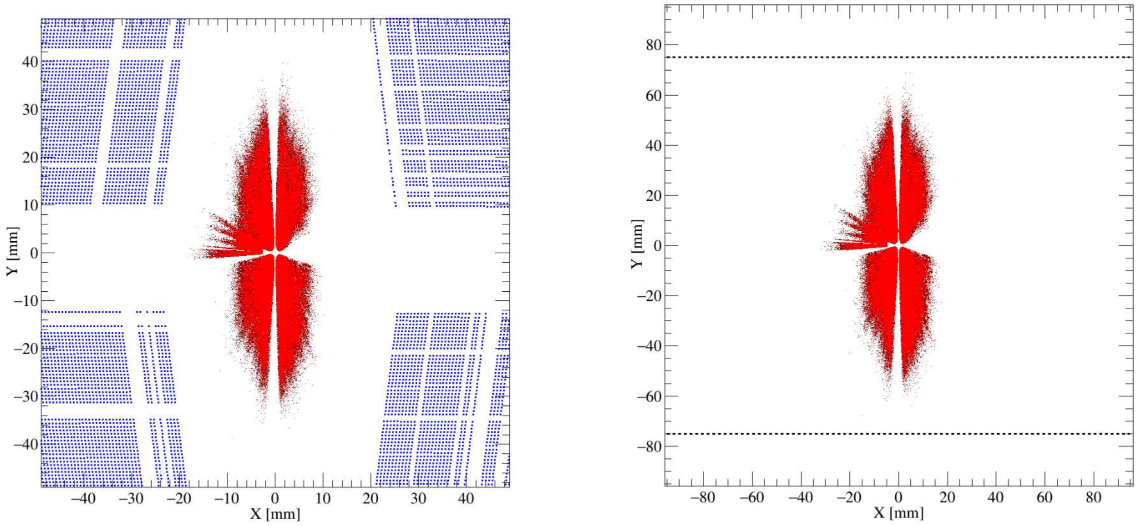

(a) Heavy recoil positions at the Z position of the downstream MUST2 detectors, relative to the innermost corners of the MUST detectors (blue).

(b) Heavy recoil positions at the Z position of the VAMOS++ entrance window, relative to the closest edges of the acceptance window (black dashed lines).

Figure A.2: Positions of reconstructed heavy recoil events (red), compared to (a) the downstream MUST2 detectors, and (b) the VAMOS++ entrance window, showing no heavy recoils are in danger of being lost to geometrical inefficiencies.

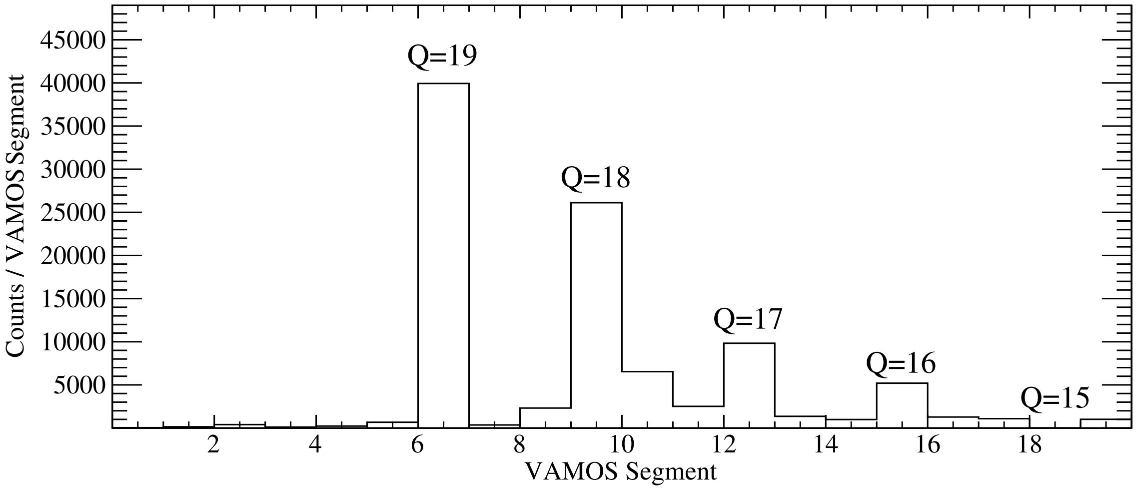

Figure A.3: Counts in each 50 mm segment of the PPAC in the VAMOS spectrometer focal plane. For clarity, only events in coincidence with elastic scattering detected in the perpendicular MUST2 detector are shown. Different ^{47}K charge states are marked.

A.3 Poisson statistical analysis of counts per pulse

In Section 4.3.1, true transfer reaction events were found to have timing signals larger than the major coincidence peak. This statistical analysis is intended to determine the likelihood of the timing STOP signal being sent by some particle in the subsequent beam pulses.

The probability of the STOP signal arriving in a given beam pulse (P_{STOP}) is the product of the probability of a beam particle being in that pulse, $P(\mu, 1)$, and the probability of there having been no particles in the preceding beam pulses, $P(\mu(n-1), 0)$. This can be determined using the Poisson probability formula;

$$P(\lambda, r) = \frac{\lambda^r e^{-\lambda}}{r!} = \frac{(\mu t)^r e^{-\mu t}}{r!} \tag{A.1}$$

where r is the number of events in time interval t, the rate of detections is μ, and the expected number of detections in the time interval is $\lambda = \mu t$. Here, it is determined that

$$P(\mu, 1) = \frac{\mu^1 e^{-\mu}}{1!} \tag{A.2}$$

$$= \mu e^{-\mu} \tag{A.3}$$

and

$$P(\mu(n-1), 0) = \frac{(\mu(n-1))^0 e^{-\mu(n-1)}}{0!} \tag{A.4}$$

$$= e^{-\mu(n-1)} \tag{A.5}$$

ergo, the probability of a STOP signal in any given pulse n is

$$P_{\text{STOP}} = P(\mu, 1) \cdot P(\mu(n-1), 0) \tag{A.6}$$

$$= \mu e^{-\mu} e^{-\mu(n-1)} \tag{A.7}$$

$$= \mu e^{-\mu n} \tag{A.8}$$

Hence, the probability decays exponentially. In this experiment, μ is on the order of 0.04. This approximate rate of decay is indeed observed in the number of *true* reaction counts in each subsequent beam pulse after the major timing coincidence peak.

A.4 Weisskopf estimates

In this work, γ-ray transitions below 5 MeV are observed in the relatively low-mass nuclei ^{46,48}K. All states populated in ^{48}K have negative parity, limiting their decays to odd-*M* and even-*E*; most likely, *M1* or *E2*. **Figure A.4a** shows the relative probabilities of each decay, indicating that *M1* is far more likely. This is in agreement with observation, as all of the ^{48}K γ-ray transitions observed in this work have ΔJ $\leq$ 1.

The same is largely true for ^{46}K, which is broadly separated into high-energy positive parity states, and low-energy negative parity states. Decays within these two groups will primarily be *M1* in character, ΔJ $\leq$ 1. Alternatively, decays between the two parity groups can be *M2* or *E1*, with *E1* dominating (see **Figure A.4b**).

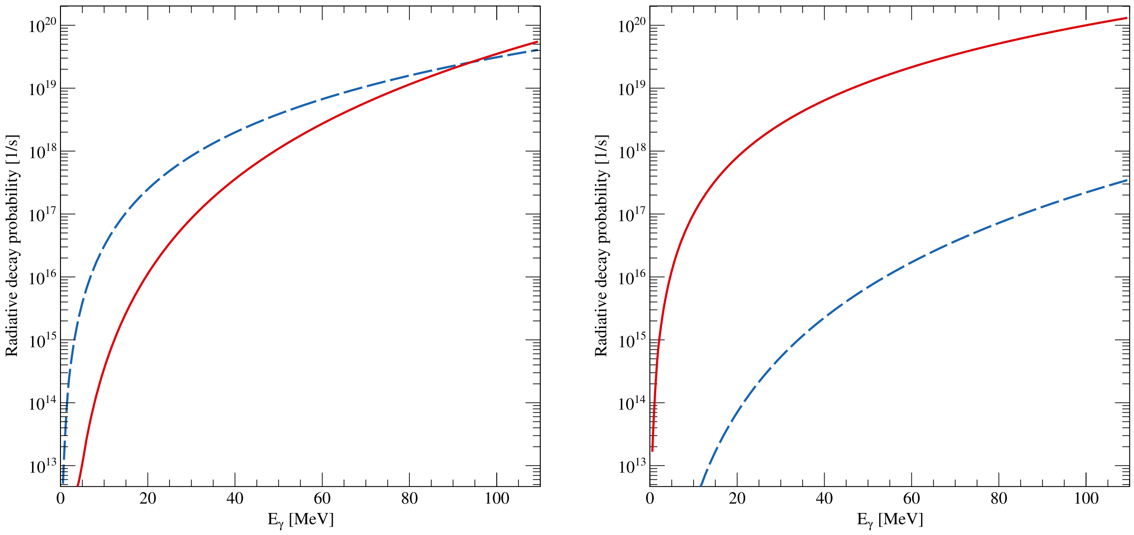

(a) Relative probability of *M1* (blue, dashed line) and *E2* (red, solid line) transitions in ^{48}K.

(b) Relative probability of *M2* (blue, dashed line) and *E1* (red, solid line) transitions in ^{46}K.

Figure A.4: Weisskopf decay probabilities for (a) no parity change in ^{48}K and (b) parity change in ^{46}K. Figure plotted according to the formulae from Ref. [43, p. 69].

Appendix B

Details of excited states

In this appendix, spectra relating to the interpretation of ‘simple’ states (i.e. those that did not require specific additional techniques) are presented.

B.1 ^{47}K(d,p)^{48}K

The ground state of ^{48}K is examined through the comparison of excitation spectra with and without coincident γ-ray detections. These normalised spectra can be seen in **Figure B.1**, and show a decrease in the number of counts in the lowest energy peak. Hence, the ground state is populated in the ^{47}K(d,p) reaction.

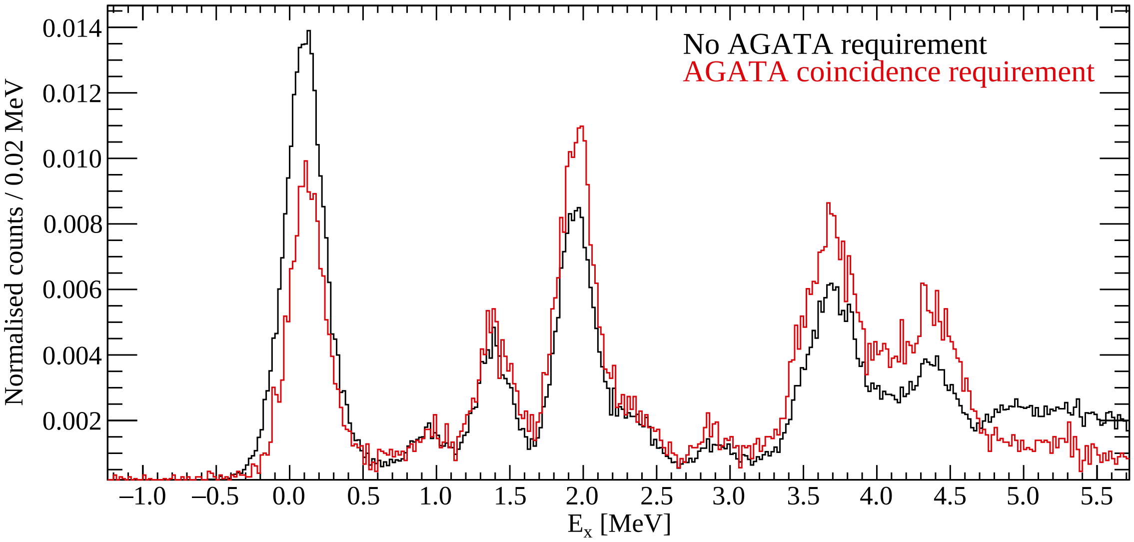

Figure B.1: Normalised counts of ^{48}K with and without a γ-ray coincidence requirement, showing that the coincidence requirement suppresses the lowest energy peak, indicating a population of the ground state.

The 0.143 MeV state in ^{48}K, known in the literature, is strongly populated in this reaction. Only one γ-ray is seen in coincidence with this peak – the transition to the ground state – in line with expectation.

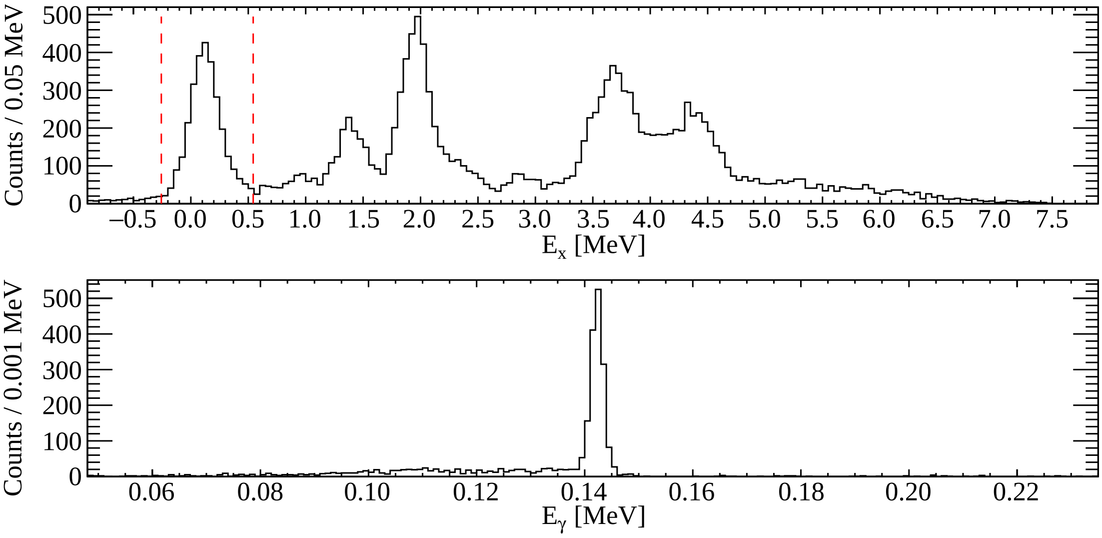

Figure B.2: Gate: $E_x = 0.143 \pm 0.4$ MeV. The only significant γ-ray coincidence is the 0.143 MeV transition.

The novel 0.967 MeV has only coincident decay – the transition to the 1^- ground state. This unique signature supports a 0^- assignment. This state is fed by the 1.978 MeV state, as shown in **Figure B.3**.

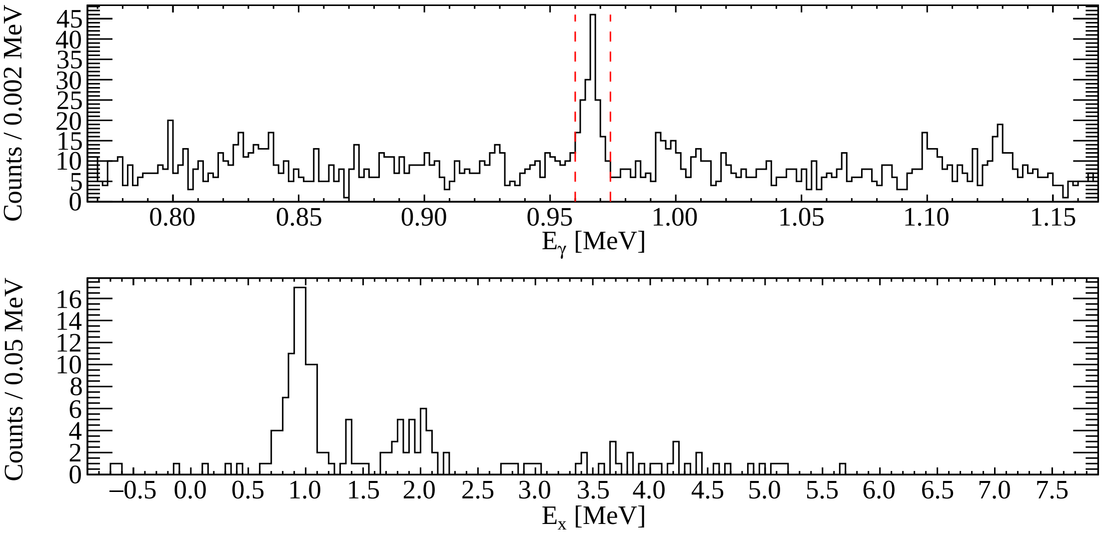

Figure B.3: Gate: $E_\gamma = 0.967$ MeV. Primarily in coincidence with the 0.967 MeV state, with some feeding from 1.978 MeV.

The novel 1.409 MeV state has three observed decays; to the ground state, 0.143 MeV, and 0.279 MeV. The spectrum in **Figure B.4** shows these decays, as well as subsequent de-excitations.

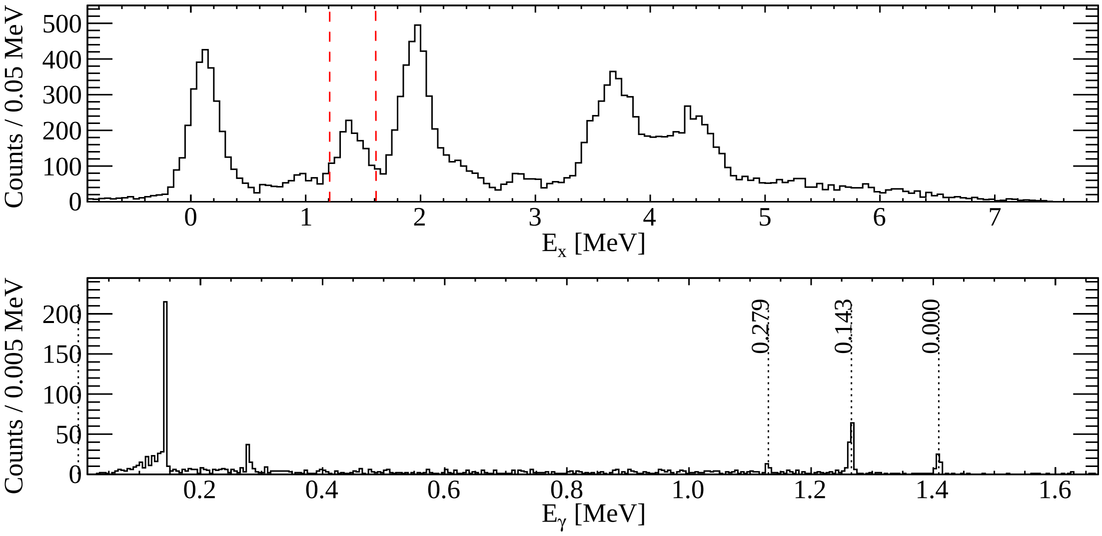

Figure B.4: Gate: $E_x = 1.409 \pm 0.2$ MeV. Transitions are marked with the γ-ray energy subtracted from the state energy. This state decays to the ground state, 0.143 MeV and 0.279 MeV states.

The novel 1.978 MeV state has three observed decays; to the ground state, 0.143 MeV, and 0.967 MeV. The spectrum in **Figure B.5** shows these decays, as well as subsequent de-excitations.

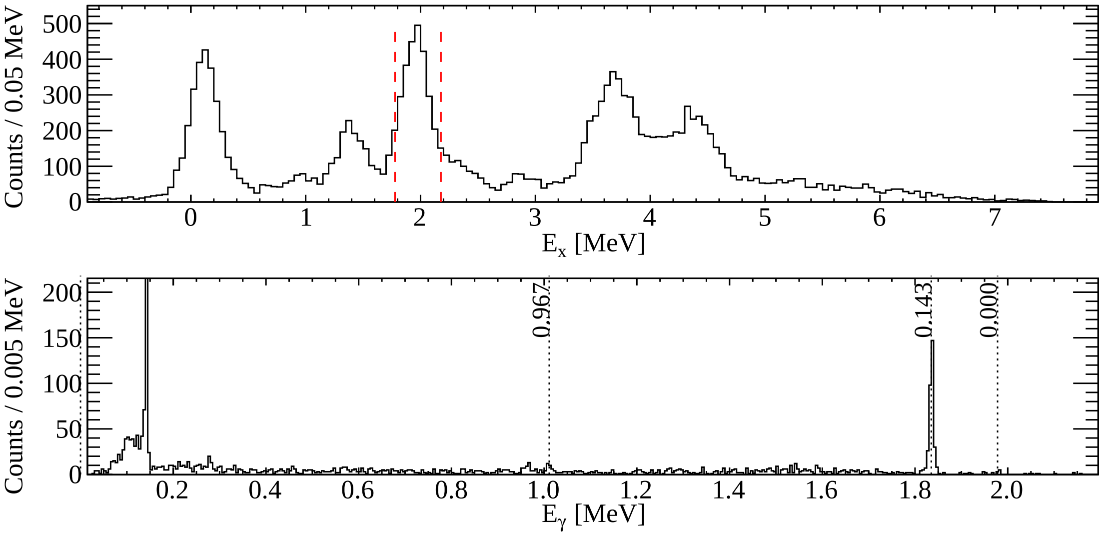

Figure B.5: Gate: $E_x = 1.978 \pm 0.2$ MeV. This state decays nearly exclusively to the 0.143 MeV state, with weak branches to the ground state and 0.967 MeV states.

The novel 2.407 MeV state is not completely resolved from the stronger 1.978 MeV state, and so a background gate is presented in **Figure B.6**. This state decays only to 1^- states, indicating a 0^- assignment.

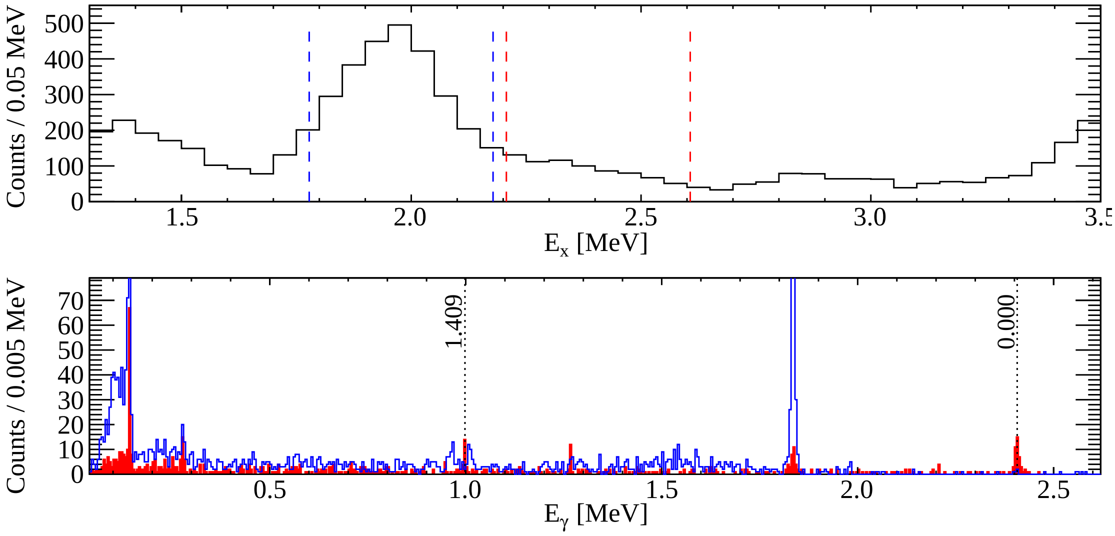

Figure B.6: Gate: $E_x = 2.407 \pm 0.2$ MeV (blue) with background gate on 1.978 MeV (red).

The novel 2.908 MeV state is weakly populated and appears to decay only to the 0.143 MeV ground state. The apparent 0.279 MeV coincidence is background from a poorly resolved weak state.

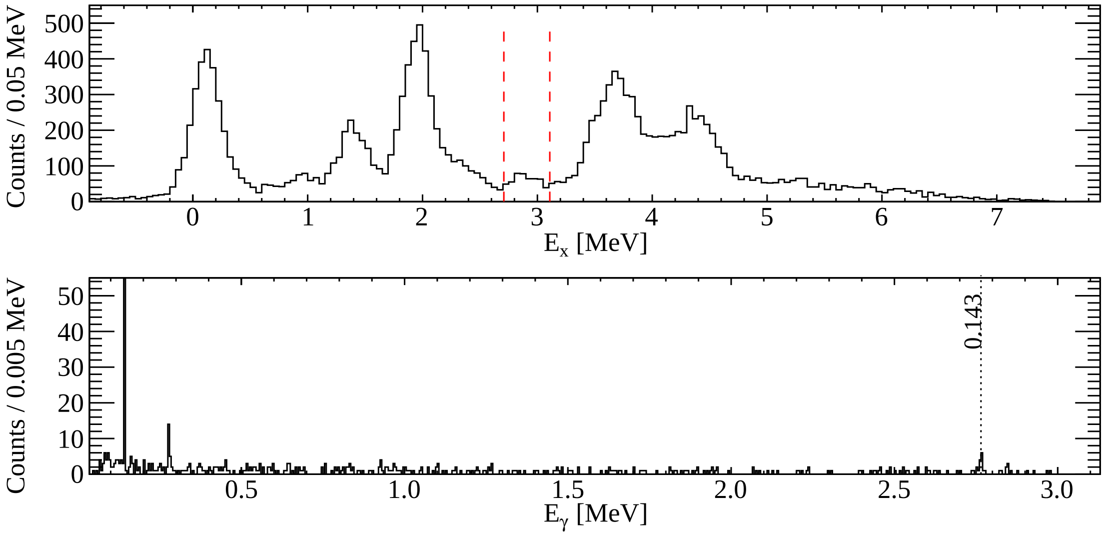

Figure B.7: Gate: $E_x = 2.908 \pm 0.2$ MeV. This state decays only to the 0.143 MeV state.

The novel 3.601 MeV state is the strongest of the pure $\ell = 3$ states, but is poorly resolved from many neighbouring states. As a result, there is a large background component in the coincidence spectra. Despite this, many transitions have been firmly identified as originating from this state, having observed transition to every state in the region of 0 to 1.5 MeV that is accessible by *M1* transition.

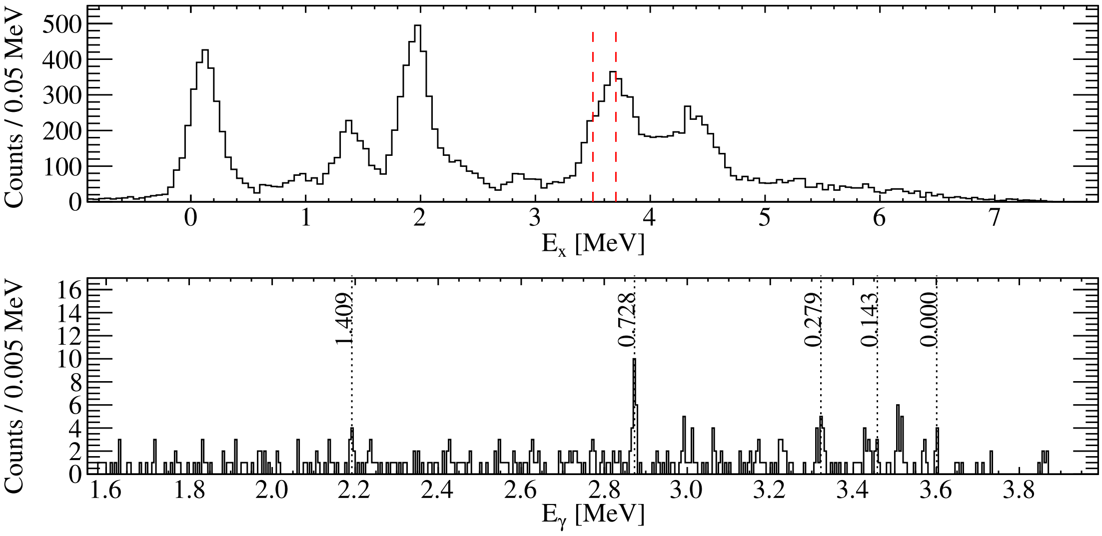

Figure B.8: Gate: $E_x = 3.601 \pm 0.1$ MeV. This state has a very fractured decay pattern – each of these transitions is confirmed by reverse gating.

B.2 ^{47}K(d,t)^{46}K

As in ^{48}K, the ground state of ^{46}K is examined through the comparison of excitation spectra with and without coincident γ-ray detections. These normalised spectra can be seen in **Figure B.9**, and show an elimination of the lowest energy peak when γ-ray coincidences are required. Hence, the ground state is populated in the ^{47}K(d,t) reaction.

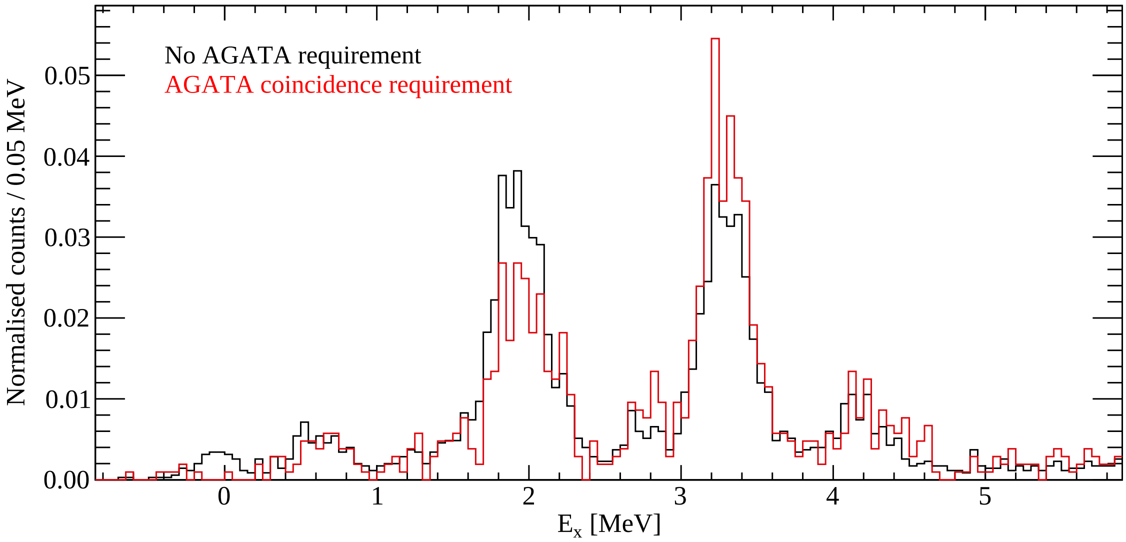

Figure B.9: Normalised counts of ^{46}K with and without a γ-ray coincidence requirement, showing that the coincidence requirement suppresses the peak at 0 MeV, indicating a population of the ground state.

The 1.945 MeV and 2.233 MeV states have been previously observed in the literature, and the 1.945 MeV to ground state decay had been established. New from this work, however, is the 0.288 MeV γ-ray transition, shown in **Figure B.10**. This transition can firmly determine the energy of the higher energy, refining it from the literature value of 2.222 MeV [39].

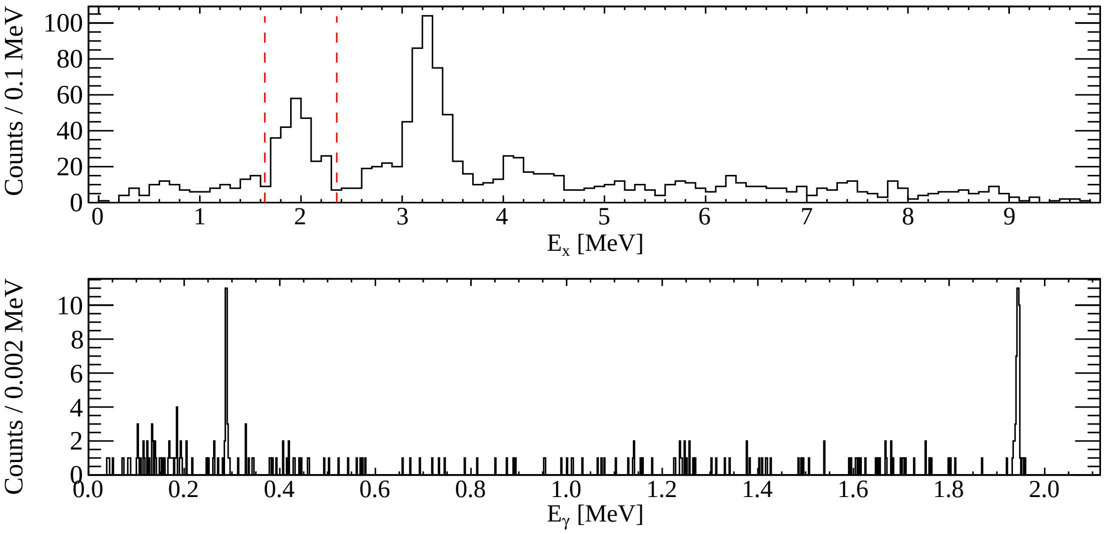

Figure B.10: Gate: $E_x = 2.0 \pm 0.4$ MeV. This gate covers the 1.945 MeV and 2.233 MeV states, with the 1.45 MeV and 0.288 MeV decays clearly visible.

The 2.73 MeV state is not fully resolved from the strong 3.4 MeV doublet, but it is clearly populated by the ^{47}K(d,t) reaction. A ground state decay is observed, as shown in **Figure B.11**. The three-count bin at 1.41 MeV is not at the correct energy to be a decay to the 1.37 MeV state, but an *E1* transition to this state could be allowed.

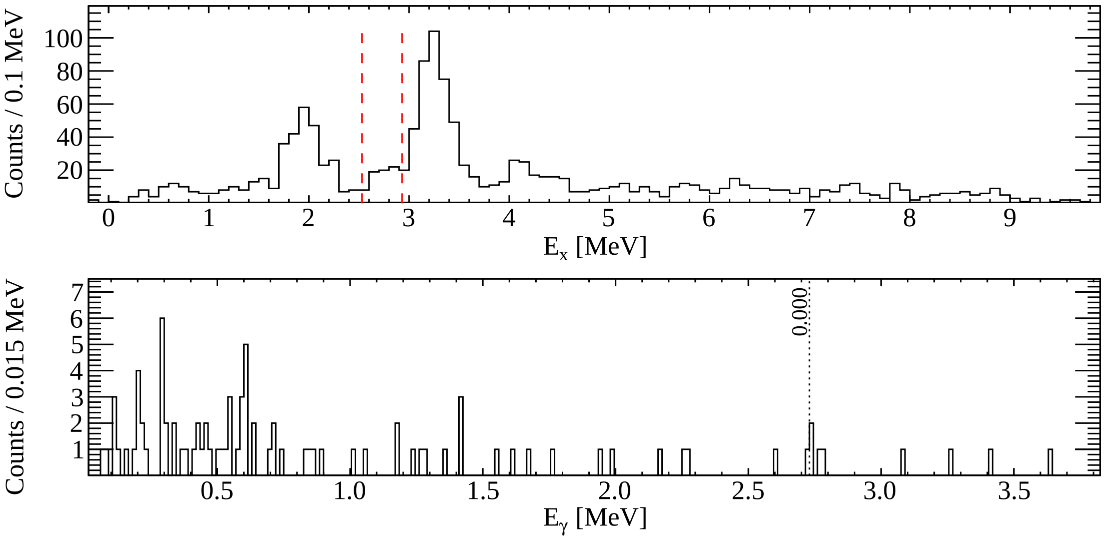

Figure B.11: Gate: $E_x = 2.73 \pm 0.2$ MeV. This peak, which is clear in the E_x spectrum, has a ground state decay that is confirmed by reverse gating.